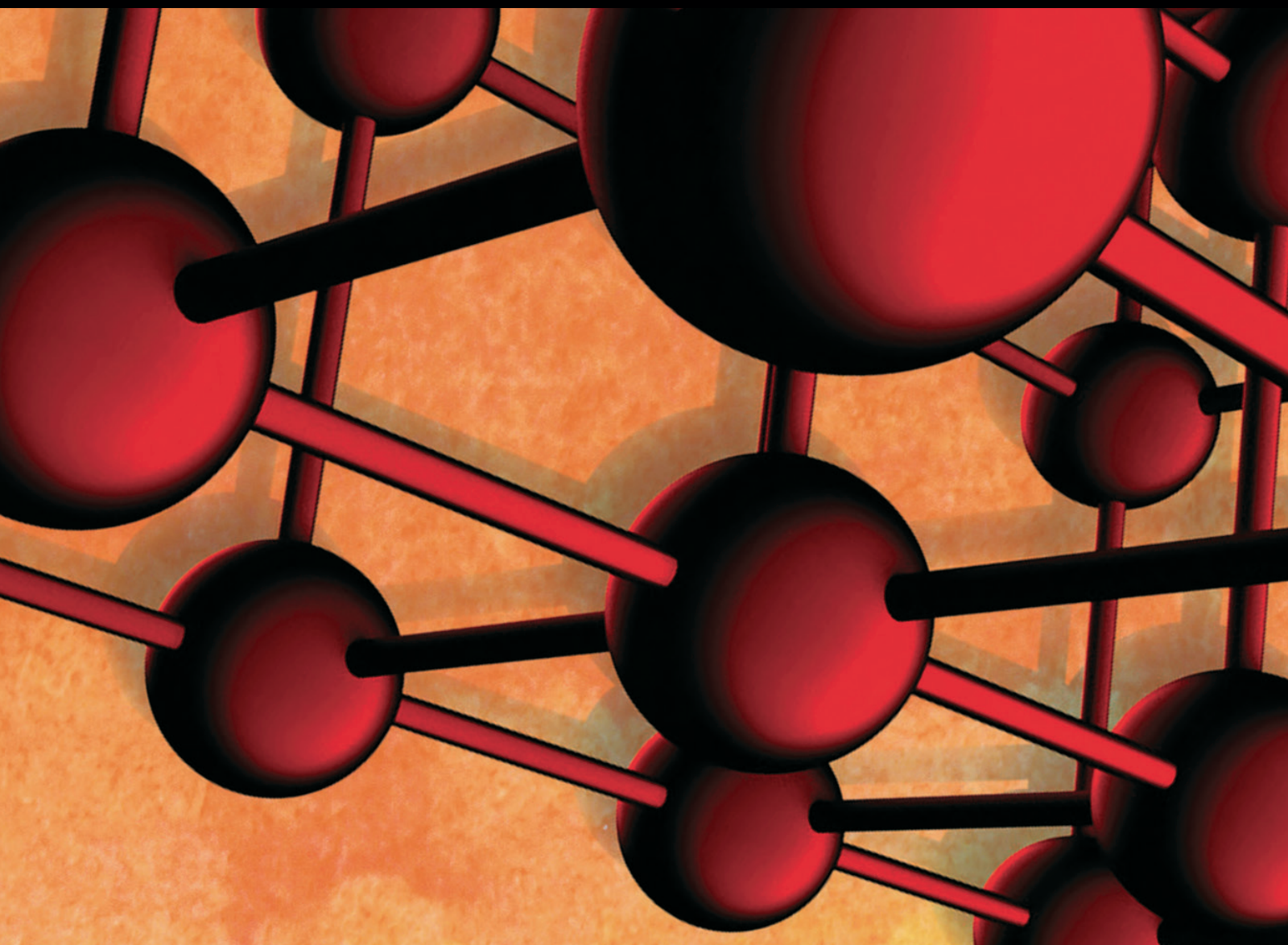


Advances in Materials Science and Engineering

# Integrated Lightweight Composites and Structures with Multifunctional Properties for Engineering Application

Lead Guest Editor: Rujie He

Guest Editors: Kai Wei and Bing Zhang





---

**Integrated Lightweight Composites  
and Structures with Multifunctional  
Properties for Engineering Application**


Advances in Materials Science and Engineering

---

**Integrated Lightweight Composites  
and Structures with Multifunctional  
Properties for Engineering Application**

Lead Guest Editor: Rujie He

Guest Editors: Kai Wei and Bing Zhang



---

Copyright © 2018 Hindawi. All rights reserved.

This is a special issue published in “Advances in Materials Science and Engineering.” All articles are open access articles distributed under the Creative Commons Attribution License, which permits unrestricted use, distribution, and reproduction in any medium, provided the original work is properly cited.

## Editorial Board

- Antonio Abate, Germany  
Michael Aizenshtein, Israel  
Hamed Akhavan, Portugal  
Jarir Aktaa, Germany  
Amelia Almeida, Portugal  
Rajan Ambat, Denmark  
K. G. Anthymidis, Greece  
Santiago Aparicio, Spain  
Raul Arenal, Spain  
Alicia E. Ares, Argentina  
Farhad Aslani, Australia  
Apostolos Avgeropoulos, Greece  
Renal Backov, France  
Markus Bambach, Germany  
Amit Bandyopadhyay, USA  
Massimiliano Barletta, Italy  
Stefano Bellucci, Italy  
Avi Bendavid, Australia  
Brahim Benmokrane, Canada  
Jamal Berakdar, Germany  
Jean-Michel Bergheau, France  
Guillaume Bernard-Granger, France  
Giovanni Berselli, Italy  
Patrice Berthod, France  
Michele Bianchi, Italy  
Hugo C. Biscaia, Portugal  
Antonio Boccaccio, Italy  
Susmita Bose, USA  
H.-G. Brokmeier, Germany  
Steve Bull, UK  
Gianlorenzo Bussetti, Italy  
Jose M. Cabrera, Spain  
Antonio Caggiano, Germany  
Veronica Calado, Brazil  
Marco Cannas, Italy  
Paolo Andrea Carraro, Italy  
Victor M. Castaño, Mexico  
Michelina Catauro, Italy  
Robert Černý, Czech Republic  
Jose Cesar de Sa, Portugal  
Daolun Chen, Canada  
Wensu Chen, Australia  
Francisco Chinesta, France  
Er-Yuan Chuang, Taiwan  
Gianluca Cicala, Italy  
Francesco Colangelo, Italy  
Marco Consales, Italy  
José A. Correia, Portugal  
María Criado, Spain  
Gabriel Cuello, France  
Lucas da Silva, Portugal  
Narendra B. Dahotre, USA  
João P. Davim, Portugal  
Angela De Bonis, Italy  
Abílio De Jesus, Portugal  
Luca De Stefano, Italy  
Francesco Delogu, Italy  
Luigi Di Benedetto, Italy  
Aldo Di Carlo, Italy  
Maria Laura Di Lorenzo, Italy  
Marisa Di Sabatino, Norway  
Luigi Di Sarno, Italy  
Ana María Díez-Pascual, Spain  
Guru P. Dinda, USA  
Nadka Tzankova Dintcheva, Italy  
Hongbiao Dong, China  
Mingdong Dong, Denmark  
Frederic Dumur, France  
Stanislaw Dymek, Poland  
Kaveh Edalati, Japan  
Philip Eisenlohr, USA  
Claude Estournès, France  
Luis Evangelista, Norway  
Michele Fedel, Italy  
Isabel J. Ferrer, Spain  
Paolo Ferro, Italy  
Dora Foti, Italy  
Massimo Fresta, Italy  
Pasquale Gallo, Japan  
Germà Garcia-Belmonte, Spain  
Santiago Garcia-Granda, Spain  
Carlos Garcia-Mateo, Spain  
Georgios I. Giannopoulos, Greece  
Ivan Giorgio, Italy  
Antonio Gloria, Italy  
Vincenzo Guarino, Italy  
Daniel Guay, Canada  
Gianluca Gubbiotti, Italy  
Jenő Gubicza, Hungary  
Xuchun Gui, China  
Benoit Guiffard, France  
Ivan Gutierrez-Urrutia, Japan  
Hiroki Habazaki, Japan  
Simo-Pekka Hannula, Finland  
Akbar Heidarzadeh, Iran  
David Holec, Austria  
Satoshi Horikoshi, Japan  
David Houivet, France  
Rui Huang, USA  
Yi Huang, UK  
Michele Iafisco, Italy  
Erdir Ibrahim, UK  
Saliha Ilcan, Turkey  
Md Mainul Islam, Australia  
Ilia Ivanov, USA  
Alfredo Juan, Argentina  
kenji Kaneko, Japan  
Fuat Kara, Turkey  
Katsuyuki Kida, Japan  
Akihiko Kimura, Japan  
Soshu Kirihara, Japan  
Paweł Kłosowski, Poland  
Jan Koci, Czech Republic  
Fantao Kong, China  
Ling B. Kong, Singapore  
Lingxue Kong, Australia  
Pramod Koshy, Australia  
Hongchao Kou, China  
Alexander Kromka, Czech Republic  
Andrea Lamberti, Italy  
Luciano Lamberti, Italy  
Fulvio Lavecchia, Italy  
Marino Lavorgna, Italy  
Laurent Lebrun, France  
Joon-Hyung Lee, Republic of Korea  
Pavel Lejcek, Czech Republic  
Cristina Leonelli, Italy  
Ying Li, USA  
Yuanshi Li, Canada  
Yuning Li, Canada  
Guang-xing Liang, China  
Barbara Liguori, Italy

Jun Liu, China  
Meilin Liu, Georgia  
Shaomin Liu, Australia  
Yunqi Liu, China  
Zhiping Luo, USA  
Fernando Lusquiños, Spain  
Peter Majewski, Australia  
Georgios Maliaris, Greece  
Muhamamd A. Malik, UK  
Dimitrios E. Manolakos, Greece  
Necmettin Maraşlı, Turkey  
Enzo Martinelli, Italy  
Alessandro Martucci, Italy  
Yoshitake Masuda, Japan  
Bobby Kannan Mathan, Australia  
Roshan Mayadunne, Australia  
Mamoun Medraj, Canada  
Shazim A. Memon, Kazakhstan  
Philippe Miele, France  
A. E. Miroshnichenko, Australia  
Hossein Moayedi, Iran  
Sakar Mohan, India  
Jose M. Monzo, Spain  
Michele Muccini, Italy  
Alfonso Muñoz, Spain  
Roger Narayan, USA  
Rufino M. Navarro, Spain  
Miguel Navarro-Cia, UK  
Ali Nazari, Australia  
Behzad Nematollahi, Australia  
Luigi Nicolais, Italy  
Peter Niemz, Switzerland  
Hiroshi Noguchi, Japan  
Chérif Nouar, France  
Olanrewaju Ojo, Canada  
Dariusz Oleszak, Poland  
Laurent Orgéas, France  
Togay Ozbakkaloglu, Australia  
Nezih Pala, USA  
Marián Palcut, Slovakia  
Davide Palumbo, Italy  
Gianfranco Palumbo, Italy  
A. Maria Paradowska, Australia  
Zbyšek Pavlík, Czech Republic

Matthew Peel, UK  
Alessandro Pegoretti, Italy  
Gianluca Percoco, Italy  
Claudio Pettinari, Italy  
Giorgio Pia, Italy  
Silvia M. Pietralunga, Italy  
Daniela Pilone, Italy  
Teresa M. Piqué, Argentina  
Candido Fabrizio Pirri, Italy  
Marinos Pitsikalis, Greece  
Alain Portavoce, France  
Simon C. Potter, Canada  
Ulrich Prah, Germany  
Viviana F. Rahhal, Argentina  
Carlos R. Rambo, Brazil  
Shahed Rasekh, Portugal  
Manijeh Razeghi, USA  
Paulo Reis, Portugal  
Yuri Ribakov, Israel  
Aniello Riccio, Italy  
Anna Richelli, Italy  
Antonio Riveiro, Spain  
Marco Rossi, Italy  
Sylvie Rossignol, France  
Pascal Roussel, France  
Fernando Rubio-Marcos, Spain  
Francesco Ruffino, Italy  
Mark H. Rummeli, China  
Pietro Russo, Italy  
Antti Salminen, Finland  
F.H. Samuel, Canada  
MariaGabriella Santonicola, Italy  
Hélder A. Santos, Finland  
Carlo Santulli, Italy  
Fabrizio Sarasini, Italy  
Michael J. Schütze, Germany  
Raffaele Sepe, Italy  
Kenichi Shimizu, USA  
Fridon Shubitidze, USA  
Mercedes Solla, Spain  
Donato Sorgente, Italy  
Charles C. Sorrell, Australia  
Andres Sotelo, Spain  
Costas M. Soukoulis, USA

Damien Soulat, France  
Adolfo Speghini, Italy  
Antonino Squillace, Italy  
Manfred Stamm, Germany  
Koichi Sugimoto, Japan  
Baozhong Sun, China  
Sam-Shajing Sun, USA  
Youhong Tang, Australia  
Kohji Tashiro, Japan  
Miguel Angel Torres, Spain  
Laszlo Toth, France  
Achim Trampert, Germany  
Tomasz Trzepieciński, Poland  
Matjaz Valant, Slovenia  
Luca Valentini, Italy  
Ashkan Vaziri, USA  
Lijing Wang, Australia  
Rui Wang, China  
Zhongchang Wang, Portugal  
Lu Wei, China  
Jörg M. K. Wiezorek, USA  
Jiang Wu, UK  
Guoqiang Xie, China  
Dongmin Yang, UK  
Zhonghua Yao, China  
Hemmige S. Yathirajan, India  
Yee-wen Yen, Taiwan  
Wenbin Yi, China  
Ling Yin, Australia  
Tetsu Yonezawa, Japan  
Hiroshi Yoshihara, Japan  
Belal F. Yousif, Australia  
Lenka Zajičková, Czech Republic  
Michele Zappalorto, Italy  
Gang Zhang, Singapore  
Jinghuai Zhang, China  
Li Zhang, China  
Mikhail Zheludkevich, Germany  
Wei Zhou, China  
You Zhou, Japan  
Hongtao Zhu, Australia  
F. J. Fernández Fernández, Spain

# Contents

## **Integrated Lightweight Composites and Structures with Multifunctional Properties for Engineering Application**

Rujie He , Kai Wei , and Bing Zhang

Editorial (2 pages), Article ID 9385203, Volume 2018 (2018)

## **A Study on the Fundamental Quality of Magnesia-Phosphate-Formed Mortar Composites Using Superabsorbent Polymer for Development of Concrete for Biological Panel**

Yun-Wang Choi , Sung-Rok Oh , Cheol-Gyu Kim , and Jae-Heun Lee 

Research Article (8 pages), Article ID 1892127, Volume 2018 (2018)

## **Undrained Dynamic Behavior of Reinforced Subgrade under Long-Term Cyclic Loading**

Min Geng , Debin Wang, and Peiyong Li



Research Article (9 pages), Article ID 5685789, Volume 2018 (2018)

## **Joining of $C_f$ /SiC Ceramic Matrix Composites: A Review**

Keqiang Zhang, Lu Zhang, Rujie He , Kaiyu Wang, Kai Wei , and Bing Zhang

Review Article (15 pages), Article ID 6176054, Volume 2018 (2018)

## **The Bending Responses of Sandwich Panels with Aluminium Honeycomb Core and CFRP Skins Used in Electric Vehicle Body**

Yong Xiao, Yefa Hu, Jinguang Zhang , Chunsheng Song , Xiangyang Huang, Jingui Yu, and Zhaobing Liu

Research Article (11 pages), Article ID 5750607, Volume 2018 (2018)

## **Improving Electromagnetic Shielding Ability of Plaster-Based Composites by Addition of Carbon Fibers**

A. Samkova , P. Kulhavy , V. Tunakova, and M. Petru 


Research Article (14 pages), Article ID 3758364, Volume 2018 (2018)

## **Improvement of the Acoustic Attenuation of Plaster Composites by the Addition of Short-Fibre Reinforcement**

P. Kulhavy , A. Samková , M. Petru , and M. Pechociakova 

Research Article (15 pages), Article ID 7356721, Volume 2018 (2018)

## **Impact Analysis of Brake Pad Backplate Structure and Friction Lining Material on Disc-Brake Noise**

Gongyu Pan and Lei Chen 

Research Article (9 pages), Article ID 7093978, Volume 2018 (2018)

## **Strength and Failure Mechanism of Composite-Steel Adhesive Bond Single Lap Joints**

Kai Wei , Yiwei Chen, Maojun Li, and Xujing Yang 

Research Article (10 pages), Article ID 5810180, Volume 2018 (2018)

## **Mechanical Characterization of Lightweight Foamed Concrete**

Marcin Kozłowski  and Marta Kadela 

Research Article (8 pages), Article ID 6801258, Volume 2018 (2018)

## Editorial

# Integrated Lightweight Composites and Structures with Multifunctional Properties for Engineering Application

Rujie He <sup>1</sup>, Kai Wei <sup>2</sup>, and Bing Zhang<sup>3</sup>

<sup>1</sup>*Institute of Advanced Structure Technology, Beijing Institute of Technology, Beijing 100081, China*

<sup>2</sup>*State Key Laboratory of Advanced Design and Manufacturing for Vehicle Body, Hunan University, Changsha 410082, China*

<sup>3</sup>*Bristol Composites Institute (ACCIS), University of Bristol, Queen's Building, University Walk, Bristol BS8 1TR, UK*

Correspondence should be addressed to Rujie He; [herujie@bit.edu.cn](mailto:herujie@bit.edu.cn)

Received 29 October 2018; Accepted 29 October 2018; Published 18 December 2018

Copyright © 2018 Rujie He et al. This is an open access article distributed under the Creative Commons Attribution License, which permits unrestricted use, distribution, and reproduction in any medium, provided the original work is properly cited.

Traditional composites, including polymer matrix composites (PMCs), metal matrix composites (MMCs), and ceramic matrix composites (CMCs), have been widely investigated for decades. Usually, the lightweight characteristic is the eternal pursuit of the composites and their structures for engineering applications, in order to improve the effective load and lower the cost. Previous works simply focused on the lightweight design of composites and structures but merely focused on the functional design of composites and structures for various engineering application environments, such as high mechanical load, high temperature, corrosion, low thermal expansion, wave absorption, wave transmission, and vibration suppression. Therefore, how to combine the lightweight and multifunctional characteristics has attracted much attention recently.

Therefore, the integrated lightweight and multifunctional composites and structures not only exhibit the lightweight behavior but also present multifunctional characteristics (e.g., load bearing, protective, ablative, heat insulative, wave absorbing and transmitting, vibration suppressing, explosion resistive, low thermal expansive, and anticorrosive properties). The main challenges involved in integrated lightweight and multifunctional composites and structures, such as the design theory and method, fabrication technology, and characterization method, need to be specially focused and studied.

The aim of this special issue is to publish the latest research progress and findings in the field of integrated lightweight and multifunctional composites and structures and to promote the applications of integrated lightweight

and multifunctional composites and structures for engineering.

The paper entitled “Mechanical Characterization of Lightweight Foamed Concrete” focused on the mechanical characterization of lightweight foamed concrete, which shows excellent physical characteristics such as low self-weight, relatively high strength, and superb thermal and acoustic insulation properties. The paper entitled “Strength and Failure Mechanism of Composite-Steel Adhesive Bond Single Lap Joints” described the strength and failure mechanism of composite-steel adhesive bond single lap joints because the joints of composite steel are very important for lightweight structures for engineering applications. The paper entitled “Undrained Dynamic Behavior of Reinforced Subgrade under Long-Term Cyclic Loading” studied the undrained dynamic behavior of reinforced subgrade under long-term cyclic loading, owing to lightweight structures sometimes working under a long-term cyclic loading environment. Sometimes, the lightweight structures sever under impact environments, so the paper entitled “Impact Analysis of Brake Pad Backplate Structure and Friction Lining Material on Disc-Brake Noise” presented the impact analysis study of the brake pad backplate structure and friction lining material on disc brake noise. The fifth paper entitled “A Study on the Fundamental Quality of Magnesia-Phosphate-Formed Mortar Composites Using Superabsorbent Polymer for Development of Concrete for Biological Panel” focused on the fundamental quality of magnesia-phosphate-formed mortar composites using the superabsorbent polymer for development of concrete for the biological panel, owing to this composite



showing excellent absorption ability together with the lightweight characteristic. For the functions of these lightweight structures, the sixth paper entitled “Improvement of the Acoustic Attenuation of Plaster Composites by the Addition of Short-Fibre Reinforcement” investigated the acoustic attenuation of plaster composites by the addition of short-fibre reinforcement. The seventh paper entitled “Improving Electromagnetic Shielding Ability of Plaster-Based Composites by Addition of Carbon Fibers” described a novel composite structure with a high electromagnetic shielding ability. The eighth paper entitled “The Bending Responses of Sandwich Panels with Aluminium Honeycomb Core and CFRP Skins Used in Electric Vehicle Body” described the bending responses of sandwich panels with an aluminium honeycomb core and CFRP skins used in the electric vehicle body. And after all, for significant ceramic matrix composites, typically C/SiC composites were also studied. Joining of C/SiC composites to other materials is very common during the application of lightweight structures; the ninth paper entitled “Joining of C<sub>f</sub>/SiC Ceramic Matrix Composites: A Review” presented a perspective review on the joining technologies of the C/SiC composites by the guest editors.

We do hope this special issue can give some thinking and references of the integrated lightweight and multifunctional composites and structures and can promote their engineering applications.

### **Conflicts of Interest**

The editors declare that they have no conflicts of interest.

*Rujie He  
Kai Wei  
Bing Zhang*

## Research Article

# A Study on the Fundamental Quality of Magnesia-Phosphate-Formed Mortar Composites Using Superabsorbent Polymer for Development of Concrete for Biological Panel

Yun-Wang Choi <sup>1</sup>, Sung-Rok Oh <sup>1</sup>, Cheol-Gyu Kim <sup>1</sup>, and Jae-Heun Lee <sup>2</sup>

<sup>1</sup>Department of Civil Engineering, Semyung University, Jecheon 27136, Republic of Korea

<sup>2</sup>Institute of Technology, Eugene Corporation Co. Ltd., Bucheon 14441, Republic of Korea

Correspondence should be addressed to Sung-Rok Oh; [cgdbs02@nate.com](mailto:cgdbs02@nate.com)

Received 5 January 2018; Revised 20 September 2018; Accepted 26 September 2018; Published 1 November 2018

Guest Editor: Rujie He

Copyright © 2018 Yun-Wang Choi et al. This is an open access article distributed under the Creative Commons Attribution License, which permits unrestricted use, distribution, and reproduction in any medium, provided the original work is properly cited.

The purpose of this study was to investigate the base material of the biological panel as one of the researches for developing the biological panel using (micro)organisms. In order to select the base material for the biological panel, the applicability of the magnesia-potassium-phosphate-foamed mortar composites material using the superabsorbent polymer was evaluated through the evaluation of basic quality and characteristics. Experiments were conducted to evaluate the fluidity, compressive strength, pH, roughness (porosity distribution), and moisture retention (absorbency) of the magnesia-phosphate-foamed mortar composites according to the additional amount of the superabsorbent polymer. Experimental results showed that the addition of a suitable superabsorbent polymer can provide good results in terms of compressive strength, workability, and moisturizing properties (absorbency). As a result, it can be used as a basic quality study data of the biological panel design.

## 1. Introduction

Due to the rapid industrial revolutions around the world and indiscriminate urban development, there is a series of serious environmental problem such as increase of CO<sub>2</sub> emissions, fine dust generation, and increase of cooling energy use due to reduction of the green area [1, 2]. In order to solve this problem, various researches and efforts have been carried out both domestically and externally in order to develop eco-friendly construction materials. However, most of them have been focused on waste resource utilization, carbon abatement type, and environmentally friendly concrete technology [3–10]. These technologies can solve the problem of CO<sub>2</sub> reduction, but it is difficult to take alternative measures to heat island phenomenon and increase of cooling energy use due to increase of city's atmospheric temperature.

In order to compensate for this, there is a way to solve the problem by installing a vertical garden inside and outside the building, but it is difficult to integrate with the exterior wall

of the structure. In addition, complex support structures and expensive maintenance and installation costs increase about three times as compared to the common garden of the same area, making it difficult to commercialize them economically [11]. Although there are sponge, mat type, block type, and lightweight soil, similar to the vertical garden, there are many durability problems [12–17].

To solve this problem, biological panels can be developed and integrated with the structure. Biological panels should be easy to put on (biology), etc., and environment should be created so that it can survive after it is rooted. However, when cement is used as a material for panel fabrication, it forms a high pH, which makes it unsuitable for survival and maintenance of living (micro)organisms [18]. In addition, smooth or dense surface makes it difficult to attach (micro)organisms, and similarly problems arise with nutrients and water supply for (micro)organisms [19].

As one of the basic studies for the development of biological panels, it was investigated whether the

magnesia-phosphate-foamed mortar composites used the superabsorbent polymer. Unlike conventional cement, magnesium-phosphate composites can form neutral pH [19]. In addition, air bubbles can form pores on the surface and inside the matrix, and adsorption of nutrients in the air through the pores can be beneficial for the growth of living (micro)organisms [19].

In addition to these, porous surfaces are important, and their supply to moisture also plays a very important role in the growth of living (micro)organisms. In order to achieve such a purpose, the superabsorbent polymer can be applied. The superabsorbent polymer can absorb more than several times its own mass of moisture, and the absorbed moisture gradually dries. When the superabsorbent polymer is applied to the biological panel, the moisture retention of the panel can be improved.

Accordingly, even in a dry environment, the absorbed moisture of the superabsorbent polymer can be utilized for the purpose of moisture supply of (micro)organisms [19].

Therefore, in this study, a magnesium-phosphate-potassium-formed mortar composites using a superabsorbent polymer was prepared as a parent material of the biological panel, and basic quality characteristics and biological characteristics were examined. The results of this study are used to reflect the quality of the biological panel design.

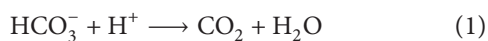
## 2. Experiment Outline

### 2.1. Experimental Materials

**2.1.1. Magnesia-Potassium-Phosphate Cement Mortar Composites.** The magnesia cement used in this experiment was dead magnesia (MgO, hereinafter referred to as "M") with a density of  $3.6 \text{ g/m}^3$  fired at a high temperature of  $1,500^\circ\text{C}$  or more. As a curing agent which reacts with dead magnesia, potassium monophosphate ( $\text{KH}_2\text{PO}_4$ , hereinafter referred to as "P") having a purity of 99% or more and a density of  $2.34 \text{ g/m}^3$  was used. In addition, boric acid ( $\text{H}_3\text{BO}_3$ , hereinafter referred to as "R") was used as a retarding agent in consideration of its workability, and silicate no. 8 (hereinafter referred to as "S") of 95% or more of  $\text{SiO}_2$  was used as a fine aggregate. Magnesia cement requires a retarder for workability due to fast curing time. And since it is made of a dense ceramic structure, it exhibits high strength of about 40 MPa in a short time.

Table 1 shows the chemical composition and physical properties of materials used in the experiment.

**2.1.2. Foaming Agent.** The foaming agent used in this experiment was sodium bicarbonate ( $\text{NaHCO}_3$ , hereinafter referred to as "F") which reacted with potassium ions and reacted with acid ions to generate bubbles. F is a suitable foaming agent that combines with ions generated by an acid-base neutralization reaction to generate a gas, and the chemical reaction formula can be expressed as follows:



The bubbles created through this bond create a rough surface through the voids inside and outside the mortar,

TABLE 1: The physical and chemical composition of the materials used in the experiments.

Type	Purity (%)	$\text{Al}_2\text{O}_3$ (%)	$\text{SiO}_2$ (%)	MgO (%)	Density ( $\text{g/m}^3$ )
M	96	0.1	1.1	95.6	3.6
P	99	—	—	—	2.34
R	99.5	—	—	—	1.4
S	95	—	95	—	2.65

which facilitates the absorption and storage of water and the adsorption of nutrients in the atmosphere [20].

**2.1.3. Superabsorbent Polymers (SAP).** The superabsorbent polymer used in this study was an acrylic acid polymer, sodium salt (sodium polyacrylate). The superabsorbent polymer is a white powder which is capable of absorbing water several hundred times its own weight. When the water is absorbed, the volume expands and reaches gel state. The swelling characteristics of such a superabsorbent polymer vary depending on the interparticle density, the chemical structure of the superabsorbent polymer, the pH of the absorbed liquid, the temperature, and the ion concentration.

**2.1.4. Experimental Plan.** In this study, first, data were collected for magnesium-phosphate-formed mortar composites (SMPFC) using the superabsorbent polymer. Through preliminary experiments, the data of more than 10 MPa of the target strength were obtained by using the water/binder ratio (W/B) 30%, MgO :  $\text{KH}_2\text{PO}_4$  ratio (P : M) 1 : 0.5, fine aggregate volume/total mortar volume ratio ( $V_s/V_m$ ) 10%, retardation 3%, and foaming agent 0.5%. Therefore, 4 levels (0.25, 0.5, 0.75, and 1.0%) were prepared for data acquisition according to SAP addition. In addition, the flow characteristics, compressive strength, pH, roughness, and moisture retentivity were measured. The bubbles were applied in the postfoaming mode. The compressive strength was set to 10 MPa or more in terms of landscaping design at 6 hours, 1 day, 3 days, and 7 days of age in accordance with the characteristics of magnesia cement. Table 2 shows the mixing ratio of SMPFC used in the experiment.

### 2.2. Experimental Method

**2.2.1. Mixing of SMPFC.** The SMPFC was subjected to dry mixing with M, P, R, and SAP for about 2 minutes. Then, the blend was then mixed with the compounding water for 2 minutes at the low speed and then for 3 minutes at the high speed. Thereafter, additional water containing F was added, and the mixture was further mixed at the high speed for one minute.

**2.2.2. Extra Water (eW) Decision.** SAP rapidly absorbs moisture when exposed to moisture. Also, the amount of absorbed water increases with time. For this reason, the unit water quantity sharply decreases, the fluidity decreases, and the workability decreases. In addition, magnesia cement

TABLE 2: Mix design.

Type	W/B (%)	Binder		R	F	SAP	Extra water (eW)
		P	M				
SMPFC-P						—	—
SMPFC-0.25						0.25% on binder	10% on W
SMPFC-0.5	35	1	0.5	3% on M	0.5% on binder	0.5% on binder	16% on W
SMPFC-0.75						0.75% on binder	22% on W
SMPFC-1.0						1.0% on binder	27% on W

requires a large amount of unit water, unlike ordinary cement. This problem can be solved by adding additional water [21].

Previous studies have shown that SAP exhibits maximum absorption after 10 minutes of contact with water and is shaped like a gel [22]. Therefore, additional water should be added before reaching maximum absorption.

As a result of the preliminary test, it was found that, to achieve the target slump, extra water should add about 6% of the unit water when the SAP is increased by 0.25%.

**2.2.3. Flow.** The flow of SMPFC was measured in accordance with the “KS L 5105 Hydraulic Cement Mortar Compressive Strength Test Method”.

**2.2.4. Compressive Strength.** The compressive strength of SMPFC was cubic-type specimens of 50 mm × 50 mm × 50 mm prepared according to “KS L 5105 Compressive Strength Test Method of Hydraulic Cement Mortar,” followed by curing. Afterwards, the sample was demolded, and the compressive strength was measured by universal testing (UTM) at each age.

**2.2.5. pH.** The pH of SMPFC was measured in accordance with KS M 0011 “Method for measuring pH of aqueous solution.” Also, the pH of SMPFC was measured according to age.

**2.2.6. Surface Roughness.** The roughness measurement of SMPFC was measured by relative comparison with the surface of the bubble-free reference specimen. Roughness is an important factor in the application of biological panels because it is one of the indicators to induce adsorption on the surface of rainwater or nutrients in the air.

**2.2.7. Moisturizing Property.** The moisture retention (moisture content) of SMPFC was measured by wetting curing of the specimen for one day according to KS F 2459 “Test method of apparent density, water content, water absorption, and compressive strength of foam concrete”. Thereafter, the mass of the dried sample in the drying furnace was measured.

### 3. Experimental Results and Discussion

**3.1. Flow.** Figure 1 shows the flow measurement result according to the addition amount of SAP of SMPFC. As a result of the experiment, the flow value decreased by about

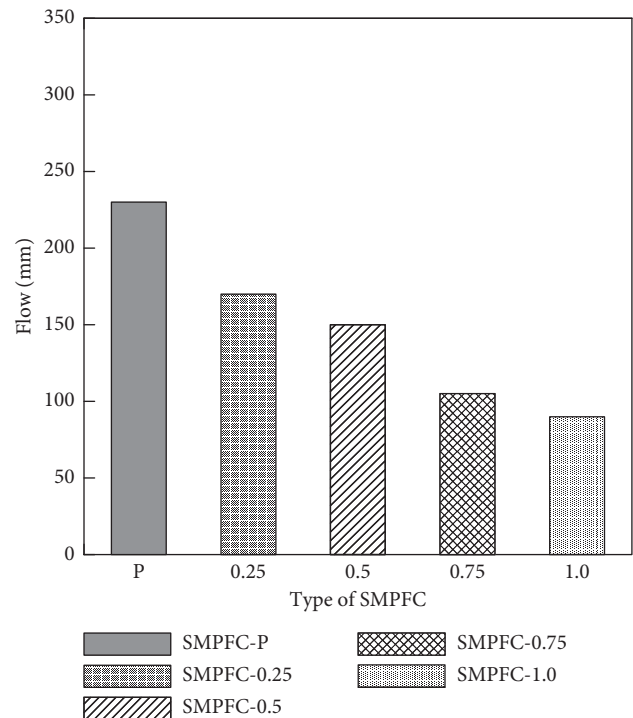


FIGURE 1: Test results of flow (extra water not added).

10% every time the SAP addition amount was increased by 0.25% without determining the additional extra water (eW). The cause of this phenomenon is considered to be the property of absorbing moisture of SAP. However, if eW is added as shown in Figure 2, the target flow can be satisfied.

**3.2. Compressive Strength.** Figures 3–6 show the results of compressive strength measurement according to the additional amount of SAP of SMPFC, and the results of the compressive strength test at 6 hours, 1 day, 3 days, and 7 days of age are shown. The compressive strength at 6 hours did not achieve the target strength in all cases. Also, the compressive strength at 1 and 3 days was more than 10 MPa for plain. A mix with SAP that could achieve the target intensity was possible after 7 days. The compressive strength of SAP 0.25% at 7 days was above 12 MPa and decreased proportionally with increasing SAP. The compressive strength of SAP 0.5% was about 8 MPa, and the compressive strength of SAP 0.75 and 1.0% was less than 5 MPa lower than the target strength. Overall, as the amount of SAP increased, the compressive strength decreased, and the specimen with 1.0% SAP was easily destroyed. However, when the addition

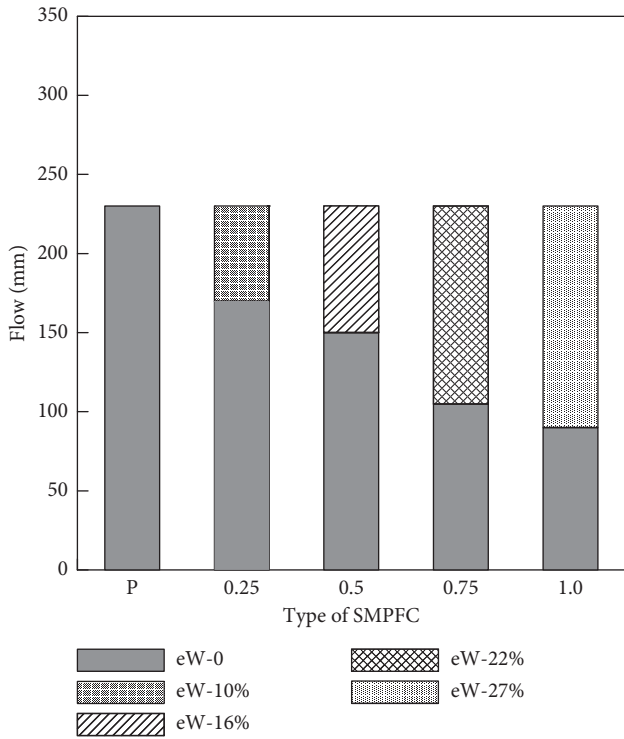


FIGURE 2: Test results of flow (extra water added).

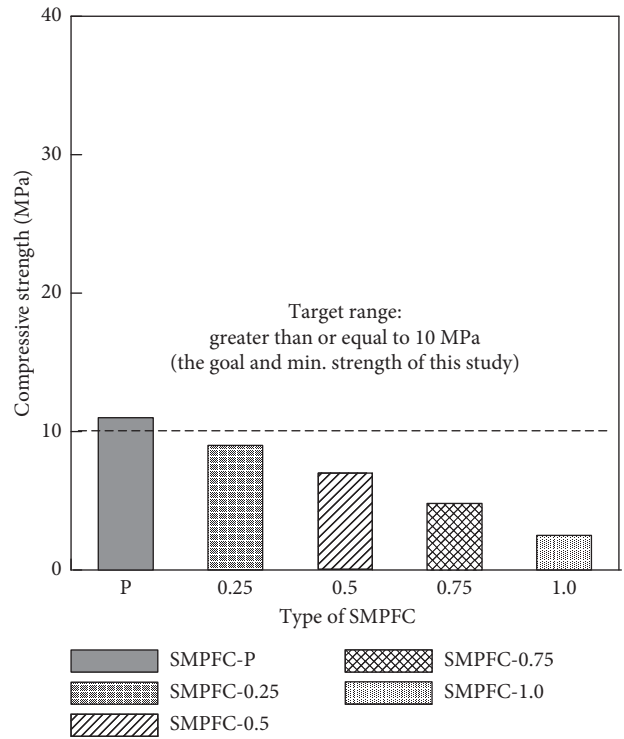


FIGURE 4: Test results of compressive strength (1D).

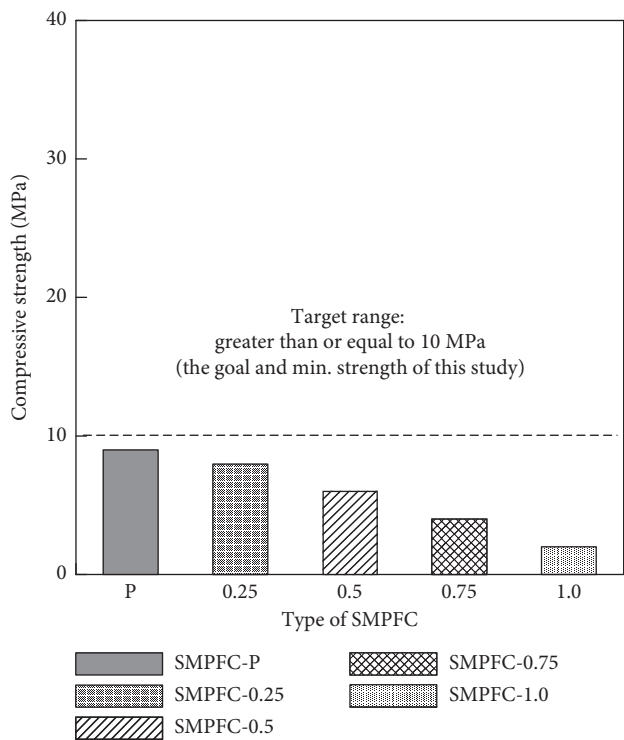


FIGURE 3: Test results of compressive strength (6H).

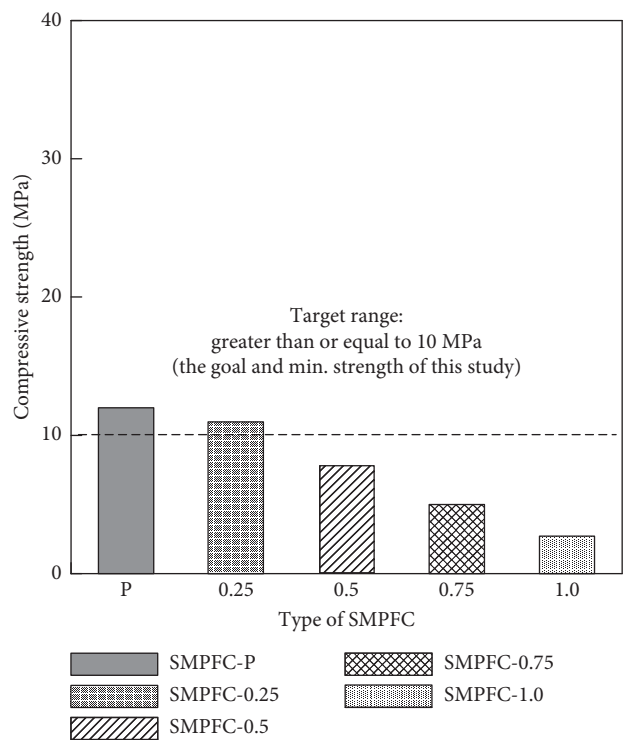


FIGURE 5: Test results of compressive strength (3D).

amount of SAP was 0.25%, similar results were obtained. Therefore, if the optimum amount of SAP is to be found, it will be possible to control the strength when applying the biological panel.

3.3. pH. Figure 7 shows the pH measurement results of SMPFC at 6 hours, 1 day, 3 days, and 7 days. As a result of the experiment, the pH of the specimen tended to increase with age. Magnesia cement was measured at pH 7-9

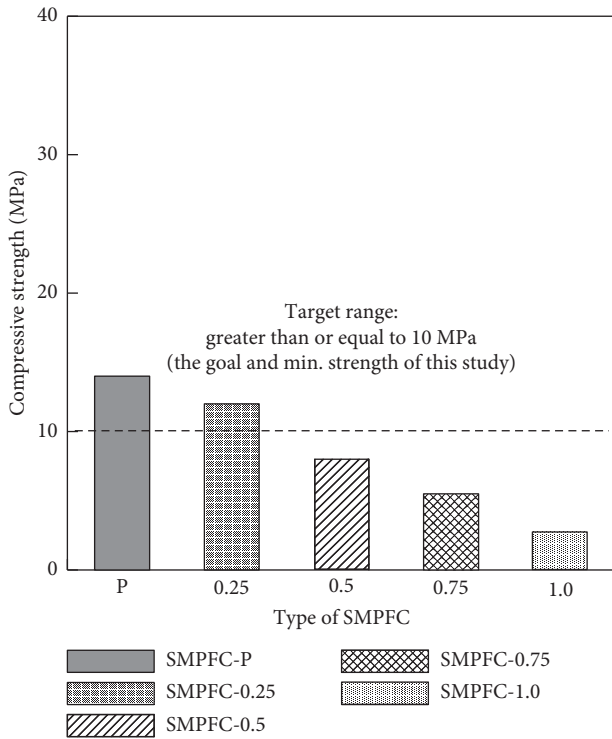


FIGURE 6: Test results of compressive strength (7D).

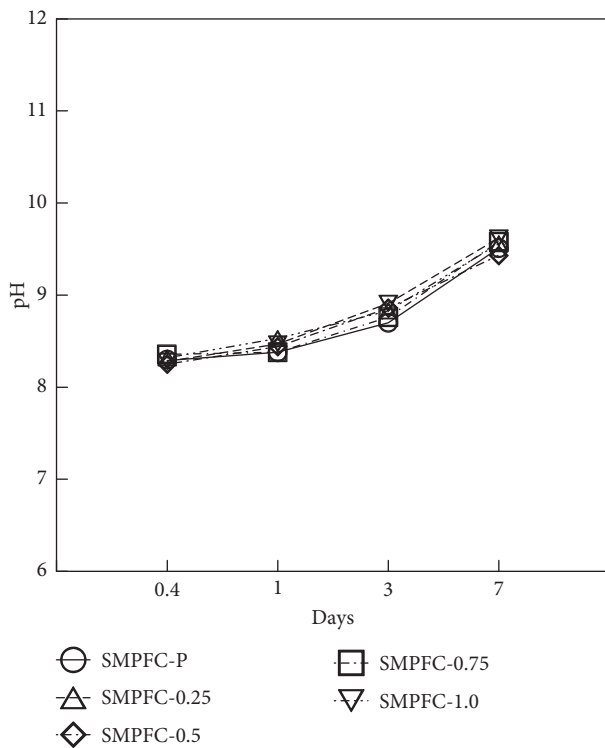


FIGURE 7: pH measurement results of SMPFC.

depending on the type of the phosphate used in the formulation. The SAP used in the experiment was a material with a pH of 6.5 and showed no significant effect on the pH change of SMPFC. The pH at 7 days was measured as 9. Since

the matrix for biological panels is important for the survival of (micro)organisms, it is necessary to examine the pH. From these results, SMPFC, which is a neutral region, would be a favorable condition for the survival environment of (micro)organisms.

**3.4. Surface Roughness.** Figure 8 shows the result of measuring the surface roughness of the SMPFC. It found that the pore depths of the 0.25% are in the range of 1.0–0.005 mm and the pore depths of the 0.5% SAP additions are in 0.1 mm. And pores visible by the naked eye were observed from the micropores.

In the case of 0.75% and 1.0% of SAP additions, SAP was observed on the surface because the amount of SAP added was too large. In addition, it was confirmed that the effect of the foaming agent was hardly observed. The reason for this is that a considerable amount of SAP absorbs moisture quickly and suppresses bubble generation. Figure 9 shows the distribution of voids on the surface of the bubbled test piece. These results suggest that SMPFC with a rough surface due to bubbles will be an advantageous growth condition of (micro)organisms and will be advantageous for the adsorption of nutrients in the air.

**3.5. Moisturizing Property.** Figures 10–14 show the measurement results of moisture content (moisture content) according to the addition amount of SAP of SMPFC. The test roughly evaluated the amount of moisture absorbed by the test piece and SAP through the pores generated on the inside and the surface of the test piece. A qualitative evaluation was performed on the assumption that the larger the pores, the more the SAP could contain in the pores and absorb a large amount of water. The weight of the dried specimen was measured first, and then, the weight of the specimen immersed in water for one day was measured. Then, the period of reaching the dry weight at room temperature was measured.

As shown in Figures 10–14, the moisture retention of SMPFC-P was about 10% larger than that of dry weight. And SMPFC-0.25 was 5% higher than SMPFC-P. As the SAP increased by 0.25%, it increased continuously by about 5%. These results show that the amount of SAP added affects the moisture retention, and the sample without SAP showed a drying time about 3 days faster than the sample with SAP added. As the amount of SAP increased, the drying time at room temperature tended to increase by 2 to 3 days compared to that of SMPFC-P. In the case of the sample with 1.0% SAP content, the complete drying time was about 9 to 10 days. These results suggest that when applied as a matrix for biological panels, the addition of SAP improves the moisture retention and absorbs moisture in the air, which may have a positive effect on the growth of the organism. However, when the amount of SAP increases, it will decrease in compressive strength and durability. Therefore, the optimal amount of SAP should be reviewed. Figure 15 shows the SAP that absorbed moisture inside the test.

These results suggest that SMPEC with improved moisture retention by SAP may contribute to the water supply of (micro)organisms to some extent. In addition, it is

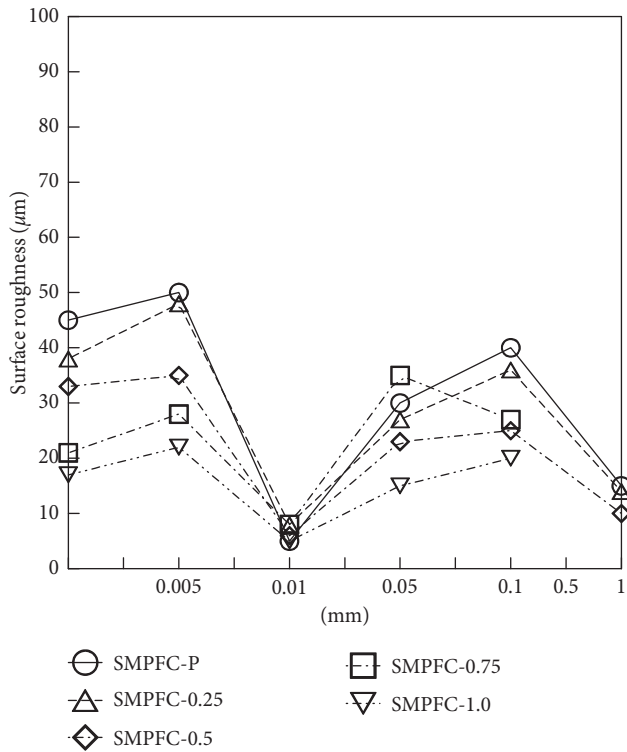


FIGURE 8: Surface roughness results of SMPFC.

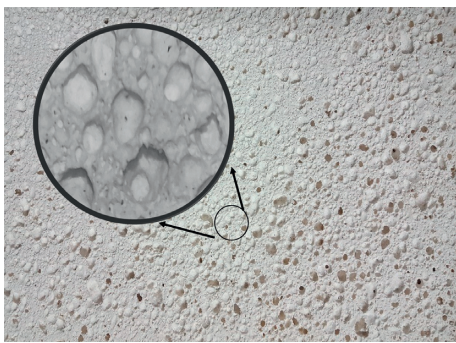


FIGURE 9: Surface of SMPFC.

considered that the moisturizing effect in the atmospheric moisture or rainy weather will be further increased.

#### 4. Conclusion

As one of the basic studies for the development of biological panels, it is investigated that the magnesia-phosphate-foamed mortar composites using the superabsorbent polymer. The following conclusions were obtained:

- (1) The magnesia-potassium-phosphate-foamed mortar composites using a superabsorbent polymer were able to satisfy the target flow when extra water was added according to the mixing ratio of the superabsorbent polymer.
- (2) The magnesia-potassium-phosphate-foamed mortar composites using a superabsorbent polymer showed a tendency to decrease in compressive strength

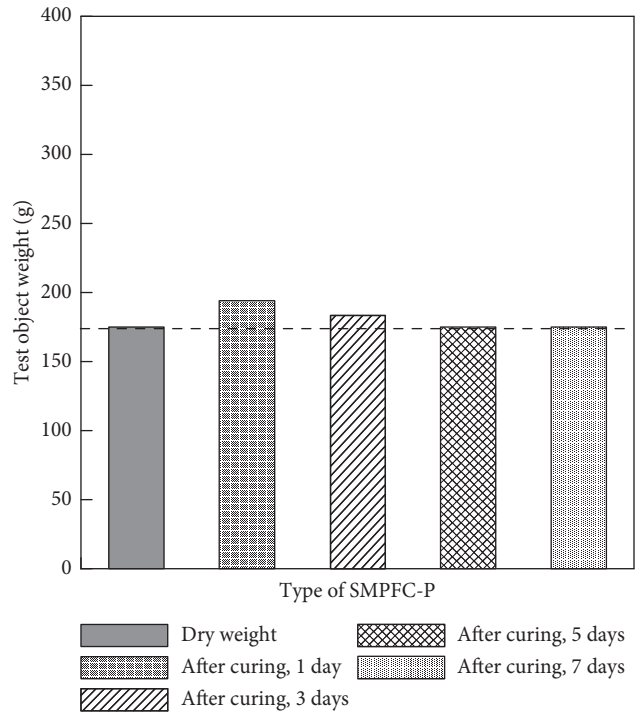


FIGURE 10: Test results of moisture content (plain).

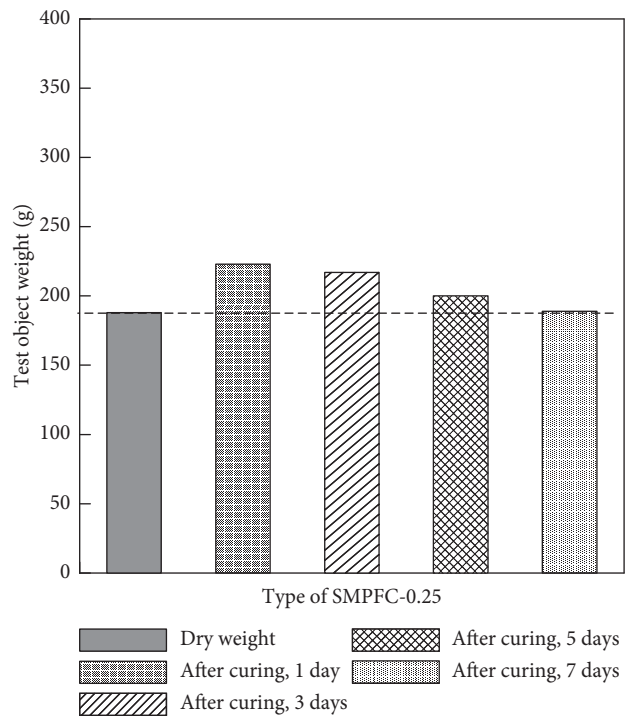


FIGURE 11: Test results of moisture content (SAP 0.25%).

depending on the mixing ratio of the superabsorbent polymer. The mixing ratio of the superabsorbent polymer satisfying the target strength was found to be within 0.25%.

- (3) The magnesia-potassium-phosphate-foamed mortar composites using a superabsorbent polymer

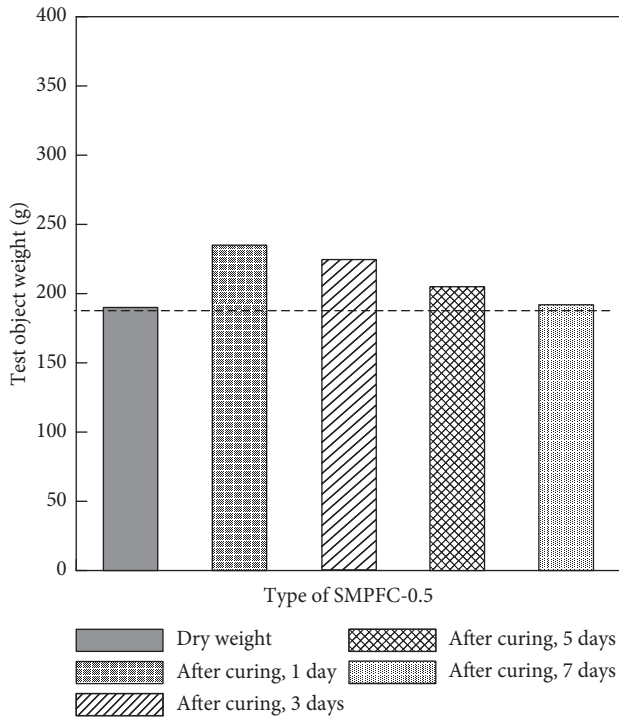


FIGURE 12: Test results of moisture content (SAP 0.50%).

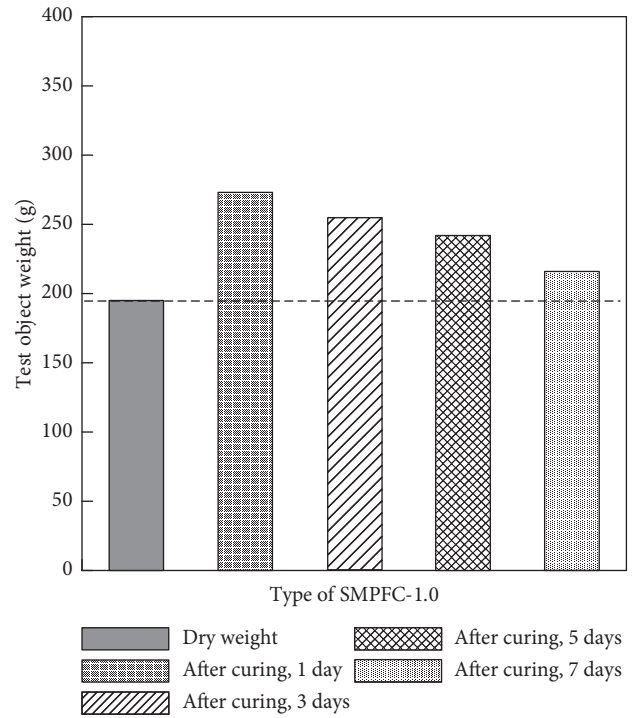


FIGURE 14: Test results of moisture content (SAP 1%).

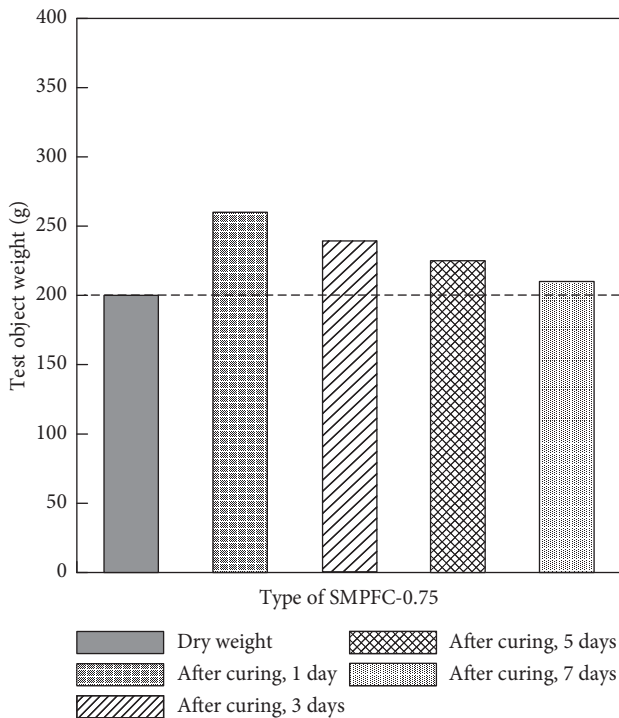


FIGURE 13: Test results of moisture content (SAP 0.75%).

showed a tendency to increase in water content according to the mixing ratio of the superabsorbent polymer. It also formed a roughened surface by bubbles.

From these results, it was confirmed that the optimum range of the superabsorbent polymer satisfying the

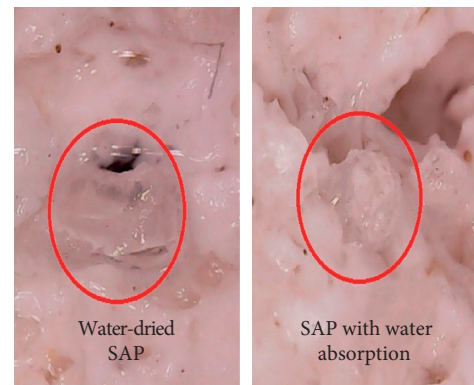


FIGURE 15: SAP absorbed inside the specimen.

target strength was 0.25%. In addition, the rough surface by the foaming agent and the moisture retention by a superabsorbent polymer will be beneficial to rooting and growth conditions of (micro)organisms. As a sequential study, studies on biological acceptability and the growth of (micro)organisms should be accompanied.

### Data Availability

The data used to support the findings of this study are available from the corresponding author upon request.

### Conflicts of Interest

The authors declare that there are no conflicts of interest regarding the publication of this paper.



## Acknowledgments

This research was supported by a grant (17CTAP-C114646-02) from Construction Technology Research Program funded by Ministry of Land, Infrastructure and Transport of Korean government.

## References

- [1] K. Perini, M. Ottel , E. Haas, and R. Raiteri, "Greening the building envelope, faade greening and living wall systems," *Open Journal of Ecology*, vol. 1, no. 1, pp. 1–8, 2011.
- [2] A. Eggert, N. H ubner, S. Klausch, U. Karsten, and R. Schumann, "Quantification of algal biofilms colonising building materials: chlorophyll a measured by PAM-fluorometry as a biomass parameter," *Biofouling*, vol. 22, no. 2, pp. 79–90, 2006.
- [3] C. G. Han and S. G. Park, *Eco-Friendly Ready Mixed Concrete Using Waste Materials and by-Products*, Magazine of the Korea Concrete Institute, Republic of Korea, 2016.
- [4] H.-G. Lee, M.-H. Gong, and Y.-S. Jung, *Field Application and Manufacturing Technology of Low Carbon Ultra High Strength Green PHC Pile using High Volume Ground Granulated Blast Furnace Slag*, Magazine of the Korea Concrete Institute, Republic of Korea, 2016.
- [5] T. W. Kim and C. H. Kang, "The self-healing and ageing effect of OPC-GGBFS cement in sea-water and tap-water," *Journal of the Korea Concrete Institute*, vol. 29, no. 1, pp. 11–21, 2017.
- [6] L. Ferrara, V. Krelani, and M. A. Carsana, "Fracture testing based approach to assess crack healing of concrete with and without crystalline admixtures," *Construction and Building Materials*, vol. 68, pp. 535–551, 2014.
- [7] Z. Jiang, W. Li, and Z. Yuan, "Influence of mineral additives and environmental conditions on the self-healing capabilities of cementitious materials," *Journal of Cement and Concrete Composites*, vol. 57, pp. 116–127, 2015.
- [8] I. You, C.-I. Jeong, C. Lyu, G. Lee, and G. Zi, *State of Research on High Durable Concrete with Waste Glass Powder for Road Structure*, Magazine of the Korea Concrete Institute, Republic of Korea, 2017.
- [9] C.-W. Baek, H.-S. Kim, S.-W. Choi, H.-T. Jo, and D.-H. Ryu, "Durability assessment of high strength concrete with high volume mineral admixture," *Journal of the Korea Concrete Institute*, vol. 27, no. 6, pp. 641–649, 2015.
- [10] Y. Halit, Y. Mert, Y. Husyinn, A. Serdar, and T. Selcuk, "Mechanical properties of reactive powder concrete containing high volumes of ground granulated blast furnace slag," *Journal of Cement and Concrete Composite*, vol. 32, no. 8, pp. 639–648, 2010.
- [11] J.-K. Jeon, Y.-S. An, and E.-J. Kim, *Performance Evaluation Study on Green-wall System Using Moss*, Magazine of the Korea Concrete Institute, Republic of Korea, 2014.
- [12] J. S. Lee, S. H. Kim, Y. S. Shin, and C. Hong, "A fundamental experiment of the artificial soil mixture using stone sludge burning pellet for applying to green roof soil," *Proceedings of the Korea Concrete Institute*, vol. 2012, no. 11, pp. 209–210, 2012.
- [13] H.-R. Gkim and T.-M. Ahn, "Cafeteria users' preference for an indoor green-wall in a university dining Hall," *Journal of Korean Institute of Landscape Architecture*, vol. 43, no. 6, pp. 62–72, 2015.
- [14] S. R. Choi, Y. S. Kim, and P. S. Yoon, "The management plan for the maintenance of the green-wall colors-focusing on the eco plaza," in *Proceedings of Korean Society of Color Studies*, pp. 38–44, 2013.
- [15] M. Ottele, K. Perini, A. L. A. Fraaij, E. M. Haas, and R. Raiteri, "Comparative life cycle analysis for green facades and living wall systems," *Energy and Buildings*, vol. 43, no. 12, pp. 3419–3429, 2011.
- [16] K. Perini, M. Ottele, E. M. Haas, and R. Raiteri, "Vertical greening systems, a process tree for green facades and living walls," *Urban Ecosystems*, vol. 16, no. 2, pp. 1–13, 2009.
- [17] H. E. Wright Wendel, R. K. Zarger, and J. R. Mihelcic, "Accessibility and usability: green space preferences, perceptions, and barriers in a rapidly urbanizing city in Latin America," *Landscape and Urban Planning*, vol. 107, no. 3, pp. 272–282, 2012.
- [18] T. H. Kim, F. Q. Li, T. W. Ahn, I. S. Choi, and J. M. Oh, "Research on improvement of water purification efficiency by concrete using bio film," *Journal of Environmental Impact Assessment*, vol. 20, no. 6, pp. 815–821, 2011.
- [19] S. Manso, W. D. Muynck, I. Segura et al., "Bioreceptivity evaluation of cementitious materials designed to stimulate biological growth," *Science of the Total Environment*, vol. 481, pp. 232–241, 2014.
- [20] C. Ma and B. Chen, "Experimental study on the preparation and properties of a novel foamed concrete based on magnesium phosphate cement," *Construction and Building Materials*, vol. 137, pp. 160–168, 2017.
- [21] S. H. Kang, J. Moon, and S. G. Hong, "Effect of internal curing by super-absorbent polymer (SAP) on hydration, autogenous shrinkage, durability and mechanical characteristics of ultra-high performance concrete (UHPC)," *Journal of the Korea Concrete Institute*, vol. 28, no. 3, pp. 317–328, 2016.
- [22] O. M. Jensen and P. F. Hansen, "Water-entrained cement-based materials: II. Experimental observations," *Cement and Concrete Research*, vol. 32, no. 6, pp. 973–978, 2002.

## Research Article

# Undrained Dynamic Behavior of Reinforced Subgrade under Long-Term Cyclic Loading

Min Geng <sup>1,2</sup>, Debin Wang,<sup>2</sup> and Peiyong Li<sup>2</sup>

<sup>1</sup>*Institute of Geotechnical Engineering, Dalian University of Technology, Dalian 116024, China*

<sup>2</sup>*School of Civil Engineering, Dalian JiaoTong University, Dalian 116028, China*

Correspondence should be addressed to Min Geng; [gengmin@dlut.edu.cn](mailto:gengmin@dlut.edu.cn)

Received 26 December 2017; Revised 1 September 2018; Accepted 12 September 2018; Published 23 October 2018

Guest Editor: Rujie He

Copyright © 2018 Min Geng et al. This is an open access article distributed under the Creative Commons Attribution License, which permits unrestricted use, distribution, and reproduction in any medium, provided the original work is properly cited.

To study the dynamic behavior of reinforced subgrade, a series of undrained cyclic triaxial tests of reinforced soil (the specimen a height of 50 cm and a diameter of 20 cm) were performed in this paper. The specimens were tested by varying confining pressure, vibration frequency, dynamic stress amplitudes, and reinforced layers. Orthogonal experiment is a better way to optimize the process of experiment. Impact on dynamic behavior of the reinforced soil specimens is discussed through orthogonal design of experiments in four factors and three levels. This study has demonstrated that the order of dynamic elastic modulus of reinforced soil is influenced by dynamic stress amplitude, frequency, reinforced layer, and confining pressure within changing in factor level. The dynamic stress amplitude has great influence on the dynamic elastic modulus of reinforced soil. The bearing capacity and dynamic elastic modulus of reinforced subgrade decrease slightly with the increase of dynamic strain. Frequency has an influence on the dynamic elastic modulus. It is shown that the cumulative strain of reinforced soil is related to the vibration frequency. The test results also exemplify the reinforced subgrade restrict lateral displacement of subgrade and reduce settlement of subgrade under long-term cyclic loading.

## 1. Introduction

In recent years, high-speed railway and heavy-haul railway have become a major tendency for the development of modern railway in China. Reinforcement is an effective and reliable technique for increasing the strength and stability of subgrade soil. This technique is used in a variety of applications ranging from retaining walls to subgrade and so on. Geogrid is a type of synthetic materials being used to improve engineering properties of soil by providing extra resistance of shear and tensile stress. The dynamic effect of train and railway track has been significantly enhanced by the acceleration of train speed and the increase of axle weight. On one hand, the vibration of the track increases under the cyclic loading, which accelerates the break of the railway track. On the other hand, the railway subgrade is composed of loose soil material with obvious anisotropy, which appears to be characterized by nonlinearity, hysteresis, and deformation accumulation. Unlike the earthquake or storm wave loading, low amplitude one-way cyclic

loading is more typical for traffic loading. Reinforced subgrade is subjected to large numbers of load applications at a stress level below their strength.

After years of railway operation, uneven settlement of the subgrade has been observed, and then the deformation accelerates, which aggravates the interaction between the railway track and the train. It can cause significant problems in railway infrastructure and is a challenge for the engineers to keep railway track working well. Therefore, it is of great practical relevance to study the dynamic behavior of reinforced subgrade under traffic loading. At present, the methods used to study the dynamic behavior of soil are divided into experimental study (field test and model test) and theoretical study (analytical method and numerical simulation).

In the past decades, many experimental studies have been carried out to investigate the dynamic behavior under long-term cyclic loading. For example, cyclic triaxial tests, resonant column tests, and shaking table tests on the dynamic behavior of reinforced soil were reported earlier by [1, 2, 3, 4, 5].

The vertical acceleration, horizontal acceleration, and vertical displacement of reinforced retaining walls increase gradually as the height of the wall grows [6]. However, the tendency of increasing of horizontal displacement is not obvious, which has a strong relation with stress waveform generated by train loads. Model tests on the reinforced retaining wall under the repeated loads were carried out to investigate the dynamic response of the retaining wall [7]. It is shown that the displacement average value of the wall is related to the height of the wall. With the increase of dynamic load, the tendency of displacement and strength of reinforced retaining wall go through three stages: vibration compaction stage, vibration shear stage, and vibration failure stage.

In addition, the residual volumetric strain and shear deformations are reduced by the reinforcement, and the model parameters become smaller [8]. With the increase of deviator stress ratio at high confining pressure, the shear modulus decreases. The rate of loss of shear modulus is found to be much lower for fiber-reinforced specimens [9]. Elastic modulus of fiber-reinforced soil increases with increase of fiber content and confining pressure and decreases with increase of loading repetition [10]. The dynamic behavior of the mixture is significantly affected by the content of injected foam and also confining stresses [11]. Stress conditions with selected levels of low confining pressure were used to simulate specific conditions. Particular attention was paid to the bedding error at the top and the bottom ends of the specimens and to fix transducers onto the membrane to be used under low confining pressure [12].

A large-scale model test of reinforced gabion walls was performed with different input sine wave frequencies and amplitudes [13]. It was found that the inside and the outside of reinforced gabion walls under loads (imposed two million times) do not show significant local and overall damage, when the vibration frequency reaches 10 Hz. But, there are great changes of vertical and horizontal acceleration and displacement response of the reinforced gabion wall. The ratio of the elasticity modulus of the material after saturation to its elasticity modulus in dry condition and the saturation induced sudden volumetric strain decrease as the confining pressure increases [14]. The decay of  $G/G_0$  observed in TS-RC tests starts at a lower strain level and is more evident, especially at high strain level and low confinement stress [15]. The dynamic deformation characteristics of the reinforced sand are defined in terms of wall lateral deformation and rotation. The results indicate the effectiveness of fiber reinforcement in improving dynamic properties of fine sand and deformation characteristics of fiber-reinforced sheet pile retaining wall during shaking [16]. Besides, a great number of researchers have conducted analysis for simulating the dynamic response of reinforced subgrade by establishing track-subgrade numerical models.

The dynamic elastic modulus and damping ratio are two of the most important indicators for design and calculation analysis of reinforced soil structure. In the present research, most analysis and calculation of the geotechnical engineering are inseparable from the two indicators, which are affected by many factors. However, previous studies have mostly focused on the silty clay, silty soil, and soft clay. No

comprehensive study has been reported concerning the undrained cyclic behavior of reinforced gravel soil, because it takes a long time and is difficult to prepare the soil samples. Compared to many other soil types, gravel soil plays an essential role in the overall deformation behavior of railway subgrade. During the construction process, gravel material layer is compacted at the densest and stiffest possible state, which can be achieved by using the optimum moisture content defined by the Proctor compaction test. After years of railway operation, the unbound gravel soil layer is exposed in specific stress conditions and traffic loads. It is customary to use a constant elastic modulus as the stiffness index of soil in traditional engineering design, while ignoring the change of stiffness of soil during cyclic loading. Actually, even under the static loading conditions, the stiffness of gravel soil can be characterized by nonlinear softening as the strain increases gradually, and the dynamic behavior is more obvious under cyclic loading [17]. However, there is no information in the literature on the effect of dynamic elastic modulus of reinforced subgrade. Furthermore, stress and deformation state of reinforced soil and interaction mechanism between reinforced and soil under cyclic loading need to be studied.

The main purpose of this study is to evaluate the effects of influence factors on dynamic elastic modulus of reinforced subgrade. Experimental investigations of reinforced soil under cyclic loading based on orthogonal array design are conducted. A series of cyclic triaxial tests were carried out by varying confining pressure, vibration frequency, reinforced layers, and dynamic stress amplitudes. Effects of these parameters on the dynamic elastic modulus of reinforced subgrade are studied. Besides, the influence factors of dynamic elastic modulus and the changing rule with the factor were also studied according to the extreme value analysis. Finally, the results of the tests were analyzed and could provide theoretical foundation and further application for the reinforced soil.

## 2. Cyclic Triaxial Tests

**2.1. Apparatus.** These cyclic triaxial tests were carried out at the laboratory of Institute of Earthquake Engineering of Dalian University of Technology. This apparatus was equipped with a pressure chamber having a diameter of 20 cm, height of 50 cm, together with vibration equipment and measurement equipment was designed and fabricated. Maximum axial pressure is 150 kN, and maximum axial tension is 100 kN. Maximum axial displacement is  $\pm 50$  mm. The biggest confining pressure is 3 MPa. Some higher frequency may be used because of the special test purpose, and the excitation system is usually set in the axial of instrument to provide different types of vibration loading. Three wave types can be adopted in test, which are impact type, periodic type, and arbitrary type, as shown in Figure 1.

Figure 2 shows the sketch of wave shape of cyclic loading. The parameters are as follows:  $\sigma_{\max}$  is the maximum stress of cyclic loading;  $\sigma_{\min}$  is the minimum stress of cyclic loading;  $\Delta\sigma$  is amplitude load,  $\Delta\sigma = \sigma_{\max} - \sigma_{\min}$ ;  $T$  is cyclic of vibration; and  $f$  is frequency and  $f = 1/T$ .

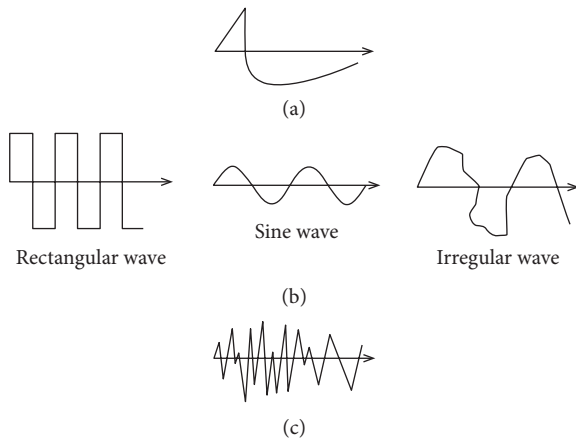


FIGURE 1: Schematic diagram of dynamic load waveform. (a) Impact type. (b) Periodic type. (c) Arbitrary type.

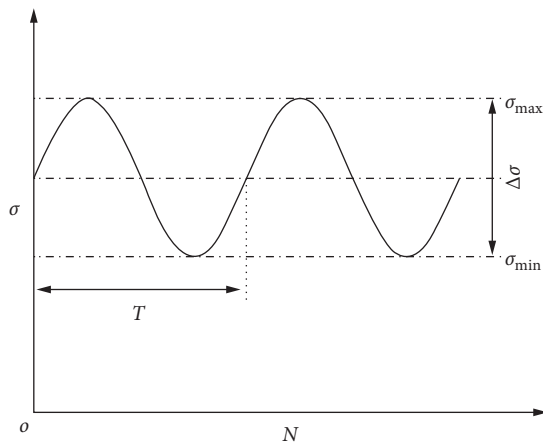


FIGURE 2: Sketch of wave shape of cyclic loading.

The vibration frequency varied from 0.1 Hz to 10 Hz. The instrument was equipped with displacement sensor and force sensor. Experimental data can be collected and analyzed automatically. High-precision hydraulic servo medium triaxial testing system is designed by anti-Semitic research institute of Dalian University of Technology by using computer and hydraulic servo technique. It was used in this experiment. A detailed sketch and a photo of the apparatus are shown in Figure 3.

## 2.2. Materials

**2.2.1. Gravel Soil.** The soil used in this study was gravel soil and was obtained from the subgrade bed of the railway track in the region of Dalian, north of China. The samples were collected in a disturbed state, by manual excavation, in sufficient quantity to complete all the tests. The coefficient of uniformity,  $C_u$ , is 17.5 and the coefficient of gradation,  $C_c$ , is 1.03. Figure 4 plots the resultant particle size distribution curve. This gravel soil sample has a good gradation and is the most commonly used as filling in the actual projects, and the essential physical parameters of soil are shown in Table 1.

**2.2.2. Geogrid.** In this study, the TGSG40-40 Bidirectional plastic geogrid was used as reinforced material. Geogrid is made of high-density polyethylene (HDPE) by thermoplastic or molded, and it is manufactured by Shandong Feicheng Lianyi Engineering Plastics limited company, China. The outlook of the Bidirectional (Biaxial) plastic geogrid is network structure like a square, and made of high-molecular polymer as its raw material through extrusion, formed and punched before longitudinally and laterally stretched. This geogrid has high tensile strength in both longitudinal and horizontal directions and provides an ideal interlocking system. It can be widely used to all kinds of roads, railways, and airports to enhance the bearing capacity of subgrade bed, to enhance slope stability, and to extend the service life of subgrade. Figure 5 shows the TGSG40-40 Bidirectional plastic geogrid that has been used as reinforcement. In order to reduce friction between geogrid and pressure chamber during the experiment, the geogrid is cut as shown in Figure 5. Physical property of geogrid is shown in Table 2.

**2.3. Sample Preparation.** The samples were prepared in cylindrical molds with a height of 50 cm and a diameter of 20 cm. The test started with vacuum extraction between mold and rubber for sample package, and then soil specimens were put by vibrating in the mold in five sequential layers. After a final setting, every filling height is 10 cm and was checked with a steel gauge. Taking into account the apparatus, three reinforcement ways can be used in the test. The first way, the soil sample is not reinforced. The second way, a layer of geogrid was placed in the middle of the sample. The third way, a layer of geogrid was placed in the middle and lower part of the mold, and another layer of geogrid was placed in the middle and top of the mold. The specimens were prepared at a density equal to approximately 96% of the maximum density at the optimum moisture content in each step. The geogrid is laid horizontally. Geogrid placement diagram is shown in Figure 6.

**2.4. Test Scheme.** There are many technical parameters affecting the test result. The orthogonal array design allows to limit the amount of research needed to achieve the desired test results, reducing the time required course for their performance and at the same time reducing costs. It is an effective way to design an experiment to find out the most influential factor. The orthogonal array with two advantages of uniformly dispersed, neat, and comparable making each test is highly representative, so the fewer times of experiments can fully reflect the impact of the different levels of each factor on the index.

The effect degree of confining pressure, reinforced way, dynamic stress amplitude, and frequency were analyzed, respectively, through orthogonal design of experiments in four factors and three levels. For better simulating dynamic characteristic of geogrid reinforced soil, different dynamic stress amplitudes were selected to simulate dynamic responses, which are caused by train with different speed or axle weight. Calculation table of dynamic stress amplitude is shown in Table 3.

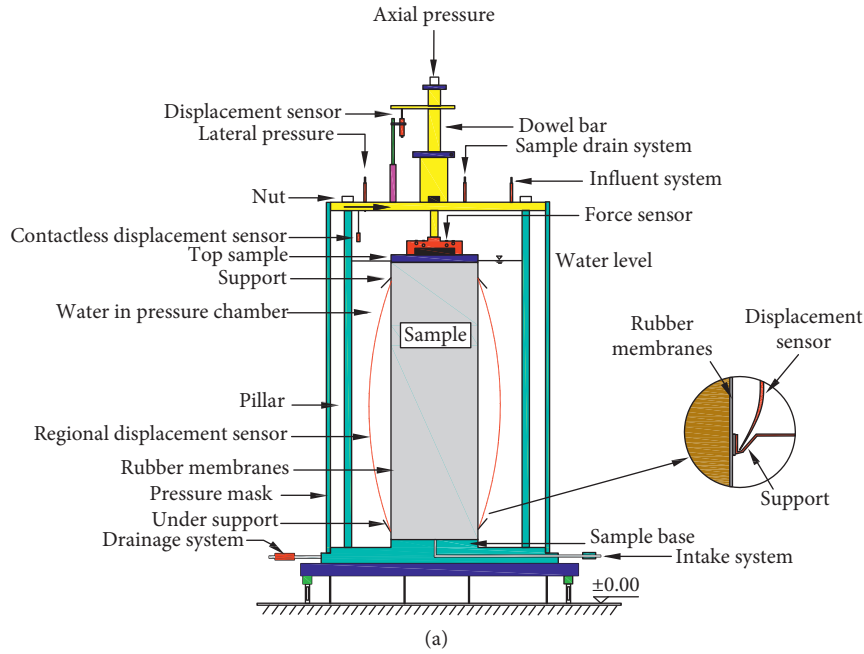


FIGURE 3: (a) A detailed sketch and (b) a photo of cyclic triaxial apparatus.

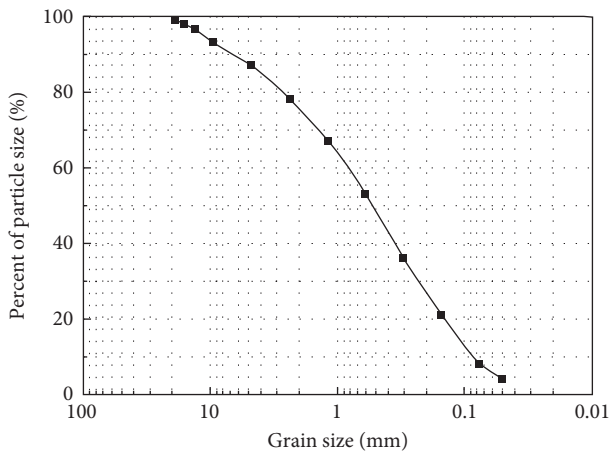


FIGURE 4: Particle size distribution of soil sample.

Three different confining pressures 60 kPa, 90 kPa, and 150 kPa are considered for simulating specific conditions in the case of railway subgrade.

TABLE 1: Essential physical parameters of soil.

Description/property	Value
Natural water content	5%
Liquid limit	26%
Plastic limit	21%
Plasticity index	5
Cohesion	15.55 (kN/m <sup>2</sup> )
Angle of friction	19.5°
Optimum moisture content (OMC)	18%
Maximum dry density (MDD)	2.1 (kN/m <sup>3</sup> )
Maximum particle size	25 mm

Considering the transient in the vibration of the subgrade during the long-term effect of the train loads, the filling was not drained by instantaneous drainage, so that the experiment was performed without drainage. The cyclic loading of different trains is simulated with MTS servo exciter. Unsaturated specimens were tested under undrained triaxial compression using monotonic and cyclic loading with frequencies in the range of 0.5~2 Hz. Sine wave was used in this study to simulate traffic loads with short

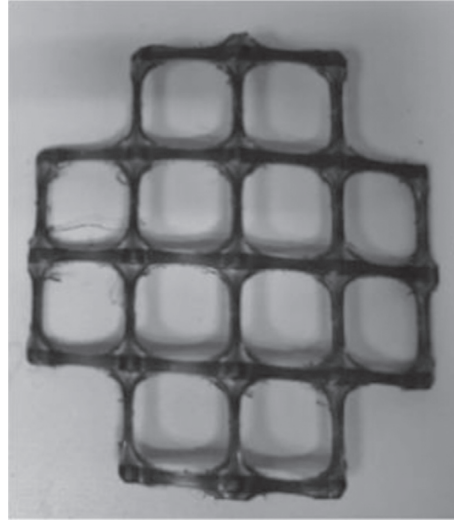


FIGURE 5: Bidirectional plastic geogrid.

TABLE 2: Physical property of geogrid.

Geometrical/physical characteristics	Value
Raw material	Polypropylene
Aperture size, (transverse length), $A_L$	35 mm
Aperture size, (longitudinal length), $A_L$	35 mm
Tensile strength (MD/CD)	$\geq 40$ kN/m
Tensile strength at 2% elongation	$\geq 14$
Tensile strength at 5% elongation	$\geq 28$
Mass area ratio	$500 \pm 50$ g/m

vibration cycle and more vibration. The consolidation stress ratio,  $K_c$ , is 1. There are three situations of reinforcement in the test, that is, no geogrid, one layer of geogrid, and two layers of geogrid. The orthogonal array of the tests is provided in Table 4.

### 3. Results and Discussion

**3.1. Dynamic Properties of Railway Subgrade under Cyclic Loading.** With the increase of vibration frequency, the fluctuation of dynamic stress increment increases. After about ten thousand times of vibration, the dynamic stress increment gradually tends to oscillate in a stable interval. Because the test data are intensive and unstable in the early cycles, some of the test data in midterm test were selected to be enlarged, as shown in Figure 7. It shows the dynamic stress's time range curve under cycle loading of 9 tests ( $N$  represents the number of load cycles). The dynamic stress increment is basically stable in the whole vibration process except a small fluctuation at some areas.

Figure 8 shows the relation curve of dynamic elastic modulus and dynamic strain. It may be seen from Figure 8 that with the increase of dynamic strain amplitude, the dynamic elastic modulus ( $E_d$ ) decreases gradually, that is, strain softening occurs. When  $\varepsilon_d < 0.25\%$  at the initial stage of the cycle, the curve is steep and the attenuation rate of  $E_d$  is faster; when the dynamic strain is greater than  $0.25\%$ , the curve tends to be gentle, and the attenuation rate of  $E_d$  tends

to be 0. Overall, the curve (the image of a power function) obtained by applying interpolation with respect to the dynamic elastic modulus is convergent.

**3.2. Maximum Dynamic Elastic Modulus.** Maximum dynamic elastic modulus ( $E_{d \max}$ ) is usually used as the design parameter in project. To quantify the dynamic behavior under cycle loading of reinforced soil, maximum dynamic elastic modulus can be defined based on curve. It can be observed that the measured data are distributed by Hardin hyperbola by analysis; that is, the dynamic constitutive relation of reinforced soil conforms to hyperbolic model, which is defined as follows:

$$E_d^{-1} = a + b\varepsilon_d, \quad (1)$$

where  $E_d$  is the dynamic elastic modulus,  $a$  and  $b$  are fitting parameters, and  $\varepsilon_d$  is the dynamic strain. From Formula (1),  $\varepsilon_d = 0, 1/a$  represents the maximum dynamic elastic modulus of reinforced soil sample  $E_{d \max}$ . The results are shown in Table 5.

According to the maximum elastic modulus, the order of influence factor is determined by means of range analysis, and the results are shown in Table 6.

Using range analysis through orthogonal design of experiments, the order of influence factor to dynamic elastic modulus in the test is determined within three factor levels. They are dynamic stress amplitude, frequency, reinforced layer, and confining pressure. That is, the influence of confining pressure to reinforced soil is the greatest.

**3.3. Analysis of Significant Influencing Factors.** The order of influence factor of reinforced soil can be determined though range analysis, but there are no comparison between the result caused by changing of factor and level and the result caused by experimental error. There is no standard to measure its significance. To solve this problem, variance

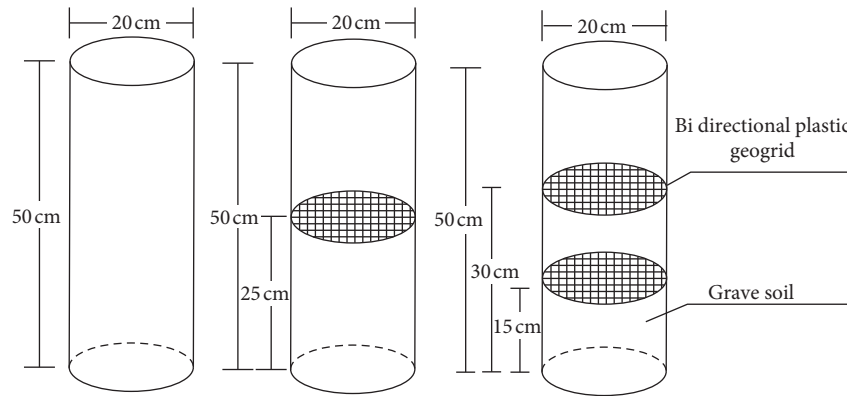


FIGURE 6: Geogrid placement diagram.

TABLE 3: Calculation table of dynamic stress amplitude.

Axle weight (T)	Axle weight (kN)	Speed (km/h)	$\sigma'_d$ (kPa)	$\sigma_d$ (kPa)
20	196	120	69.3	70
25	245	100	82.8	80
30	294	80	94.8	95

$\sigma'_d$  is a calculated value of dynamic stress amplitude by the formula  $\sigma'_d = 0.26 \times P \times (1 + 0.003 V)$ .  $P$  is the axle weight and  $V$  is the speed. To simplify the test, we denote by  $\sigma_d$  the value of dynamic stress amplitude taken in the test.

TABLE 4: The orthogonal array.

Group	$\sigma_c$ (kPa)	$\sigma_d$ (kPa)	$f$ (Hz)	Number of reinforced layers
1	56	70	1	0
2	56	80	2	1
3	56	95	0.5	2
4	90	70	2	2
5	90	80	0.5	0
6	90	95	1	1
7	150	70	0.5	1
8	150	80	1	2
9	150	95	2	0

$\sigma_c$  is confining pressure,  $f$  is frequency. In addition, it was difficult to prepare exact soil samples in cyclic triaxial tests, and there is an error during the operation of the instrument and acquisition process of the data. Therefore, it is necessary to make variance analysis on the test results.

analysis can be taken in this study. The results of variance analysis of orthogonal experiment are shown in Table 7. Variance analysis of orthogonal experiments is shown that the dynamic elastic modulus of reinforced soil is significantly affected by dynamic stress amplitude. The effect of reinforced layer on dynamic elastic modulus of reinforced soil is significant. It has been identified that frequency and confining pressure have an insignificant influence.

**3.3.1. Effects of Dynamic Stress Amplitude.** The dynamic response of reinforced subgrade, which is caused by train with different axle load and speed, can be simulated by dynamic stress amplitude. When dynamic stress is small, the strength and stiffness of soil samples are basically unchanged and the dynamic stress amplitude and dynamic

strain are basically unchanged. Dynamic stress increases with increasing the dynamic stress amplitude. At this moment, the structure of soil samples changes and the soil particles tend to be close to each other and the dynamic strain and pore pressure gradually increase. With the increase of vibration frequency, soil samples are deformed, the performance of strength and stiffness decreased, the bearing capacity of soil samples are reduced, and the elastic modulus of soil samples decreased gradually. It is noteworthy that the dynamic stress amplitude has the greatest influence on the dynamic elastic modulus of reinforced soil. The demonstration results are consistent with the fact that heavy-axle load trains cause more dynamic stress than the light-axle load trains in engineering.

**3.3.2. Effects of Frequency.** The dynamic effect caused by different speed train passing the reinforced subgrade can be stimulated by different vibration frequency. Accumulated strain of soil is related to vibration frequency under the same vibrations. With the increase of frequency, the dynamic strain of soil increased. Relative to conventional railway, it can be easily obtained from the dynamic strain in high-speed railway and the developing rate of strain is faster. Within a certain dynamic strain range, dynamic elastic modulus is increasing with the increase of frequency.

**3.3.3. Effects of Reinforced Layer.** The experimental results showed the dynamic elastic modulus gradually decrease with the increase of reinforced layer. The dynamic elastic modulus of plain soil is greater than that with only one layer of reinforcement, which is greater than that with two layers of reinforcement. Since this study is based on experiments with reinforced layers less than two, more study is needed to investigate the effect of dynamic elastic modulus.

**3.3.4. Effects of Confining Pressure.** As mentioned previously, different embedded depth of TGSG geogrid can be demonstrated by confining pressure to some extent. The effect of confining pressure plays a minor role of the dynamic elastic modulus. The test results further show that the

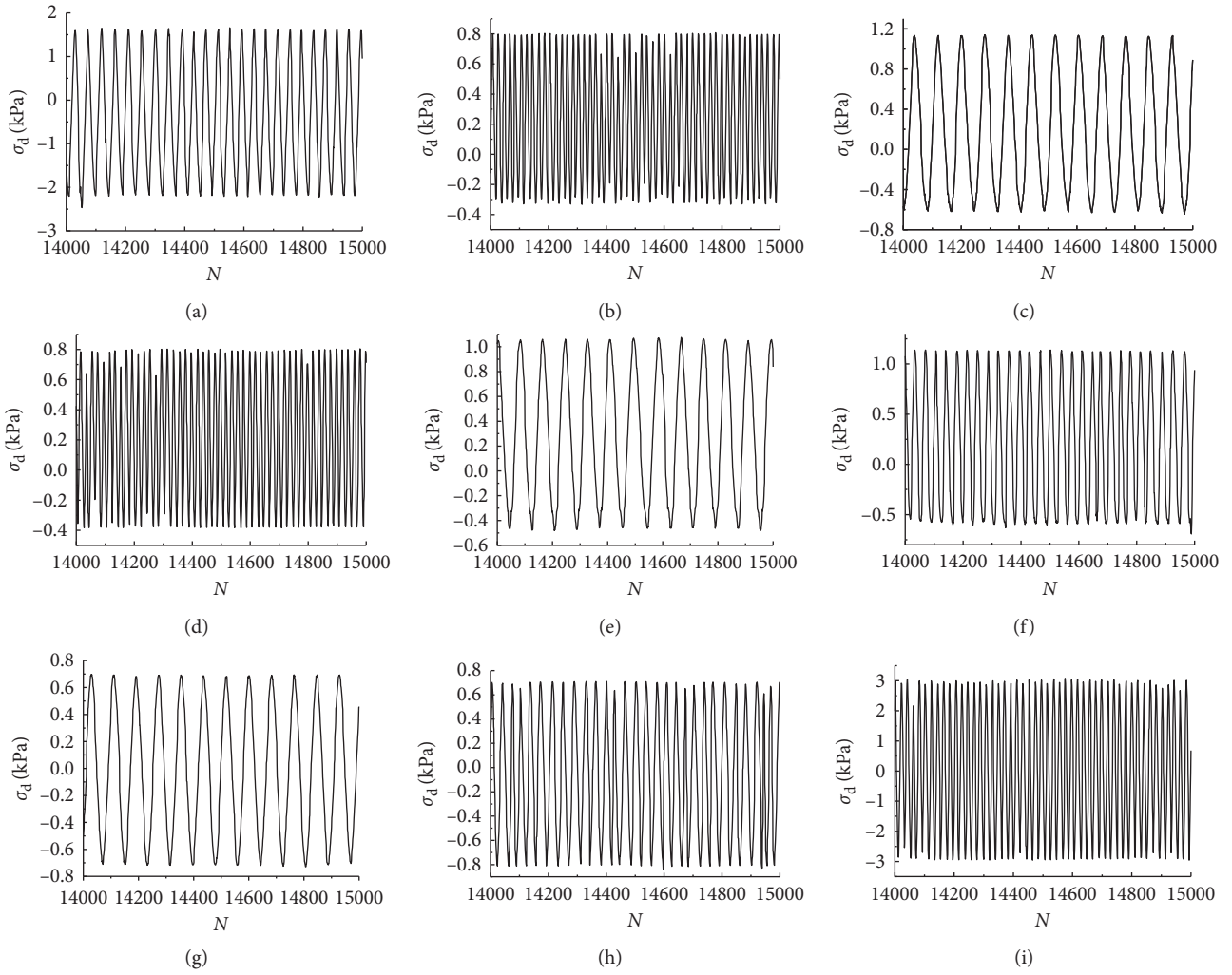


FIGURE 7: Dynamic stress time-history curves.

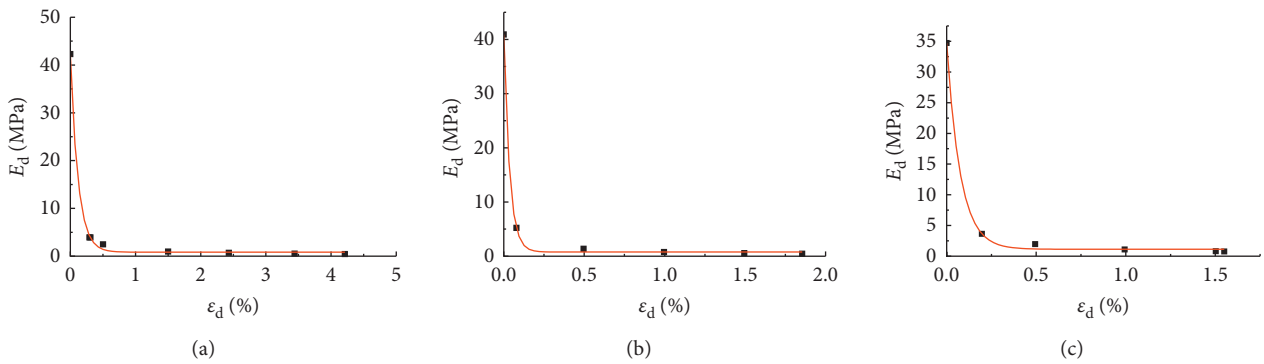


FIGURE 8: Continued.



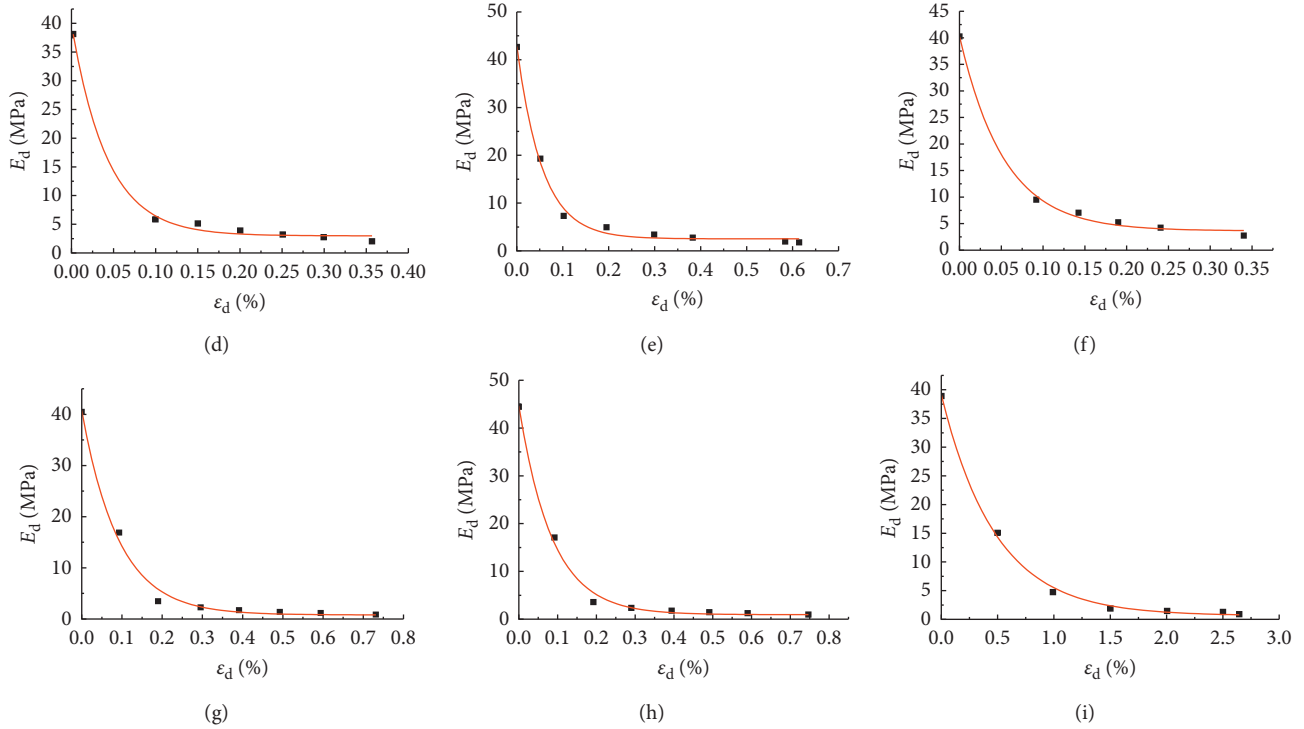
FIGURE 8: Curves for  $E_d - \varepsilon_d$ .

TABLE 5: Maximus dynamic elastic modulus and test parameters under different test conditions.

Group	$a$ (MPa $^{-1}$ )	$b$ (MPa $^{-1}$ )	$E_{dmax}$ (MPa)
1	0.02333	0.76459	42.86
2	0.02411	2.05189	41.48
3	0.02873	0.08323	34.81
4	0.02597	1.25684	38.51
5	0.02318	1.30546	43.14
6	0.02465	0.86946	40.57
7	0.02461	1.34147	40.63
8	0.02228	1.32149	44.88
9	0.02538	0.34307	39.40

adopted confining pressure with a small difference (between 60 kPa and 90 kPa or between 90 kPa and 150 kPa) can affect the test precision, because the test apparatus can apply 3 MPa confining pressure. It is observed that plastic deformation of soil can be resisted by increasing confining pressure; therefore, it improves the antideformation ability of soil.

#### 4. Conclusion

Undrained cyclic triaxial tests have been carried out using orthogonal design of experiment. The influence factors of the dynamic elastic modulus of reinforced subgrade were studied in this paper. Impacts of confining pressure, dynamic stress amplitude, frequency, and reinforced layer on dynamic elastic modulus are discussed. The order of dynamic elastic modulus of reinforced soil is influenced by

TABLE 6: Results of orthogonal design of experiment.

Group	$\sigma_c$ (kPa)	$\sigma_d$ (kPa)	$f$ (Hz)	Reinforced layer	$E_{dmax}$ (MPa)
1	56	70	1	No	42.86
2	56	80	2	One	41.48
3	56	95	0.5	Two	34.81
4	90	70	2	Two	38.51
5	90	80	0.5	No	43.14
6	90	95	1	One	40.57
7	150	70	0.5	One	40.63
8	150	80	1	Two	44.88
9	150	95	2	No	39.40
$y_{j1}$	119.15	122.00	128.31	125.40	—
$y_{j2}$	122.22	129.50	119.39	122.68	—
$y_{j3}$	124.91	114.78	118.58	118.20	—
$\bar{y}_{j1}$	39.72	40.67	42.77	41.80	—
$\bar{y}_{j2}$	40.74	43.17	39.80	40.89	—
$\bar{y}_{j3}$	41.64	38.26	39.53	39.40	—
Range	1.92	4.91	3.24	2.40	—
Order	4	1	2	3	—

$y_{j1}$  is the sum of  $E_{dmax}$ 's obtained from each group when  $\sigma_c = 56$  kPa,  $y_{j2}$  is the sum of  $E_{dmax}$ 's obtained from each group when  $\sigma_c = 90$  kPa,  $y_{j3}$  is the sum of  $E_{dmax}$ 's obtained from each group when  $\sigma_c = 150$  kPa, and  $\bar{y}_{jx} = y_{jx}/3$ , for  $x = 1, 2, 3$ .

dynamic stress amplitude, frequency, reinforced layer, and confining pressure within changing in factor level.

The dynamic stress amplitude has a marked influence on the dynamic elastic modulus of reinforced soil. With the low dynamic stress, dynamic stress amplitude and dynamic strain are basically unchanged. With the increase of dynamic

TABLE 7: Results of variance analysis of orthogonal design of experiment.

Sources of variation	$S_j$	$f_j$	$\bar{S}_j$	$F_j$
Confining pressure	0.615	2	0.308	1.000
Dynamic stress amplitude	4.013	2	2.007	36.58**
Frequency	2.159	2	1.080	2.906
Reinforced layer	0.979	2	0.490	12.679*
Error	0.002	3	0.001	
Sum	7.768	11		

$\alpha = 0.99, 0.95,$  and  $0.90$  quantiles of  $F$  distribution with degrees of freedom 2 and 3 are 30.8, 9.55, and 5.45, i.e.,  $F_{0.99}(2, 3) = 30.8$ ,  $F_{0.95}(2, 3) = 9.55$ , and  $F_{0.90}(2, 3) = 5.46$ .  $S_j$  is the sum of squares in  $j$  rows;  $f_j$  is the degree of freedom;  $\bar{S}_j$  is sum of average column variation;  $F_j$  is test statistics; \* presents significant influence when  $\alpha = 0.05$ ; \*\* presents significant influence particularly when  $\alpha = 0.01$ ; for a given level of significance  $\alpha$ , when  $F_j > F_{1-\alpha}(2, 3)$ , under test level  $\alpha$ , the factor is inferred to be outstanding, otherwise it is regarded as nonsignificant.  $\alpha$  is less, and it demonstrated that the effect of this factor to test results is significant.

stress, dynamic stress amplitude increases correspondingly and the soil particles tend to be close to each other. The bearing capacity of reinforced soil decreases and dynamic elastic modulus decreases slightly with the increase of dynamic strain.

Frequency has an influence on the dynamic elastic modulus. It is shown that the cumulative strain of reinforced soil is related to the vibration frequency. The higher the frequency is, the greater the strain caused by subgrade is.  $E_d$  increases as the vibration frequency goes up within a certain dynamic strain range. Reinforced layer has influence on the dynamic elastic modulus. With the increase of reinforced layer, the dynamic elastic modulus is decreasing gradually. The test results also exemplify the reinforced subgrade restrict lateral displacement of subgrade and reduce settlement of subgrade under long-term cyclic loading.

It should be noted that the study of dynamic behavior of reinforced soil is much needed in order to further address reinforced soil application.

## Conflicts of Interest

The authors declare that they have no conflicts of interest.

## Acknowledgments

This academic research work was supported by the Doctoral Scientific Research Foundation of Liaoning Province of China (201601255), Scientific Research Foundation of Ministry of Education of Liaoning Province of China (JDL2016017), National Natural Science Foundation of China (51408093), and Natural Science Foundation of Liaoning Province of China (21070540134). The authors thank Chenguang Zhou and Jirong Tian for their help in construction of the physical models and contributions during the cyclic triaxial tests. The authors appreciate the efforts of Qing Yang for reading the manuscript and making valuable suggestions. The authors also wish to thank the anonymous reviewers for their critical comments.

## References

- [1] B. Indraratna, D. Ionescu, and D. Christie, "Shear behavior of railway ballast based on large scale triaxial testing," *Journal of Geotechnical Geoenvironmental Engineering*, vol. 124, no. 5, pp. 439–449, 1998.
- [2] H. S. Li, G. L. Yang, and Y. S. Zou, "Analysis of dynamic character of reinforced earth retaining wall," *China Journal of Highway and Transport*, vol. 17, no. 2, pp. 28–31, 2004.
- [3] T. Tanchaisawat, D. T. Bergado, and P. Voottipruex, "Numerical simulation and sensitivity analyses of full-scale test embankment with reinforced lightweight geomaterials on soft Bangkok clay," *Geotextiles and Geomembranes*, vol. 26, no. 6, pp. 498–511, 2008.
- [4] Y. Q. Tang, Y. L. Wang, Y. Huang, and Z. Y. Zhou, "Dynamic strength and dynamic stress-strain relation of silt soil under traffic loading," *Journal of Tongji University (Natural Science)*, vol. 32, no. 6, pp. 701–704, 2004.
- [5] J. Zhou and X. N. Gong, "Study on strain soften in saturated soft clay under cyclic loading," *China Civil Engineering Journal*, vol. 33, no. 5, pp. 75–82, 2000.
- [6] M. E. Magdi and J. B. Richard, "Influence of reinforcement parameters in the seismic response of reduce-scale reinforced soil retaining walls," *Geotextiles and Geomembranes*, vol. 25, no. 1, pp. 33–49, 2007.
- [7] G. L. Yang, H. S. Li, and Y. H. Wang, "Model test on reinforced earth retaining wall under repeated load," *China Civil Engineering Journal*, vol. 36, no. 6, pp. 105–110, 2003.
- [8] D. G. Zou, J. Bi, B. Xu, X. J. Kong, and Y. Zhao, "Research on the residual deformation behavior of sand-gravel composites reinforced with geogrid," *Journal of Hydroelectric Engineering*, vol. 28, no. 5, pp. 158–162, 2009.
- [9] M. S. Masoud and H. B. Farhad, "Dynamic behavior of reinforced clayey sand under cyclic loading," *Geotextiles and Geomembranes*, vol. 42, no. 5, pp. 564–572, 2014.
- [10] J. Li and D. W. Ding, "Nonlinear elastic behavior of fiber-reinforced soil under cyclic loading," *Soil dynamics and earthquake engineering*, vol. 22, no. 9–12, pp. 977–983, 2002.
- [11] G. Iman, G. Abbas, K. J. Mohammad, and M. Mehdi, "Dynamic properties of polyurethane foam-sand mixtures using cyclic triaxial tests," *Construction and Building Materials*, vol. 118, pp. 104–115, 2017.
- [12] L. Stanislav, K. Junichi, M. Yukika, and S. Takeshi, "Large-scale triaxial tests of dense gravel material at low confining pressures," *Soils and Foundations*, vol. 54, no. 1, pp. 45–55, 2014.
- [13] Y. Li, G. L. Yang, and Y. L. Lin, "Dynamic characteristics of reinforced gabion walls subjected to cyclic loading," *Journal of Highway and Transportation Research and Development*, vol. 28, no. 2, pp. 1–6, 2011.
- [14] H. Aliakbar, T. Ahmadreza, S. Hossein, and H. T. Saeed, "Effect of stress conditions on collapse deformation behavior of a rockfill material," *KSCE Journal of Civil Engineering*, vol. 19, no. 6, pp. 1637–1646, 2015.
- [15] L. Verrucci, G. Lanzo, P. Tommasi, and T. Rotonda, "Cyclic and dynamic behavior of a soft pyroclastic rock," *Geotechnique*, vol. 65, no. 5, pp. 359–373, 2015.
- [16] R. Jamshidi, I. Towhata, H. Ghiassian, and A. R. Tabarsa, "Experimental evaluation of dynamic deformation characteristics of sheet pile retaining walls with fiber reinforced backfill," *Soil Dynamics and Earthquake Engineering*, vol. 30, no. 6, pp. 438–446, 2010.
- [17] F. Y. Liu, Y. Q. Cai, C. J. Xu, and J. Wang, "Degradation of dynamic elastic modulus of soft clay under cyclic loading," *Journal of Zhejiang University (Engineering Science)*, vol. 42, no. 9, pp. 1479–1483, 2008.

## Review Article

# Joining of C<sub>f</sub>/SiC Ceramic Matrix Composites: A Review

Keqiang Zhang,<sup>1</sup> Lu Zhang,<sup>1</sup> Rujie He ,<sup>1</sup> Kaiyu Wang,<sup>2</sup> Kai Wei ,<sup>2</sup> and Bing Zhang<sup>3</sup>

<sup>1</sup>Institute of Advanced Structure Technology, Beijing Institute of Technology, Beijing 100081, China

<sup>2</sup>State Key Laboratory of Advanced Design and Manufacturing for Vehicle Body, Hunan University, Changsha 410082, China

<sup>3</sup>Bristol Composites Institute (ACCIS), University of Bristol, Queen's Building, University Walk, Bristol BS8 1TR, UK

Correspondence should be addressed to Rujie He; herujie@bit.edu.cn

Received 1 March 2018; Revised 20 June 2018; Accepted 19 July 2018; Published 4 October 2018

Academic Editor: Mikhael Bechelany

Copyright © 2018 Keqiang Zhang et al. This is an open access article distributed under the Creative Commons Attribution License, which permits unrestricted use, distribution, and reproduction in any medium, provided the original work is properly cited.

Carbon fiber-reinforced silicon carbide (C<sub>f</sub>/SiC) ceramic matrix composites have promising engineering applications in many fields, and they are usually geometrically complex in shape and always need to join with other materials to form a certain engineering part. Up to date, various joining technologies of C<sub>f</sub>/SiC composites are reported, including the joining of C<sub>f</sub>/SiC-C<sub>f</sub>/SiC and C<sub>f</sub>/SiC-metal. In this paper, a systematic review of the joining of C<sub>f</sub>/SiC composites is conducted, and the aim of this paper is to provide some reference for researchers working on this field.

## 1. Introduction

With the rapid development of high-tech in aerospace and other industry fields, the demands for new materials, which can work in extreme harsh working environment of high temperatures, are growing. The needs for better efficiency and higher thrust-to-weight ratio promote the development of advanced materials at high temperatures, such as superalloys [1–3], ceramics [4–6], composites [7–10], and so on. Among these advanced materials, ceramic matrix composites (CMCs) are drawn great attentions for their engineering applications under extreme conditions because they can maintain low density, high strength, wear resistance, oxidation resistance, thermal shock resistance, corrosion resistance, and some other functions together [11].

Carbon fiber-reinforced silicon carbide (C<sub>f</sub>/SiC) ceramic matrix composites, one of the most famous CMCs, are becoming the most promising candidates for high-temperature structural applications (as illustrated in Figure 1), such as sharp leading edges, nose cones, aeronautic jet engines, thermal protection systems for reusable atmosphere reentry vehicles [12, 13], as well as optical components [14] and nuclear fusion/fission reactors [15, 16], owing to their relatively low density (~2 g/cm<sup>3</sup>), high thermal conductivity (~67 W/(m·K)), high strength (300–800 MPa) [17–19], low

coefficient of thermal expansion (CTE, 3.0–3.1 × 10<sup>-6</sup>·K<sup>-1</sup>), especially good stability and excellent oxidation and creep resistance at elevated temperatures [13, 21–23, 25]. In particular, C<sub>f</sub>/SiC composites have shown significant improvements in fracture toughness and thermal shock resistance. These improvements in mechanical properties are dependent on the specific properties of the carbon fiber and the silicon carbide. According to the type of carbon fiber, it can be divided into 1D C<sub>f</sub>/SiC, 2D C<sub>f</sub>/SiC, 2.5D C<sub>f</sub>/SiC, and 3D C<sub>f</sub>/SiC and applied in different fields.

For aerospace applications, as reported by NASA, the X-37B and X-38 aircrafts employed a large number of C<sub>f</sub>/SiC composites in their nose cone [25], leading edge wing and engine components [11, 26, 27, 29]. For nuclear applications, C<sub>f</sub>/SiC composites are used as the cladding materials in pressurized water reactors and flow channel insert materials in thermonuclear fusion reactors [29, 30, 32]. In most cases, typically, C<sub>f</sub>/SiC composite components are usually geometrically complex in shape and always need to join with other materials to form a certain engineering part. However, unfortunately, due to their poor machinability and toughness, C<sub>f</sub>/SiC composites lack good processing performance like metal material and thus cannot be processed into complex-shaped components by forging, extrusion molding, and other traditional methods. It is very difficult to produce

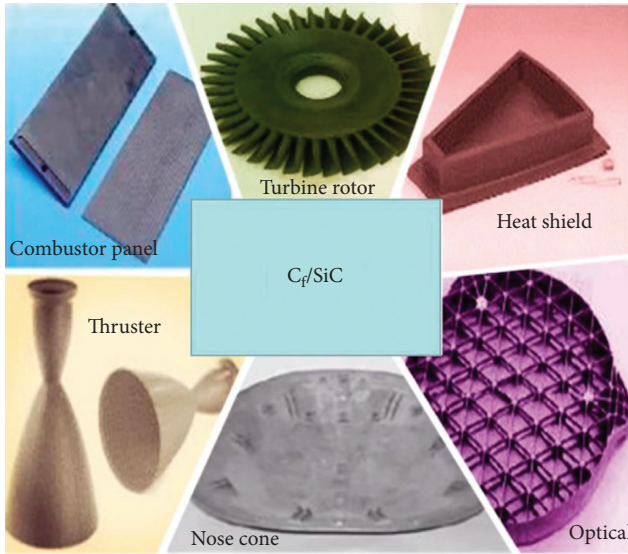


FIGURE 1: Various engineering applications of  $C_f/SiC$  composites.

large-size  $C_f/SiC$  composite components with complex shapes, resulting in they must be joined with themselves or other materials by appropriate joining technologies [32–34, 37]. There have been numerous reports on the joining of  $C_f/SiC$  composites in the past two decades, including self-joining of  $C_f/SiC$  composites [36, 37, 39], and joining of  $C_f/SiC$  composite to dissimilar materials, such as Ti [39, 40], Nb [41, 42, 45], Ni [44, 45, 48], TiAl alloys [47], and so on.

Up to date, various joining technologies of  $C_f/SiC$  composites are reported, including the joining of  $C_f/SiC$ - $C_f/SiC$  and  $C_f/SiC$ -metal. Table 1 lists commonly used joining technologies, such as direct bonding of  $C_f/SiC$ - $C_f/SiC$ , indirect bonding of  $C_f/SiC$ - $C_f/SiC$ , brazing of  $C_f/SiC$ -metal, diffusion bonding of  $C_f/SiC$ -metal, online liquid infiltration of  $C_f/SiC$ -metal, ultrasonic-assisted joining of  $C_f/SiC$ -metal, and electric-assisted joining of  $C_f/SiC$ -metal. To the best knowledge of the authors, however, there has been no systematic summary of the joining of  $C_f/SiC$  composites. Therefore, we herein conduct a systematic review of the joining of  $C_f/SiC$  composites, and the aim of this paper is to provide some reference for researchers working on this field.

## 2. Self-Joining of $C_f/SiC$ Composites

In some conditions, in order to obtain large size and complex-shaped  $C_f/SiC$  composite components, it is necessary that  $C_f/SiC$  composites should be joined with  $C_f/SiC$  composites themselves, named as “self-joining.” There have been many reports about the self-joining of  $C_f/SiC$  composites in the last decades, usually including direct bonding and indirect bonding method.

**2.1. Direct Bonding.** Direct bonding method is a self-joining of  $C_f/SiC$  composites by solid-phase diffusion without any other materials (Figure 2(a)). As reported in previous papers,

TABLE 1: Commonly used joining methods of  $C_f/SiC$  composites.

Joining materials	Joining methods
$C_f/SiC$ - $C_f/SiC$	Direct bonding
	Indirect bonding
$C_f/SiC$ -metal	Brazing
	Diffusion bonding
	Online liquid infiltration
	Ultrasonic-assisted joining
	Electric-assisted joining

the main procedure of direct bonding usually includes three procedures: (1) plastic deformation, (2) diffusion, and (3) creep. Plastic deformation occurs on the interface because of heat and pressure; diffusion includes surface diffusion, bulk diffusion, grain boundary diffusion, and interfacial diffusion to achieve  $C_f/SiC$  bonding. Creep refers to the permanent movement or deformation of metal.

However, the bonding strength of the directly joined  $C_f/SiC$  composite is usually very low because a strong bonding of  $C_f/SiC$  composite is difficult to obtain without any other transition phases and because the diffusion between  $C_f/SiC$  composites is not easy owing to the strong covalent bond and the poor deformation ability of the SiC in the composites. Rizzo et al. [48] reported that a CVD-SiC coated  $C_f/SiC$  composite was directly joined to its counterparts using spark plasma sintering (SPS) technology. The results showed that the cracks in the CVD-SiC coating were visible among the interface and propagated from the SiC coating through the joint area (as is shown in Figure 3), due to the CTE mismatch between SiC coating and  $C_f/SiC$  substrate (as is shown in Table 2), and the apparent shear strength was as low as 5.6 MPa.

Therefore, direct bonding method is merely used owing to the low bonding strength. However, it is still very promising for direct bonding method of  $C_f/SiC$  composites, especially for extreme applications where it demands to avoid a second material.

**2.2. Indirect Bonding.** It is well known that it is very difficult to form diffusion between  $C_f/SiC$  composites owing to the strong covalent bond and the poor deformation ability of the SiC in  $C_f/SiC$  composites, thus resulting in a weak bonding strength of direct bonding joint (Figure 2(b)). Therefore, second-phase materials with plastic deformability, such as Ag-Cu-Ti [30, 49], Ti-Zr-Be [50], Ni [31, 51, 52, 55], calcia-alumina (CA) glass-ceramic [54],  $Ti_3SiC_2$  [16, 36, 55, 56] and Si resin [57], and  $MoSi_2$  [58], were widely reported to be used for the joining of  $C_f/SiC$  composites. These kinds of joining are known as indirect bonding method, always including using metal filler or nonmetal filler.

**2.2.1. Metal Fillers.** This method means that  $C_f/SiC$  composites are bonded with  $C_f/SiC$  composites using metal fillers, such as pure metal or alloys. Table 3 lists some typical reports on the self-joining of  $C_f/SiC$  composites using metal fillers.

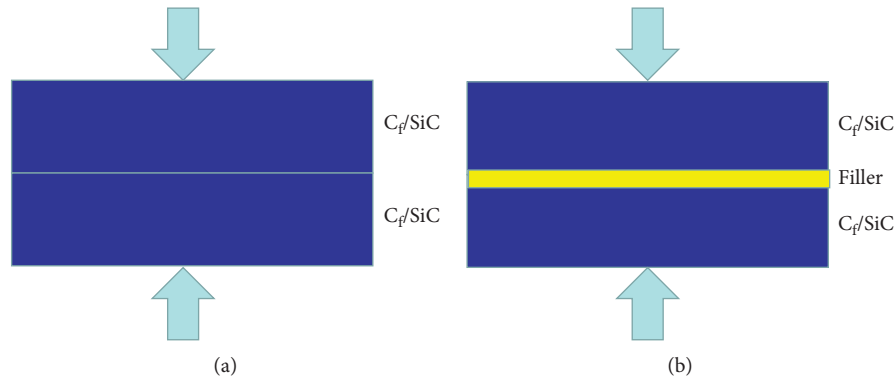


FIGURE 2: The diagram of (a) direct bonding and (b) indirect bonding.

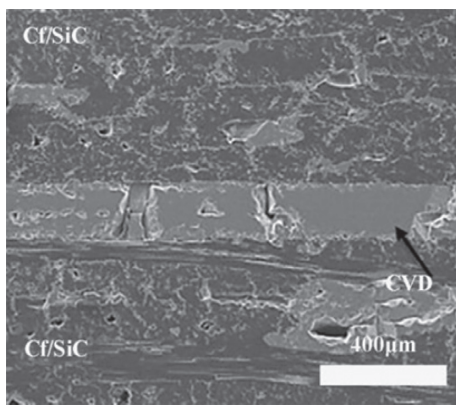


FIGURE 3: Scanning electron microscopy of polished cross sections of  $C_f/SiC$  specimens joined by SPS: direct bonding [48].

TABLE 2: CTE of typical materials (room temperature).

Materials	CTE ( $\times 10^{-6} \cdot K^{-1}$ )
$C_f/SiC$	3.0–3.1
Ti	8
Al	23.5
Cu	16.5
Ni	13
Ag	19.5
Nb	7.2
Mo	5.2
W	4.43
Zr	5.2
Co	6.8
Ta	6.7
C	1.5
TiAl	10.8
CrMo	12.5
SiC	4.8
$Ti_3SiC_2$	9.1
TiC	7.4

The low-temperature active filler is a relatively mature technology and widely used in  $C_f/SiC$  composites; however, the joint phase such as Ag, Cu, and other metals, usually with low melting point, leads to poor high-temperature strength and oxidation resistance. Therefore,  $C_f/SiC$  composites

joined by metal fillers can only be used in low-temperature environment ( $<500^\circ C$ ).

Liu et al. [30] reported the  $C_f/SiC$  composites joined by ternary Ag-35.25 wt% Cu-1.75 wt% Ti and demonstrated that the mechanical strength decreased with the increase in temperature owing to the softening of filler. The flexural strength decreased to 46% and 26% at 300 and 500°C compared with that at room temperature, respectively. Stefano et al. [48] fabricated  $C_f/SiC$ -Ti- $C_f/SiC$  sandwich by SPS and used pure Ti foils as filler. They also found that a Ti-Si-C-based phase ( $Ti_3SiC_2$ , as is shown in Figure 4) was the main reaction product, usually induced to strength decrease.

High-temperature metal fillers, such as Ni and its alloys, are reported and found to greatly improve the high-temperature resistance of the joint [61, 62]. Cheng [51, 52, 55] developed a novel joining process to join the 2D/3D  $C_f/SiC$  composites. Porous  $C_f/SiC$  composites were fabricated through chemical vapor infiltration (CVI) process, and Ni alloy was used to join the  $C_f/SiC$  composites together. Figure 5 shows the diagram of this joining process. Because the Ni alloy had a favorable wettability with  $C_f/SiC$  composites, melted Ni alloy easily infiltrated into the pores among  $C_f/SiC$  composites. Hence, the contact surface between Ni alloy and  $C_f/SiC$  composites matrix was greatly increased, thereby improved the bonding strength. Besides, Ni alloy had a higher melting point; hence, the joint was expected to be used at high temperatures ( $>1000^\circ C$ ).

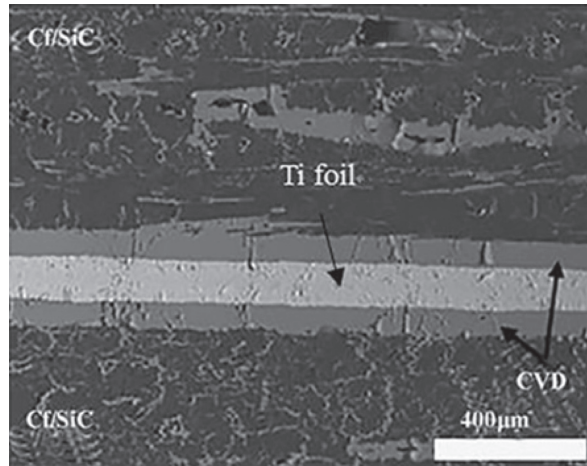
Table 4 lists some typical reports on the self-joining of  $C_f/SiC$  composites with high-temperature fillers (Ni alloy). As a nontraditional joining method, the self-joining process using Ni alloy is usually carried out during composite preparation procedure, and the damage is minimal. And after the joining process, an afterward CVD process is conducted, which not only densify the porous composites but also provides antioxidation coating for the matrix and the joint.

**2.2.2. Nonmetal Fillers.** Nonmetal fillers, such as MAX ceramic [16, 36, 55, 56, 63], ceramic precursors [64], Si resin [57], and  $MoSi_2$  [58], are also reported to be used in the self-joining of  $C_f/SiC$  composites (as listed in Table 5).

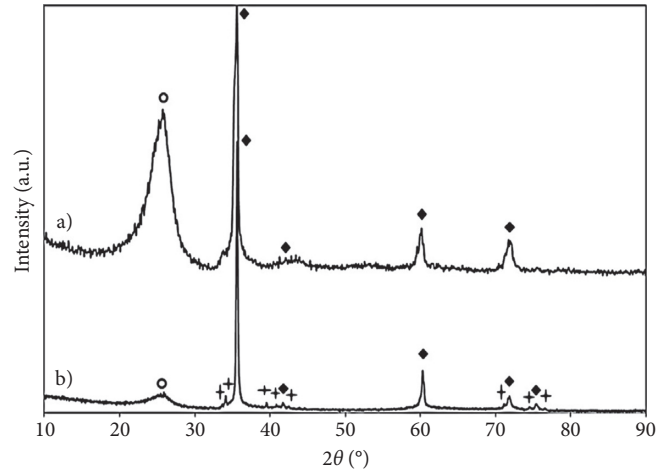
MAX phase ceramics are reported to exhibit not only high-temperature performance, thermal shock resistance,

TABLE 3: Self-joining of  $C_f/SiC$  composites using metal filler (SS = shear strength).

CMCs	Basic information	Metal filler	Process parameters	Bend strength (MPa)	Ref.
$C_f/SiC$	CVD-SiC	Ti	1700°C, 3 min, 60 MPa, vacuum	24.6 (SS)	[48]
$C_f/SiC$	3D, 10.0 vol.%, PIP	Cu-Au-Pd-V	1170°C, 10 min, $1.5 \times 10^{-3}$ Pa	135	[59]
$C_f/SiC$	3D	Pd-Co-V	1250°C, 20 min, $3.0-7.0 \times 10^{-3}$ Pa	—	[60]
$C_f/SiC$	3D, PIP, 10.0 vol.%	Cu-Pd-V	1170°C, 10 min, $3.0-7.0 \times 10^{-3}$ Pa	128	[61]



(a)



(b)

◆ SiC  
+  $Ti_3SiC_2$   
○ C

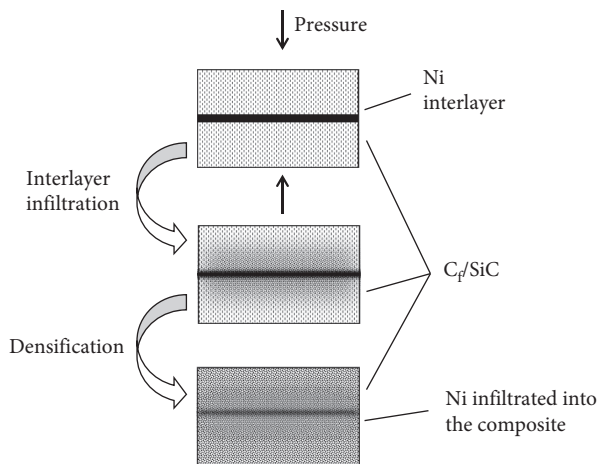
FIGURE 4: (a) Backscattered electron images of polished cross sections and (b) micro-XRD on the fracture surfaces of  $C_f/SiC$  joined by SPS with Ti foil [48].

FIGURE 5: The diagram of self-joining using Ni alloy.

and wear resistance but also a good plastic deformation capacity. Among various MAX phase ceramics,  $Ti_3SiC_2$  presents a suitable wettability and CTE toward  $C_f/SiC$  composite matrix (as is shown in Table 2) and is thus believed to be a promising candidate for the self-joining of  $C_f/SiC$  composites [16, 55, 56]. Dong et al. [55] used  $Ti_3SiC_2$  as the nonmetal filler to join  $C_f/SiC$  composite together

through hot pressing. The shear strength of the joint was reported as high as 110.4 MPa (56.7% of the  $C_f/SiC$  composite matrix). Chemical reactions took place at the interface between  $Ti_3SiC_2$  and  $C_f/SiC$ , and residual thermal stress was investigated. The phase compositions of the fracture surfaces for the  $C_f/SiC$  joints joined at various temperatures were also analyzed by XRD (as is shown in Figure 6). In addition, the fracture behavior of joining interface and brazing application was explored in previous articles [9, 65, 66, 69]. Interfacial reactions can affect the formation of a joint from the onset of bonding through the development of equilibrated microstructure and to the optimization of the mechanical properties. It has been demonstrated that an adequate joining interface could lead to improvements of the composite wettability by  $C_f/SiC$  [39].

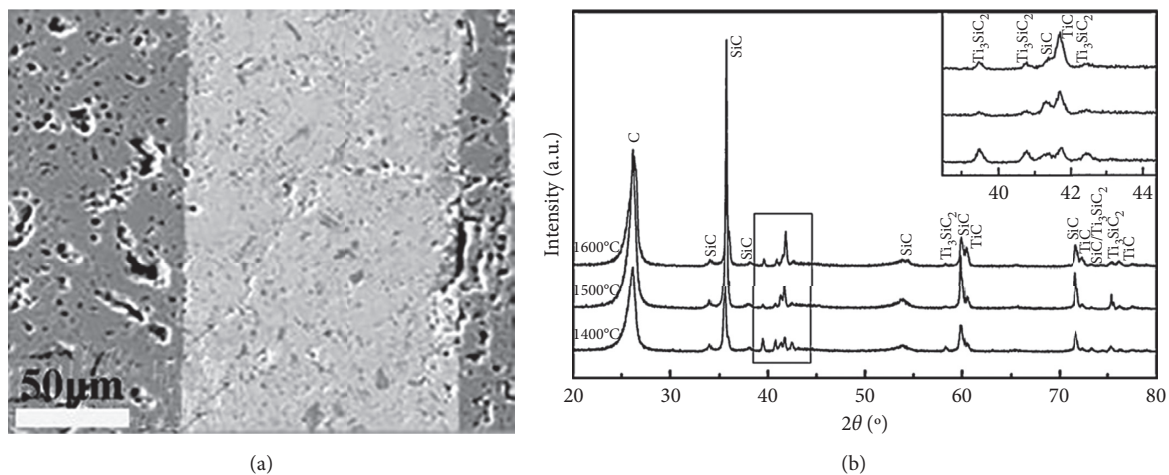
Besides, ceramic precursors are also used as nonmetal fillers for the self-joining of  $C_f/SiC$  composites. The ceramic precursor is transformed into amorphous ceramic at a certain temperature, and the composition and structure of the precursor are similar to those of the composite matrix. At the same time, the pyrolysis products are directly bonded with the composite matrix by chemical bonds. The thermodynamic properties of the joining layer obtained by this method are similar to those of the matrix [64]. And it has good compatibility with the composite matrix. Therefore,

TABLE 4: Self-joining of  $C_f/SiC$  composites with high-temperature fillers.

CMCs	Basic information	Joining material	Process parameters	Bend strength (MPa)	Ref.
$C_f/SiC$	3D, CVI	Ni alloy	1300°C, 45 min, 20 MPa, vacuum	260.3	[52]
$C_f/SiC$	2D, CVI	Ni alloy	1300°C, 45 min, 20 MPa, vacuum	60	[51]
$C_f/SiC$	2D, CVI	Ni alloy	1300°C, 15 MPa, vacuum	58	[53]

TABLE 5: Self-joining of  $C_f/SiC$  composites using inorganic filler (BS = bend strength).

CMCs	Basic information	Joining material	Process parameters	Shear strength (MPa)	Ref.
$C_f/SiC$	2D, CVI, 2.05 g/cm <sup>3</sup> , 40 MPa	Ti <sub>3</sub> SiC <sub>2</sub>	1600°C, 30 min, 20–40 MPa, Ar	110.4 (BS)	[55]
$C_f/SiC$	3D, CVI	PSZ	1300°C, N <sub>2</sub>	29.6	[64]
$C_f/SiC$	3D, PIP, 1.9 g/cm <sup>3</sup>	Si resin	1400°C, 5 h, Ar	3.51	[57]
$C_f/SiC$	2D, CVI, 1.7–2.2 g/cm <sup>3</sup>	MoSi <sub>2</sub> /Si	1450°C, 5 min, Ar	—	[58]

FIGURE 6: (a) The backscattered electron images and (b) XRD patterns of the fracture surfaces of the  $C_f/SiC$  joints [55].

the joint exhibits good mechanical strength. Previous reports showed that  $C_f/SiC$  composite was joined using Si-O-C ceramic precursor as filler [57].

Si resin is transformed into Si-O-C ceramic at low temperature; the Si-O-C ceramics infiltrating into the substrate improve the filler contact with the substrate closely and increase the connection area. Moreover, the Si-O-C ceramics infiltrating into the pits can form tiny “pins,” thus increasing the shear strength of the joints. Gianchandani et al. [58] reported that a MoSi<sub>2</sub>/Si composite obtained in situ by reaction of silicon and molybdenum at 1450°C in Ar flow is proposed as pressure-less joining material for  $C_f/SiC$  composites.

To sum up, we can know that the application of non-metal fillers method due to the phase consistency of joining material and matrix was similar, which not only avoid the CTE mismatch between the joining material and the matrix (CTE of typical materials is shown in Table 2) but also inhibit the adverse reactions of interface. It will be a very promising method in the future.

### 3. Joining of $C_f/SiC$ Composites to Metals

In order to obtain large size and complex-shaped components, the joining of  $C_f/SiC$  composites to metals such as Ti

[40], Nb [42, 68, 69], Ni [70], and TiAl alloys [30, 46, 71] is necessary. Due to the differences in physical, chemical and mechanical properties between  $C_f/SiC$  composites and metals, there are several problems for the joining of  $C_f/SiC$  composites to metals: firstly, the chemical bonds of  $C_f/SiC$  composites are ionic bond and covalent bond and the valence state is stable, whereas metals mostly are metal bond and therefore it is difficult to wet the surface of  $C_f/SiC$  composites by metal [40]. Secondly, the CTE mismatch between metals and  $C_f/SiC$  composites is very large, which will produce residual stress at the joint interface; hence, cracks, pores, and other defects exist after cooling [41, 72, 73]. At last, a variety of chemical reactions occur in the interface, resulting in brittle compounds with high hardness, which usually is the reason for the brittle fracture of the joint during working [30].

At present, there are many technologies solving the above problems during the joining process. Brazing and diffusion bonding are the most commonly used methods. In addition, online liquid infiltration joining, ultrasonic-assisted joining, and electric-assisted field joining are also reported.

**3.1. Brazing.** Brazing is one of the earliest and most commonly used methods for joining CMCs to metals

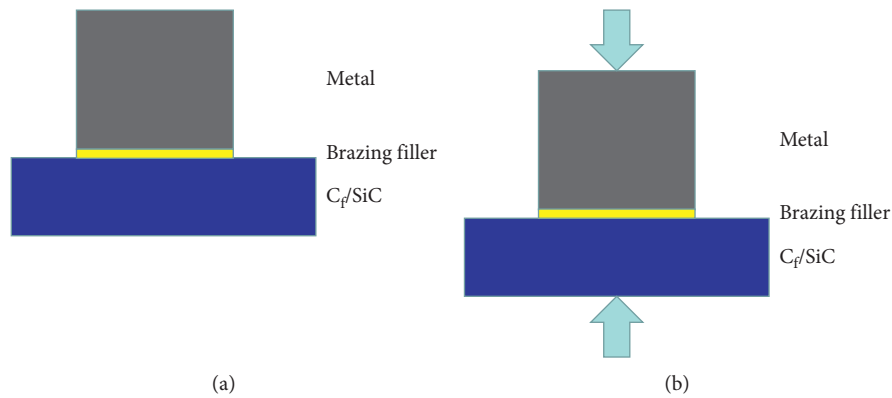


FIGURE 7: The schematic diagram of (a) brazing method and (b) diffusion bonding method.

(Figure 7(a)). It is divided into two kinds as follows: (1) metallizing the  $C_f/SiC$  composite surface and then brazing with ordinary brazing filler metals, usually known as indirect brazing, and (2) wetting CMCs surface directly using active metal, known as reactive brazing. Compared with indirect brazing, the scopes of application of reactive brazing are more extensive. Usually, metals and alloys with lower melting points are selected as the brazing fillers, and then the joint is heated to a certain temperature, which is higher than the melting point of brazing filler, and then brazing is conducted [74].

**3.1.1. Low-Temperature Fillers.** Low-temperature filler is a kind of metal with low melting point, such as Ag and Cu, which can form brazing filler at lower temperature to realize the joining of metal. Due to the low joining temperature, the damage is low.

Brazing method is simple and convenient; however, the brazing filler is mainly active metal elements, so it is necessary to protect the active metal elements from oxidation. Once the active element is oxidized, it is difficult to react with  $C_f/SiC$  composites and to form a reliable joint; consequently, the joint strength is low. Therefore, brazing method is generally carried out in vacuum conditions or inert protective gases [39, 75]. Feng et al. [72, 76] investigated the microstructural evolution and joint strength of between TiAl alloys and  $C_f/SiC$  composite via vacuum brazing using Ag-Cu and Ag-Cu-Ti fillers. The diffusion of Al and Ti from TiAl to the matrix had an important effect on the structure and strength of joints. When active element Ti diffused into  $C_f/SiC$  composite, the formation of  $AlCu_2Ti$  and Ag solid solution was detected with the dissolved Ti and Al; moreover,  $Ti_5Si_3$  phase and TiC also formed adjacent to the composite (as is shown in Figure 8). The maximum shear strength achieved 85 MPa with the thickness of TiC layer of 4–5  $\mu m$ . The fracture of the joint went through the TiC layer adjacent to its interface with the Ag solid solution and TiC bond layer.

As is shown in Table 6, Ag-Cu, Ag-Cu-Ti, and others are low-temperature fillers (900°C) and have low yield strength and good deformation ability, which is helpful to alleviate the residual stress of the joint, thus increasing the shear strength of the joints.

**3.1.2. High-Temperature Fillers.** Ag-Cu-Ti alloys have good plastic deformation behaviors (as is shown in Table 7); nevertheless, they always have low melting points and can only be used in low-temperature environments (<800°C). Once the temperature increased, the strength of the joint drops sharply. Therefore, it is necessary to develop suitable high-temperature brazing filler for high-temperature conditions.

Huang et al. [46] joined  $C_f/SiC$  composite to  $TC_4$  alloy using (Ti-Zr-Cu-Ni) and W powder as brazing fillers. Ti and Zr elements reacted with C, Cu, and Ni in the interlayer. As elements diffused to each other, a reaction layer was formed between the  $C_f/SiC$  composite and  $TC_4$  alloy. The brazing parameters had a significant effect on the interfacial reaction between  $C_f/SiC$  composite and joining material, which affected the shear strength of the joints. A continuous reaction layer adjacent to  $C_f/SiC$  composite and a diffusion layer near  $TC_4$  alloy can be clearly observed (Figures 9 and 10). The addition of appropriate W powder helped to relieve residual stress and improved the strength of the joints. The shear strength of the joint was 166 MPa and 96 MPa at room temperature and 800°C, respectively. Therefore, the joint can be used under high temperature.

However, the effect of W powder on the residual stress was small and the residual stress was still high. Ti-Zr-Cu-Ni alloy and pure Ti metals were used as joining materials [30]; the molten Ti-Zr-Cu-Ni reacted with solid Ti in the liquid-solid reaction to form an in situ alloy. The effects of Ti contents on the strength of joints were explored. With the increase in the Ti content, more tearing ridges appeared in the fracture surfaces, which indicated that the fracture possessed more plasticity. When the Ti content reached up to 40%, the shear strength of the joint reached up to 283 MPa, which was 79% higher than using Ti-Zr-Cu-Ni alone. The main reason was that the metal Ti had better plasticity, and the proper addition was beneficial for improving the interfacial reaction between  $C_f/SiC$  composite and Ti-6Al-4V alloy.

There are many research studies using brazing method for joining  $C_f/SiC$  to metals as listed in Table 7. The low-expansion material (W), the soft metal (Ni), and the high-temperature metal (Mo) as the reinforcing phase are added into the brazing filler, so that the CTE of the brazing filler is



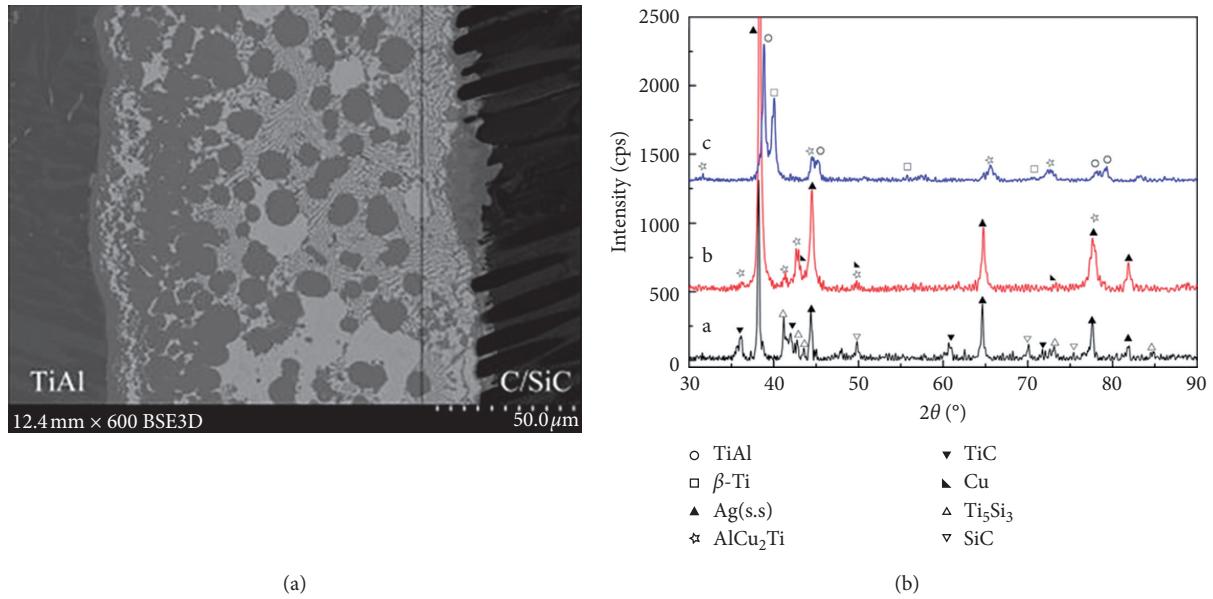


FIGURE 8: (a) Microstructures and (b) XRD patterns of the joint from C/SiC composites to TiAl brazed at 900°C for 10 min [72].

TABLE 6: Brazing of  $C_f/SiC$  composites to metals with low-temperature fillers.

CMCs	Basic information	Metal	Brazing material	Process parameters	Shear strength (MPa)	Ref.
$C_f/SiC$	3D, PIP, 1.86 g/cm <sup>3</sup>	Ti Al alloys	Ag-Cu	900°C, 10 min, $5 \times 10^{-3}$ Pa	85	[72]
$C_f/SiC$	3D, CVI	TC <sub>4</sub> alloys	Ag-Cu-Ti	900°C, 5 min, $10^{-4}$ Pa	102	[77]
$C_f/SiC$	—	Nb alloys	Ag-Cu-Ti	930°C, 15 min, $2 \times 10^{-3}$ Pa	—	[68]
$C_f/SiC$	3D, 1.8 g/cm <sup>3</sup> , 10–15%	Ti alloys	$C_f/Ag-Cu-Ti$	900°C, 30 min, $2.2 \times 10^{-3}$ MPa, $6 \times 10^{-3}$ Pa	84	[40]

TABLE 7: Brazing of  $C_f/SiC$  composites to metals with high-temperature fillers.

CMCs	Basic information	Metal	Brazing material	Process parameters	Shear strength (MPa)	Ref.
$C_f/SiC$	3D, 2.0–2.1 g/cm <sup>3</sup> , 10–15 vol.%, 400 MPa	Ti alloys	Ag-Cu-Ti + 15 vol.% W	900°C, 5 min, $2.2 \times 10^{-3}$ MPa, $6 \times 10^{-3}$ Pa	180	[38]
$C_f/SiC$	3D, PIP, 1.7–1.8 g/cm <sup>3</sup> , 10–15 vol.%, 400 MPa	TC <sub>4</sub> alloys	Ti-Zr-Cu-Ni + 15 vol.% W	930°C, 20 min, $6 \times 10^{-3}$ Pa	166	[46]
$C_f/SiC$	3D	42CrMo	Ag-Cu-Ti + 5 vol.% Mo	900°C, 10 min, vacuum	587 (BS)	[78]
$C_f/SiC$	3D, PIP	Nb	Ti-Cu-Ni-Zr	930°C, 10 min, $5 \times 10^{-3}$ Pa	124	[69]
$C_f/SiC$	3D	Ti-6Al-4V	Ti + (Ti-Cu-Ni-Zr)	940°C, 20 min, $5 \times 10^{-3}$ Pa	283	[47]
$C_f/SiC$	3D, PIP, 1.98 g/cm <sup>3</sup> , 21.5 vol.%	Nb-1Zr	Ti-Co-Nb	1280°C, 10 min, $1.0-3.0 \times 10^{-3}$ Pa	242	[43]
$C_f/SiC$	3D, PIP, 1.86 g/cm <sup>3</sup> , 11.7 vol.%	Ti Al alloys	TiH <sub>2</sub> -Ni-B	1180°C, 10 min, $5 \times 10^{-3}$ Pa	105	[71]

reduced and the residual stress of the joint is facilitated. However, there are still some shortcomings for brazing process, such as the interface reaction is intense, to produce brittle compounds, which requires the appropriate adjustment of brazing filler and process parameters. More importantly, avoiding bad excessive interface reaction and accessing to excellent mechanical properties of joints are essential.

**3.2. Diffusion Bonding.** In mid-1950s, the former Soviet Union scientists proposed a diffusion bonding method

which was widely used to join ceramic to metals, including the joint of  $C_f/SiC$  composites to metals (as shown in Figure 7(b)).  $C_f/SiC$  composites and metals are contacted with each other under high temperatures, vacuum or inert atmospheres and pressures, and the plastic formation of connected surfaces is close to each other. After a certain period of soaking time, the intermolecular diffusion and chemical reaction are realized. During the diffusion bonding process, the interface is bonded by plastic deformation, diffusion, and creep mechanism. The joining temperature is high, the CTE and elastic modulus of the composites and

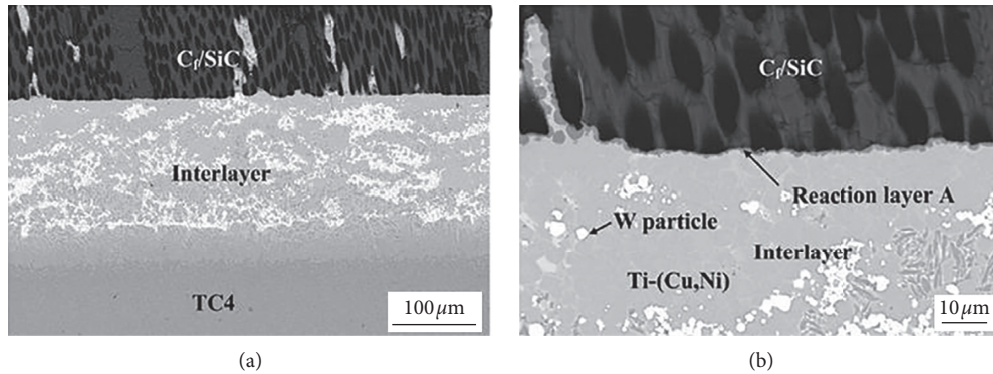


FIGURE 9: BSE images of the joint: (a) micrograph of the joint; (b) interface between  $C_f/SiC$  composite and interlayer [46].

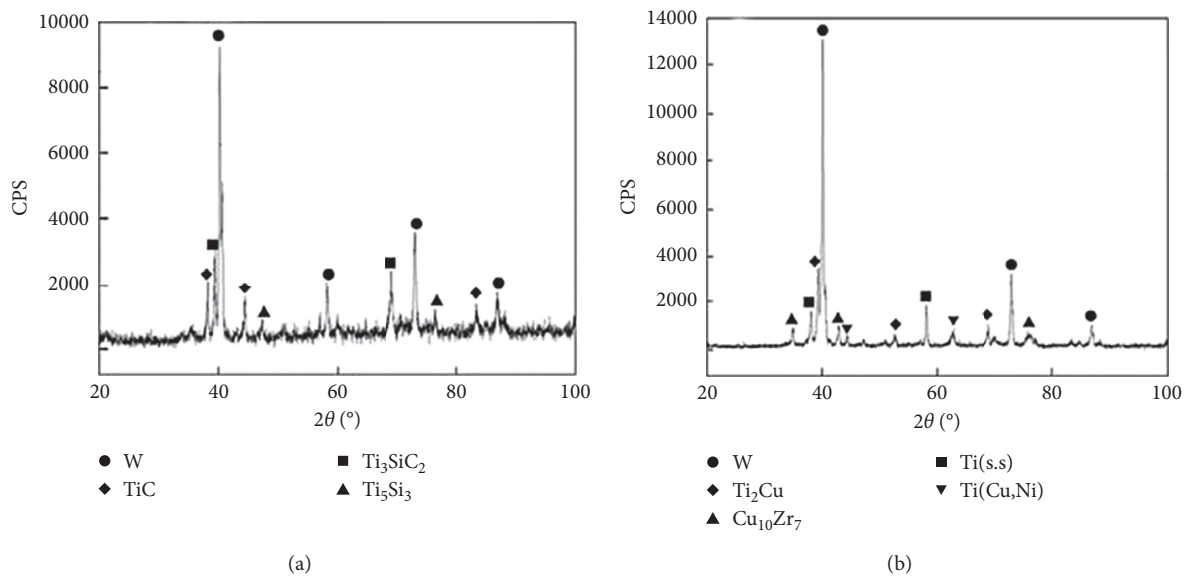


FIGURE 10: XRD pattern of the joint: (a) interface between  $C_f/SiC$  composite and interlayer; (b) interlayer [46].

metals are mismatch, and it is easy to induce high residual stress. Due to sharp structural transition near the interface and the lack of a buffer layer to relax the stress, the residual stress is high enough to lead to a lower joint strength.

Simply, diffusion bonding method is a solid-state bonding process, which has been demonstrated as a viable method to overcome the problems encountered in welding. There are many reports on the diffusion bonding  $C_f/SiC$  composites to metals. In order to join 3D/2D  $C_f/SiC$  composite to Nb alloy, Xiong et al. [41, 42] used Ti-Cu foil as the joining material to join  $C_f/SiC$  composite to Nb alloy through a two-stage joining process: solid-phase diffusion bonding and transient liquid-phase diffusion bonding. It was found that the Ti-Cu liquid eutectic alloy was formed by the reaction of Ti and Cu, not only infiltrated into open pores and microcracks as a nail but also reacted with ceramic coating. The remaining Cu was deformed by own plastic deformation and released the residual stress. In addition, the liquid layer formed by interlayer in the TLP-DB process had good wettability to  $C_f/SiC$  composite and can infiltrate into

$C_f/SiC$  composite matrix and encapsulated  $C_f$  between the interlayer and  $C_f/SiC$  interface region. These processes were very beneficial for the mechanical strength of the joint. The shear strength of the joint between 2D  $C_f/SiC$  composite and Nb alloy was 14.1 MPa, and the shear strength of the joint between 3D  $C_f/SiC$  composite and Nb alloy reached up to 34.1 MPa. To our best knowledge, there were mainly two factors leading to a low shear strength of the joint between 2D  $C_f/SiC$  composite and Nb alloy: the CTE mismatch between 2D  $C_f/SiC$  composite and Nb alloy was larger compared with 3D  $C_f/SiC$  composite and Nb, resulting in a large residual stress, and the fiber direction among 2D  $C_f/SiC$  composite was parallel to the joining interface, whereas the fiber direction among 3D  $C_f/SiC$  composite was perpendicular to the joining interface. When the fiber was perpendicular to the joining interface, "nail effect" formed between reaction layer and  $C_f$  and shared more load than other regions in fracture test (as is shown in Figure 11). These results demonstrated that the direction of fiber was directly related to the interface structure of the joint, which

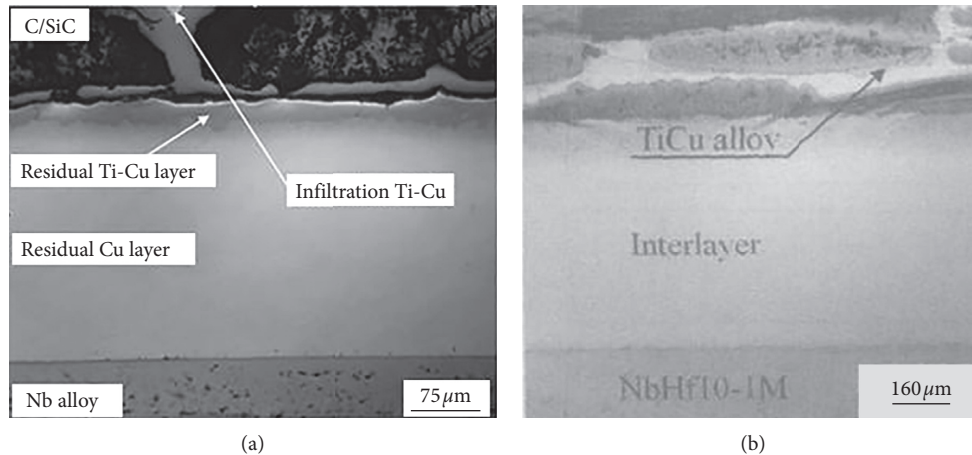


FIGURE 11: SEM micrograph of the joint: (a) 3D  $C_f/SiC$  and (b) 2D  $C_f/SiC$  [41, 42].

in turn affected the shear strength of joint. In this kind of research work, the influence of fiber must be considered; however, this interesting topic has not yet been studied systematically.

In addition, the reactions between joining material and composite matrix have been recently recognized as critical factors for determining the strength of the joint.  $C_f/SiC$  composite and Ti-6Al-4V alloy were joined by Ban et al. [79] with the mixed powder of Cu, Ti, and graphite under vacuum environment. In situ synthetic TiC that reduced the thermal stress significantly was synthesized by interdiffusing of C element in the graphite particle and Ti element in the liquid bonding layer (as is shown in Figure 12). The positive effect of TiC on joint strength was also described in other papers [56, 72, 80]. Table 8 summarizes the data of diffusion bonded joining. The utility model has the advantages of high strength, stable joint quality, and good corrosion resistance, especially for the joining of  $C_f/SiC$  composites and metals for high-temperature and corrosion-resistance application.

**3.3. Online Liquid Infiltration Joining.** Online liquid infiltration joining is a novel technology, which is applied to the joining of fiber-reinforced ceramic matrix composites.  $C_f/SiC$  composites are usually porous both for CVI and PIP processing. An online liquid infiltration joining method that is suitable for the composites was reported. The porosity of  $C_f/SiC$  composites was controlled and then the compact process was carried out after the joining has finished, which reduced the damage of joints as much as possible. The wettability between the joining material and  $C_f/SiC$  composite was improved; moreover, the joining material could be melted and infiltrated into the  $C_f/SiC$  matrix, which increased the joining area and reinforced the joint strength [81, 82]. In addition, a root-like morphology was formed in  $C_f/SiC$  composite substrate, which could greatly enhance the reliability of joint [83].

The only paper that attempts to join  $C_f/SiC$  composite to metal via online liquid infiltration joining was presented in 2004 [84]. The authors joined 2D/3D  $C_f/SiC$  composites to Nb with Ni-based filler by the online liquid infiltration

joining method (as shown in Figure 13). The joint between 2D  $C_f/SiC$  composite and Nb was failure and separated during the cooling. However, the favorable joint between 3D  $C_f/SiC$  composite and Nb was obtained. Approaches such as reactive brazed [68, 69] and diffusion bonding [41, 42] have also been successfully used to join  $C_f/SiC$  composites to Nb alloy. Unfortunately, the bonding processes above were usually conducted after the preparation of the composite matrix, which damaged the strength of the matrix. Online liquid infiltration joining, which is completed in the preparation process, is different from the above methods. Afterward, chemical vapor deposition (CVD) process not only complete the preparation of materials but also can provide antioxidation coating for the matrix and the joint, reflects the joining, preparation, and processing integration [51, 85].

**3.4. Ultrasonic-Assisted Joining.** Ultrasonic-assisted joining is employed to join aluminum alloy structural parts at first. Afterward, ultrasonic is used for copper and alloy, gradually widely used in CMCs and metals, as shown in Figure 14 [86]. Since ultrasound exists as an energy form, it produces some unique ultrasonic effects when it propagates in the medium. The ultrasonic-assisted joining utilizes ultrasonic vibrations to interact the contact area of the CMCs with the metal. The ultrasonic effect causes the liquid joining material to spread on the surface of the matrix and form a joint with the metal [87]. In 1990s, ultrasonic-assisted joining technology facilitated the wetting of materials with poor wetting properties such as ceramics, glass, and stainless steel [88–90, 94]. The liquid-connecting materials spread and moisten, through the ultrasonic wave effect that from the vibrations of ultrasonic, the surface of the CMCs and metal to achieve good connection. Moreover, it is worth mentioning that ultrasonic-assisted joining technology can improve the wettability of connection materials on the surface of matrixes such as ceramics, glass, and stainless steel. Therefore, this technology has been widely applied in many fields.

The joining of SiC and Ti-6Al-4V alloy via ultrasonic-assisted joining was conducted by Chen et al. [91, 92]. SiC

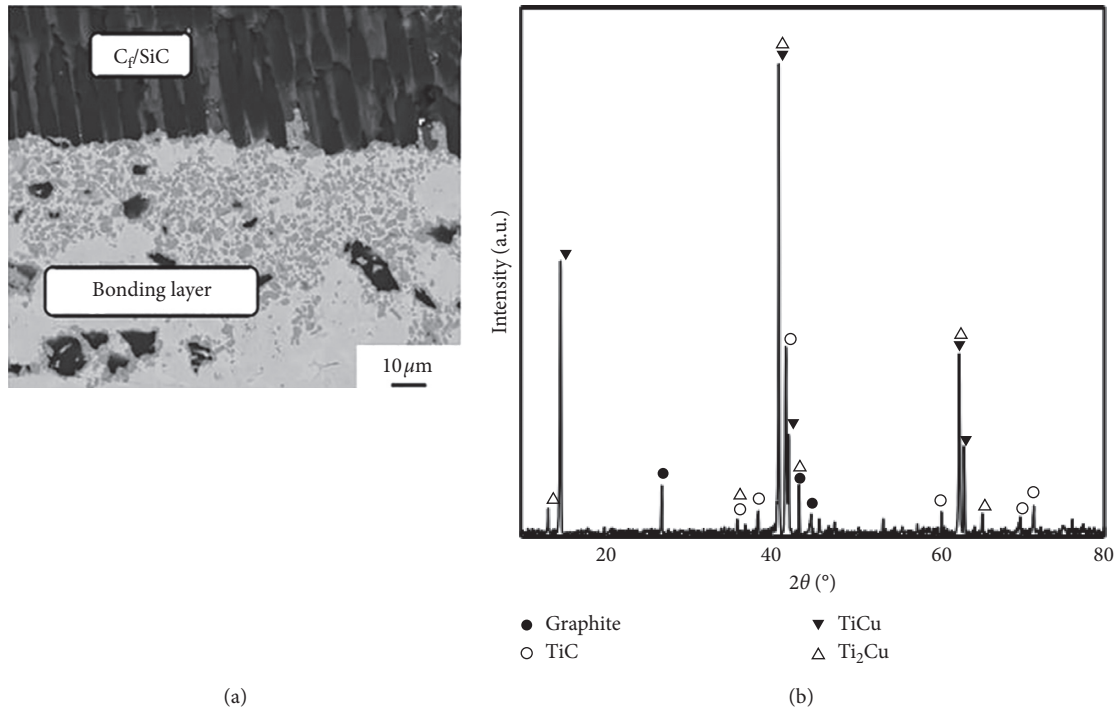


FIGURE 12: (a) Micrographs and (b) XRD pattern of the interface [79].

TABLE 8: Diffusion bonding of C<sub>f</sub>/SiC composites to metals.

CMCs	Basic information	Metal	Joining material	Process parameter	Shear strength (MPa)	Ref.
C <sub>f</sub> /SiC	3D, CVI, 2.1 g/cm <sup>3</sup>	Nb alloy	Ti-Cu bi-foil	800°C, 30 min, 6 MPa; 1020°C, 60 min, 0.05 MPa, 3.2 × 10 <sup>-3</sup> Pa	34.1	[41]
C <sub>f</sub> /SiC	2D, CVI, 16 vol.%	Nb alloy	Ti-Cu-Cu	850°C, 40 min, 8 MPa; 980°C, 30 min, 0.05 MPa, 3.2 × 10 <sup>-3</sup> Pa	14.1	[42]
C <sub>f</sub> /SiC	3D, 2.0–2.1 g/cm <sup>3</sup> , 10–15 vol.%, 400 MPa	TC <sub>4</sub> alloy	Cu-Ti-C	900–950°C, 5–30 min, 6.0 × 10 <sup>-3</sup> Pa	—	[79]
C <sub>f</sub> /SiC	3D, 15 vol.%, 500 MPa	Ni alloy	Zr/Ta	1050°C, 10 min, 40.8 MPa, 10 <sup>-2</sup> Pa	110.89 (BS)	[70]

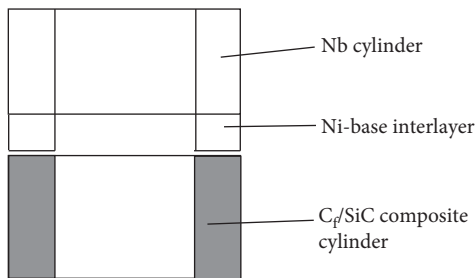


FIGURE 13: The diagram of specimens before being joined.

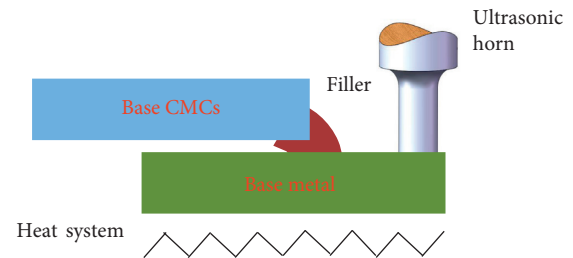


FIGURE 14: The diagram of capillary process that filler gets into clearance by action of ultrasonic vibration.

was employed by a joining material with an Al-12Si alloy at low temperature (620°C), and the shear strength of the joint was 84–94 MPa. In their study, the oxide layer of the matrix was broken by the ultrasonic, and the joining material can form a good interface between SiC and Ti-6Al-4V alloy. However, cracks were observed in SiC material and the

propagation direction was parallel to joint. The main reason was that the nonuniform shrinkage of material at the joint and residual stress, which leads to crack formation in the SiC substrate, was produced during the cooling process. They obtained an integrated joint when using the novel joining

material in their study. SiC and Ti-6Al-4V alloy were joined with AlSnSiZnMg mixed metal, which reduced the joining temperature and the residual stress of the joint, inhibiting the occurrence of cracks and other defects. Unfortunately, the shear strength of the joint was not improved (77.8 MPa).

On the other hand, ultrasonic-assisted joining technology can also be used to join oxide ceramics to metals. Naka et al. [88] joined  $\text{Al}_2\text{O}_3$  to Cu with Zn, Zn-5Al, and  $\text{Zn}_{100-x}(\text{Al}_{0.6} + \text{Cu}_{0.4})_x$  ( $x = 0-30$ ) as the joining materials. It was shown that with the time and joining temperature increased, the shear strength of the joint with Zn-6Al-4Cu filler was improved and reached  $\sim 62$  MPa. In the above literatures, some of them were reported that the ultrasound was beneficial to improve the wettability of  $\text{Al}_2\text{O}_3$  and metals.

The mechanism of ultrasonic effect on the joining process can be summarized as follows: (1) the macroscopic bubbles between the filled metal and the ceramic were removed by the ultrasonic cavitation; (2) the  $\text{C}_f/\text{SiC}$  substrate surface was subjected to high-speed impact of atoms under ultrasonic vibration; (3) the ultrasonic vibration and friction between the joining material and metal.

**3.5. Electric-Assisted Field Joining.** Although diffusion bonding is widely used to join CMCs and metals, generally, it requires high temperatures, high pressure, vacuum or inert atmosphere, and long joining time [93, 94, 98]. Electric-assisted field joining is an effective way to solve these above problems, as shown in Figure 15. Since the joining between CMCs and metal was realized by chemical reaction, interfacial structure formed by reaction determines the mechanical properties of the joint. Better joint can be obtained using the electric-assisted field method.

The interface between CMCs and metal were polarized under electrostatic field. On the one hand, it promotes atomic migration and vacancy diffusion. On the other hand, it accelerates the interface reaction, which reduces the joining temperature, the pressure, and the residual stress. Moreover, the interface reaction is easy to control, and joining time is very short [96–98, 101].

Initially, the electric-assisted field joining is mainly employed for joining ceramics to metals [100]. The interface composition and mechanical properties of joints between SiC and Ti were investigated by Wang et al. [98] in the electric field. It was shown that the external electric field reduced the joining temperature and time and improved the shear strength. It is important that the external electric field can improve the diffusion rate of interface atoms. Moreover, it promoted the interface reaction and improved the joining efficiency.

Owing to its simplicity and efficiency, electric-assisted field joining became a useful method employed for joining  $\text{C}_f/\text{C}$  composites [101] and  $\text{C}_f/\text{SiC}$  composites [48].  $\text{C}_f/\text{C}$  composites were firstly joined by combining electric field-assisted sintering technology and using a  $\text{Ti}_3\text{SiC}_2$  tape film as the interlayer [101]. In their work, the interdiffusion speed between the interlayer and the metal was accelerated by an electric field and the joining time was only 12 min. To our

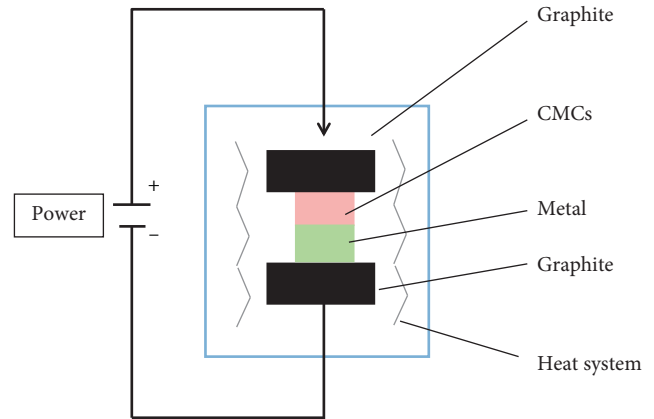


FIGURE 15: The diagram of the experimental equipment under electric field.

knowledge, the  $\text{Ti}_3\text{SiC}_2$  exhibited pseudoplastic at  $1300^\circ\text{C}$  or higher [102, 103]. Therefore,  $\text{Ti}_3\text{SiC}_2$  infiltrated into the composite matrix and a “nail” that clamps the matrix was observed, as shown in Figure 16, which improved shear strength of the joint. In the joining process, two key factors affected the strength of the joint: (1) the interdiffusion between the joining material and the matrix was promoted by electric field and (2)  $\text{Ti}_3\text{SiC}_2$  showed good plastic deformation ability in the electric field.

Atoms spread to the interface under electric field. It is necessary to pass through the potential through the gap, the original position occupied by their own formed a new space. The energy of the atoms across the barrier was provided by the electric field. At the same time, the atoms across the barrier potential energy are reduced by the electric field. Combined with these two effects, the diffusion activation of atoms can be greatly reduced, thereby increasing the diffusion rate of solute atoms and obtaining a uniform structure [104]. Therefore, the electric-assisted fields joining method has drawn great attention and is expected to become an important way for the joining of  $\text{C}_f/\text{SiC}$  composites in the future.

## 4. Summary

With the rapid development of high-tech in aerospace and other industry fields, carbon fiber-reinforced silicon carbide ( $\text{C}_f/\text{SiC}$ ) ceramic matrix composites, one of the most famous CMCs, are becoming the most promising candidates for high-temperature structural applications. In most cases, typically, it is very difficult to produce large-size  $\text{C}_f/\text{SiC}$  composite components with complex shapes, resulting in that they must be joined with themselves or other materials by appropriate joining technologies. At present, various joining technologies of  $\text{C}_f/\text{SiC}$  composites are reported, including the joining of  $\text{C}_f/\text{SiC}$ - $\text{C}_f/\text{SiC}$  and  $\text{C}_f/\text{SiC}$ -metal, such as direct bonding of  $\text{C}_f/\text{SiC}$ - $\text{C}_f/\text{SiC}$ , indirect bonding of  $\text{C}_f/\text{SiC}$ - $\text{C}_f/\text{SiC}$ , brazing of  $\text{C}_f/\text{SiC}$ -metal, diffusion bonding of  $\text{C}_f/\text{SiC}$ -metal, online liquid infiltration of  $\text{C}_f/\text{SiC}$ -metal, ultrasonic-assisted joining of  $\text{C}_f/\text{SiC}$ -metal, and electric-assisted joining of  $\text{C}_f/\text{SiC}$ -metal.

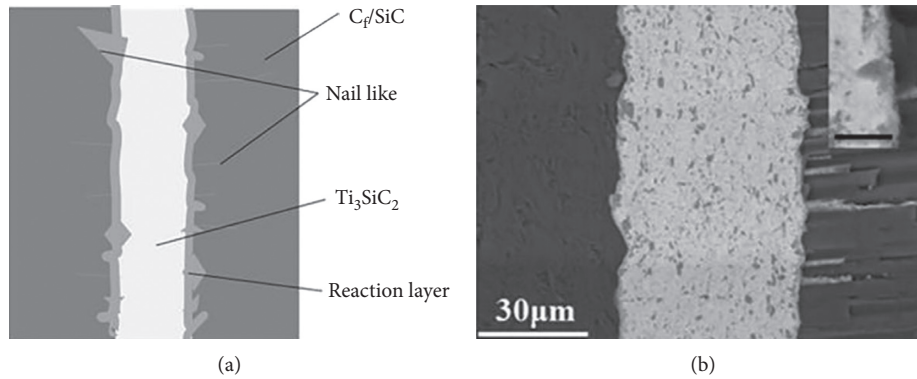


FIGURE 16: (a) The schematic diagram of “nail” like and (b) BSE image [101].

To the best knowledge of the authors, however, there has been no systematic summary of the joining of C<sub>f</sub>/SiC composites. In this paper, a systematic review of the joining of C<sub>f</sub>/SiC composites is conducted, and the aim of this paper is to provide some reference for researchers working on this field.

### Conflicts of Interest

The authors declare that they have no conflicts of interest.

### Acknowledgments

The authors sincerely thank the Young Elite Scientist Sponsorship (YESS) Program by CAST (No. 2015QNR001) and the Beijing Institute of Technology Research Fund Program for Young Scholars.

### References

- [1] A. Luna Ramírez, J. Porcayo-Calderon, Z. Mazur et al., “Microstructural changes during high temperature service of a cobalt-based superalloy first stage nozzle,” *Advances in Materials Science and Engineering*, vol. 2016, pp. 1–7, 2016.
- [2] A. Baldan, “Progress in Ostwald ripening theories and their applications to nickel-base superalloys. Part I: Ostwald ripening theories,” *Journal of Materials Science*, vol. 37, no. 11, pp. 2171–2202, 2002.
- [3] M. V. Acharya and G. E. Fuchs, “The effect of long-term thermal exposures on the microstructure and properties of CMSX-10 single crystal Ni-base superalloys,” *Materials Science and Engineering: A*, vol. 381, no. 1-2, pp. 143–153, 2004.
- [4] B. S. Sung and Y. H. Yun, “SiC conversion coating prepared from silica-graphite reaction,” *Advances in Materials Science and Engineering*, vol. 2017, no. 5, pp. 1–8, 2017.
- [5] N. S. Jacobson, K. N. Lee, and D. S. Fox, “Reactions of silicon carbide and silicon(IV) oxide at elevated temperatures,” *Journal of the American Ceramic Society*, vol. 75, no. 6, pp. 1603–1611, 1992.
- [6] S. V. Ushakov and A. Navrotsky, “Experimental approaches to the thermodynamics of ceramics above 1500°C,” *Journal of the American Ceramic Society*, vol. 95, no. 5, pp. 1463–1482, 2012.
- [7] J. Llorca and R. N. Singh, “Influence of fiber and interfacial properties on fracture behavior of fiber-reinforced ceramic composites,” *Journal of the American Ceramic Society*, vol. 74, no. 11, pp. 2882–2890, 1991.
- [8] Q. Xie and S. N. Wosu, “Dynamic fracture toughness of TaC/CNTs/SiC CMCs prepared by spark plasma sintering,” *Advances in Materials Science and Engineering*, vol. 2015, no. 2, pp. 1–8, 2015.
- [9] C. J. Liu, W. F. Ding, T. Y. Yu, and C. Y. Yang, “Materials removal mechanism in high-speed grinding of particulate reinforced titanium matrix composites,” *Precision Engineering*, vol. 51, pp. 68–77, 2018.
- [10] X. Ma, S. A. Chen, M. Mei et al., “Microstructure and mechanical behaviors of T700 carbon fiber reinforced C/SiC composites via precursor infiltration and pyrolysis,” *Materials Science and Engineering: A*, vol. 666, pp. 238–244, 2016.
- [11] S. Schmidt, S. Beyer, H. Knabe et al., “Advanced ceramic matrix composite materials for current and future propulsion technology applications,” *Acta Astronautica*, vol. 55, no. 3, pp. 409–420, 2004.
- [12] L. Wang, F. Hou, X. Wang, J. C. Liu, and A. Guo, “Preparation and mechanical properties of continuous carbon nanotube networks modified C<sub>f</sub>/SiC composite,” *Advances in Materials Science and Engineering*, vol. 2015, no. 12, pp. 1–7, 2015.
- [13] M. Z. Berbon, D. R. Dietrich, and D. B. Marshall, “Transverse thermal conductivity of thin C/SiC composites fabricated by slurry infiltration and pyrolysis,” *Journal of the American Ceramic Society*, vol. 84, no. 10, pp. 2229–2234, 2001.
- [14] W. Yang, L. Zhang, L. Cheng et al., “Oxidation behavior of C<sub>f</sub>/SiC composite with CVD SiC-B<sub>4</sub>C coating in a wet oxygen environment,” *Applied Composite Materials*, vol. 16, no. 2, pp. 83–92, 2009.
- [15] G. Boitier, J. L. Chermant, and J. Vicens, “Bridging at the nanometric scale in 2.5D C<sub>f</sub>-SiC composites,” *Applied Composite Materials*, vol. 6, no. 5, pp. 279–287, 1999.
- [16] P. Tatarko, Z. Chlup, A. Mahajan et al., “High temperature properties of the monolithic CVD-SiC materials joined with a pre-sintered MAX phase Ti<sub>3</sub>SiC<sub>2</sub> interlayer via solid-state diffusion bonding,” *Journal of the European Ceramic Society*, vol. 37, no. 4, pp. 1205–1216, 2017.
- [17] G. B. Zheng, H. Sano, Y. Uchiyama, K. Kobayashi, and H. M. Cheng, “The properties of carbon fibre/SiC composites fabricated through impregnation and pyrolysis of polycarbosilane,” *Journal of Materials Science*, vol. 34, no. 4, pp. 827–834, 1999.
- [18] K. Jian, Z. H. Chen, Q. S. Ma, and W. W. Zheng, “Effects of pyrolysis processes on the microstructures and mechanical properties of C<sub>f</sub>/SiC composites using polycarbosilane,”

- Materials Science and Engineering: A*, vol. 390, no. 1, pp. 154–158, 2005.
- [19] K. Jian, Z. H. Chen, Q. S. Ma, H. F. Hu, and W. W. Zheng, “Processing and properties of 2D-C<sub>f</sub>/SiC composites incorporating SiC fillers,” *Materials Science and Engineering: A*, vol. 408, no. 1, pp. 330–335, 2005.
- [20] C. C. Zhou, C. R. Zhang, H. F. Hu et al., “Preparation of 3D-C<sub>f</sub>/SiC composites at low temperatures,” *Materials Science and Engineering: A*, vol. 488, no. 1, pp. 569–572, 2008.
- [21] M. Broda, A. Pyzalla, and W. Reimers, “X-ray analysis of residual stresses in C/SiC composites,” *Applied Composite Materials*, vol. 6, no. 1, pp. 51–66, 1999.
- [22] J.-C. Bae, K.-Y. Cho, D.-H. Yoon et al., “Highly efficient densification of carbon fiber-reinforced SiC-matrix composites by melting infiltration and pyrolysis using polycarbosilane,” *Ceramics International*, vol. 39, no. 5, pp. 5623–5629, 2013.
- [23] Z. S. Rak, “A process for C<sub>f</sub>/SiC composites using liquid polymer infiltration,” *Journal of the American Ceramic Society*, vol. 84, no. 10, pp. 2235–2239, 2001.
- [24] L. B. Li, “Comparison of fatigue life between C/SiC and SiC/SiC ceramic-matrix composites at room and elevated temperatures,” *Applied Composite Materials*, vol. 23, no. 5, pp. 913–952, 2016.
- [25] G. V. Samsonov and B. A. Kovenskaya, “The nature of the chemical bond in borides,” in *Boron and Refractory Borides*, pp. 19–30, Springer-Verlag, Berlin, Germany, 1977.
- [26] S. Suyama, T. Kameda, and Y. Itoh, “Development of high-strength reaction-sintered silicon carbide,” *Diamond and Related Materials*, vol. 12, no. 3, pp. 1201–1204, 2003.
- [27] Y. Z. Zhu, Z. R. Huang, and S. M. Dong, “Manufacturing 2D carbon-fiber-reinforced SiC matrix composites by slurry infiltration and PIP process,” *Ceramics International*, vol. 34, no. 5, pp. 1201–1205, 2008.
- [28] Q. Zhou, S. M. Dong, X. Y. Zhang, and D. Jiang, “Fabrication of C<sub>f</sub>/SiC composites by vapor silicon infiltration,” *Journal of the American Ceramic Society*, vol. 89, no. 7, pp. 2338–2340, 2006.
- [29] M. N. Saleh, Y. Wang, A. Yudhanto et al., “Investigating the potential of using off-axis 3D woven composites in composite joints’ applications,” *Applied Composite Materials*, vol. 24, no. 2, pp. 377–396, 2017.
- [30] D. Y. Fan, J. H. Huang, X. P. Zhao et al., “Joining of C<sub>f</sub>/SiC composite to Ti-6Al-4V with (Ti-Zr-Cu-Ni)+Ti filler based on in-situ alloying concept,” *Ceramics International*, vol. 43, no. 5, pp. 4151–4158, 2017.
- [31] Y. Katoh, L. L. Snead, T. Cheng et al., “Radiation-tolerant joining technologies for silicon carbide ceramics and composites,” *Journal of Nuclear Materials*, vol. 448, no. 1, pp. 497–511, 2014.
- [32] G. D. Li, Y. D. Zhang, C. R. Zhang et al., “Design, preparation and properties of on-line-joints of C/SiC-C/SiC with pins,” *Composites Part B: Engineering*, vol. 48, pp. 134–139, 2013.
- [33] Z. B. He, L. T. Zhang, Y. Zhang et al., “Microstructural characterization and failure analysis of 2D C/SiC two-layer beam with pin-bonded hybrid joints,” *International Journal of Adhesion and Adhesives*, vol. 57, pp. 70–78, 2015.
- [34] J. A. Fernie, *Joining Ceramic Materials*, American Ceramic Society, Westerville, OH, USA, 1997.
- [35] X. Y. Wang, Y. Li, S. Z. Wei, and X. D. Ma, “Research progress in connecting techniques of ceramics and metals,” *Casting Forging Welding*, vol. 38, no. 13, pp. 144–148, 2009.
- [36] P. Tatarko, V. Casalegno, C. F. Hu et al., “Joining of CVD-SiC coated and uncoated fibre reinforced ceramic matrix composites with pre-sintered Ti<sub>3</sub>SiC<sub>2</sub> MAX phase using spark plasma sintering,” *Journal of the European Ceramic Society*, vol. 36, no. 16, pp. 3957–3967, 2016.
- [37] R. H. Jones, L. Giancarli, A. Hasegawa et al., “Promise and challenges of SiC<sub>f</sub>/SiC composites for fusion energy applications,” *Journal of Nuclear Materials*, vol. 307, pp. 1057–1072, 2002.
- [38] G. B. Lin, J. H. Huang, H. Zhang, and H. Y. Liu, “Microstructure and mechanical performance of brazed joints of Cf/SiC composite and Tialloy using Ag-Cu-Ti-W,” *Science and Technology of Welding and Joining*, vol. 11, no. 4, pp. 379–383, 2006.
- [39] J. K. Li, L. Liu, Y. T. Wu et al., “Microstructure of high temperature Ti-based brazing alloys and wettability on SiC ceramic,” *Materials and Design*, vol. 30, no. 2, pp. 275–279, 2009.
- [40] G. B. Lin, J. H. Huang, and H. Zhang, “Joints of carbon fiber-reinforced SiC composites to Ti-alloy brazed by Ag-Cu-Ti short carbon fibers,” *Journal of Materials Processing Technology*, vol. 189, no. 1, pp. 256–261, 2007.
- [41] J. T. Xiong, J. L. Li, F. S. Zhang, and W. Huang, “Joining of 3D C/SiC composites to niobium alloy,” *Scripta Materialia*, vol. 55, no. 2, pp. 151–154, 2006.
- [42] J. T. Xiong, J. L. Li, F. S. Zhang et al., “Joining of 2D C/SiC composites with niobium alloy,” *Journal of Inorganic Materials*, vol. 21, no. 6, pp. 1391–1396, 2006.
- [43] Q. Zhang, L. B. Sun, Q. Y. Liu, G. Wang, and Y. Xuan, “Effect of brazing parameters on microstructure and mechanical properties of Cf/SiC and Nb-1Zr joints brazed with Ti-Co-Nb filler alloy,” *Journal of the European Ceramic Society*, vol. 37, no. 3, pp. 931–937, 2017.
- [44] S. J. Li, Y. Zhou, and H. P. Duan, “Joining of SiC ceramic to Ni-based superalloy with functionally gradient material fillers and a tungsten intermediate layer,” *Journal of Materials Science*, vol. 38, no. 19, pp. 4065–4070, 2003.
- [45] C. Jiménez, C. Wilhelmi, and T. Speliotis, “Joining of C/SiC Ceramics to Nimonic Alloys,” *Journal of Materials Engineering and Performance*, vol. 21, no. 5, pp. 683–689, 2012.
- [46] B. Cui, J. H. Huang, C. Cai, S. Chen, and X. Zhao, “Microstructures and mechanical properties of C<sub>f</sub>/SiC composite and TC<sub>4</sub> alloy joints brazed with (Ti-Zr-Cu-Ni)+W composite filler materials,” *Composites Science and Technology*, vol. 97, pp. 19–26, 2014.
- [47] Y. Liu, Z. R. Huang, and X. J. Liu, “Joining of sintered silicon carbide using ternary Ag-Cu-Ti active brazing alloy,” *Ceramics International*, vol. 35, no. 8, pp. 3479–3484, 2009.
- [48] S. Rizzo, S. Grasso, M. Salvo et al., “Joining of C/SiC composites by spark plasma sintering technique,” *Journal of the European Ceramic Society*, vol. 34, no. 4, pp. 903–913, 2014.
- [49] B. Chen, H. P. Xiong, Y. Y. Cheng et al., “Microstructure and strength of Cf/SiC joints with Ag-Cu-Ti brazing fillers,” *Journal Materials Engineering*, vol. 329, pp. 27–31, 2010.
- [50] D. Y. Fan, J. H. Huang, X. W. Sun et al., “Correlation between microstructure and mechanical properties of active brazed C<sub>f</sub>/SiC composite joints using Ti-Zr-Be,” *Materials Science Engineering: A*, vol. 667, pp. 332–339, 2016.
- [51] Q. Y. Tong, L. F. Cheng, and L. T. Zhang, “Microstructure and properties of joints of 2D C/SiC composites,” *Materials Engineering*, vol. 11, pp. 14–16, 2002.
- [52] Q. Y. Tong, L. F. Cheng, and L. T. Zhang, “On-line joining of 3D fiber reinforced C/SiC composites,” *Rare Metal Materials and Engineering*, vol. 33, no. 1, pp. 101–104, 2004.

- [53] Q. Y. Tong and L. F. Cheng, "Liquid infiltration joining of 2D C/SiC composite," *Science Engineering Composites Materials*, vol. 13, no. 1, pp. 31–36, 2006.
- [54] Y. Katoh, M. Kotani, A. Kohyama et al., "Microstructure and mechanical properties of low-activation glass-ceramic joining and coating for SiC/SiC composites," *Journal of Nuclear Materials*, vol. 283, pp. 1262–1266, 2000.
- [55] H. Y. Dong, S. J. Li, Y. Y. Teng, and W. Ma, "Joining of SiC ceramic-based materials with ternary carbide  $Ti_3SiC_2$ ," *Materials Science and Engineering: B*, vol. 176, no. 1, pp. 60–64, 2011.
- [56] X. B. Zhou, Y. H. Han, X. F. Shen et al., "Fast joining SiC ceramics with  $Ti_3SiC_2$  tape film by electric field-assisted sintering Technol.," *Journal of Nuclear Materials*, vol. 466, pp. 322–327, 2015.
- [57] J. Suo, Z. H. Chen, W. M. Han, and W. Zheng, "Joining of ceramic materials by ceramic bonding transformed from silicone resin at high temperature," *Journal of The Chinese Ceramic Society*, vol. 33, no. 3, pp. 386–390, 2005.
- [58] P. K. Gianchandani, V. Casalegno, F. Smeacetto, and M. Ferraris, "Pressure-less joining of C/SiC and SiC/SiC by a  $MoSi_2/Si$  composite," *International Journal of Applied Ceramic Technology*, vol. 14, no. 3, pp. 305–312, 2017.
- [59] H. P. Xiong, B. Chen, Y. Pan, H. S. Zhao, and L. Ye, "Joining of  $C_f/SiC$  composite with a Cu-Au-Pd-V brazing filler and interfacial reactions," *Journal of the European Ceramic Society*, vol. 34, no. 6, pp. 1481–1486, 2014.
- [60] H. P. Xiong, B. Chen, W. Mao, and X. H. Li, "Joining of  $C_f/SiC$  composite with Pd-Co-V brazing filler," *Welding in the World*, vol. 56, no. 1-2, pp. 76–80, 2012.
- [61] H. P. Xiong, B. Chen, Y. Pan, W. Mao, and Y. Y. Cheng, "Interfacial reactions and joining characteristics of a Cu-Pd-V system filler alloy with  $C_f/SiC$  composite," *Ceramics International*, vol. 40, no. 6, pp. 7857–7863, 2014.
- [62] E. S. Karakozov, G. V. Konyushkov, and R. A. Musin, "Fundamentals of welding metals to ceramic materials," *Welding International*, vol. 7, no. 12, pp. 991–996, 1993.
- [63] M. W. Barsoum, T. El-Raghy, C. J. Rawn et al., "Thermal properties of  $Ti_3SiC_2$ ," *Journal of Physics and Chemistry of Solids*, vol. 60, no. 4, pp. 429–439, 1999.
- [64] H. L. Liu, C. Y. Tian, and M. Z. Wu, "Technique of joining of  $C_f/SiC$  composite via preceramic silicone polysilazane and joining properties," *Chinese Journal of Nonferrous Metals*, vol. 18, no. 2, pp. 278–281, 2008.
- [65] B. Zhao, T. Y. Yu, W. F. Ding, and X. Y. Li, "Effects of pore structure and distribution on strength of porous Cu-Sn-Ti alumina composites," *Chinese Journal of Aeronautics*, vol. 30, no. 6, pp. 2004–2015, 2017.
- [66] W. F. Ding, C. W. Dai, Y. Tian, J. H. Xu, and Y. C. Fu, "Grinding performance of textured monolayer CBN wheels: undeformed chip thickness nonuniformity modeling and ground surface topography prediction," *International Journal of Machine Tools and Manufacture*, vol. 122, pp. 66–80, 2017.
- [67] Y. J. Zhu, W. F. Ding, T. Y. Yu et al., "Investigation on stress distribution and wear behavior of brazed polycrystalline cubic boron nitride superabrasive grains: numerical simulation and experimental study," *Wear*, vol. 376-377, pp. 1234–1244, 2017.
- [68] Y. J. Lu, X. Y. Zhang, J. X. Chu, X. Liu, and Z. Fang, "Study on active reactive brazing of C SiC ceramic to Nb alloy," *Chinese Journal of Rare Metals*, vol. 32, no. 5, pp. 636–640, 2008.
- [69] C. Y. Liang, Y. G. Du, W. J. Zhang et al., "Joining of  $C_f/SiC$  composites with Niobium alloy," *Aerospace Materials and Technology*, vol. 39, no. 3, pp. 45–48, 2009.
- [70] J. J. Zhang, S. J. Li, H. P. Duan, and Y. Zhang, "Joining of  $C_f/SiC$  to Ni-based superalloy with Zr/Ta composite interlayers by hot-pressing diffusion welding," *Rare Metal Materials and Engineering*, vol. 31, no. s1, pp. 393–396, 2002.
- [71] Z. W. Yang, L. X. Zhang, X. Y. Tian et al., "Interfacial microstructure and mechanical properties of TiAl and  $C_f/SiC$  joint brazed with  $TiH_2$ -Ni-B brazing powder," *Materials characterization*, vol. 79, pp. 52–59, 2013.
- [72] Z. W. Yang, P. He, and J. C. Feng, "Microstructural evolution and mechanical properties of the joint of TiAl alloys and C/SiC composites vacuum brazed with Ag-Cu filler metal," *Materials Characterization*, vol. 62, no. 9, pp. 825–832, 2011.
- [73] Z. H. Zhong, T. Hinoki, H.-C. Jung, Y. H. Park, and A. Kohyama, "Microstructure and mechanical properties of diffusion bonded SiC/steel joint using W/Ni interlayer," *Materials and Design*, vol. 31, no. 3, pp. 1070–1076, 2010.
- [74] Y. J. Li, *Selection of Welding Materials*, Chemical Industry Press, Beijing, China, 2004.
- [75] B. Riccardi, C. A. Nannetti, T. Petrisor, and M. Sacchetti, "Low activation brazing materials and techniques for  $SiC_f/SiC$  composites," *Journal of Nuclear Materials*, vol. 307, pp. 1237–1241, 2002.
- [76] H. J. Liu, J. C. Feng, and Y. Y. Qian, "Microstructure and strength of the SiC/TiAl joint brazed with Ag-Cu-Ti filler metal," *Journal of Materials Science Letters*, vol. 19, no. 14, pp. 1241–1242, 2000.
- [77] M. Singh, R. Asthana, and T. P. Shpargel, "Brazing of ceramic-matrix composites to Ti and Hastealloy using Ni-base metallic glass interlayers," *Materials Science and Engineering: A*, vol. 498, no. 1, pp. 19–30, 2008.
- [78] Y. M. He, J. Zhang, X. Wang, and Y. Sun, "Effect of brazing temperature on microstructure and mechanical properties of  $Si_3N_4/Si_3N_4$  joints brazed with Ag-Cu-Ti +Mo composite filler," *Journal of Materials Science*, vol. 8, pp. 2796–2804, 2010.
- [79] Y. H. Ban, J. H. Huang, H. Zhang et al., "Microstructure of reactive composite brazing joints of  $C_f/SiC$  composite to Ti-6Al-4V alloy with Cu-Ti-C filler material," *Rare Metal Materials and Engineering*, vol. 38, no. 4, pp. 713–716, 2009.
- [80] X. R. Song, H. J. Li, V. Casalegno et al., "Microstructure and mechanical properties of C/C composite/Ti6Al4V joints with a Cu/TiCuZrNi composite brazing alloy," *Ceramics International*, vol. 42, no. 5, pp. 6347–6354, 2016.
- [81] Q. Y. Tong, *Microstructure and Properties of the On-Line Liquid Infiltrate Joining of  $C_f/SiC$  Dissertation for Ph.D. thesis*, Northwestern Polytechnical University, Xi'an, China, 2003.
- [82] Q. Q. Ke, L. F. Cheng, Q. Y. Tong et al., "Joining methods for continuous fiber reinforced ceramic matrix composites," *Materials Engineering*, vol. 11, pp. 58–63, 2005.
- [83] J. Wang, K. Z. Li, W. Li et al., "The preparation and mechanical properties of carbon/carbon composite joints using Ti-Si-SiC-C filler as interlayer," *Materials Science and Engineering: A*, vol. 574, pp. 37–45, 2013.
- [84] Q. Y. Tong, L. F. Cheng, and L. T. Zhang, "Liquid infiltration joining of C/SiC and Nb," *Journal of Aeronautical Materials*, vol. 24, no. 1, pp. 54–56, 2004.
- [85] Q. Q. Ke, L. F. Chen, Q. Y. Tong et al., "Microstructure and properties of joints of 2D C/SiC composites by riveting," *Rare Metal Materials and Engineering*, vol. 35, no. 9, p. 1497, 2006.



- [86] V. L. Lanin, "Ultrasonic soldering in electronics," *Ultrasonics Sonochemistry*, vol. 8, no. 4, pp. 379–385, 2001.
- [87] W. W. Zhao, J. C. Yan, W. Yang, and S. Q. Yang, "Capillary filling process during ultrasonically brazing of aluminium matrix composites," *Science and Technology of Welding and Joining*, vol. 13, no. 1, pp. 66–69, 2008.
- [88] M. Naka and M. Maeda, "Application of ultrasound on joining of ceramics to metals," *Engineering Fracture Mechanics*, vol. 40, no. 4-5, pp. 951–956, 1991.
- [89] M. H. El-Sayed and M. Naka, "Structure and properties of carbon steel-aluminium dissimilar joints," *Science and Technology of Welding and Joining*, vol. 10, no. 1, pp. 27–31, 2005.
- [90] M. H. El-Sayed, K. M. Hafez, and M. Naka, "Interfacial structure and bond strength of ultrasonic brazed Al-304 stainless steel dissimilar joints," *Science and Technology of Welding and Joining*, vol. 9, no. 6, pp. 560–564, 2004.
- [91] X. G. Chen, J. C. Yan, S. C. Ren, J. Wei, and Q. Wang, "Ultrasonic-assisted brazing of SiC ceramic to Ti-6Al-4V alloy using a novel AlSnSiZnMg filler metal," *Materials Letters*, vol. 105, pp. 120–123, 2013.
- [92] X. G. Chen, R. S. Xie, Z. W. Lai et al., "Interfacial structure and formation mechanism of ultrasonic-assisted brazed joint of SiC ceramics with Al 12Si filler metals in air," *Journal of Materials Science and Technology*, vol. 33, no. 5, pp. 492–498, 2017.
- [93] M. C. Halbig, R. Asthana, and M. Singh, "Diffusion bonding of SiC fiber-bonded ceramics using Ti/Mo and Ti/Cu interlayers," *Ceramics International*, vol. 41, no. 2, pp. 2140–2149, 2015.
- [94] J. K. Liu, J. Cao, X. G. Song, Y. Wang, and J. C. Feng, "Evaluation on diffusion bonded joints of TiAl alloy to  $Ti_3SiC_2$  ceramic with and without Ni interlayer: interfacial microstructure and mechanical properties," *Materials and Design*, vol. 57, pp. 592–597, 2014.
- [95] J. Cao, J. K. Liu, X. G. Song, X. Lin, and J. C. Feng, "Diffusion bonding of TiAl intermetallic and  $Ti_3AlC_2$  ceramic: Interfacial microstructure and joining properties," *Materials and Design*, vol. 56, pp. 115–121, 2014.
- [96] J. S. Varsanik and J. J. Bernstein, "Voltage-assisted polymer wafer bonding," *Journal of Micromechanics and Microengineering*, vol. 22, no. 2, article 025004, 2012.
- [97] C. R. Liu, J. F. Zhao, X. Y. Lu et al., "Field-assisted diffusion bonding and bond characterization of glass to aluminum," *Journal of Materials Science*, vol. 43, no. 15, pp. 5076–5082, 2008.
- [98] Q. Wang, Q. H. Li, D. L. Sun, X. Han, and Q. Tian, "Microstructure and mechanical properties of SiC/Ti diffusion bonding joints under electric field," *Rare Metal and Materials*, vol. 45, no. 7, pp. 1749–1754, 2016.
- [99] T. Okuni, Y. Miyamoto, H. Abe, and M. Naito, "Joining of silicon carbide and graphite by spark plasma sintering," *Ceramics International*, vol. 40, no. 1, pp. 1359–1363, 2014.
- [100] R. Pan, Q. Wang, D. L. Sun, and P. He, "Effects of electric field on interfacial microstructure and shear strength of diffusion bonded  $\alpha-Al_2O_3/Ti$  joints," *Journal of the European Ceramic Society*, vol. 35, no. 1, pp. 219–226, 2015.
- [101] X. B. Zhou, H. Yang, F. Y. Chen et al., "Joining of carbon fiber reinforced carbon composites with  $Ti_3SiC_2$  tape film by electric field assisted sintering technique," *Carbon*, vol. 102, pp. 106–115, 2016.
- [102] T. El-Raghy, M. W. Barsoum, A. Zavaliangos, and S. R. Kalidindi, "Processing and mechanical properties of  $Ti_3SiC_2$ : II, effect of grain size and deformation temperature," *Journal of the American Ceramic Society*, vol. 82, no. 10, pp. 2855–2860, 1999.
- [103] X. M. Fan, X. W. Yin, Y. Z. Ma, L. Zhang, and L. Cheng, "Oxidation behavior of C/SiC- $Ti_3SiC_2$  at 800–1300°C in air," *Journal of the European Ceramic Society*, vol. 36, pp. 2427–2433, 2016.
- [104] D. Yu, L. Y. Cao, and X. L. Dong, "Effects of pulse field on solution microstructure and solution technique of Al-4% Cu alloy," *Material and Heat Treatment*, vol. 39, no. 2, pp. 144–146, 2010.

## Research Article

# The Bending Responses of Sandwich Panels with Aluminium Honeycomb Core and CFRP Skins Used in Electric Vehicle Body

Yong Xiao,<sup>1,2</sup> Yefa Hu,<sup>1,2</sup> Jinguang Zhang ,<sup>1,2</sup> Chunsheng Song ,<sup>1,2</sup> Xiangyang Huang,<sup>1,3</sup> Jingui Yu,<sup>1</sup> and Zhaobing Liu<sup>1,2</sup>

<sup>1</sup>School of Mechanical and Electronic Engineering, Wuhan University of Technology, Luoshi Road 122, Wuhan, Hubei 430070, China

<sup>2</sup>Institute of Advanced Materials Manufacturing Equipment and Technology, Wuhan University of Technology, Luoshi Road 122, Wuhan, Hubei 430070, China

<sup>3</sup>Fujian Hishan Machinery Co., Ltd., Hishan Road 666, Putian, Fujian 351100, China

Correspondence should be addressed to Jinguang Zhang; [cfrp204@163.com](mailto:cfrp204@163.com)

Received 29 January 2018; Revised 31 May 2018; Accepted 19 June 2018; Published 7 August 2018

Academic Editor: Rujie He

Copyright © 2018 Yong Xiao et al. This is an open access article distributed under the Creative Commons Attribution License, which permits unrestricted use, distribution, and reproduction in any medium, provided the original work is properly cited.

The aim of this paper was to investigate bending responses of sandwich panels with aluminium honeycomb core and carbon fibre-reinforced plastic (CFRP) skins used in electric vehicle body subjected to quasistatic bending. The typical load-displacement curves, failure modes, and energy absorption are studied. The effects of fibre direction, stacking sequence, layer thickness, and loading velocity on the crashworthiness characteristics are discussed. The finite element analysis (FEA) results are compared with experimental measurements. It is observed that there are good agreements between the FEA and experimental results. Numerical simulations and experiment predict that the honeycomb sandwich panels with  $\pm 30^\circ$  and  $\pm 45^\circ$  fibre direction, asymmetrical stacking sequence ( $45^\circ/-45^\circ/45^\circ/-45^\circ$ ), thicker panels (0.2 mm~0.4 mm), and smaller loading velocity (5 mm/min~30 mm/min) have better crashworthiness performance. The FEA prediction is also helpful in understanding the initiation and propagation of cracks within the honeycomb sandwich panels.

## 1. Introduction

Carbon fibre-reinforced plastic (CFRP) has been proven to be an effective energy absorbing material; it has been widely used in various industrial applications [1–8]. Moreover, the honeycomb filling has been shown to be efficient in improving the energy absorption characteristics of filling structures [9–16]. The honeycomb sandwich structures are widely used in several engineering applications in the transport industry.

There have been extensive studies regarding the impact and bending behaviour of aluminium honeycomb panels with and without external skins. Liu et al. [2] explored the crashworthiness of CFRP square tubes filled with aluminium honeycomb subjected to quasistatic axial crushing. By comparison, the peak load and absorbed energy of the filled tubes increased by more than 10% as compared with those of the bare CFRP tubes, ranging approximately from 12.41% to 27.22% and from 10.49% to 21.83%, respectively.

For three-point bending (TPB), energy absorption (EA) and specific energy absorption (SEA) were found by Sun et al. [17] to be largely influenced by the structural parameters in the honeycomb core, but not much by the skin thickness. They also compared the crashworthiness of empty circular CFRP with CFRP/aluminium/steel tubes filled with aluminium foam or aluminium honeycomb under axial quasistatic crushing. With the increase in  $R$  of CFRP tubes, both the energy absorption and loading capacities increase, with specific energy absorption (SEA) increasing from 48.60 J/g to 60.37 J/g. The SEAs of CFRP tubes filled with honeycomb were slightly lower than the empty counterparts but far better than those of all metal specimens [18]. Hazizan et al. [19] investigated the low-velocity impact response of two glass fibre/epoxy aluminium honeycomb sandwich structures. Crupi et al. [20] investigated the mechanical behaviour under bending and impact loading of AHS panel reinforced by GFRP outer skins and a comparison with the

AHS panels (without GFRP skins) was done. The experimental tests demonstrated that the amount of energy absorption of the honeycomb sandwiches was highly improved, reinforcing them by means of GFRP outer skins. Hussein et al. [21] studied the axial crushing behaviour of aluminium honeycomb-filled square carbon fibre-reinforced plastic (CFRP) tubes. The results showed that the energy absorption (EA) of aluminium honeycomb-filled CFRP tubes increased from 20% to 36% more than the energy absorption of hollow CFRP tubes at different crushing velocities. Liu and Wu [22] investigated the lateral planar crushing and bending responses of CFRP square tubes filled with aluminium honeycomb. The results of lateral three-point bending tests showed that the peak load, EA, and SEA of honeycomb-filled CFRP tubes increased by 17%, 32%, and 0.9%, respectively, compared with the CFRP hollow tubes.

Although the honeycomb sandwich panels have been widely studied, there have been limited studies on the honeycomb sandwich panels with CFRP skins. Furthermore, it is a new attempt that the lightweight sandwich panels with aluminium honeycomb core and CFRP skins are applied to the body panel in our developed lightweight CFRP electric vehicle, which would be subject to lateral bending load. Therefore, their application requires a better understanding of the bending response of such lightweight composites, and most of the studies do not consider the material design of CFRP to improve bending performance.

## 2. Problem Definitions

**2.1. The CAD Model of Sandwich Panels with Aluminium Honeycomb Core and CFRP Skins.** The CAD model of sandwich panels with aluminium honeycomb core and CFRP skins is shown in Figure 1. It is made of two parts, known as upper and lower CFRP skins and middle aluminium honeycomb core. The CFRP skins are bonded to aluminium honeycomb core by DG-4 epoxy adhesive. The adhesive can be cured at room temperature and withstand temperatures from  $-60^{\circ}\text{C}$  to  $+120^{\circ}\text{C}$ . Moreover, the bonding process is simple, convenient to use and fast curing. The length and width of CFRP skins are 200 mm and 30 mm, respectively, and the thickness of CFRP skin is determined by layer thickness. The aluminium honeycomb core is made from the aluminium alloy with the cell thickness of 0.07 mm and side length of 4 mm. The height of aluminium honeycomb is 8.4 mm.

**2.2. The Material Property of Sandwich Panels with Aluminium Honeycomb Core and CFRP Skins.** Upper and lower CFRP skins are full carbon fibre structures, and their material is T700/FAW100. Table 1 lists the material properties of CFRP T700/FAW100. Nine material constants in Table 1 will be used in the finite element analysis.

The middle aluminium honeycomb core has an isotropic material property, and its material is 3003 aluminium alloy. The material properties are shown in Table 2.

**2.3. Lay-Up Schemes of Sandwich Panels with Aluminium Honeycomb Core and CFRP Skins.** In order to analyze the

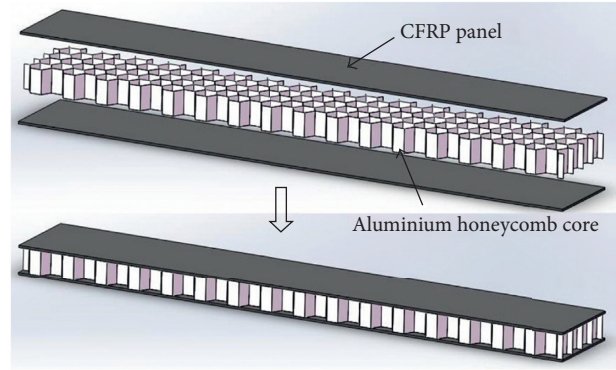


FIGURE 1: CAD model of sandwich panels with aluminium honeycomb core and CFRP skins.

effect of stacking sequence, fibre direction, and layer thickness on the crashworthiness of sandwich panels, the specimens in this study are divided into three groups (Group A/Group B/Group C) as listed in Table 3. A total of eight different lay-up schemes (A/B/C/D/E/F/G) are considered. The fibre directions with  $15^{\circ}$ ,  $30^{\circ}$ ,  $45^{\circ}$ ,  $60^{\circ}$ , and  $75^{\circ}$  are mainly considered. The purpose of Group A is to compare and analyze the effect of fibre direction on the crashworthiness of sandwich panels. The purpose of Group B is to compare and analyze the effect of stacking sequence on the crashworthiness of sandwich panels. The purpose of Group C is to compare and analyze the effect of layer thickness on the crashworthiness of sandwich panels.

**2.4. Testing Methods.** Different from the bending mechanical properties of conventional solid metal materials, the quasi-static three-point bending test is based on the GB/T1449-2005 Testing Standard "Test method for bending properties of carbon fiber reinforced plastics." As shown in Figure 2, the sandwich panel with aluminium honeycomb core and CFRP skins is placed parallel to the center position of the support seat of the universal testing machine. The loading roller moves downward at a constant rate of  $V$  until the specimen is broken. The load-displacement data are recorded during loading, and the experimental results of different cases are compared and analyzed.

## 3. Methods of Analyses

**3.1. Orthotropic Material Property.** Under the Cartesian coordinate 1-2-3, the constitutive equation of the orthotropic material such as carbon fibre-reinforced plastic is [22] as follows:

$$\begin{bmatrix} \sigma_{11} \\ \sigma_{22} \\ \sigma_{33} \\ \tau_{23} \\ \tau_{31} \\ \tau_{12} \end{bmatrix} = \begin{bmatrix} C_{11} & C_{12} & C_{13} & 0 & 0 & 0 \\ C_{21} & C_{22} & C_{23} & 0 & 0 & 0 \\ C_{31} & C_{32} & C_{33} & 0 & 0 & 0 \\ 0 & 0 & 0 & C_{44} & 0 & 0 \\ 0 & 0 & 0 & 0 & C_{55} & 0 \\ 0 & 0 & 0 & 0 & 0 & C_{66} \end{bmatrix} \begin{bmatrix} \varepsilon_{11} \\ \varepsilon_{22} \\ \varepsilon_{33} \\ \gamma_{23} \\ \gamma_{31} \\ \gamma_{12} \end{bmatrix}. \quad (1)$$

TABLE 1: The material properties of CFRP T700/FAW100.

$E_1$ (GPa)	$E_2$ (GPa)	$E_3$ (GPa)	$\nu_{21}$	$\nu_{32}$	$\nu_{31}$	$G_{12}$ (GPa)	$G_{23}$ (GPa)	$G_{13}$ (GPa)
150	9	9	0.24	0.24	0.28	5.12	5.12	3.34

$E_1$ : longitudinal modulus,  $E_2, E_3$ : transverse modulus;  $\nu_{21}$ : 21-direction Poisson's ratio,  $\nu_{31}$ : 31-direction Poisson's ratio,  $\nu_{32}$ : 32-direction Poisson's ratio;  $G_{12}$ ,  $G_{13}$ : 12-direction, 13-direction shear modulus,  $G_{23}$ : 23-direction shear modulus.

TABLE 2: The material properties of the aluminium honeycomb core.

$E$ (GPa)	$\nu$	$\rho$ (kg/m <sup>3</sup> )	$\sigma_s$ (Pa)
70	0.33	2.70E+03	2.76E+07

$E$ : elastic modulus,  $\nu$ : Poisson's ratio;  $\rho$ : density,  $\sigma_s$ : yield strength.

TABLE 3: Lay-up schemes of sandwich panels.

Case	Stacking
Group A	
A	[45°/-45°/45°/-45°]
B	[30°/-30°/30°/-30°]
C	[60°/-60°/60°/-60°]
D	[75°/-75°/75°/-75°]
E	[60°/-15°/15°/-60°]
Group B	
A	[45°/-45°/45°/-45°]
F	[45°/-45°/-45°/45°]
Group C	
A	[45°/-45°/45°/-45°]
G	[45°/-45°/45°]
H	[45°/-45°]

The abovementioned equation can be written in a simple form:

$$\{\sigma\} = [C]\{\varepsilon\}, \quad (2)$$

where  $\{\sigma\}$ ,  $\{\varepsilon\}$ , and  $[C]$  are the stress, strain, and stiffness matrix, respectively. The compliance matrix  $[S]$  is the inverse of  $[C]$  as follows:

$$[S] = [C]^{-1} = \begin{bmatrix} \frac{1}{E_1} & \frac{-\nu_{21}}{E_2} & \frac{-\nu_{31}}{E_3} & 0 & 0 & 0 \\ \frac{-\nu_{12}}{E_1} & \frac{1}{E_2} & \frac{-\nu_{32}}{E_3} & 0 & 0 & 0 \\ \frac{-\nu_{13}}{E_1} & \frac{-\nu_{23}}{E_2} & \frac{1}{E_3} & 0 & 0 & 0 \\ 0 & 0 & 0 & \frac{1}{G_{23}} & 0 & 0 \\ 0 & 0 & 0 & 0 & \frac{1}{G_{31}} & 0 \\ 0 & 0 & 0 & 0 & 0 & \frac{1}{G_{12}} \end{bmatrix}, \quad (3)$$

where  $E_i$ ,  $G_{ij}$ , and  $\nu_{ij}$  are Young's modulus, shear modulus, and Poisson's ratio, respectively. The symmetrical matrix  $[S]$

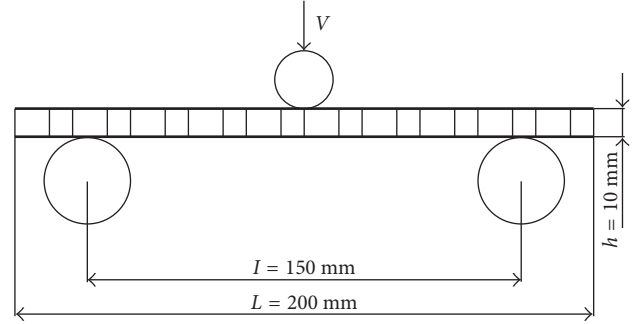


FIGURE 2: Schematic of quasistatic three-point bending test.

in (3) has nine independent material constants for the orthotropic material.

In the carbon/epoxy composite laminate, each ply has the orthotropic material property. The fibre directions of each ply can be different for practical applications. The bicycle frame is a full carbon fibre structure, and its material is T700/FAW100. Table 1 lists the material properties of CFRP T700/FAW100. Nine material constants in Table 1 will be used in the finite element analysis.

**3.2. Finite Element Analysis (FEA).** In this study, finite element analysis (FEA) is performed using ABAQUS software including model and mesh, load, boundary condition, solving, and postprocessing. Figure 3 shows the finite element model of sandwich panels with aluminium honeycomb core and CFRP skins. It is supported by a rigid support seat at the bottom. The rigid loading roller moving at a constant velocity was built to represent the loading for three-point bending. The sandwich panels necessitate a progressive failure model for solid elements using a modified Chang-Chang failure criterion, which is capable of predicting tensile and compressive fibre failure, as well as tensile and compressive matrix failure. The aluminium honeycomb is modelled by solid elements with isotropic material property. There are three types of contact defined between the loading roller, CFRP skins, aluminium honeycomb core, and support seat, namely, automatic single surface, tied surface to surface, and automatic nodes to surface (as illustrated in Figure 3). The loading speed and boundary conditions were prescribed consistently with the experimental setup.

**3.3. Crashworthiness Criteria.** To quantify the crashworthiness, several different criteria are often used, namely, initial peak force ( $F_{\max}$ ), mean crushing force (MCF), crush force efficiency (CFE), energy absorption (EA), and specific energy absorption (SEA) [3].

The initial peak force ( $F_{\max}$ ) can be obtained directly from the load-displacement curve which separates the

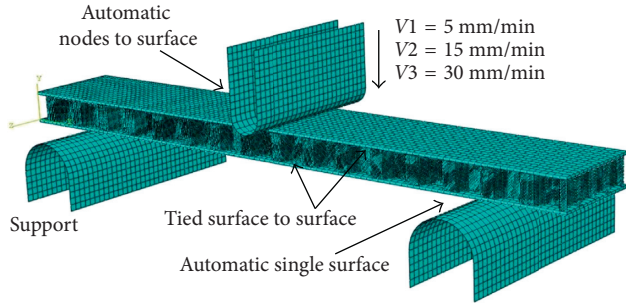


FIGURE 3: Schematic of finite element model.

loading process into the initial elastic bending stage and bending collapse stage.

The value of average crushing force ( $F_{avg}$ ) is defined mathematically as

$$F_{avg} = \frac{1}{d} \int_0^d F(\delta) d\delta, \quad (4)$$

where  $d$  is the collapse distance and  $F(\delta)$  is the instantaneous crush force.

Crush force efficiency (CFE), defined as the ratio of the mean crushing force (MCF) to the initial peak force ( $F_{max}$ ), is used to measure the uniformity of crushing force as

$$CFE = \frac{F_{avg}}{F_{max}}. \quad (5)$$

The higher the value of CFE, the better the crashworthiness performance.

The energy absorption (EA) is obtained by integrating the load-displacement curve during the loading process as

$$EA = \int_0^d F(\delta) d\delta. \quad (6)$$

The higher the energy absorption (EA), the better the crashworthiness. To account for the effect of mass (weight), specific energy absorption (SEA), defined as

$$SEA = \frac{E_a}{m} = \frac{\int_0^d F(\delta) d\delta}{m}, \quad (7)$$

is frequently used as one of the most critical crashworthiness criteria.

## 4. Experimental Procedures

**4.1. Specimen Preparation.** For electric vehicles, the most effective way to increase the extension mileage is to reduce weight. The traditional materials of vehicle body are high-strength steel or aluminium alloys, which are heavy and do not meet the growing extensive mileage requirements of electric vehicles. The sandwich panels with aluminium honeycomb core and carbon fibre-reinforced plastic (CFRP) skins can be reasonably designed to make electric vehicle body with the advantages of lightweight and better energy absorption performance. As shown in Figure 4, the filled structures are applied to the typical structural elements such as the body panels in our developed lightweight CFRP

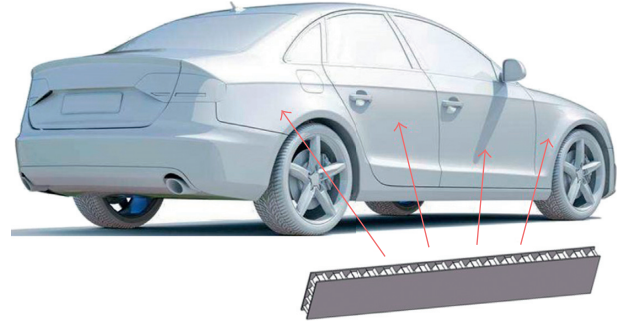


FIGURE 4: Schematic of sandwich structures with aluminium honeycomb core and CFRP skins in vehicle body.

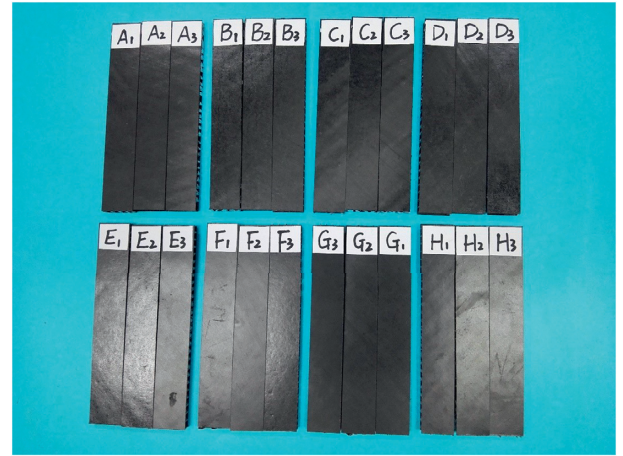


FIGURE 5: Specimens before quasistatic three-point bending test with different lay-up schemes.



FIGURE 6: Specimens before quasistatic three-point bending test with different loading speeds.

electric vehicle, which would be subject to lateral bending load. This work aimed at investigating the lateral bending capability of sandwich panels with aluminium honeycomb core and CFRP skins. Figure 5 shows the specimens of sandwich panels with eight different lay-up schemes. In order to analyze the effect of stacking sequence, fibre direction, and layer thickness on the crashworthiness of sandwich panels, a total of eight different lay-up schemes (A/B/C/D/E/F/G/H) are considered. To ensure the accuracy of the experimental results, each case is repeated three times

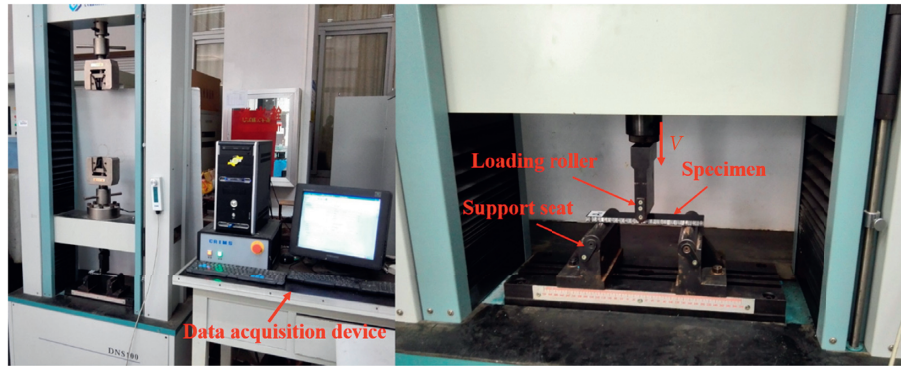


FIGURE 7: Specimens tested in the electronic universal testing machine.



FIGURE 8: Damaged specimens after quasistatic bending.

under the same testing conditions. In addition, in order to analyze the effect of loading velocity on the crashworthiness of sandwich panels, the loading experiments are carried out at different loading rates for Case E4, Case E5, and Case E6, respectively, and the specimens of Case E4, Case E5, and Case E6 are shown in Figure 6.

**4.2. Quasistatic Three-Point Bending Test.** The quasistatic three-point bending tests are carried out to study the bending behaviours of these different sandwich panels. All the tests are performed at room temperature in the electronic universal testing machine DNS-100 with a loading capacity of 100 kN. As shown in Figure 7, the speed of the loading roller is from 5 mm/min to 30 mm/min. When the specimens of three groups are tested, the loading velocity of the loading roller is set as 5 mm/min.

In order to analyze the effect of loading velocity on the crashworthiness of sandwich panels, the quasistatic loading test of the specimens of Case E4, Case E5, and Case E6 is carried out, and the loading rates are 5 mm/min, 15 mm/min, and 30 mm/min, respectively. The final bending displacement is set as 25 mm to ensure complete damage for each specimen. The bending load and its corresponding displacement are recorded by a data acquisition system, where the load-displacement curves can be plotted by the system. The deformation behaviours of the specimens are photographed during the quasistatic bending process. The specimens after quasistatic bending failure are shown in Figure 8.

## 5. Results and Discussion

**5.1. Load-Displacement Curves.** The load-displacement curves of the sandwich panels with aluminium honeycomb core and CFRP skins under the three-point bending test are shown in Figure 9. The curves can be divided into two stages, namely, the initial elastic bending stage and bending collapse stage [23]. Taking the specimens of Case D (D1, D2, and D3) as an example, in the initial elastic bending stage, the bending load kept increasing until it reaches the first peak (the average value is 435 kN). Following the first peak, extensive microfracture was observed at the corner of the upper panel in contact with the loading roller; the fracture spread quickly in a direction perpendicular to the CFRP skin, causing several drops in the bending load curve within the bending collapse stage as shown in Figure 9; and the numerically predicted peak load matched the experimental measurement with a small error given except for the specimen of Case D1. It is seen that the duration of the elastic deformation stage is very short and the collapse stage is the main energy absorption stage during the bending.

**5.2. Failure Modes.** The failure progress of the sandwich panels with aluminium honeycomb core and CFRP skins subjected to three-point bending is shown in Figure 10. It shows a complex failure mode, including the plastic hinges, buckling, indentation, core failure, and shear interaction. It is evident that the microfracture initiated at the corner of the top wall in contact with the loading roller

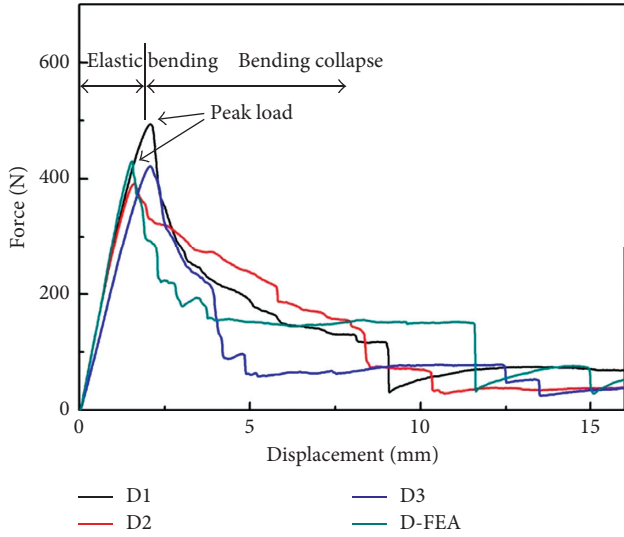


FIGURE 9: Typical load-displacement curves of specimens in three-point bending tests.

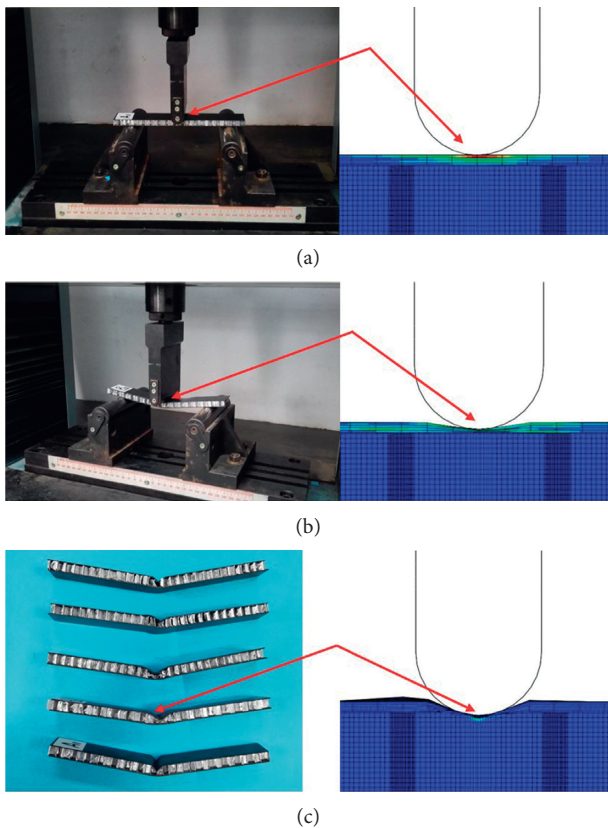


FIGURE 10: The failure process of sandwich panels in three-point bending tests.

because of the stress concentration. The cracks spread from the top wall of the filled CFRP panels to the aluminium honeycomb. In the bending process, the hexagonal cell layers of aluminium honeycomb are squeezed each other on the upper surface (compression surface) and the cell layers stretched on the bottom surface (tensile surface), leading to

TABLE 4: Different fibre directions for FEA and experimental results.

Case	$m$ (g)	$F_{\max}$ (N)	$F_{\text{avg}}$ (N)	CFE	EA (J)	SEA (J/g)
A1-specimen	22	316	145.7	0.46	3.06	0.14
A2-specimen	20	260	117.1	0.45	2.46	0.12
A3-specimen	20	301	130	0.43	2.73	0.14
<b>A-average</b>	<b>20.7</b>	<b>292.3</b>	<b>131</b>	<b>0.45</b>	<b>2.75</b>	<b>0.14</b>
A-FEA	19.8	300	120	0.40	2.8	0.14
B1-specimen	23	536.7	192.4	0.36	4.81	0.21
B2-specimen	23	525.7	257.6	0.49	6.44	0.28
B3-specimen	23	480.4	231.6	0.48	5.79	0.25
<b>B-average</b>	<b>23</b>	<b>514.3</b>	<b>227.2</b>	<b>0.44</b>	<b>5.68</b>	<b>0.25</b>
B-FEA	19.8	530	245	0.46	5.98	0.30
C1-specimen	23	504	110	0.22	2.75	0.12
C2-specimen	23	533.3	126	0.24	3.15	0.14
C3-specimen	23	481.4	127.2	0.26	3.18	0.14
<b>C-average</b>	<b>23</b>	<b>506.2</b>	<b>121</b>	<b>0.24</b>	<b>3.03</b>	<b>0.13</b>
C-FEA	19.8	527.2	127	0.24	3.1	0.16
D1-specimen	22	492.7	115	0.23	2.99	0.14
D2-specimen	22	389.6	108.8	0.28	2.83	0.13
D3-specimen	22	421.2	87.3	0.21	2.27	0.10
<b>D-average</b>	<b>22</b>	<b>434.5</b>	<b>103.7</b>	<b>0.24</b>	<b>2.7</b>	<b>0.12</b>
D-FEA	19.8	430.7	97.7	0.23	2.54	0.13
E1-specimen	22	341	120.8	0.35	3.14	0.14
E2-specimen	23	372.8	108.8	0.29	2.83	0.12
E3-specimen	23	407.7	85.4	0.21	2.22	0.10
<b>E-average</b>	<b>22.7</b>	<b>373.8</b>	<b>105</b>	<b>0.28</b>	<b>2.73</b>	<b>0.12</b>
E-FEA	19.8	362	120	0.33	3	0.15

a fan shape. But the bending deformation was not enough to induce the cells of the aluminium honeycomb debonding from the adjacent adhesive layers. Therefore, the damage of degumming between aluminium honeycomb cell layers was not found in these three-point bending tests [23].

**5.3. Effect of Fibre Direction on Crashworthiness.** The FEA and experimental results of about five kinds of cases (Case A, Case B, Case C, Case D, and Case E) with different fibre directions are listed in Table 4. It indicates that Case A with  $\pm 45^\circ$  fibre direction has the lowest  $F_{\max}$  (the average value is 294.2 N). On the contrary, Case C with  $\pm 60^\circ$  fibre direction has the highest  $F_{\max}$  (the average value is 511.5 N). The average value of  $F_{\max}$  of Case B with  $\pm 30^\circ$  fibre direction is 385.5 N. In addition, the value of  $F_{\text{avg}}$  of Case B is the highest in these cases. The comparison of CFE of these five different cases is shown in Table 4, and both the CFEs of Case A and Case B are the highest in these cases, indicating that they have the smoothest loading-displacement process. The CFE of these cases are in a range from 0.21 to 0.49 as listed in Table 4. The SEA and EA of these cases are also listed in Table 4. It can be observed that both the SEA and EA of Case B are much higher than those of the other cases, indicating better crashworthiness performance. Except for Case B, both the SEA and EA of Case A are close to those of other cases.

From the above study, the crashworthiness of sandwich panels with aluminium honeycomb core and CFRP skins can be affected by fibre direction. These FEA and experimental results revealed that Case A with  $\pm 45^\circ$  fibre direction has the

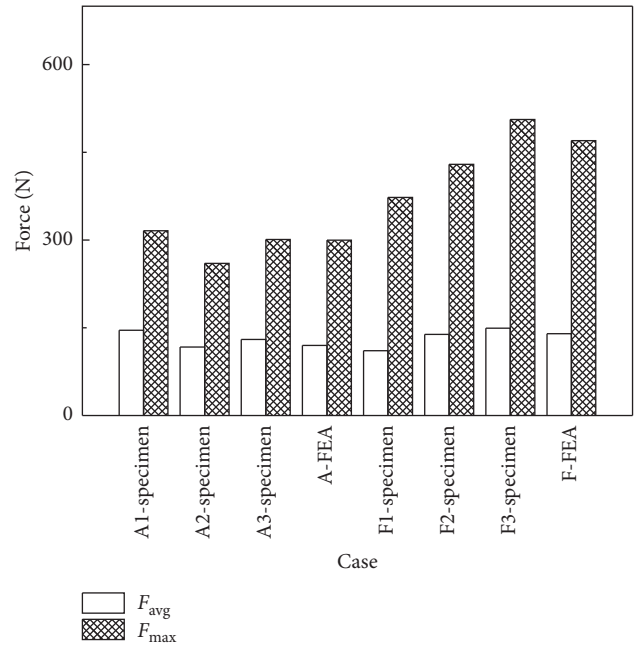
TABLE 5: The deviation values of the experimental results for different fibre directions.

Case	$F_{\max}$ error (%)	$F_{\text{avg}}$ error (%)	CFE error (%)	EA error (%)	SEA error (%)
A1-specimen	6.3	8.1	11.2	2.2	11.3
A2-specimen	3.4	11	10.6	0	10.5
A3-specimen	3.4	2.9	0.7	4.4	0.7
<b>A-average</b>	<b>4.4</b>	<b>7.3</b>	<b>7.5</b>	<b>2.2</b>	<b>7.5</b>
B1-specimen	4.4	15.3	18.2	15.3	16
B2-specimen	2.2	13.4	11.4	13.4	12
B3-specimen	6.6	1.9	9	1.9	0
<b>B-average</b>	<b>4.4</b>	<b>10.2</b>	<b>12.9</b>	<b>10.2</b>	<b>9.3</b>
C1-specimen	0.4	9	8.3	9.2	7.6
C2-specimen	5.4	4.1	0	4	7.7
C3-specimen	4.9	5.1	8.3	4.9	7.7
<b>C-average</b>	<b>3.6</b>	<b>6.1</b>	<b>5.5</b>	<b>6.0</b>	<b>7.7</b>
D1-specimen	13.4	10.9	4.2	10.7	16.7
D2-specimen	10.3	4.9	16.7	4.8	8.3
D3-specimen	3	15.8	12.5	15.9	16.7
<b>D-average</b>	<b>8.9</b>	<b>10.5</b>	<b>11.1</b>	<b>10.5</b>	<b>13.9</b>
E1-specimen	8.8	15	25	15	16.7
E2-specimen	0.3	3.6	35.7	3.6	0
E3-specimen	9	18.7	25	18.7	16.7
<b>E-average</b>	<b>6.0</b>	<b>12.4</b>	<b>28.6</b>	<b>12.4</b>	<b>11.1</b>

lowest  $F_{\max}$ , but not the highest EA and SEA. In addition, Case B with  $\pm 30^\circ$  fibre direction has the highest EA and SEA, but not the lowest  $F_{\max}$ . The lowest  $F_{\max}$ , highest EA, and highest SEA indicate better crashworthiness performance. Summarizing the respective advantages of fibre direction of  $\pm 30^\circ$  and  $\pm 45^\circ$ , both of these fibre directions should be considered in the ply design. The deviation values of the experimental results for different fibre directions are shown in Table 5. It is found that the deviation values are less than 10%. Therefore, the results of the experimental results for different fibre directions are reliable. It is noted that because the values of CFE are very small, it will lead to a large deviation in calculations.

**5.4. Effect of Stacking Sequence on Crashworthiness.** Case A and Case F are considered to analyze the effect of stacking sequence on crashworthiness performance. The comparison of  $F_{\max}$  and  $F_{\text{avg}}$  of the two cases is shown in Figure 11. It indicates that the  $F_{\max}$  of Case A is lower than that of Case F. The  $F_{\text{avg}}$  of Case A is close to that of Case F. As shown in Figure 12, the CFE of Case A is higher than that of Case F, indicating that Case A has the smoother loading-displacement process. The SEA and EA of these two cases are shown in Figure 13. It can be observed that the SEA and EA of Case A are higher than those of Case F, indicating better crashworthiness performance.

It can be concluded that the crashworthiness of sandwich panels with aluminium honeycomb core and CFRP skins can be affected by the stacking sequence. By comparing both Case A and Case F crashworthiness criteria, the results reveal that Case A with an asymmetrical stacking sequence design has better crashworthiness performance.

FIGURE 11: Comparison of different stacking sequence for specimens:  $F_{\max}$  and  $F_{\text{avg}}$ .

**5.5. Effect of Layer Thickness on Crashworthiness.** As shown in Table 6, there are three kinds of cases (Case A, Case G, and Case H) with different layer thicknesses. For Case A, the layer thickness is 0.8 mm; for Case G, the layer thickness is 0.6 mm; and for Case H, the layer thickness is 0.4 mm. With the increase in the layer thickness, both the  $F_{\text{avg}}$  and CFE increase. Interestingly, the  $F_{\max}$  is approximately the same. With the increase in the layers thickness, both the EA and SEA increase. Both the EA and SEA of Case A are the highest of these three kinds of cases. Therefore, in general, with increase in the layer thickness, the sandwich panels with aluminium honeycomb core and CFRP skins would have higher energy absorption capacities. The deviation values of the experimental results for different layer thicknesses are shown in Table 7. It was found that the deviation values are less than 10%. Therefore, the experimental results for different fibre directions are reliable.

**5.6. Effect of Loading Velocity on Crashworthiness.** To investigate the effect of loading velocity on the crashworthiness of sandwich panels with aluminium honeycomb core and CFRP skins, the load-displacement curves of specimens (Case E4, Case E5, and Case E6) with different velocities are plotted in Figure 14. With the increase in the loading velocity, the  $F_{\max}$  of specimens of Case E increases. When the loading velocity is 30 mm/min, the  $F_{\max}$  of the specimen of Case E6 is the highest.

The comparison of CFE of three specimens (Case E4, Case E5, and Case E6) with different loading velocities is graphed in Figure 15, and the  $F_{\max}$  and  $F_{\text{avg}}$  are also graphed in Figure 15. The CFE of the specimen of Case E5 with minimum loading velocity is the highest.



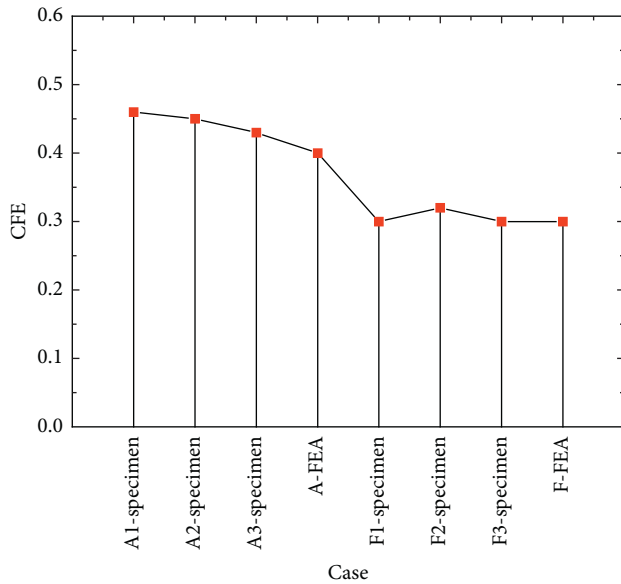


FIGURE 12: Comparison of different stacking sequence for specimens: CFE.

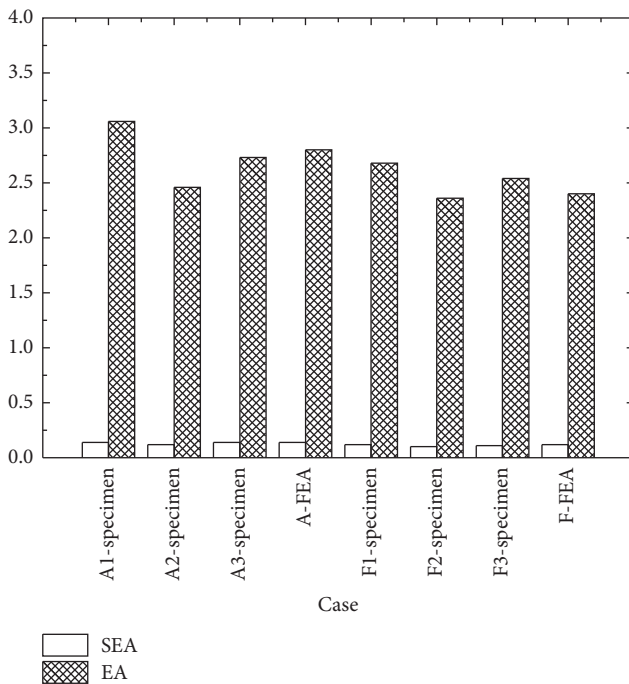


FIGURE 13: Comparison of different stacking sequence for specimens: EA and SEA.

The EA and SEA of three specimens (Case E4, Case E5, and Case E6) are graphed in Figure 16. It can be observed that the EA and SEA of the specimen of Case E5 with minimum loading velocity are much higher than those of other specimens.

It can be concluded the crashworthiness of sandwich panels with aluminium honeycomb core and CFRP skins can be affected by loading velocity. By comparing the crashworthiness criteria, the results reveal that the specimen of

TABLE 6: Different layer thicknesses for FEA and experimental results.

Case	$m$ (g)	$F_{\max}$ (N)	$F_{\text{avg}}$ (N)	CFE	EA (J)	SEA (J/g)
A1-specimen	22	316	145.7	0.46	3.06	0.14
A2-specimen	20	260	117.1	0.45	2.46	0.12
A3-specimen	20	301	130	0.43	2.73	0.14
<b>A-average</b>	<b>20.7</b>	<b>292.3</b>	<b>131</b>	<b>0.45</b>	<b>2.75</b>	<b>0.14</b>
A-FEA	19.8	300	120	0.40	2.8	0.14
G1-specimen	23	329.6	88.7	0.27	1.33	0.06
G2-specimen	22	360.8	100.6	0.28	1.51	0.07
G3-specimen	22	351	94	0.27	1.41	0.06
<b>G-average</b>	<b>22.3</b>	<b>347.1</b>	<b>94.4</b>	<b>0.27</b>	<b>1.41</b>	<b>0.06</b>
G-FEA	15.5	328	90	0.27	1.38	0.09
H1-specimen	16	316.6	69.3	0.22	1.04	0.07
H2-specimen	16	282.2	84	0.30	1.26	0.08
H3-specimen	16	301.9	80.7	0.27	1.21	0.08
<b>H-average</b>	<b>16</b>	<b>300.2</b>	<b>78</b>	<b>0.26</b>	<b>1.17</b>	<b>0.08</b>
H-FEA	11.3	300	77	0.26	1.1	0.10

TABLE 7: The deviation values of the experimental results for layer thicknesses.

Case	$F_{\max}$ error (%)	$F_{\text{avg}}$ error (%)	CFE error (%)	EA error (%)	SEA error (%)
A1-specimen	6.3	8.1	11.2	2.2	11.3
A2-specimen	3.4	11	10.6	0	10.5
A3-specimen	3.4	2.9	0.7	4.4	0.7
<b>A-average</b>	<b>4.4</b>	<b>7.3</b>	<b>7.5</b>	<b>2.2</b>	<b>7.5</b>
G1-specimen	5	6	0	5.7	0
G2-specimen	3.9	6.6	3.7	7.1	16.7
G3-specimen	11.2	0.4	0	0	0
<b>G-average</b>	<b>6.7</b>	<b>4.3</b>	<b>1.2</b>	<b>4.3</b>	<b>5.6</b>
H1-specimen	5.5	11	15.4	11	12.5
H2-specimen	6	7.7	15.4	7.7	0
H3-specimen	5.7	3.5	3.8	3.4	0
<b>H-average</b>	<b>5.7</b>	<b>7.4</b>	<b>11.5</b>	<b>7.4</b>	<b>4.2</b>

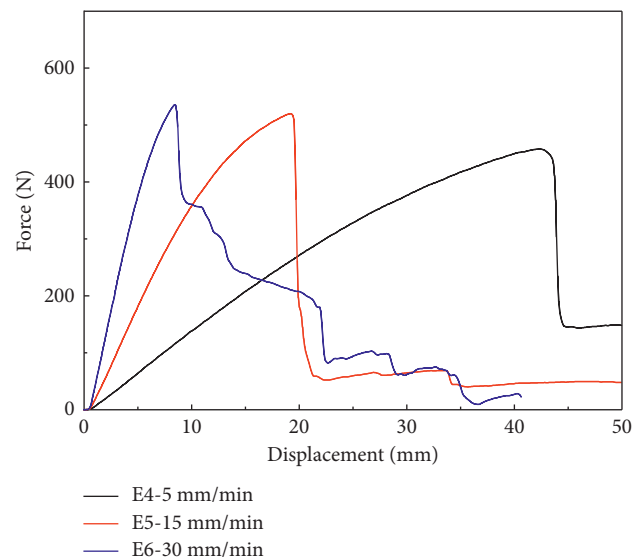


FIGURE 14: Load-displacement curves of specimens with different velocities on crashworthiness.

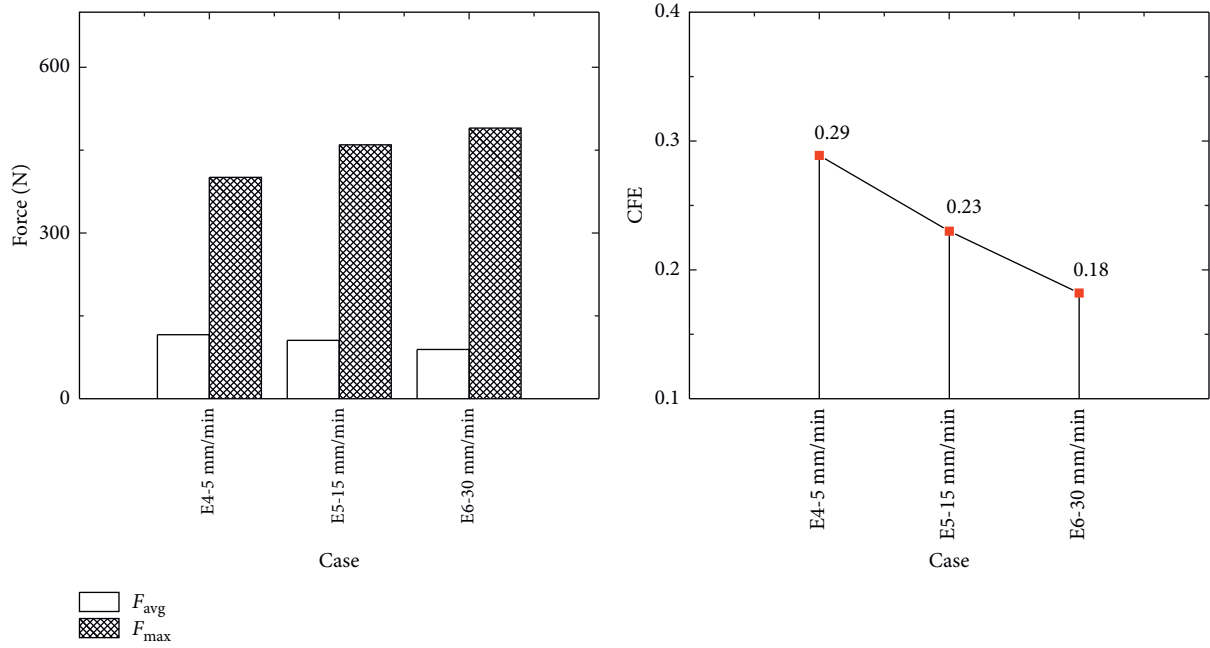


FIGURE 15: Comparison of different loading velocities for specimens:  $F_{max}$ ,  $F_{avg}$ , and CFE.

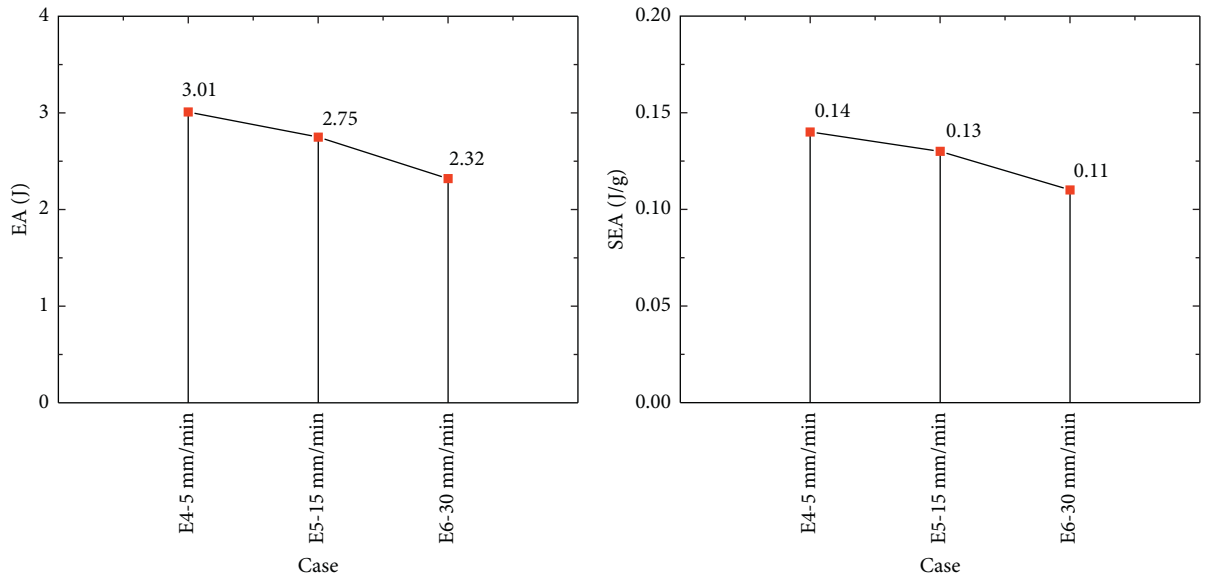


FIGURE 16: Comparison of different loading velocities for specimens: EA and SEA.

Case E5 with minimum loading velocity has the best crashworthiness performance.

### 6. Conclusions

This study presented a numerical and experimental study on bending responses of sandwich panels with aluminium honeycomb core and CFRP skins under quasistatic bending load. The typical load-displacement curves, failure modes, and energy absorption are explored. Within the limitation of the study, the following conclusions can be drawn:

- (1) The load-displacement curves of the sandwich panels with aluminium honeycomb core and CFRP skins

under the three-point bending test can be divided into the initial elastic bending stage and bending collapse stage. The sandwich panels with aluminium honeycomb core and CFRP skins absorbed most of the energy during bending collapse stage.

- (2) The FEA prediction and experiment are used in understanding the initiation and propagation of cracks within the sandwich panels with aluminium honeycomb core and CFRP skins. The microfracture initiates at the corner of the top wall in contact with the loading roller. The cracks spread from the top wall of the filled CFRP skins to the aluminium honeycomb. In the bending process, the hexagonal cell layers of

aluminium honeycomb are squeezed each other, leading to a fan shape. But the bending deformation was not enough to induce the cells of the aluminium honeycomb debonding from the adjacent adhesive layers.

- (3) The crashworthiness of sandwich panels with aluminium honeycomb core and CFRP skins can be affected by fibre direction. Case A with  $\pm 45^\circ$  fibre direction has the lowest  $F_{\max}$ , but not the highest EA and SEA. In addition, Case B with  $\pm 30^\circ$  fibre direction has the highest EA and SEA, but not the lowest  $F_{\max}$ . Therefore, both of these fibre directions should be considered in the ply design.
- (4) The crashworthiness of sandwich panels with aluminium honeycomb core and CFRP skins can be affected by the stacking sequence. By comparing both Case A and Case F crashworthiness criteria, the results reveal that Case A with symmetrical ply design has a better crashworthiness performance.
- (5) In general, with the increase in the layer thickness, the sandwich panels with aluminium honeycomb core and CFRP skins would have higher energy absorption capacities. The crashworthiness of sandwich panels can be affected by loading velocity. The experimental results reveal that the specimen of Case E5 with minimum loading velocity (5 mm/min) has the best crashworthiness performance.

In summary, this study demonstrates the potential of sandwich panels with aluminium honeycomb core and CFRP skins to be an energy absorber used in electric vehicle body; and the experimental results can also be used for validating the numerical simulation for design optimization of the sandwich panels with aluminium honeycomb core and CFRP skins in the future.

## Data Availability

The data used to support the findings of this study have been included within the article.

## Conflicts of Interest

The authors declare that there are no conflicts of interest regarding the publication of this paper.

## Acknowledgments

This work was supported by the National Natural Science Foundation of China-China Aerospace Science and Technology Corporation joint fund of aerospace advanced manufacturing technology research (no. U1537103), the Fundamental Research Funds for the Central Universities (WUT: 2017III047), and the Fundamental Research Funds for the Central Universities (WUT: 2018IVA023).

## References

- [1] Q. Liu, Z. Ou, Z. Mo, Q. Li, and D. Qu, "Experimental investigation into dynamic axial impact responses of double hat shaped CFRP tubes," *Composites Part B: Engineering*, vol. 79, pp. 494–504, 2015.
- [2] Q. Liu, Z. Mo, Y. Wu, J. Ma, G. C. P. Tsui, and D. Hui, "Crush response of CFRP square tube filled with aluminum honeycomb," *Composites Part B: Engineering*, vol. 98, pp. 406–414, 2016.
- [3] Q. Liu, J. Ma, X. Xu, Y. Wu, and Q. Li, "Load bearing and failure characteristics of perforated square CFRP tubes under axial crushing," *Composite Structures*, vol. 160, pp. 23–35, 2017.
- [4] S. Hou, S. Zhao, L. Ren, X. Han, and Q. Li, "Crashworthiness optimization of corrugated sandwich panels," *Materials and Design*, vol. 51, pp. 1071–1084, 2013.
- [5] O. T. Thomsen and W. M. Banks, "An improved model for the prediction of intra-cell buckling in CFRP sandwich panels under in-plane compressive loading," *Composite Structures*, vol. 65, no. 3–4, pp. 259–268, 2004.
- [6] S. Shi, Z. Sun, X. Hu, and H. Chen, "Flexural strength and energy absorption of carbon-fiber–aluminum–honeycomb composite sandwich reinforced by aluminum grid," *Thin-Walled Structures*, vol. 84, pp. 416–422, 2014.
- [7] I. Ivañez and S. Sanchez-Saez, "Numerical modelling of the low-velocity impact response of composite sandwich beams with honeycomb core," *Composite Structures*, vol. 106, no. 12, pp. 716–723, 2013.
- [8] Y. Wu, Q. Liu, J. Fu, Q. Li, and D. Hui, "Dynamic crash responses of bio-inspired aluminum honeycomb sandwich structures with CFRP panels," *Composites Part B: Engineering*, vol. 121, pp. 122–133, 2017.
- [9] M. Paulino, F. Teixeira Dias, C. P. Gameiro, and J. Cirne, "Hyperelastic and dynamical behaviour of cork and its performance in energy absorption devices and crashworthiness applications," *International Journal of Materials Engineering Innovation*, vol. 1, no. 2, p. 197, 2009.
- [10] R. D. Hussein, D. Ruan, and J. W. Yoon, "An experimental study of square aluminium tubes with honeycomb core subjected to quasi-static compressive loads," *Key Engineering Materials*, vol. 626, pp. 91–96, 2015.
- [11] Y. Zhang, Z. Zong, Q. Liu, J. Ma, Y. Wu, and Q. Li, "Static and dynamic crushing responses of CFRP sandwich panels filled with different reinforced materials," *Materials and Design*, vol. 117, pp. 396–408, 2017.
- [12] N. Tomizawa, T. Tsujimoto, K. Itoh, T. Ogino, K. Nakamura, and S. Hara, "Numerical and experimental study of crashworthiness parameters of honeycomb structures," *Thin-Walled Structures*, vol. 78, no. 4, pp. 87–94, 2014.
- [13] A. Ashab, R. Dong, G. Lu, and Y. C. Wong, "Quasi-static and dynamic experiments of aluminum honeycombs under combined compression-shear loading," *Materials and Design*, vol. 97, pp. 183–194, 2016.
- [14] X. Zhang, H. Zhang, and Z. Wen, "Experimental and numerical studies on the crush resistance of aluminum honeycombs with various cell configurations," *International Journal of Impact Engineering*, vol. 66, pp. 48–59, 2014.
- [15] K. B. Shin, J. Y. Lee, and S. H. Cho, "An experimental study of low-velocity impact responses of sandwich panels for Korean low floor bus," *Composite Structures*, vol. 84, no. 3, pp. 228–240, 2008.
- [16] C. C. Foo, G. B. Chai, and L. K. Seah, "Quasi-static, and low-velocity impact, failure of aluminium honeycomb sandwich panels," *Proceedings of the Institution of Mechanical Engineers Part L: Journal of Materials: Design and Applications*, vol. 220, no. 2, pp. 53–66, 2006.

- [17] G. Sun, X. Huo, D. Chen, and Q. Li, "Experimental and numerical study on honeycomb sandwich panels under bending and in-panel compression," *Materials and Design*, vol. 133, pp. 154–168, 2017.
- [18] G. Sun, S. Li, Q. Liu, G. Li, and Q. Li, "Experimental study on crashworthiness of empty/aluminum foam/honeycomb-filled CFRP tubes," *Composite Structures*, vol. 152, pp. 969–993, 2016.
- [19] M. A. Hazizan and W. J. Cantwell, "The low velocity impact response of an aluminium honeycomb sandwich structure," *Composites Part B: Engineering*, vol. 34, no. 8, pp. 679–687, 2003.
- [20] V. Crupi, E. Kara, G. Epasto, E. Guglielmino, and H. Aykul, "Theoretical and experimental analysis for the impact response of glass fibre reinforced aluminium honeycomb sandwiches," *Journal of Sandwich Structures and Materials*, vol. 20, no. 1, pp. 42–69, 2016.
- [21] R. D. Hussein, R. Dong, G. Lu, and I. Sbarski, "Axial crushing behaviour of honeycomb-filled square carbon fibre reinforced plastic (CFRP) tubes," *Composite Structures*, vol. 140, pp. 166–179, 2016.
- [22] J. C. Liu and H. C. Wu, "Fiber direction and stacking sequence design for bicycle frame made of carbon/epoxy composite laminate," *Materials and Design*, vol. 31, no. 4, pp. 1971–1980, 2010.
- [23] Q. Liu, X. Xu, J. Ma, J. Wang, Y. Shi, and D. Hui, "Lateral crushing and bending responses of CFRP square tube filled with aluminum honeycomb," *Composites Part B: Engineering*, vol. 118, pp. 104–115, 2017.

## Research Article

# Improving Electromagnetic Shielding Ability of Plaster-Based Composites by Addition of Carbon Fibers

A. Samkova <sup>1</sup>, P. Kulhavy <sup>2</sup>, V. Tunakova,<sup>1</sup> and M. Petru <sup>2</sup>

<sup>1</sup>Faculty of Textile Engineering, Technical University of Liberec, Studentska 2, 461 17 Liberec, Czech Republic

<sup>2</sup>Institute for Nanomaterials, Advanced Technologies and Innovation, Technical University of Liberec, Studentska 2, 461 17 Liberec, Czech Republic

Correspondence should be addressed to A. Samkova; [alzbeta.samkova@tul.cz](mailto:alzbeta.samkova@tul.cz)

Received 5 January 2018; Revised 14 May 2018; Accepted 19 June 2018; Published 26 July 2018

Academic Editor: Bing Zhang

Copyright © 2018 A. Samkova et al. This is an open access article distributed under the Creative Commons Attribution License, which permits unrestricted use, distribution, and reproduction in any medium, provided the original work is properly cited.

The size of electromagnetic shielding in plaster composites by the means of different volume fractions of carbon fibers was studied in this paper. Conventional types of plaster, which are commonly used in industry, that is, cement, lime, gypsum, and lime cement (Thermo UM), were the base materials of the created composites. The fundamental idea of improving the electromagnetic shielding properties was verified based on a numerical simulation conducted by means of electromagnetic module in Comsol Multiphysics. The carbon microfibers with the above-critical length of 8 mm were added as the reinforcing and simultaneously shielding element into the plaster samples. From the viewpoint of the mechanical properties, fibers shorter than the critical length do not provide sufficient reinforcement. The samples were created at three different volume fractions of the dispersion and one without any reinforcement for the possibilities of their mutual comparison. The results of the carried measurement show that the electromagnetic shielding in the plaster composite grows with the increase of fiber content within the tested ratio proportionately. Also, the dependency of shielding ability on the inner material moisture has been studied. Any measureable influence of the moisture content on to the total shielding effect has not been found. Only in the lime plaster reinforced with fibers, the increased moisture could significantly decrease the shielding effect.

## 1. Introduction

Over the last few years, there has been mounting concern about the possibility of adverse health effects resulting from exposure to radiofrequency electromagnetic (EM) fields, such as those emitted by wireless communication devices [1]. This phenomenon is connected with extensive development of electronic systems and telecommunications including generation and transmission of electricity, domestic appliances and industrial equipment, and telecommunications and broadcasting, whereas electrical and EM fields in certain frequency bands have wholly beneficial effects, which are applied in medicine, other nonionizing frequencies sourced from extremely low frequencies, power lines or certain high-frequency waves used in the fields of radar, telecommunications, and mobile communications, and they

appear to have more or less potentially harmful, nonthermal, biological effects on plants, insects, and animals as well as the human body [2–4].

For the reasons given above, a demand for protection of human beings against undesirable influence of EM signals and troublesome charges (especially for professional use) has been increasing. The best material for shielding or absorption of EM wave must have both high electric conductivity (imparts higher reflection of EM wave especially at lower frequencies) and high magnetic permeability (provides higher absorption of EM wave especially at lower frequencies); therefore, shields based on the use of metals, magnetic alloys, and carbon-based materials are the best ones [5]. The materials used in the shielding of radiofrequency fields are usually copper, aluminum, or silver based (in the form of wires, metal plating, or conductive

fillers) [6–10]. These shields work by reflecting the waves because these metals have a high electric conductivity. To shield a magnetic field, materials must have a high magnetic permeability to be able to absorb the fields [5]. Carbon-based materials such as carbon fibers, carbon particles, carbon nanotubes, and so on fully fulfill this requirement [11–13].

One way to protect human beings is to use protective clothing made of textile materials with increased electrical conductivity [14, 15]. These fabrics are usually based on the use of very thin metal fibers incorporated to the structure of yarn from which woven or knitted fabric is made [10]. By these fabrics, sufficient electrical conductivity connected with certain level of electromagnetic shielding protection is achieved, but on the other hand, this method of protection brings some disadvantages. For example, by addition of conductive components (metal fiber), thermophysiological comfort properties of clothes are usually deteriorated [16]. In addition, even the appearance (color) of these special fabrics is also very often influenced [17].

It seems that more robust solution offers controlled insulation of whole buildings. However, it is clear that just the passive instruments, such as wall cladding by damping panels and the use of electro conductive curtains or special wallpapers solve only the consequences and not the causes of electromagnetic radiation. Since in many cases the passive instruments are the only possible solution, they are sometimes necessary and therefore must be addressed.

The most important material in the building industry is cement. Dried cement composites do not contain any free electrical charge carriers. Their specific electrical resistance in the fully dried state is around  $10^9 \Omega\text{m}$ , making it one of the best insulators, which means they are fully transparent to electromagnetic radiation of higher frequencies [18]. The increased moisture content of cement composites results in a reduction of specific electrical resistance. This is due to salt ions contained in the pore solution. Significant reduction of electrical resistivity accompanied with the increase of electromagnetic shielding ability of cement composites occurs after an addition of a sufficient amount of electrically conductive additives to form conductive paths. The dominant charge carrier in this case is the electron [18].

There are many references in the literature concerning the addition of a varying amount of conductive filler as a reinforcing element to a cement matrix in order to produce an electrically conductive, electromagnetic shielding material with favorable mechanical properties such as tensile strength, compressive strength, or impact strength. For example, Wang et al. [19] prepared multiwalled carbon nanotube (MWCNT)/cement composites and studied the effect of sample thickness and the nanodispersion content on the shielding effectiveness. It was found that at MWCNT content 0.6 wt.%, the cement mortar sample with a thickness of 25 mm remarkably absorbs electromagnetic waves close to the absorbing peaks in the frequency range of 2–8 GHz. Yawen et al. [20] described investigation of main properties of high-structure carbon-black (CB) cement-based composites (CBCCs). It was confirmed that these composites exhibit good performance in the absorption of electromagnetic waves in the frequencies higher than 8 GHz. For

CBCC containing 2.5 wt.%, the minimum reflectivity reaches about 20 dB, but compressive strength significantly decreases with the increase of CB content. Unfortunately, both mentioned papers analyze only reflection part of electromagnetic shielding effectiveness, whereas it is expected from theory [5] that for carbon-based materials, main portion of electromagnetic shielding effectiveness will be created by absorption coefficient. Khushnood et al. [21] focused their work on the usage of cost-effective material (pyrolyzed agricultural wastes such as peanut and hazelnut shells) for enhancing the electromagnetic shielding effectiveness of cement composites. Numerically evaluated electromagnetic shielding effectiveness showed that shielding ability of composite is poor at low frequencies (about 0.2 GHz). The shielding ability is close to 10 dB at the highest of evaluated frequency (10 GHz) using the highest portion of conductive component that is 5 wt.% of carbonized peanut shells or 0.5 wt.% of carbonized hazelnut shells.

As mentioned above, the use of fibrous materials as reinforcing elements is favorable especially for its high aspect ratio (length/diameter ratio). It was proven that fibrous materials contribute to improvements in their mechanical properties [22]. In the authors' previous studies [23], it was reported that usage of optimal volume ratio of fibers (1% to 2% of reinforcement) shows significant improvement in the main mechanical properties of plaster composites. With the higher volume of fibers, the improvement is not proportional, and the demanded effect is just minimal.

The aim of the carried work was to find out whether the addition of fibrous reinforcement could improve the electromagnetic shielding ability. To achieve the required effect, some conductive components must be added to the plaster. Carbon fiber shows very good electrical and thermal conductivity, good strength properties, and improved environmental resistance of the final plaster [24].

## 2. Materials and Preparation

In the previous works of the author [23, 25], all realistic combinations of plasters and fibers have been tested with respect to their mechanical properties (Figure 1). Some glass, carbon, basalt fibers, and even polyvinyl butyral nanofibrous dispersion have been used as the reinforcing element of composites. The thickness of plasters has been chosen based on the real values used in the construction industry. The results show that the mechanical properties (flexural tensile strength, compressive strength, and impact strength) of plasters could be significantly improved by using the weight ratio of fiber reinforcement of 1% to 2%. Higher content of carbon reinforcement does not have any equivalent effect or could even worsen the mechanical parameters [23]. The content of the fibrous reinforcement in concrete materials is usually 6%. However, a mixture of the plasters and fibers with such high contents usually causes problems in their bonding [23, 26]. For this reason, the content of the fibrous reinforcement has been set to 1%, 2%, and 3%. The calculation (1) of the mixing ratio [27] is based on the percentage of the components in the composite and their densities.

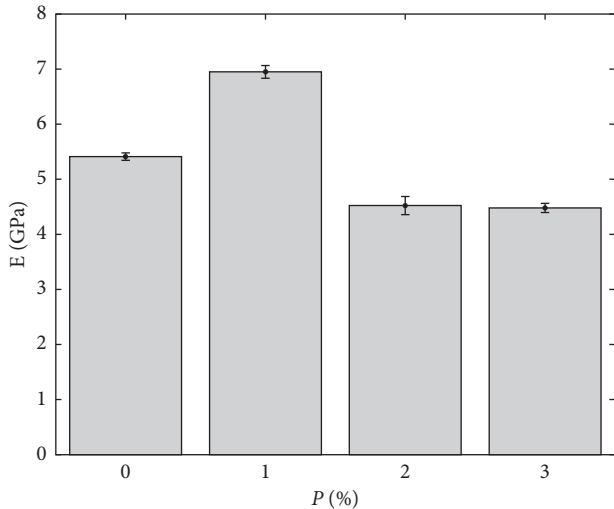


FIGURE 1: Comparison of the modulus of elasticity in the tension  $E$  (GPa) of the Thermo UM Xtra plaster with different volume fractions ( $P$  (%)) of the carbon reinforcement.

The mutual conversion between the mass and volume fraction is in Table 1.

$$w_i = \frac{V_i \times \rho_i}{\sum V_i \rho_i}, \quad (1)$$

where  $w_i$  (%) is the mass fraction of the  $i$ th component,  $V_i$  (%) is the volume fraction of the  $i$ th component, and  $\rho_i$  ( $\text{kg}/\text{m}^3$ ) is the density of the  $i$ th component.

With the higher volume fraction, the mechanical properties suddenly start falling down because the reinforcement is transformed into a bundle of stress concentrators and the rupture initiators. Based on these results, four types of plasters, whose mechanical properties could be improved or at least not worsened, have been chosen. For the mutual comparison and consistency of the results, pure plasters without any fiber dispersion were tested. Because of the natural climatic loading of the plasters, the samples were also tested at different humidities (0.8%, 2.2%, and “wet” – not physically possible to measure). The individual plasters were prepared according to the recommended manufacturer’s technical standards. The inner moisture content was measured after acclimatization of the samples in the standardized ambient conditions, and the so called “wet” was achieved by simultaneous spraying of the samples by water. The carbon fibers with the declared mean diameter  $1.76 \mu\text{m}$  were selected to achieve the shielding effect. For plaster composites with microfiber reinforcement, it was necessary to compute the critical fiber length: the final length of carbon fibers is 8 mm. The fiber distribution in the tested parts was assessed by image analysis on randomly selected samples. However, it is possible to say, that after approx. 20 min of mixing, the distribution is equal. The main physical properties of the used materials are given in Table 2.

**2.1. Plaster.** The type and amount of the used binder influences the resulting plaster properties, so it is one of the

TABLE 1: Volume fraction of the individual components.

Volume fraction $w_i$	1%	2%	3%
	Mass fraction (%)		
Thermo UM	3.98	7.74	11.28
Cement	0.75	1.51	2.27
Lime	1.79	3.55	5.29
Gypsum	1.96	3.87	5.75

TABLE 2: Mechanical properties of the base used materials.

Material	Length (mm)	Diameter ( $\mu\text{m}$ )	Density ( $\text{kg}\cdot\text{m}^{-3}$ )	$E$ (GPa)	$\nu$ (–)
Carbon fiber	8	1.6	1800	241	0.27
Thermo UM	—	—	551	5.4	0.18
Gypsum	—	—	1100	14	0.27
Cement	—	—	3020	39	0.2
Lime	—	—	1250	8.8	0.21

main criteria based on which the plasters could be divided. The first plaster selected for the study was the lime-cement. This plaster belongs among extremely effective heat-insulating plasters with the trade name Thermo UM (this designation is used in this study). Another significant feature of this material is low bulk density; compared to commonly used plasters, it could be up to 4 times lighter. Due to its low bulk density and low modulus of elasticity, the plaster eliminates the volume or shape changes in the base wall material, thus creating no cracks. Above all, the Thermo UM plaster is characterized by a high value of the thermal conductivity coefficient, and the chemical composition of the plaster eliminates growth of microorganisms, algae, and fungi on its surface [28].

Another type, the gypsum plaster, is generally cheaper material characterized by good thermal and acoustic resistance. Due to its thermal properties, the plaster is perceived as a hygroscopic material, which allows the regulation of the microclimate in the room [29, 30]. This plaster is vapor-permeable, does not close the water in the construction, and at the same time allows the natural drying of residual water from the blocks. The gypsum plaster is suitable for antibacterial environments because the smoothness of its surface prevents dust from settling on. At high temperatures, gypsum is released by water vapor, which is often used to increase fire resistance [31].

The cement plaster [32] exceeds especially with the high strength, resistance to mechanical damage, and very good adhesion to the basic substrate. This kind of plaster is therefore commonly used for highly loaded areas and areas where frost and weather-resistant is also required.

The lime plaster is characterized by very good water vapor permeability and ability to absorb moisture from surrounding bricks. It does not retain capillary water and it also dries very well. These properties allow lime plasters to regulate indoor climate. Lime plaster is very flexible, making it suitable for uneven surfaces. Another advantage is its ability to absorb all odors [33]. The microimages of the individual types of plaster with the carbon dispersion are in Figure 2.

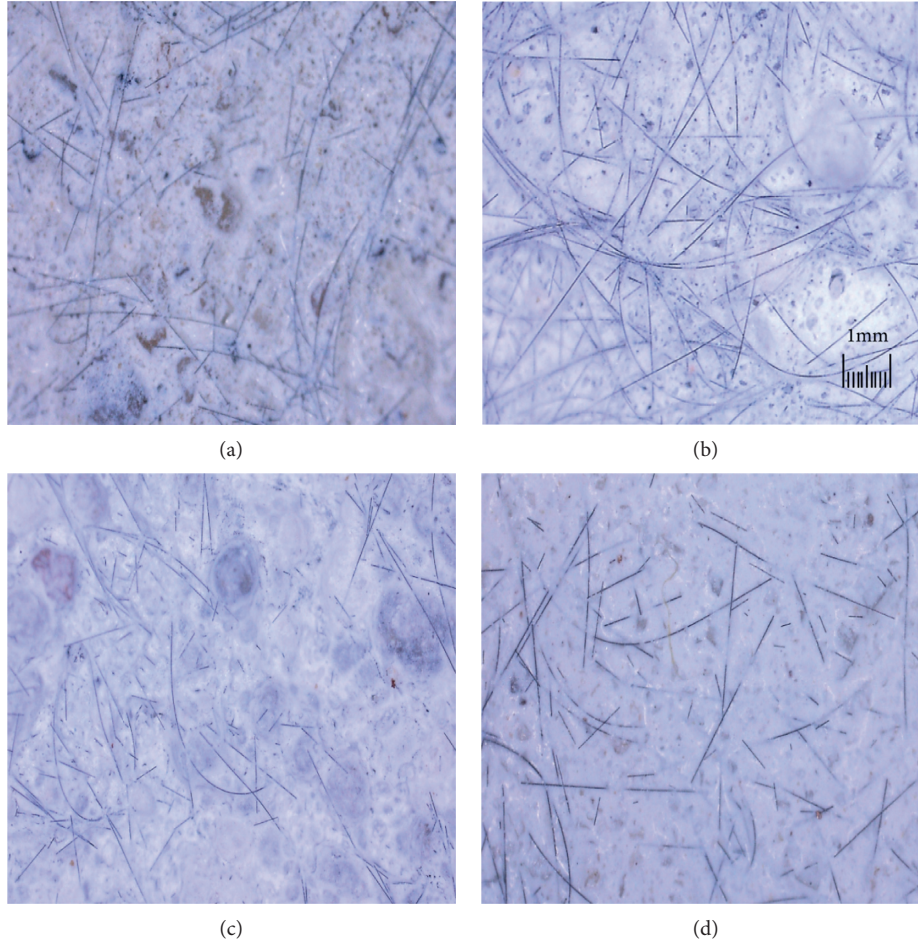


FIGURE 2: The studied plasters reinforced with carbon fibers: (a) cement, (b) gypsum (c) Thermo UM, and (d) lime.

**2.2. Fiber Dispersion.** The carbon “*An old but still new material*” and its natural or synthetic compounds exceed the number of all the compounds of all other elements together, which is about a million. This is possible even though the carbon materials are composed of only one element. The properties of these materials could not be predicted or estimated based on the known composition, as is the case of, for example, conventional metal alloys. The fibers are commercially available on fiber coils of several hundred meters in length, and each bundle consists of 1000 to 10000 filaments with a diameter of 5–12  $\mu\text{m}$ . Standard carbon fibers have a tensile strength between 3 and 4 GPa, and the modulus of elasticity of 230–300 GPa [34, 35]. Carbon fibers have the largest range of properties. High strength, modulus, and heat resistance with low density are associated with carbon fibers. Very good thermal and electrical conductivity were the important criterion for selecting this fiber for our study [36]. The importance of carbon fibers is growing steadily despite the fact that compared to glass fibers, their price is ten to hundred times more expensive. However, due to their characteristics, customers’ constant interest could be expected. In recent years, the carbon fibers have become an integral part of modern civil engineering. They are primarily used to increase the load-bearing capacity of building components and to perform building reconstructions. In such cases, not only the

simple carbon fiber is used, but carbon reinforcement in the form of rods, lamellas, and carbon fabric is used as well.

The potential of using those fibres also in the civil engineering could lay in utilization of some wasted carbon fibres, remaining in a big amounts from manufacturing of composite parts for vehicles and airplanes. Due to the fact that once the fibers are cut or split, there is no possibility to merge or dissolve them again, and they are usually just energetically utilized by burning in the heating plants. To add them into building materials is significantly a better idea.

The conductance (2) is a physical parameter that describes the material ability to lead an electrical current.

$$G = \frac{I}{U} = \sigma \frac{S}{l} = \frac{1}{R}, \quad (2)$$

where  $I$  (A) is the electric current flowing through the conductor,  $U$  (V) is the voltage at the ends of the conductor,  $\sigma$  (SI) is the conductivity of the substance,  $S$  ( $\text{m}^2$ ) is the cross-sectional area,  $l$  (m) is the length of the conductor, and  $R$  ( $\Omega$ ) indicates the electrical resistance.

### 3. Modeling

The created model of the electromagnetic absorption has been created in the Comsol Multiphysics. The model uses



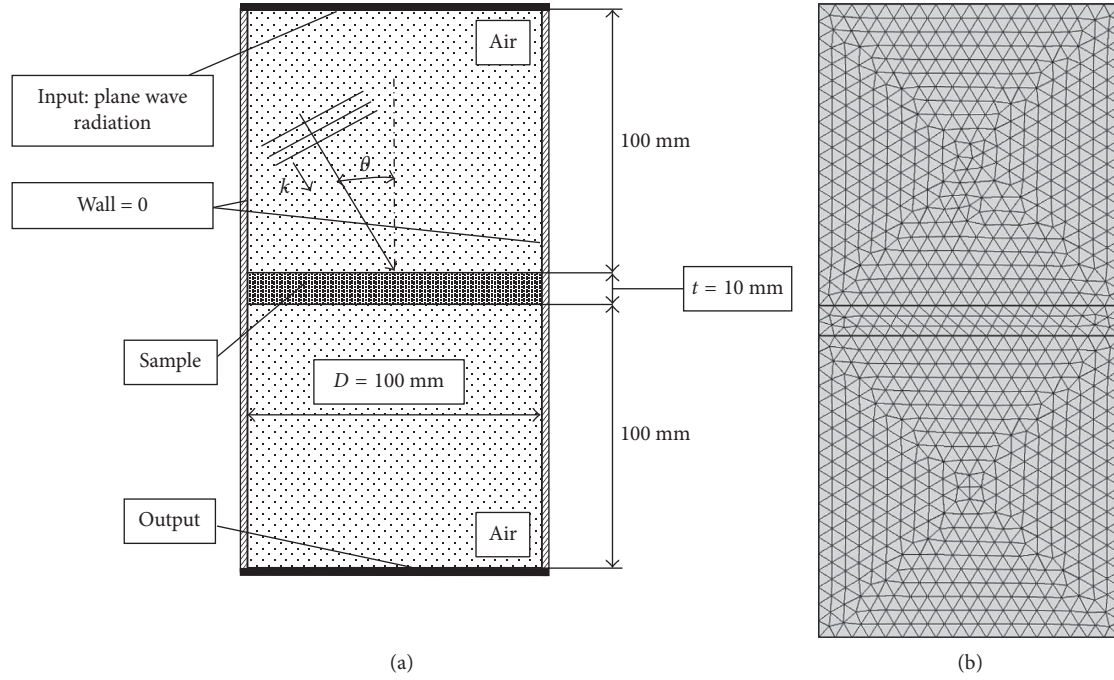


FIGURE 3: Scheme of the created FEM model and boundary conditions (a) and FEM model (b).

a 2D geometry of such a system (Figure 3). The aim of the model is to characterize the absorption properties—more specifically, the specific surface impedance with and without the conductive reinforcement. The base models of the four samples (Thermo UM, gypsum, cement, and lime) were created using the module Acoustic-Electromagnetic Interaction and Radiation, with the frequency domain. Layers are also assumed to be infinite in the lateral dimensions; the only geometric information is then the sample. The surrounding fluid is air. The incidence angle is given as (3). The task was solved with two directions of acting waves  $0^\circ$  and  $45^\circ$  as could be seen in Figure 4. As shown in Figure 5, the only solid body in the created model was the disk with diameter  $D = 100$  mm, thickness  $t = 10$  mm, and material properties of the individual materials (density, conductivity, moisture, and resistivity). The maximal frequency in the model is 1000 Hz.

$$k = k_0 (\sin \theta, \cos \theta), \quad (3)$$

where  $\theta$  is the incidence angle and  $k_0$  is the wave number in the free field.

The orthogonal impact of the wave to the partition is the worst case in terms of shielding. Therefore, it is not necessary to calculate any other impacting angles for comparison of the numerically obtained results with the experiments. In order to determine the shielding efficiency, it is necessary to determine the value of the incident electromagnetic waves  $H_t$  transmitted through the insulated sample described by the parameters  $\mu$ ,  $G$ , and the sample thickness  $t$ . Where  $\mu$  is the permeability of vacuum ( $\text{H}\cdot\text{m}^{-1} = \text{N}\cdot\text{A}^{-2}$ ). Parameters of the free continuum filled with air around the simulated sample are the permeability constant  $\mu_0 = 4\pi \times 10^{-7} \text{H}\cdot\text{m}^{-1}$  and the vacuum permittivity  $\epsilon_0 = 8854 \times 10^{-12} \text{F}\cdot\text{m}^{-1}$ . The characteristic impedance of the free space on both sides of

the sample is  $Z_0$  (4), and the characteristic impedance of the sample is  $Z_S$  (5). Subsequently, the shielding efficiency can be expressed by impedance according to the following:

$$Z_0 = \sqrt{\frac{\mu_0}{\epsilon_0}}, \quad (4)$$

$$Z_S = \sqrt{\frac{j\omega\mu}{G}}, \quad (5)$$

$$SE = 20 \cdot \log \left| \frac{(Z_0 + Z_S)^2}{4Z_0Z_S} \cdot e^{\gamma t} \cdot \left[ 1 - \left( \frac{Z_0 - Z_S}{Z_0 + Z_S} \right)^2 \right] \cdot e^{-2\gamma t} \right|, \quad (6)$$

where  $\gamma$  denotes the number of wavelengths per unit length (propagation constant) of the electromagnetic wave in space  $\gamma = \sqrt{j\omega\mu(G + j\omega\mu)} = \alpha + j\beta$ , where  $\alpha$  ( $\text{dB}\cdot\text{m}^{-1}$ ) is the attenuation constant and  $\beta$  ( $\text{rad}\cdot\text{m}^{-1}$ ) is the phase constant. The overall shielding efficiency can be broken down into several components. The reflection of electromagnetic wave occurs when the wave arrives from the free space to the sample surface and then again when passing through the sample into the free space. The total attenuation caused by reflection  $R$  (the electrical resistance—already defined in (2)) defined according to (7) could be subsequently described by 2 parameters  $R_1$  and  $R_2$ . The characteristic reflection on the first (input) and on the second partition interface, where a part of the unattenuated wave and a part of the attenuated wave, is shown in Figure 5.

$$R = R_1 + R_2 = 20 \cdot \log \left| \frac{Z_0 + Z_S}{2Z_S} \cdot \frac{Z_0 + Z_S}{2Z_0} \right|. \quad (7)$$

When some shielding material is used, the greatest number of the reflected waves belongs to the first interface. This phenomenon could be easily observed on some metallic

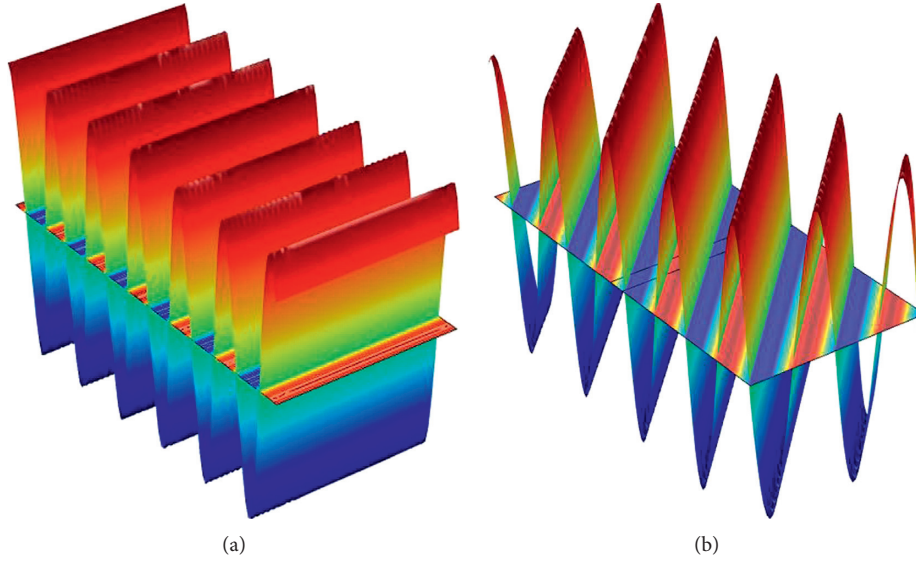


FIGURE 4: FEM model: examples of the incident waves in the two computed directions  $\theta = 0^\circ$  (a),  $\theta = 45^\circ$  (b).

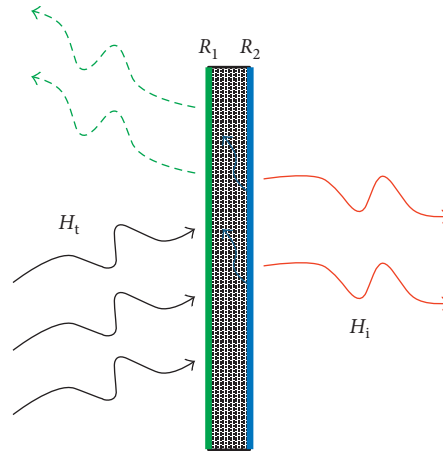


FIGURE 5: Model scheme of propagation, reflection, and attenuation of an electromagnetic wave in a solid partition.

materials where the best possible conductivity is necessary to obtain the highest shielding efficiency. When the electromagnetic wave passes through a metal wall of the enclosure, portion of its energy is dissipated as heat. The size of the absorbed portion of the energy depends on the wall material, its thickness, and frequency of the waves. Therefore, in a case of modeling of nonmetallic materials with just a minimal primary conductivity, such are the tested materials: Thermo UM, gypsum, cement and lime, it is necessary to use conductive dispersion that could affect their permeability because the greatest absorption  $\vartheta$  (dB) can be achieved by a composite material with high permeability, whose thickness exceeds the wavelength of the penetrating waves

$$\vartheta = 20 \cdot \log e^{t/\delta}, \quad (8)$$

where  $t$  is the material thickness and  $\delta$  is the depth of the impacting wave penetration, which is dependent on field frequency, permeability, and material resistance  $\delta = \sqrt{(2\rho/\omega\mu)}$ , where  $\rho$  is the specific resistance ( $\Omega \cdot \text{mm}^2 \cdot \text{m}^{-1}$ ).

The dispersion used in the form of added fibers affects the resulting permeability and the overall absorption shielding. However, the problem could be to determine the optimal amount of the fiber dispersion. The optimal added fiber ratio could cause positive increase, whereas in the case of nonoptimal amount, the reflected and pulsed waves within the structure may have even a negative effect on the overall shielding efficiency. The shielding efficiency caused by multiple reflections  $\vartheta_M$  (dB) could be then expressed as

$$\vartheta_M = 20 \cdot \log \left[ \left| 1 - \left( \frac{Z_0 - Z_S}{Z_0 + Z_S} \right)^2 \cdot e^{-(2t/\delta)} \cdot e^{-j(2t/\delta)} \right| \right]. \quad (9)$$

When the shielding structure is designed from the material where  $Z_0 \gg Z_S$  and when the wall thickness is greater than the wave's penetration depth  $t \gg \delta$ , then the value of  $\vartheta_M$  is approaching zero, and therefore, the effect of multiple reflections of electromagnetic waves on the overall shielding could be neglected. The reflected wave is easily

converted to heat by the means of absorption attenuation. However, if the wall thickness is less than the penetration depth, of the ratio  $(t/\delta) \leq 1$ , then  $\mathcal{D}_M$  achieves negative values, and thereby, the overall shielding efficiency is reduced, as stated by Mardiguian or Chatterton et.al. [37, 38].

#### 4. Experiment and Testing

Electromagnetic shielding effectiveness (SE) of composites was measured according to ASTM D 4935-10 [39] for planar materials using a plane-wave, far-field EM wave. SE of samples was measured over the frequency range of 30 MHz to 3 GHz. The most common wireless technologies such as the broadcasting television and radio, cell phones, satellite radio and TV, wireless computer networks, Bluetooth, GPS, and so on use radio frequencies, which extend from about 10 kHz to 300 GHz and match wavelengths within the range 30 km to 0.1 mm. Majority of practical applications is working at frequencies below 30 GHz. Table 3 summarizes the approximate frequency bands used by the most present wireless technologies [2], which means that the measured frequency range includes working frequencies of the most common equipment for public communication and data transfer.

The setup consisted of a sample holder with its input and output connected to the network analyzer (Figure 6). A shielding effectiveness test fixture (Electro-Metrics, Inc., model EM-2107A) was used to hold the sample. The design and dimension of the sample holder follows the ASTM method mentioned above. Network analyzer Rohde & Schwarz ZN3 was used to generate and receive the electromagnetic signals. Sinusoidal signal was generated over the mentioned frequency range with the use of 50  $\Omega$  output impedance to minimize reflections caused by mismatches. The standard mentioned above determines the electromagnetic shielding effectiveness of the fabric using the insertion-loss method. A reference measurement for the empty cell was required for the shielding effectiveness assessment.

Samples were air-conditioned before testing ( $T = 22^\circ\text{C} \pm 3$ ,  $\text{RH} = 50\% \pm 10\%$ ). In addition, effect of moisture content was studied. Samples of dimensions  $10 \times 150 \times 150$  mm were produced for this testing. Five samples were produced for each conductive component content in order to the conduct subsequent statistical analysis.

The total shielding of a solid material with no apertures is equal to the sum of the absorption loss ( $A$ ) plus the reflection loss ( $R$ ) plus a correction factor ( $B$ ) to account for multiple reflections in thin shields. Total electromagnetic shielding effectiveness therefore can be written as (10) [5]:

$$\text{SE} = A + R + B \text{ (dB)}. \quad (10)$$

The reflection is usually the primary mechanism of electromagnetic interference shielding. The wave, which is incident to the boundary with the second medium, is partially reflected back and partially transmitted to second medium. The same situation occurs at the interface between the second and third material. Reflection loss for plane waves

TABLE 3: Frequency range for different applications [40].

Application	Frequency or frequency range
AM broadcast	530 kHz~1.7 MHz
Broadcast TV	54~88, 174~261, 470~698 MHz
FM broadcast	88~108 MHz
Cell phones	~850, ~900, ~1800, ~1900 MHz
GPS	~1.5 GHz
Satellite radio	~2.3 GHz
Wireless Comp. Network	2.4 & ~5.8 GHz
Satellite TV	~12 GHz

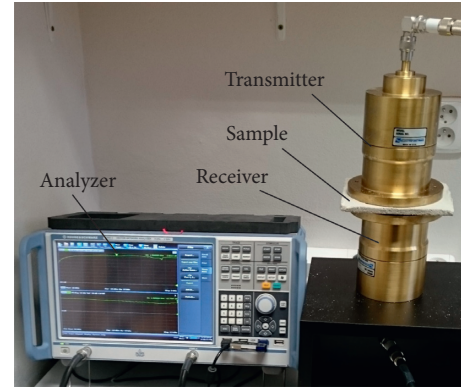


FIGURE 6: The testing equipment.

is greater at low frequencies and for high conductivity materials [5].

Secondary mechanism of EMI shielding is usually absorption. When an electromagnetic wave passes through a medium, its amplitude decreases exponentially. This decay occurs because currents induced in the shield produce ohmic losses and heating of material. General expression for absorption loss can be written as (11) [20]:

$$A = 0.0848t\sqrt{f\mu_r\sigma_r} \text{ (dB)}, \quad (11)$$

where  $t$  is the thickness of the shield in meters. For significant absorption of the radiation by the shield, the shield should have electric and/or magnetic dipoles, which interact with the electromagnetic fields in the radiation. The electric dipoles may be provided by materials having a high value of the dielectric constant. The magnetic dipoles may be provided by materials having a high value of the magnetic permeability.

The absorption loss is a function of the product  $\sigma_r \cdot \mu_r$ , whereas the reflection loss is a function of the ratio  $(\sigma_r/\mu_r)$ , where  $\sigma_r$  is the electrical conductivity relative to copper and  $\mu_r$  is the relative magnetic permeability. Silver, copper, gold, and aluminum are excellent for reflection due to their high conductivity. Super-malloy and mu-metal are excellent for absorption due to their high magnetic permeability. The reflection loss decreases with increasing frequency, whereas absorption loss increases with increasing frequency [5].

Other than reflection and absorption, a mechanism of shielding is based on multiple reflections ( $B$ ), which refer to the reflections at various surfaces or interfaces in the shield. This mechanism requires the presence of a large surface area

or interface area in the shield. An example of a shield with a large surface area is a porous or foam material. The loss due to multiple reflections can be neglected when the distance between the reflecting surfaces or interfaces is large compared to the skin depth.

Operation of the electromagnetic shield could be characterized by the so called shielding attenuation coefficient (dimensionless) defined as a ratio between electromagnetic field power density in a specific place of shielded space  $P_t$  and incident electromagnetic wave power density  $P_i$  ( $\text{W}/\text{m}^2$ )

$$SE = \frac{P_t}{P_i} (-). \quad (12)$$

Logarithmic size of this coefficient called electromagnetic shielding effectiveness (SE) is used more frequently:

$$SE = 10 \log \frac{P_t}{P_i} = 20 \log \frac{H_t}{H_i} \text{ (dB)}, \quad (13)$$

where  $H_t$ ,  $E_t$ , and  $P_t$  are the electric field strength, magnetic field strength, and electromagnetic field density values measured in the presence of the textile material, whereas  $H_i$ ,  $E_i$ , and  $P_i$  are the same values measured without the textile material.

For the analysis of the shielding effectiveness of test samples, a formula expressing absorption loss  $A_{\text{sheet}}$  (dB) and reflection loss  $R_{\text{sheet}}$  (dB) can be used expressed as

$$A_{\text{sheet}} = 0.0848 \times t \sqrt{\frac{K}{K_C}} f, \quad (14)$$

$$R_{\text{sheet}} = C + 10 \log \left( \frac{K}{K_C f} \right), \quad (15)$$

where the constant  $C$  is listed in Table 4 for plane waves, electric fields, and magnetic fields, respectively.  $K$  (S/cm) is the volume conductivity,  $K_C$  (S/cm) is cooper conductivity,  $f$  (MHz) is the frequency, and  $t$  (m) is thickness of the shield [41].

During the experiment, the dependency of inner material moisture has also been measured. The measured moistures were 0.8% for the dried samples, 2.2% for the normalized samples, and for the higher level of the inner humidity, it was not possible to set the value because of the physical limits of the measuring tools.

## 5. Result and Discussion

First of all, the theoretical model was prepared to study electromagnetic shielding ability of plaster composites with different thicknesses, containing different fiber reinforcements, and applying different types of incident wave. Based on findings gained from modeling, real composite samples were produced, and effect of plaster type, effect of conductive reinforcement content, and effect of moisture content on total electromagnetic shielding effectiveness were studied. A comparison of the FEM model and experimental measurement revealed similar results of electromagnetic shield by testing materials obtained from the measurements;

TABLE 4: Constants used in (7) and (8).

Type of field	C
Electric field	322
Plane wave	168
Magnetic field	14.6

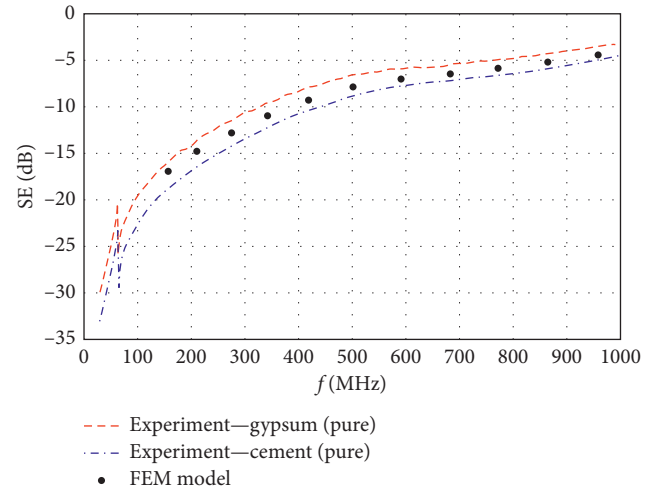


FIGURE 7: A comparison of the FEM model and experimental measurement.

however, Figure 7 shows a uniform course. The FEM model also shows a study of the absorption coefficient where it is evident that in the mixture of the selected plaster types without fiber dispersion the absorption coefficient of the electromagnetic waves is low and remains almost unchanged. Improvement can be achieved by adding conductive carbon fibers with value of about  $\leq 3\%$  in our case. As shown in Figures 8 and 9, it is possible to achieve an increase in the effective plaster thickness by the fiber addition and the final electromagnetic shielding could also be improved. As it was already mentioned in the description of materials, the plaster itself, due to brittleness and porosity, does not have the corresponding elastic properties. However, when reinforcing the plaster with just small ratio of fibers (1-2%), composite material with significantly improved elastic and damping properties can be obtained. This phenomenon is illustrated in Figure 9, where the FEM model compares the structure of the pure and the reinforced plaster. Figure 9 shows the overall shielding efficiency, where the density of intensity of the overall attenuation of the electromagnetic shield  $R$  is defined by (7), whereas in case of a nonreinforced sample, the shielding intensity decreases steeply beginning by the first contact of waves and material boundary; the increased absorption is evident in the entire thickness of the reinforced sample; thus, less of undamped waves pass through the reinforced sample.

The electromagnetic shielding ability was measured for three sets of samples having 4 different types of plaster with the various carbon fiber weight ratios (from 0 to 3 wt.%). Figure 10 shows the variation in SE for composites with

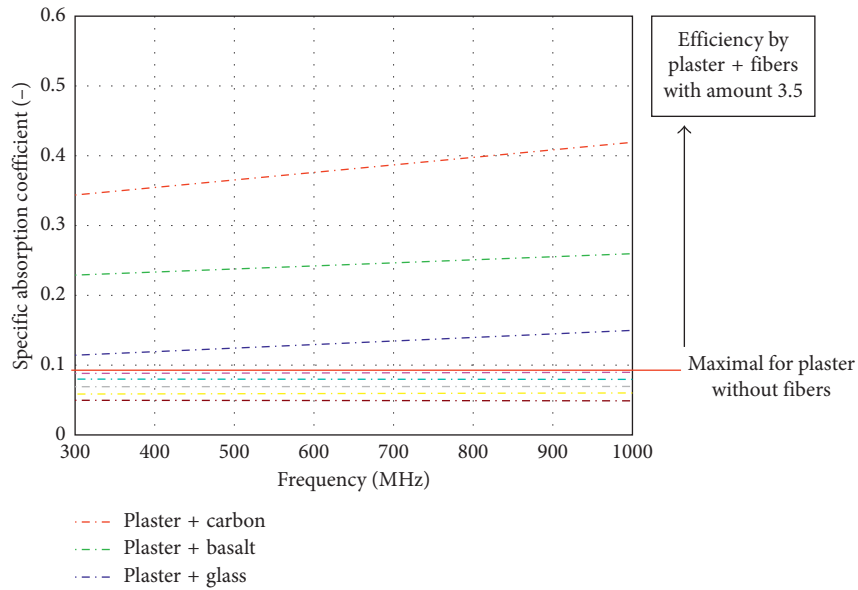


FIGURE 8: FEM model: study of absorption coefficient for plaster.

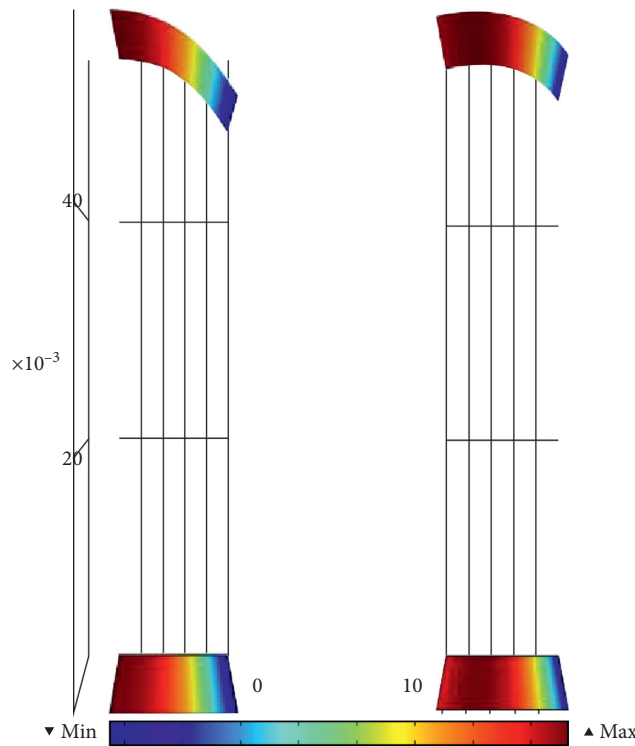


FIGURE 9: FEM model: comparison of intensity of electromagnetic shielding for the same thickness of sample—the plaster without the fibers (left) and in the plaster with the fibers (right).

incident frequency in the range of 30–3000 MHz. It can be concluded that electromagnetic shielding effectiveness (SE) in (dB) is dependent not only on carbon fiber content but also on the type of plaster. Assumption based on theory saying that addition of conductive component guarantees improved shielding ability of material validated by modeling was also confirmed by experimental evaluation of real

samples. It is visible that pure plasters regardless of its type show poor electromagnetic shielding effectiveness higher than  $-10$  dB for frequency range 500–3000 MHz, whereas by addition of carbon fiber, SE can be decreased up to  $-60$  dB for higher frequencies. When studying frequency-dependent behavior, Thermo UM, cement, and lime plaster embody similar behavior with the increase of SE in lower frequencies

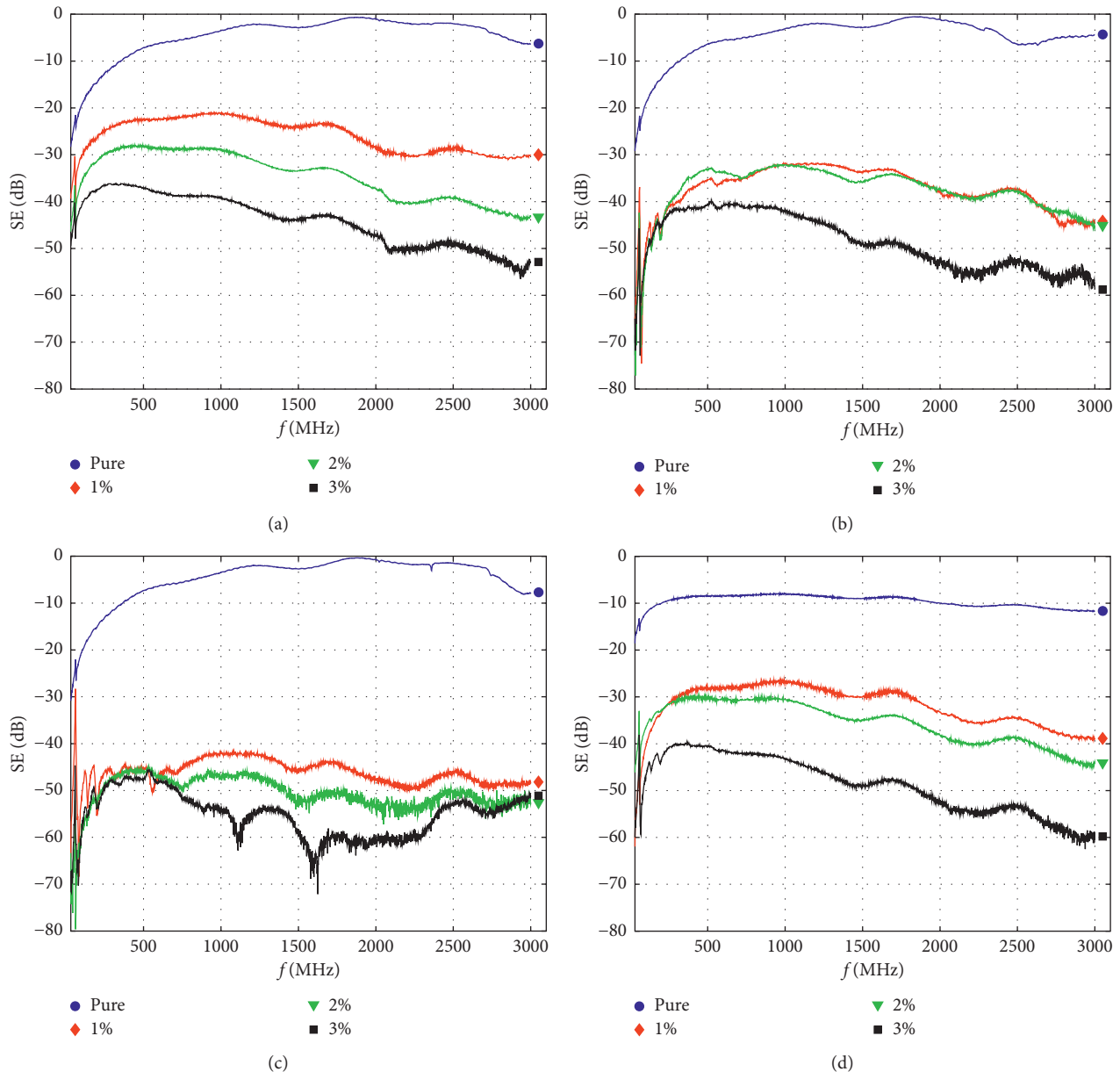


FIGURE 10: Frequency-dependent electromagnetic shielding ability of samples with different carbon fiber contents and different plaster types: (a) Thermo UM, (b) cement, (c) gypsum, and (d) lime.

( $f < 500$  MHz) followed by decrease of SE in a higher frequency range. Gypsum plaster behaves differently having almost constant SE on the whole measured frequency range. In Figure 11, the dependence of SE on carbon fiber weight content for all plaster materials for frequency 1.5 GHz is shown. This frequency was found interesting because many devices use this frequency to operate. It is visible that SE increases with increasing carbon fiber content. Dependence of SE on fiber content can be described using a power function. The solid lines in this graph correspond to the regression models (straight line) with parameters obtained by the minimizing sum of squared errors. High coefficients of determination displayed in the figure indicate the good quality of fit. From this figure, effect of plaster type on SE

can also be studied. All pure plasters have very poor shielding ability ( $SE > -10$  dB), whereas gypsum plaster provides the highest SE ( $SE = 60$  dB at 3 wt.% of carbon fiber) compared to other plasters when conductive fibers are added to the composite structure. On the contrast, Thermo UM plaster has the poorest shielding ability accompanied by the highest SE values ( $SE = 43$  dB at 3 wt.% of carbon fiber). This phenomenon is in agreement with electric properties of plasters, namely, its electric conductivity. Thermo UM plaster is thermally insulating plaster having low thermal conductivity and also very low electric conductivity. Gypsum plaster is known for its hygroscopic behavior, which means that this material can attract and hold water molecules from the surrounding

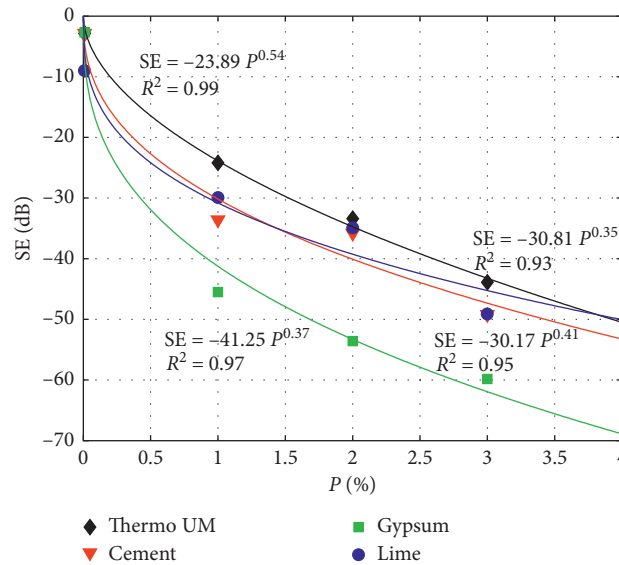


FIGURE 11: The dependence of SE on carbon fiber content  $P$  for all plaster types for frequency 1.5 GHz.

environment, which can cause higher electric conductivity accompanied by greater electromagnetic shielding ability. It is known from theory that shielding effectiveness of material is directly proportional to its electric conductivity, see (14) and (15).

Effect of moisture content on electromagnetic shielding ability of carbon fiber-reinforced plaster-based composites was also studied. It has been found that analyzed moisture content has very low impact on output variable. That is why, only the frequency-dependent SE of samples with 0 and 2% of reinforcement for all plaster types are shown in Figure 12. It is known from theory that increased moisture content increases electric conductivity and also positively influences electromagnetic shielding ability because liquid water has a broad absorption spectrum in the microwave region (300 MHz–300 GHz). It is visible from figures that this effect was not uniquely confirmed. Especially for pure samples, the effect of moisture content is neglectable. Difference in shielding effectiveness of samples with 2% of carbon fiber with different moisture contents was also not statistically significant. The observed phenomenon is presumably caused by very low level of moisture in the structure of composites. To notice the increase of electromagnetic shielding ability, the water content in the sample should be much higher as shown in [10].

## 6. Conclusion

Based on the measured data, it is possible to declare that with increasing content of fibers, the shielding ability of the plaster composites grows significantly. For samples containing 1% of fiber reinforcement, the highest value of the elastic module was measured, and at the same time, it was confirmed that the carbon content had a statistically significant effect on the module. Despite this fact, the content of fibrous reinforcement of more than 3% is less suitable because of arising negative impact to the basic mechanical

properties and their sudden degradation, as could be read in the author's previous articles, for example [23, 25]. Also, when we consider the value of improved shielding properties achieved with 1-2% of carbon content, it is not effective to try to use more dispersion because the obtained benefits will only be small. In the future work, it would be advisable to consider the possibility of optimizing shielding capabilities using not only the conductive fibers (1-2%) but also conductive particles. This method could lead to the maintenance of optimal mechanical properties to increase the electromagnetic shielding. This could be beneficial especially when using the mentioned wasted composite fibers and particles. From the global manufacturing processes of composite materials, there are a lot of waste carbon fibers, which are not possible to be used again. However, their usage as the plaster filling could be a way to use them. Another possibility could be the use of conductive grids.

The content 1-2% of carbon dispersion, which according to Table 5 means shielding group: good–very good, is the most suitable. From the measured results, it is obvious that the sample's inner moisture does not have a major impact on the shielding effect. The only noticeable differences in shielding occurred in lime plaster. The reason could be the ability of the plaster to accept moisture from the surrounding environment and its good vapor permeability.

The numerical simulation has been one of the fundamental parts of the work. The main problem is to define the constitute equations or parameters in the material model because it is really difficult to obtain some of the required constants, and often it was necessary to rely just on the literature. However, the main dependency on the variable dispersion content has been verified. It could be stated that it is possible to predict the trends in shielding properties based on the simulation with sufficient accuracy.

Therefore, it is advisable to measure, calculate, or estimate the frequency of unwanted signals and based on that

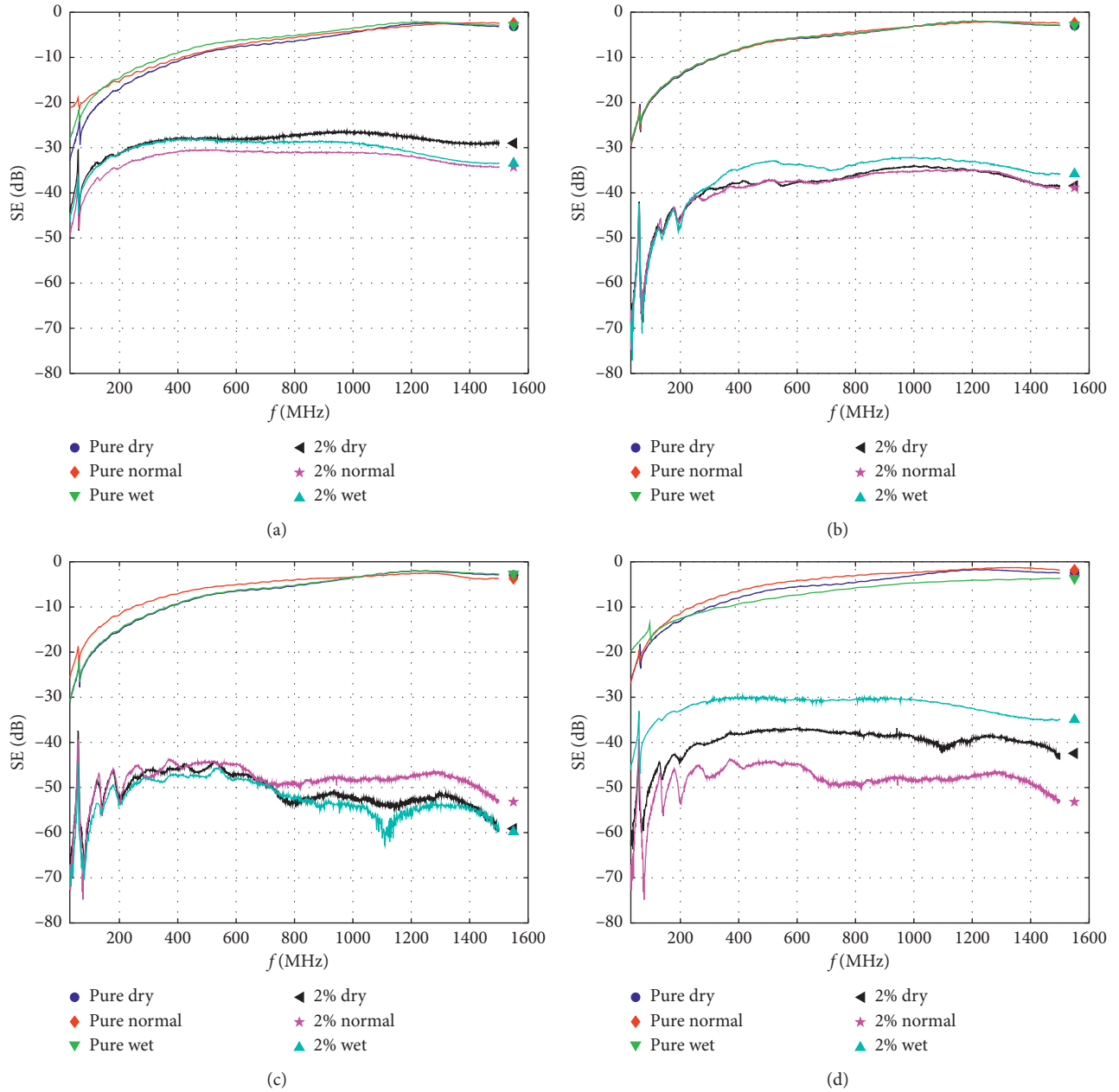


FIGURE 12: Frequency-dependent electromagnetic shielding ability of samples with different moisture content: (a) Thermo UM, (b) cement, (c) gypsum, and (d) lime.

TABLE 5: Classes for professional use [42].

Grade	5, excellent	4, very good	3, good	2, moderate	1, fair
Electromagnetic effectiveness range	SE > 60 dB	60 dB ≥ SE > 50 dB	50 dB ≥ SE > 40 dB	40 dB ≥ SE > 30 dB	30 dB ≥ SE > 20 dB

choose the shielding material and thickness of the enclosure, before designing the main shielding element. It is possible to state that at lower frequencies, the reflection of the waves prevails, whereas the absorption effect increases at higher frequencies. Therefore, the conductive nonmagnetic materials are suitable for reflection, and the thickness of the shielding layer is not a critical parameter. This finding corresponds with

the probably most common example of electromagnetic shielding in microwave ovens, where just a thin transparent conductive film on the door provides sufficient protection.

The future of our work should be based on the numerical modeling with the use of numerical optimization in order to set the optimal length and content of fibers and thickness of the base materials.



## Data Availability

The data used to support the findings of this study are available from the corresponding author upon request.

## Conflicts of Interest

The authors declare that they have no conflicts of interest.

## Acknowledgments

This publication was written at the Technical University of Liberec as part of the project “Assessment of change physical behavior of plaster reinforced by fibre material” (21252) with the support of the Specific University Research Grant, as provided by the Ministry of Education, Youth and Sports of the Czech Republic in the year 2017, and the results of this project (LO1201) were obtained with cofunding from the Ministry of Education, Youth and Sports as part of targeted support from the “Národní program udržitelnosti I” program.

## References

- [1] A. Zamania and C. Hardiman, “Electromagnetic radiation and human health, a review of sources and effects,” *High Frequency Electronics Summit Technical Media*, vol. 4, no. 7, pp. 16–25, 2005.
- [2] World Health Organization, *Establishing a Dialogue on Risks from Electromagnetic Fields*, WHO, Geneva, Switzerland, 2002.
- [3] Agriculture and Local and Regional Affairs, *The Potential Dangers of Electromagnetic Fields and Their Effect on the Environment*, Committee on the Environment, Strasbourg, France, 2011.
- [4] J. F. B. Bolte and M. J. M. Pruppers, *Electromagnetic Fields in the Working Environment*, Netherlands Ministry of Social Affairs and Employment, Hague, Netherlands, 2006.
- [5] H. W. Ott, *Electromagnetic Compatibility Engineering*, John Wiley & Sons, Hoboken, NJ, USA, 2009.
- [6] M. S. Ersoy and E. Onder, “Electroless silver coating on glass stitched fabrics for electromagnetic shielding applications,” *Textile Research Journal*, vol. 84, no. 19, pp. 2103–2114, 2014.
- [7] A. Ali, V. Baheti, J. Militky et al., “Copper coated multi-functional cotton fabrics,” *Journal of Industrial Textiles*, 2017, In press.
- [8] R. Guo, X. Jing, L. Peng et al., “Nickel-catalyzed deposition of Cu film on PET fabric with supercritical fluid,” *Journal of Materials Science: Materials in Electronics*, vol. 28, no. 22, pp. 16618–16626, 2017.
- [9] I. Su and J. T. Chern, “Effect of stainless steel-containing fabrics on electromagnetic shielding effectiveness,” *Textile Research Journal*, vol. 74, no. 1, pp. 51–54, 2004.
- [10] V. Safarova and J. Militky, “Multifunctional metal composite textile shields against electromagnetic radiation—effect of various parameters on electromagnetic shielding effectiveness,” *Polymer Composites*, vol. 38, no. 2, pp. 309–323, 2017.
- [11] S. I. Mistik, E. Sancak, S. Ovali et al., “Investigation of electromagnetic shielding of boron, carbon and boron-carbon fibre hybrid woven fabric and their polymer composites,” *Journal of Electromagnetic Waves and Applications*, vol. 31, no. 13, pp. 1289–1303, 2017.
- [12] J. M. Keith, N. B. Janda, and J. A. King, “Shielding effectiveness density theory for carbon fiber/nylon 6,6 composites,” *Polymer Composites*, vol. 26, no. 5, pp. 671–678, 2005.
- [13] J. M. Thomassin, C. Jerome, T. Pardoën et al., “Polymer/carbon based composites as electromagnetic interference (EMI) shielding materials,” *Materials Science and Engineering*, vol. 74, no. 7, pp. 211–232, 2013.
- [14] B. Saravanja, K. Malric, T. Pusic et al., “Impact of dry cleaning on the electromagnetic shield characteristics of interlining fabric,” *Fibres and Textiles in Eastern Europe*, vol. 23, no. 1, pp. 104–108, 2015.
- [15] A. Asghar, M. R. Ahmad, M. F. Yahya et al., “An alternative approach to design conductive hybrid cover yarns for effective electromagnetic shielding fabrics,” *Journal of Industrial Textiles*, vol. 48, no. 1, pp. 38–57, 2017.
- [16] S. Palanisamy, V. Tunakova, D. Karthik et al., “Study on textile comfort properties of polypropylene blended stainless steel woven fabric for the application of electromagnetic shielding effectiveness,” *IOP Conference Series: Materials Science and Engineering*, vol. 254, no. 7, article 072018, 2017.
- [17] V. Tunakova, Z. Hrubosova, M. Tunak et al., “Laser surface modification of electrically conductive fabrics: material performance improvement and design effects,” *Optics and Laser Technology*, vol. 98, pp. 178–189, 2018.
- [18] G. E. Monfore, *The Electrical Resistivity of Concrete*, Portland Cement Association, New York, NY, USA, 1968.
- [19] B. Wang, Z. Guo, Y. Han, and T. Zhang, “Electromagnetic wave absorption properties of multi-walled carbon nanotube/cement composites,” *Construction and Building Materials*, vol. 46, pp. 98–103, 2013.
- [20] D. Yawen, S. Mingqing, L. Chenguo et al., “Electromagnetic wave absorbing characteristics of carbon black cement-based composites,” *Cement and Concrete Composites*, vol. 32, no. 7, pp. 508–513, 2017.
- [21] R. Khushnood, S. Ahmad, P. Savi, J. Tulliani, M. Giorcelli, and G. A. Ferro, “Improvement in electromagnetic interference shielding effectiveness of cement composites using carbonaceous nano/micro inerts,” *Construction and Building Materials*, vol. 85, pp. 208–216, 2015.
- [22] P. K. Mallick, *Fiber-Reinforced Composites: Materials, Manufacturing, and Design*, CRC Press, Boca Raton, FL, USA, 2007.
- [23] A. Samkova, P. Kulhavy, and M. Pechociakova, “Optimization parameters of plaster composites,” in *Proceedings of the 54th International Conference on Experimental Stress Analysis*, Pilsen, Czech Republic, June 2016.
- [24] C. Bing, W. Ker, and Y. Wu, “Conductivity of carbon fiber reinforced cement-based composites,” *Cement and Concrete Composites*, vol. 26, no. 4, pp. 291–297, 2004.
- [25] A. Samkova, P. Kulhavy, and M. Pechociakova, “Fibre reinforcement effect on plaster composite properties,” in *NART Conference Proceedings*, pp. 189–195, Liberec, Czech Republic, August 2015.
- [26] A. Samková, P. Kulhavy, and M. Pechočiaková, “Possibilities to improve electromagnetic shielding of plaster composites adding carbon fibers,” *IOP Conference Series: Materials Science and Engineering*, vol. 254, no. 4, 2017.
- [27] Standard ČSN EN 1015-14, *Methods of Test for Mortar for Masonry-Part*, Czech Standards Institute, Prague, Czech Republic, 2000.
- [28] *Material and Technical List of the Manufacturer: SATSYS*, <https://www.maxit.de/produkte/putzl/>.

- [29] D. A. Kontogeorgos and M. A. Founti, "Gypsum board reaction kinetics at elevated temperatures," *Thermochimica Acta*, vol. 529, pp. 6–13, 2012.
- [30] S. L. Manzello, R. G. Gann, S. R. Kukuck, and B. L. David, "Influence of gypsum board type (X or C) on real fire performance of partition assemblies," *Fire and Materials*, vol. 31, no. 7, pp. 425–442, 2007.
- [31] P. Kulhavy, T. Martinec, O. Novak, M. Petru, and S. Pavel, "Testing fireproof materials in a combustion chamber," *EPJ Web of Conferences*, vol. 143, article 02058, 2017.
- [32] M. Bentchikou, A. Guidoum, K. Scrivener, K. Silhadi, and S. Hanini, "Effect of recycled cellulose fibres on the properties of lightweight cement composite matrix," *Construction and Building Materials*, vol. 34, pp. 451–456, 2012.
- [33] *Material and Technical List of the Manufacturer: MAXIT PUTZ*, <https://www.maxit.de/produkte/putz/>.
- [34] S. Chand, "Carbon fibers for composites," *Journal of Materials Science*, vol. 35, 2000.
- [35] R. W. Cahn and B. Harris, *Newer Forms of Carbon and Their Uses*, University of Sussex, Brighton, UK, 1969.
- [36] E. Fitzer and L. M. Manocha, *Carbon Reinforcements and Carbon/Carbon Composites*, Springer-Verlag, Berlin, Heidelberg, Germany, 1998.
- [37] M. Mardiguian, *Controlling Radiated Emissions by Design*, Springer, Berlin, Germany, 2014.
- [38] P. A. Chatterton and M. A. Houlden, *EMC-Electromagnetic Theory to Practical Design*, John Wiley & Sons, Hoboken, NJ, USA, 1992.
- [39] Standard ASTM D4935–10, *Test Method for Measuring the Electromagnetic Shielding Effectiveness of Planar Materials*, ASTM International, West Conshohocken, PA, USA, 2010.
- [40] A. V. Raisanen and A. Lehto, *Radio Engineering for Wireless Communication and Sensor Applications*, Artech House, London, UK, 2003.
- [41] V. Šafářová, M. Tunák, and J. Militký, "Prediction of hybrid woven fabric electromagnetic shielding effectiveness," *Textile Research Journal*, vol. 85, no. 7, pp. 673–686, 2015.
- [42] Committee for Conformity Assessment on Accreditation and Certification of Functional and Technical Textiles, *Specified Requirements of Electromagnetic Shielding Textiles*, 2010, <http://www.ftts.org.tw/images/fa003E.pdf>.

## Research Article

# Improvement of the Acoustic Attenuation of Plaster Composites by the Addition of Short-Fibre Reinforcement

P. Kulhavý <sup>1</sup>, A. Samková <sup>2</sup>, M. Petru <sup>1</sup> and M. Pechociakova <sup>2</sup>

<sup>1</sup>*Institute for Nanomaterials, Advanced Technologies and Innovation, Technical University of Liberec, Studentska 2, 461 17, Liberec, Czech Republic*

<sup>2</sup>*Faculty of Textile Engineering, Technical University of Liberec, Studentska 2, 461 17, Liberec, Czech Republic*

Correspondence should be addressed to P. Kulhavý; petr.kulhavy@tul.cz

Received 5 January 2018; Revised 31 March 2018; Accepted 16 April 2018; Published 16 May 2018

Academic Editor: Bing Zhang

Copyright © 2018 P. Kulhavý et al. This is an open access article distributed under the Creative Commons Attribution License, which permits unrestricted use, distribution, and reproduction in any medium, provided the original work is properly cited.

Noise attenuation is a key contemporary issue associated with the protection of human health. In this study, the possibilities of affecting acoustic properties of plaster composites by the addition of short-fibre reinforcement are described. The improvement of attenuation abilities was first verified using a simple numerical model with a pure plaster followed by using a reinforced plaster. The model results revealed a mutual correlation between the fibre ratio and dissipated acoustic energy. Hence, typical plasters used in the building industry (e.g., plaster, lime cement, and cement) are used as the base materials of the tested composites. The reinforcing dispersion in the form of short fibres (basalt and glass) with a defined length was selected after evidence from previously reported studies and after the comparison of some other fibres with respect to the trade-off between the rendered mechanical properties and cost. Transfer functions of the tested samples were measured using an impedance tube with two microphones, followed by the calculation of the total acoustic absorption. On the other hand, cement and plaster materials exhibited a low damping ability, and the absorption could be considerably increased by the addition of fibres, especially in the area around 1 kHz. In contrast, the UM plaster exhibited good damping properties even without the dispersion, and the addition of improper fibres such as glass ones possibly worsened the properties. The acoustic attenuation of the plaster composites can be improved by the appropriate combination of the base material and fibre dispersion. However, it is not possible to generalise this improvement for all possible combinations.

## 1. Introduction

Currently, the enormous technological development could be observed in a lot of everyday life sectors such as transport and other industries. In addition, this phenomenon exerts some negative effects, one of them being the increasing noise levels. The increase in industrialisation and transport technologies has led to a rapidly increasing number of people being affected by residing in an extremely noisy environment. Several detailed physiological and hygienic studies have revealed that noise is one of the most widespread harmful factors not only in workplaces, but also in everyday life [1]. Long-term, frequent exposure to noise affect not only the mental state (e.g., tiredness or concentration ability), but also the overall health of the human

beings, as well as cause some irreversible harm. Hence, it is crucial to protect human beings by decreasing noise levels [1, 2]. Issues associated with noise in such environments are constantly increasing; therefore, common people, employers, and employees require their homes and working places to be protected [3]. Requirements related to this issue are reflected in the directives and regulations, and the European Union also recognises environmental noise as one of the most important environmental issues. Because of this fact, laws regulating noise levels are valid in several countries [4]. Noise reduction should be conceptually solved with regard to the interactive approach, especially with respect to the noise source and its surroundings. Despite the fact that passive measures, such as wall cladding panels with porous materials and resonators, address only the consequences but

not the main causes of noise, these factors are often the only possible and viable solution. The ability of building materials to absorb sound waves typically depends on their stiffness, density, and porosity [5–7]. The function of the absorption coefficient exists in order to quantify the ability of materials to absorb sound waves at a specific frequency. When sound reaches a specific part, it dissipates, passes through, or reflects depending on the physical properties and microstructure of materials [8]. Therefore, parts such as walls and roofs of buildings, which constitute the main parts of a residential or industrial object require materials with a high absorption coefficient such as wool glass, foam, mineral wools, or their composites [9]. Currently, various products such as chopped fibres, grids, steel truss, rovings, and veils can improve the mechanical and acoustic properties of the main building materials. Pedreño-Rojas et al. have added some recycled wood to the gypsum matrix [10]. Their experiments revealed that by increasing the percentage of the added wood waste, the mass of the new material decreases while simultaneously improving its thermal and sound absorption properties. Their group has revealed that the best results (with respect to the acoustic and mechanical properties) are achieved by the addition of up to 10%–20% of wood shavings or sawdust composites.

Generally, the mechanical and physical properties of typically used construction materials (fired and silicate bricks, bricks, concrete, aerated concrete, steel-reinforced concrete, glass wool, and polystyrene) have been extensively investigated. However, the materials used in this sector are often produced from nonrenewable natural resources, and the production of these materials adversely affects the environment [11, 12]. Hence, in recent years, increased efforts to use materials, including some typical natural materials such as flax, hemp, wood, straw, reeds, and others that can reduce the negative impact on the environment have been observed. Typically, flax and hemp fibres are used to insulate buildings. Wood and wood sawdust can be used on walls and as a filler for building materials, respectively. Another well-known conventional method is to use reed bundles as roofing and straw in combination with clay for wall filling and reinforcement [13]. Randazzo et al. [14] have tested some commercially available clay plasters typically used in Europe for exploring the manner in which mineralogical and textural properties can affect their physical parameters; that is moisture absorption, thermal conductivity, and noise attenuation. Results obtained from the tests revealed that the addition of natural fibres slightly increases the open porosity; hence, because of its relatively higher pore volume, the obtained final sound absorption is possibly higher.

Porosity considerably affected the material's ability to absorb sound waves. The principle is mainly caused by different resistivities of individual materials (such as solid and air) and phenomena occurring at their mutual interfaces. Generally, several routes of energy dissipation simultaneously occur, that is, reflection at the boundaries, deflection caused by different speeds of sound propagation in individual materials, and friction of air on the walls in micropores. Pore size can be categorised at different scales (i.e., micropores, interparticle pores, and mesopores). Cannabis

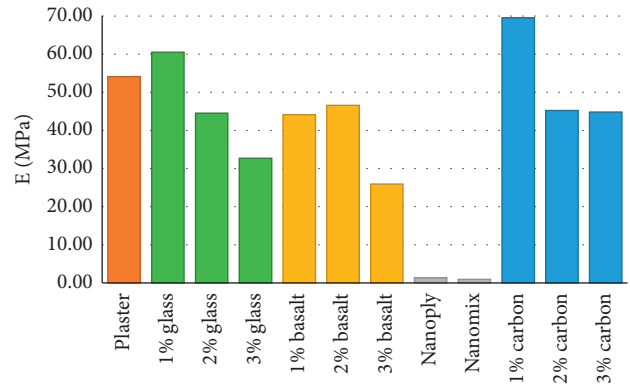


FIGURE 1: Comparison of Young's modulus of the Thermo UM lime-cement plaster with various types of reinforcement.

and lime-based composites exhibit one of the highest porosities (70%–80%) [15]. Gle et al. [16] have extensively examined the acoustic benefits observed with the use of cannabis composites. This study revealed that the level of sound absorption in hemp-reinforced concrete can be controlled and significantly increased using suitable components with specified manufacturing processes.

As has been previously mentioned, fibrous materials are typically added to building materials as a reinforcing element to modify their mechanical properties, such as tensile strength, compressive strength, or impact strength. Previous studies [17] have reported significant improvement in the main mechanical properties of plaster composites by the addition of an appropriate volume ratio of fibres (1%–2% of reinforcement). Glass and basalt fibres were used as the reinforcing elements. Similar issues have been reported by Blankenhorn and Soroushian [18, 19] with focus on cellulose-cement composites. Neithalath et al. [20] have investigated the effects of natural fibre reinforcement to the morphological changes in acoustic and mechanical properties. The results obtained from their study clearly revealed the increasing dependence of the acoustic absorption coefficient on the fibre volume. In other independent studies reported by Kalinova and Mohrova [21, 22], the use of nanofiber structures as sound-absorbing elements and nanomembranes as resonators has been described.

Experimental studies have reported improvement in the acoustic, thermal, and mechanical properties of plasters by the addition of short-fibre cellulose [20, 23] or polypropylene [24] as reinforcement. However, according to [24], the improvement of the aforementioned properties by fiber count is questionable.

This study focuses on the sound attenuation characteristics in plaster composites. Three typical plasters (viz., gypsum, lime cement, and cement, resp.) were reinforced with glass and basalt fibres, and impedance tube measurements were carried out.

## 2. Materials and Methods

Typical plaster and cement plaster were completed with lime-cement plaster that exhibits enhanced thermoinsulating

TABLE 1: Mechanical properties of the base materials.

Material	Length (mm)	Diameter ( $\mu\text{m}$ )	Density ( $\text{kg m}^{-3}$ )	E (GPa)	$\mu$ (-)
Basalt fibre	7.7	13	2650	110	0.26
Glass fibre	12	14	2600	76	0.22
Thermo UM	—	—	551	5.4	0.18
Gypsum	—	—	1100	14	0.27
Cement	—	—	3020	39	0.2

properties (Thermo UM); these plaster materials are typically suitable for the central European climate, which can be possibly prepared even under laboratory conditions, without the requirement of any specific machinery. Furthermore, plasters such as gravel, perlite, mineral, or stucco plaster are also available in the market. Flass, carbon, basalt fibres, and even some nanofibrous dispersions were used as reinforcing elements for composites. In previously reported papers by the authors of this study [17], all possible combinations of typical plasters and fibre reinforcements have been investigated with respect to their mechanical properties (Figure 1). The results revealed that when using a suitable mass ratio (1%–2% of fibre reinforcement), the mechanical properties (flexural or tensile strength, compressive strength, and impact strength) of the plaster composites possibly improved significantly [17]. Based on those results, three plasters and two fibre reinforcement materials, the mechanical properties of which can be improved, or at least not worsened, were selected for their acoustic attenuation. Although the carbon fibres should be considered on the basis of the obtained mechanical properties, the fibres were not included for additional tests because the cost of the dispersion was greater than that of the base plaster material. Table 1 summarises the fundamental mechanical properties of the base materials.

Similar to that carried out during the initial verification of the model, the pure plaster without any fibre dispersion was investigated. The second set of samples contained 7.7 mm-long basalt fibres with a diameter of 13  $\mu\text{m}$ . The final sets were created from alkalisied glass fibre with a length of 12 mm and a diameter of 14  $\mu\text{m}$ . The fibre length was selected on the basis of the determined critical length of the individual types of fibre dispersion [25].

*2.1. Basic Theory for the Study of Acoustic Quantities.* The mechanical oscillation of liquid, solid, or gas particles spread as waves called sound, which is always connected to energy transfer. Pressure oscillations in the surroundings, typically gaseous environment, can produce acoustic field or just generally the sound. These pressure changes are caused by the oscillation of the cover surfaces of individual parts or entire systems. When considering noise in a structure, subjective noise perception must be considered, particularly in an urban environment [26]. Sound field is described by changes in steady-state variables, such as pressure, speed, temperature, and density, which describes the state of the environment in which sound spreads. The actual sound velocity  $c$ , which depends on the modulus of elasticity  $E$  and the density of the material  $\rho$ , is determined by the spreading velocity of the longitudinal waves in an unbounded space

according to (1). Energy dissipation occurs because of the absorption of sound by the material; therefore, the velocity potential  $\phi$ , where the velocity is equal to the negative velocity gradient (2), could be introduced. The speed potential permits the definition of sound pressure  $p$  according to (3). The specific mechanical impedance  $Z$  (4) can be used to quantify the sound transfer between the two materials as the ratio of the passing and impacting energy. To understand the basics of sound propagation and attenuation, it is possible to use the basic assumptions that can be well characterised by a simplified 1D structure as mentioned in references [26, 27]. Considering a 1D structure in which some planar or longitudinal wave spreads, this phenomenon is associated with structural deformation. Then, the ratio between the passing energy and the incident energy can be expressed as the ratio between the through and incident wave intensities, according to (5). Based on this assumption, transfer attenuation (6) can be defined using the transfer coefficient (5). An example involves the steel-aluminium combination when it is possible to obtain a transmission attenuation coefficient of only 1.6 dB. On the other hand, for steel PVC, the attenuation could reach up to 14 dB [26]. By simplifying the problem according to (5) and (6) where some factors of the acoustic system were neglected, it is possible to obtain the corresponding mathematical expression that can be used to optimise the intensity of the passing waves.

$$c = \sqrt{\frac{E}{\rho}}, \quad (1)$$

$$c = -\nabla\phi, \quad (2)$$

$$p = \rho \left[ \frac{\partial\phi}{\partial t} - \frac{1}{2} \left( \frac{\partial\phi}{\partial x} \right)^2 \right], \quad (3)$$

$$Z = \rho \cdot c, \quad (4)$$

$$d = \frac{4Z_i Z_j}{(Z_i + Z_j)^2}, \quad (5)$$

$$D = 10 \log \frac{1}{d}, \quad (6)$$

where  $Z_i$  and  $Z_j$  represent  $i$  and  $j$ -materials, respectively.

The final attenuation is attributed to the combination of different damping properties of individual materials. Therefore, for modelling and describing the attenuation, it is crucial to introduce the complex dynamic modulus  $\tilde{E}$  (7), where the inner damping coefficient  $\eta$  of materials can be

TABLE 2: Typical physical properties of typical materials [26, 27].

Material	Density ( $\text{kg m}^{-3}$ )	E (Pa)	$c$ ( $\text{m s}^{-1}$ )	Z ( $\text{N}\cdot\text{s}\cdot\text{m}^{-3}$ )	Absorption (-)
Air	1.21	—	344	$4.14 \times 10^2$	—
Rubber	900	$4.4 \times 10^4$	70	$6.3 \times 10^4$	0.02–1
Concrete	2300	$1.0 \times 10^{10}$	3100	$7.1 \times 10^6$	0.007
Aerated concrete	900	$2.9 \times 10^9$	1800	$1.6 \times 10^6$	0.005–0.012
Bricks	2000	$1.6 \times 10^{10}$	2800	$5.6 \times 10^6$	0.009–0.1
Wood	650	$1.0 \times 10^{10}$	3900	$2.5 \times 10^6$	0.015
Aluminium	2700	$6.2 \times 10^{10}$	4800	$1.3 \times 10^7$	$7.1 \times 10^{-10}$
Steel	7850	$2.6 \times 10^{11}$	5750	$4.5 \times 10^7$	$1.1 \times 10^{-4}$

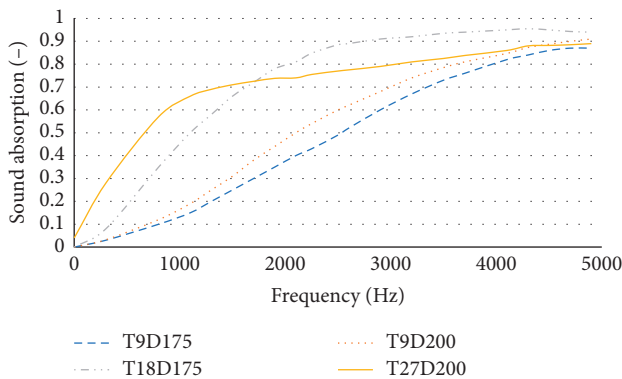


FIGURE 2: Results from the absorption coefficient of basalt layers from the study by Moretti et al. [30].

defined by relation (8). Table 2 summarises the internal damping coefficients of several selected materials. Extremely dense materials that reflect 100% sound exhibit a sound absorption coefficient equal to 0 [28].

$$\tilde{E} = E(1 + i\eta), \quad (7)$$

$$\eta = \frac{I_m\{\tilde{E}\}}{R_e\{\tilde{E}\}}, \quad (8)$$

The sound absorption of plasters at a frequency of 1000 Hz is 0.02–0.05 [29]. The absorption coefficient of the fibrous layers is affected by the thickness and density of these layers. Moretti et al. [30] have tested basalt layers of different thicknesses and densities. From the results obtained (Figure 2), fibrous layers exhibit an extremely good absorption coefficient, especially at high frequencies. Figure 2 shows sound absorption properties for some chosen fibres with a layer thickness  $T$  of 9, 18, and 27 mm and densities  $D$  of 175 and 200  $\text{kg}\cdot\text{m}^{-3}$ , which is taken from the study by Moretti et al. [30]. In particular, at low frequencies, sound absorption depends on the fibre thickness.

Wang and Torng have also carried out a similar study [31] in which the absorption characteristics of porous materials reinforced with glass and basalt fibres were investigated. The 50 mm-thick glass fibre layer with a bulk density of  $100 \text{ kg}\cdot\text{m}^{-3}$  exhibits an absorption coefficient of 0.82. The basalt layer with the same thickness and bulk density exhibits an absorption coefficient of 0.9. Their results revealed that both fibres exhibit similar sound absorption.

**2.2. Plaster.** Plasters are mainly categorised according to the binder used. The binder ensures adhesion to the masonry as well as plaster strength and durability (the ability to withstand environmental impacts). The plaster is formed after hardening of the mortar mixture.

The first of the plasters selected herein was lime cement with enhanced thermal insulation properties, that is, Thermo UM. Another significant feature of this material is low bulk density compared to typically used plasters: This plaster is 4 times lighter. Because of its low bulk density and low modulus of elasticity, the plaster eliminates volume or shape changes in the base wall material, thereby not creating any cracks. Thermo UM plaster is characterised by a high thermal conductivity coefficient and the plaster's chemical composition eliminates microbial, algal, and fungal growth on its surface [32].

Another plaster, referred to as gypsum plaster, is a typically cheaper material. It exhibits good thermal insulation and acoustic attenuation. Owing to its thermal properties, the plaster is thought to be a hygroscopic material, which permits the regulation of the room microclimate [33, 34]. Vapour can permeate into the plaster and does not close the water in the construction while simultaneously permitting the natural drying of residual water from the blocks. Gypsum plaster is suitable for antibacterial environment because its smooth surface prevents dust from settling on it. At high temperatures, water vapour is released by gypsum, which is typically used to increase fire resistance [35].

The last plaster, which is referred to as cement plaster, is designed for highly loaded areas; it exhibits increased strength, water resistance, and adhesion to the base substrate, as well as frost and weather resistance.

**2.3. Fibre Types and Proportion.** In this study, short glass and basalt fibres were used as dispersion elements. Such fibres are typically used in the building industry particularly because of the cost-effectiveness as well as acoustic and thermal insulation properties.

Basalt is typically formed by decompression melting in the Earth's upper mantle. This rock is made up of different species such as pyroxene, magnetite, olivine, and plagioclase [36]. The basic technological condition for selecting optimal kind of basalt for producing fibres is the so-called acidity factor  $M_k$  (9). Militky [37] has reported that the acidity factor ranges from 1.1 to 3. The most appropriate technological condition for producing fibres is at  $M_k = 1.65$ .

$$M_k = \frac{\text{SiO}_2 + \text{Al}_2\text{O}_3}{\text{CaO} + \text{MgO}}. \quad (9)$$

The selection of basalt rocks for producing fibres is affected not only by the chemical and mineralogical composition, but also by the rock texture [38]. The resulting quality of fibres is affected by the level of technological equipment and the entire technological production process. Moretti et al. [30] have developed a mineral fibre acoustic absorption panel for a highly efficient power system in buildings. The results of their application revealed extremely good acoustic and thermal properties for these panels. The additional advantage is chemical stability, low thickness, and considerable mechanical strength.

Compared to glass, basalt fibres are more stable in a strongly alkaline environment, but in a strongly acidic environment, the fibres exhibit lower stability [39]. The glass fibre base comprises tetrahedrons ( $\text{SiO}_4$ )<sup>4-</sup> and contains different oxides. The individual types of glass fibres can be distributed according to their oxide content. For producing fibres, not only glass stones, but also different processed glass metaproducts such as glass beads, rods, frits, or waste glass shards were used. The base glass composition significantly affects the properties of the resulting fibres [40].

One of the most frequently declared fibre parameters is their linear mass density  $t$  (10):

$$t [\text{tex}] = \frac{m}{l} = \frac{sl\rho}{l} = s\rho, \quad (10)$$

where  $m$  is the mass (g),  $l$  is the length (km),  $s$  is equivalent to the fibre diameter ( $\mu\text{m}$ ), and  $\rho$  is the fibre density ( $\text{kg}/\text{m}^3$ ).

The  $d$  value can also be calculated according to (11) for noncircular cross sections. Then,  $d$  is called the equivalent fibre diameter.

$$d = \sqrt{\frac{4S}{\pi}} = \sqrt{\frac{4t}{\pi\rho}}. \quad (11)$$

**2.4. Porosity.** With respect to the sound attenuation and thermal insulation purposes, the porosity of the resulting part of the fibre-filled materials is crucial compared to the basic physical properties. The porosity  $\psi$  (12) represents the proportion of the fibre structure that is filled with air. As has been already mentioned, the sound absorption mechanism depends on the amount and mutual bonding of the pores inside the material. Good sound-absorbing materials contain interconnected pores, which enable further sound propagation and permit air flow under acoustic oscillation. Hence, the first principle of acoustic energy dissipation caused by friction is used. To express pore volume, an analogy based on the determination of porosity in thick nonwoven formations has been used. This idea could be valid on the basis of the assumption [41] that the fibre surface is approximately equal to the pore surface. This method is probably not the most suitable one, and direct measurement

based on some screening methods can be used to possibly set statistically more precise results, but only to estimate porosity, sufficiently precise results should be obtained:

$$\psi = \frac{V_c - V - V_p}{V_c}, \quad (12)$$

where  $V_c$  is the total volume of the body,  $V_p$  is the pore volume, and  $V$  is the fibre volume.

As the same volume of air may be found in a few large pores or in a number of small pores, the median pore size  $\xi$  is determined:

$$\xi = \frac{V_p}{A_p}, \quad (13)$$

where  $A_p$  is the pore area.

$V_p$  (or simply the air volume) in fibre formation can be calculated as follows:

$$V_p = V_c - V. \quad (14)$$

An important prerequisite according to reference [41] is that where the fibre ends, the air around it begins. Thus, the fibre surface is also the pore surface. Based on this assumption, the pore surface  $A_p$  can be obtained from

$$A_p = A = L \times p, \quad (15)$$

where  $A$  is the fibre surface,  $L$  is the total length of all fibres in the fibrous structure, and  $p$  is the cross-sectional circumference of the fibre.

The shape of the interfacial pores is complicated; hence, the interfibrillar pores are considered to be shaped as capillaries. The pores can be imagined as air fibres, and then their surface can be calculated as follows:

$$A_p = L_p \pi d_p (1 + q_p), \quad (16)$$

where  $L_p$  is the length of the pore capillaries in the fibrous form,  $d_p$  is the equivalent pore diameter, and  $q_p$  is the pore shape factor, which is defined as

$$q_p = \frac{p}{\pi d_p} - 1. \quad (17)$$

Because the geometric characteristics  $\xi$  (13) depend on the pore shape, it is possible to use the simple assumption that the shape of the pores is still the same. Therefore, for the pore shape factor, it is possible to set  $q_p = \text{constant}$  and fibre shape factor  $q = \text{constant}$  and hence

$$\frac{1 + q_p}{1 + q} = k. \quad (18)$$

Subsequently, pore volume (19) can then be expressed as follows:

$$V_p = \frac{\pi d_p^2}{4} L_p. \quad (19)$$

Figure 3 shows the ratio of pores in the studied samples determined by the aforementioned method.

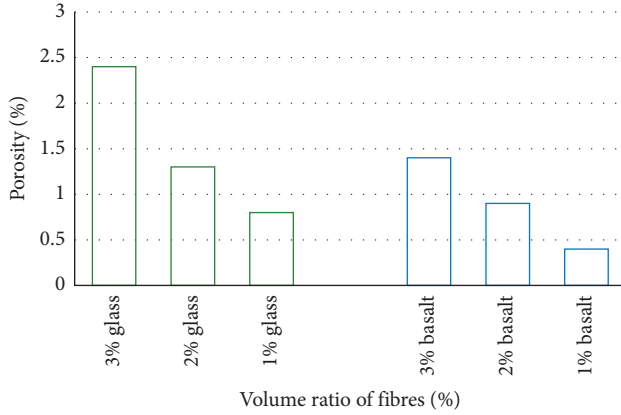


FIGURE 3: Porosity of materials with the specified fibre volume ratio.

**2.5. Sample Preparation and Testing.** Typically, 6% of the fibre reinforcement is used in concrete materials. However, blending the plaster and fibres with such a high content can cause some problems in their bonding. The fibre reinforcement content in this experiment was 1% (Figure 3 and Table 3) because the optimal improvement of mechanical properties as has been reported in a previous study in which the glass and basalt filaments were used as the reinforcing elements was observed at weight ratios of 1%, 2%, and 3% [17]. The calculation of the mixing ratio (20) is based on the percentage of the components in the composite and their densities:

$$w_i = \frac{V_i \cdot \rho_i}{\sum V_i \rho_i}, \quad (20)$$

where  $w_i$  (%) is the mass fraction of the  $i$ th component,  $V_i$  (%) is the volume fraction of the  $i$ th component, and  $\rho_i$  ( $\text{kg}\cdot\text{m}^{-3}$ ) is the density of the  $i$ th component.

Experimental samples (Figure 4) were created in circular releasable moulds with a diameter 99.8 mm (required for an impedance tube inner diameter of 100 mm at the tolerance field K7) and a thickness of 10 mm.

Figure 5 shows the microscopic pictures of all combinations of plaster and fibre. The legend of Table 4 provides an overview of the photograph and material combination.

**2.6. Experimental Measurement and Modelling.** Basically, the improvement of the acoustic absorption was first verified by the addition of fibres using a simple numerical model simulating the passage of sound waves through the plaster as well as fibre-reinforced plaster. Even if the first simplified model of inner porosity and all necessary mechanical properties were not precise, the simulation revealed that the principle should work in theory. This is a model of acoustic absorption using a porous acoustic open cell sample. In porous materials, sound propagates in a network of small interconnected pores. Because of small pore dimensions, losses occur particularly because of thermal conduction and viscous friction. This model aims to characterise the absorption properties, more specifically, the specific surface

TABLE 3: Volume fraction of the individual components.

Volume fraction, $V_i$ 1%	Mass fraction (%) of glass fibres	Basalt fibres
Thermo UM	4.38	5.05
Gypsum	2.15	2.49
Cement	0.83	0.96

impedance and absorption coefficient in terms of sound incidence angle and frequency. The model uses a 2D geometry of such a system. The models were created in COMSOL. Base models of the samples (plaster Thermo UM, gypsum, and cement) were created using the Pressure Acoustics user interface with a rigid Biot equivalent fluid model [42, 43]. The surrounding fluid is air, and the incident pressure  $p_{\text{inp}}$  is expressed as shown in the following equation:

$$p_{\text{inp}} = e^{-i(kx)}, \quad (21)$$

$$k = k_0 (\sin \theta, \cos \theta),$$

where  $\theta$  and  $k_0$  are the incidence angle and wavenumber in the free field (air domain), respectively. The pressure  $p$  solved in this model is the total field, and the scattered field  $p_{\text{scat}}$  is expressed as  $p_{\text{scat}} = p - p_{\text{inp}}$ . Notably, this expression for the scattered field is only valid in the air domain as the incident field is not known a priori for porous materials. Two parameters that characterise the absorption properties of the porous absorber are the specific surface impedance  $Z$  and the absorption coefficient  $\alpha$  (Table 1). The absorption coefficient, which represents the ratio of the absorbed and incident energy, is defined as follows:

$$\alpha = 1 - |R|^2; \quad (22)$$

$$R = \frac{p_{\text{scat}}}{p_{\text{inp}}},$$

where  $R$  is the pressure reflection coefficient that expresses the ratio of the scattered to the incident pressure.

Subsequently, geometric dimensions (sample diameter  $D = 100$  mm and sample thickness = 10 mm) and material properties of the sample were determined and maintained constant (porosity, speed of sound, dynamic viscosity, thermal conductivity, and density). The modelled frequencies range from 100 Hz to 1.2 kHz at a minimal wavelength of 0.0344 m, and the absolute pressure is 1 bar. Figure 6 shows the layout of the modelled domain. An approach similar to the boundary conditions has been used according to the study reported by Cox and Antonio [44]. For investigating the acoustic absorption, it is crucial to prepare samples with a precise cylindrical profile such that they can accurately fit into the clamping part of the impedance tube. As mentioned previously, three plasters (i.e., gypsum, cement and lime, resp.) and two fibres (i.e., glass and basalt, resp.) have been tested. Based on the basic characteristics of the individual materials, the best results for acoustic absorption can be assumed to be achieved using basalt-fibre-reinforced



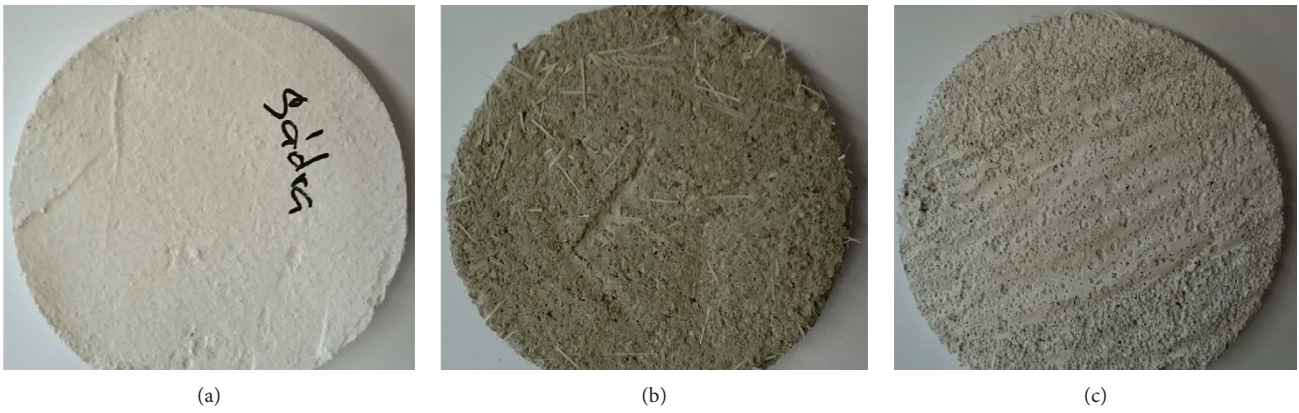


FIGURE 4: Tested samples: (a) gypsum, (b) cement with glass fibre, and (c) lime cement.

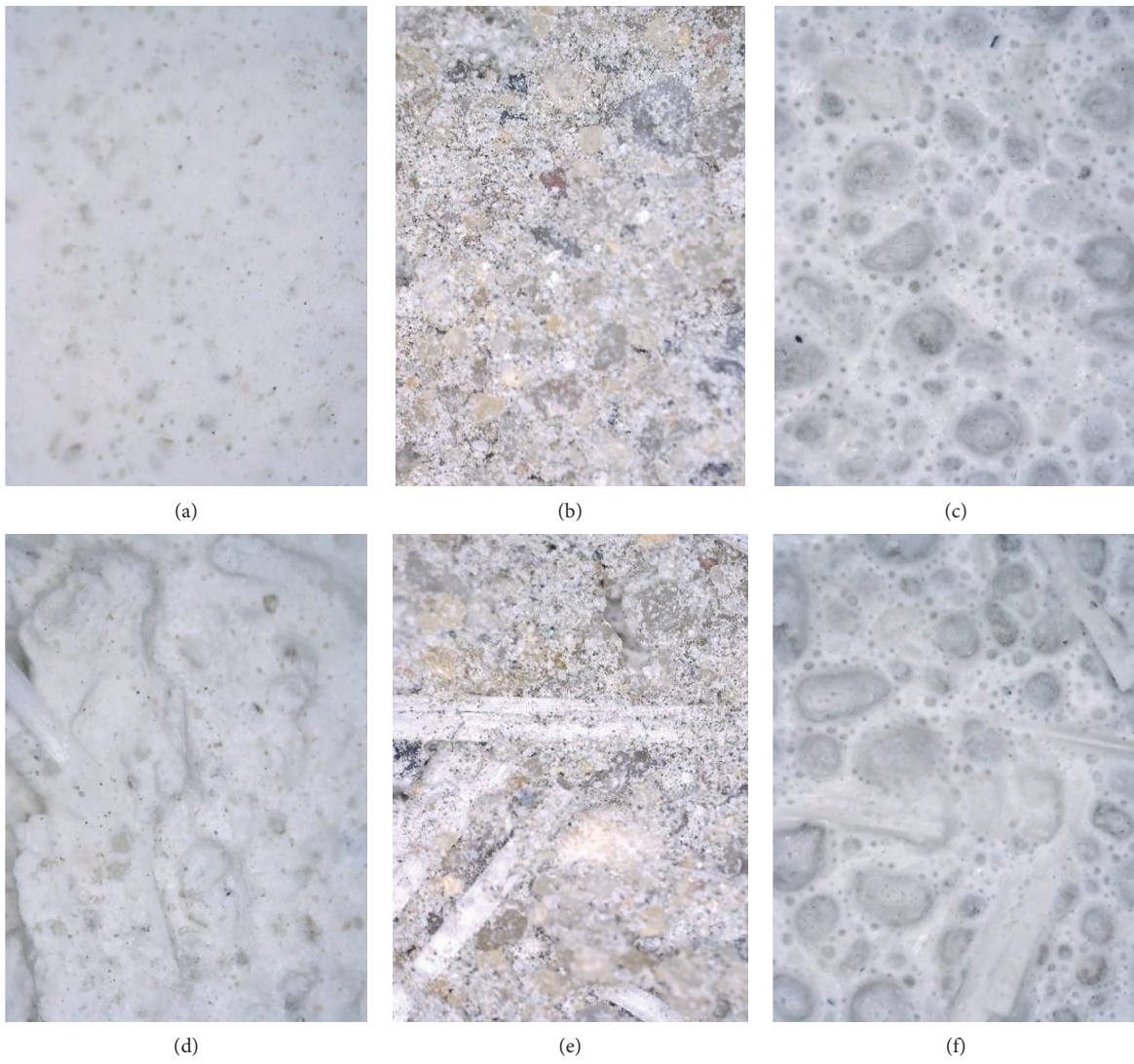


FIGURE 5: Continued.

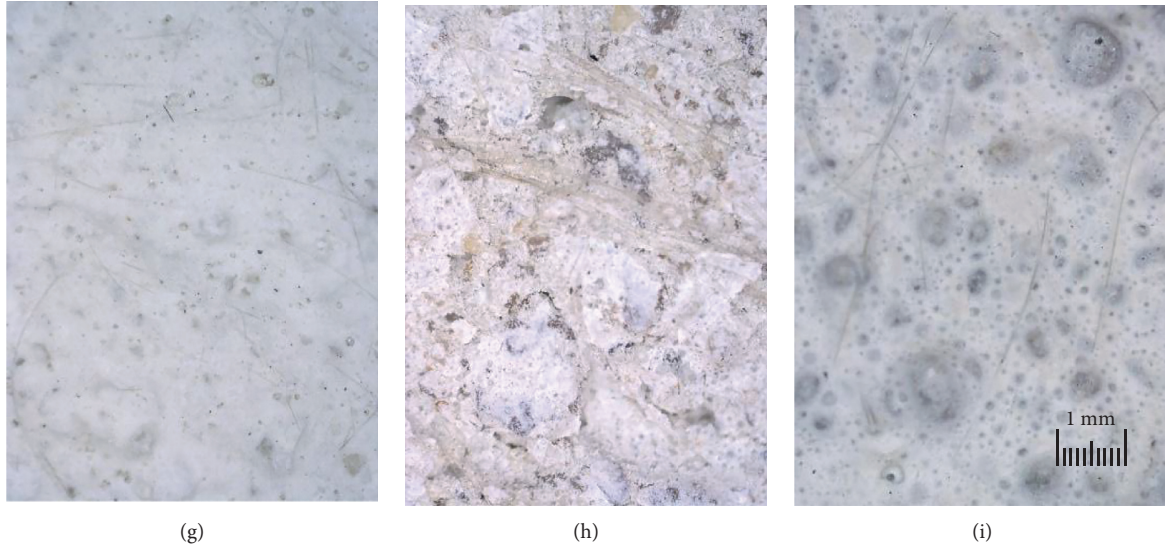


FIGURE 5: Microstructure of all tested samples and scale used in micrometres.

lime cement according to the study by Wang and Torng [31]. The reason for this assumption was that hollow silicate beads were present inside the mixture of lime-cement plaster, which basically serve as pores that render high thermal and acoustic properties. Figure 7 schematically shows the experimental apparatus, where the test was carried on a Brüel & Kjaer impedance tube 4206, with two microphones and amplifiers. This device permits the measurement of  $\alpha$  for perpendicularly impacting waves. The impedance tube comprises a loudspeaker and two measuring microphones that are connected to the evaluation unit. Lengths of  $X_1 = 0.15$  m,  $X_2 = 0.1$  m, and  $X_V = 10$  mm reflect the actual thickness of tested sample.

As the measurement signal, pink noise was used. The so-called pink noise is a signal with a frequency spectrum such that the power spectral density (PSD, energy, or power per frequency interval) is proportionally inverse to the signal frequency [45]. In the pink noise, each octave (halving/doubling in frequency) carries an equal amount of noise energy. Noise records with various statistical characteristics, for example, uniform and Gaussian distributions, can be generated. However, generally, this noise exhibits a “white” spectrum, implying that the noise retains its statistical characteristic at all frequencies. With respect to power at a constant bandwidth, pink noise falls off at 3 dB per octave. The pink or typically so-called  $1/f$  noise is one of typical ambient noises in nature and transport or even could describe a flowing river and beating heart [46]. Gildeen et al. have reported an unusual study where they described connection with human cognition [47]. That is, when a person attempts to remember, for example, a temporal interval, some errors are inevitably associated with the estimate. The sequences of errors in spatial and temporal replications were found to fluctuate as  $1/f$  noises. As reported by McClain [45], researchers often create  $1/f^2$  noise as a mistake instead of their required results. The generation of  $1/f$  noise involves amplitude scaling in the frequency domain by  $1/\sqrt{f}$  and not just by  $1/f$  itself. Generally, the magnitude of acoustic

variables depends on the frequency  $f$ . In actual cases in which frequency spectra would be measured with a step  $df = 1$  Hz, their processing would be extremely complicated. In these cases, frequency bands with the percentually constant width are introduced. This condition is satisfied by octave or third-octave frequency bands.

Typically, ten octaves are characterised by  $f_2/f_1 = 2$ , where indexes 2 and 1 represent the higher and lower frequencies, respectively. Each octave is marked by the middle frequency  $f_m$ :

$$f_m = \sqrt{f_1 \cdot f_2}. \quad (23)$$

The third-octave band is created by the octaves to their logarithmical thirds. Therefore, 30 bands are obtained.

The frequencies  $f_1$  and  $f_4$  border the one octave band and  $f_2$  and  $f_3$  indicate the frequencies of the inner thirds of the octave. Then, it is possible to claim that the log of inner frequencies ratio is equal to

$$\log \frac{f_2}{f_1} + \log \frac{f_3}{f_2} + \log \frac{f_4}{f_3} = \log \frac{f_4}{f_1} = \log 2. \quad (24)$$

Based on (25), the ratio between any adjacent frequencies is constant.

$$\frac{f_2}{f_1} = \frac{f_3}{f_2} = \frac{f_4}{f_3} = \sqrt[3]{2}. \quad (25)$$

Finally, the dependence between two consecutive lying middle frequencies of the third-octave bands is

$$f_{mi} \cdot \sqrt[3]{2} = f_{mi+1}. \quad (26)$$

In our case, the third-octave bands were used to describe the acoustic absorption level.

During measurements, the actual distance between the microphones and sample must be considered relative to the speed of sound in the ambient medium, which was done on

TABLE 4: The created combinations of matrix (plaster), dispersion (fibres), and number of their picture below.

	Gypsum	Cement	Thermo UM
Pure	Figure 5(a)	Figure 5(b)	Figure 5(c)
Glass	Figure 5(d)	Figure 5(e)	Figure 5(f)
Basalt	Figure 5(g)	Figure 5(h)	Figure 5(i)

the basis of  $k$ . The final  $k$  factor is a complex number with the real part  $k'$  (27) and the imaginary part  $k''$  (28):

$$k' = \frac{2\pi f}{c}, \quad (27)$$

$$k'' = 0.194 \times \frac{f^{1/2}}{c^{0.635}}. \quad (28)$$

Then,  $H$  is equal to the multiplication of complex numbers  $K$  and distance  $x_i$ . Based on those results and from the data measured on the two microphones at sampling ratios of 48 kHz and 4097 complex samples, the final value of the absorption coefficient can be obtained. During operation, it is crucial to find the real and imaginary parts of reflection, transfer function  $H_{12}$ , phase shift  $\varphi_{12}$ , and their exponential shape  $e^{j\varphi_{12}}$  and set the absorption coefficient  $r_i$ . Finally, the absorption coefficient  $\eta$  is computed as (29) or in the same manner only using a different formula (8):

$$\eta = 1 - (\text{real } r_i^2 + \text{im } r_i^2). \quad (29)$$

### 3. Results and Discussion

The fundamental material properties of samples significantly affect sound absorption. In particular, one of the most important parameters is porosity. According to the FEM simulation, the best absorption should be observed for Thermo UM (Figure 8). Figures 8–10 show the model results obtained from the sound absorption shown at a frequency of 1000 Hz. However, the model can be used at any frequency within the defined range. Based on the model results obtained in Figures 8–10, it is also possible to determine the effective thickness in which samples should be used. As can be observed for the cement sample (Figure 9), only  $\sim 2/3$  of the thickness effectively shield, thereby decreasing absorption. Hence, the structure of the material does not use the entire sample thickness with a constant acoustic attenuation efficiency. With the possible improvement in the effective absorption thickness of the samples and internal material attenuation, the fibres were added into FEM. In the model simulation of the gypsum sample, the effect of glass and basalt fibres was examined. Clearly, fibres significantly affect the total absorption (Figure 10). Basalt fibres, not glass fibres, are extremely suitable for increasing the sound absorption at a high thickness. However, this statement cannot be generalised because it depends on the combination of the plaster and fibres used. With other plasters, better results can be achieved with glass fibres and worse results were observed with the basalt fibres (Figure 11). Probably, compared simply to the fundamental physical properties, the extent to which the added fibre

reinforcement can increase the inner porosity of the material used is key. Hence, in this case, it is not possible to strictly rely only on model simulation, but it is necessary to conduct experiments with actual reinforced materials.

At the start of measurements, the repeatability of the main process and sample behaviour were verified. For the same samples, repeatable results were obtained, without any significant deviation from several sets of samples. However, the testing process was extremely sensitive to the actual sample shape (Figure 9). In case of a gap between the specimen and inner tube wall, measurement results were overestimated on account of the undiluted waves as well as the occurrence of vibrations from the imperfectly touching parts. Figure 12 shows the comparison of two ideal samples (dashed) and one nonideally circular sample number 3 (straight grey line). A comparison of the FEM model revealed similar results obtained from the measurements; however, Figure 13 shows a more uniform course. Figures 14–16 show the dependence of the acoustic absorption of each tested plaster material on the type of fibres used. The best acoustic absorption was achieved by the basalt-fibre-reinforced cement plaster. For better clarity, the results are also shown in the third-octave band in Figure 17.

In addition, the cement plaster with no fibre reinforcement exhibited the worst acoustic absorption. On the other hand, a lime-cement plaster with thermal insulating properties exhibited good acoustic absorption, even without fibre reinforcement, which was related to the nature of the inner mixture.

Dry plaster mixture contained hollow silicate beads, which positively affected the acoustic properties of the mixture and led to increased attenuation (Figure 14). However, by the addition of a fibrous dispersion into this mixture, the acoustic properties were degraded. On the other hand, the most significant increase in acoustic absorption occurred by the addition of fibres into the cement plaster, which was predicted after image analysis because in the basic material, the inner sample structure was clearly homogeneous with minimum pores. Therefore, it is not possible to state that the addition of a fibrous dispersion into plaster materials will generally improve their acoustic damping or favour a particular reinforcement that would be universal for all plasters. Randazzo et al. [14] have tested clay plasters, and their results revealed that the addition of natural fibres leads to increased open pores and subsequently improved acoustic absorption. With these results, it is possible to agree, but not generalise. Similar results were also reported by Neithalath et al. [20], who examined the effect of cellulose fibres on the acoustic absorption of cement composites. He found that the acoustic absorption coefficient increases with the volume of fibres in the composite. This viewpoint can be slightly misleading because with a high fibre content, the mechanical properties are degraded, and the effectiveness of the increased attenuation is not proportional. Bentchikou et al. [23], who examined the mechanical properties of the resultant cement composite by the addition of cellulosic fibres to cement, were aware of this issue. Their results, similar to those discussed herein, revealed that the addition of a high amount of fibres generally leads to the decrease in the

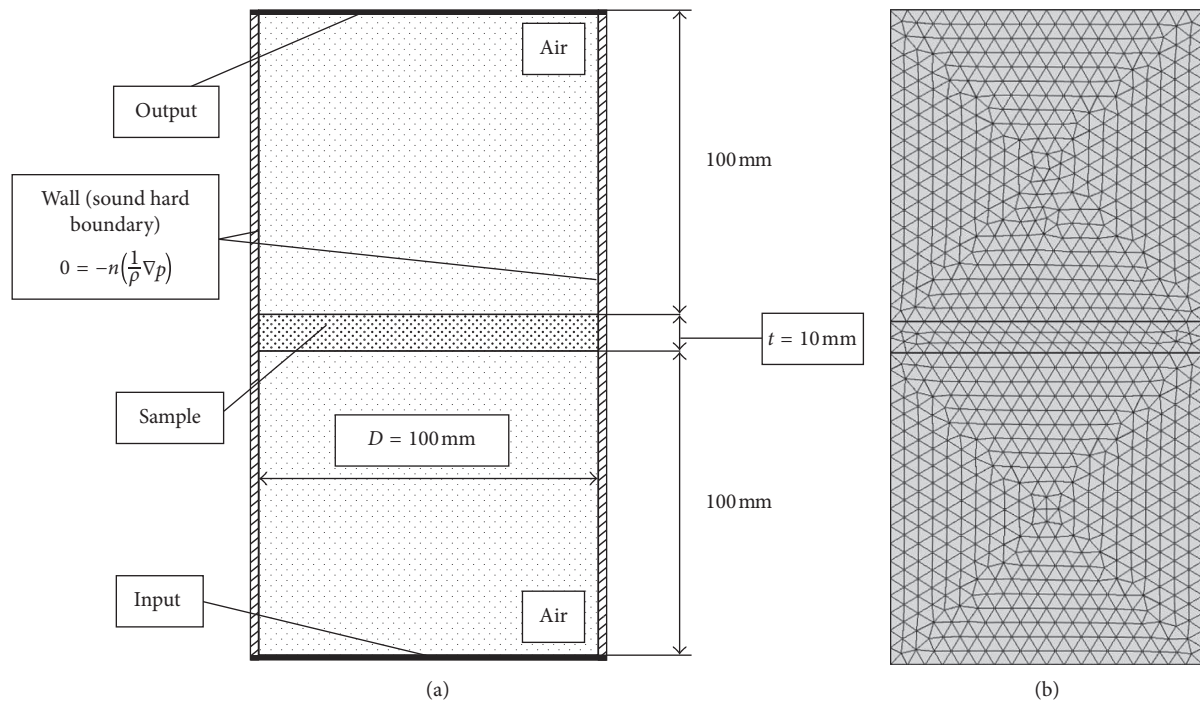


FIGURE 6: FEM model scheme and the mesh domain.

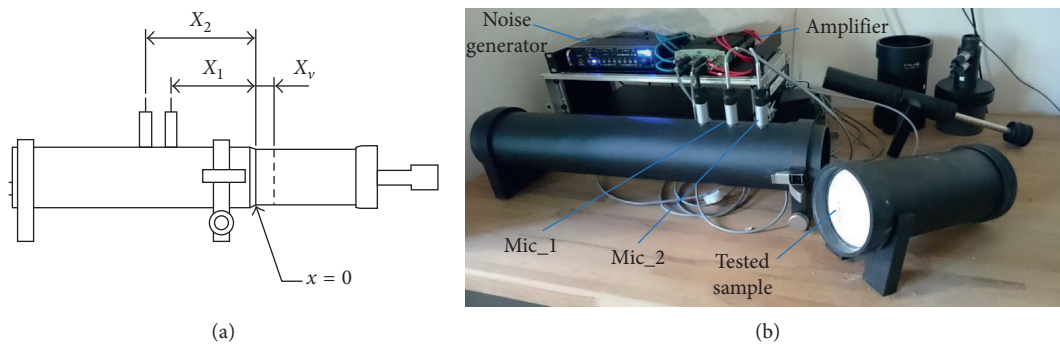


FIGURE 7: Experimental measurement (scheme and real device).

compressive and tensile strength. Hence, 1% of fibre reinforcement is examined to improve the acoustic properties and prevent the degradation of mechanical properties in the tested materials.

#### 4. Conclusion

Modern science does not emphasise only on the improvement of technologies, materials and their properties, but also focuses on the environment as well as the protection and comfort of human health. Hence, the effect of natural fibre reinforcement on the acoustic absorption of plaster composites is investigated herein. After the initial study, typical plasters were selected for experimental and numerical studies to determine the possibilities observed by the effects of the addition of fibre reinforcement on their acoustics properties. Lime cement, cement, and gypsum plasters were

selected not only for their physical properties but also for their typical use in the construction industry under geographical conditions. Plaster materials are disadvantageous because of their low tensile strength, which decreases the plaster life and causes visible defects and cracks. After previous studies reported by Samková et al. [17] on the amount of materials and fibres, glass and basalt fibres were added to the plasters as 1% by weight ratio of the fibrous reinforcement to improve the mechanical properties. The acoustic attenuation of plaster composites was not considerably affected by the mechanical properties of the fibres, but it was affected by final structure of the plaster mixture, especially the amount, size, and pore structure. Both fibres are typically used in the industry in different applications and forms, which is attributed to their good mechanical and physical properties, cost-effectiveness, and medical benign nature. Another important conclusion was the dependence

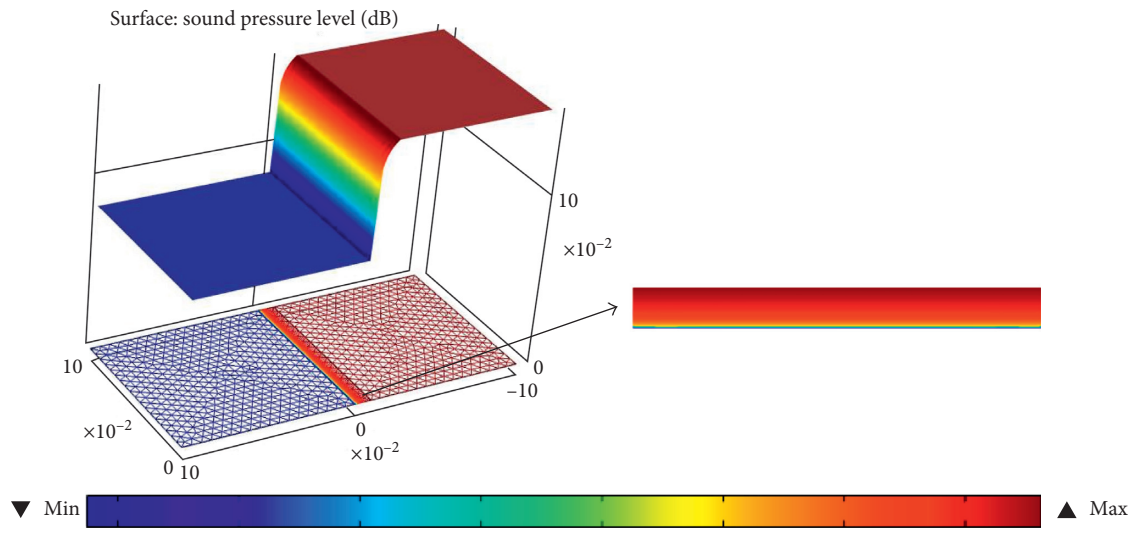


FIGURE 8: FEM model with the Thermo UM sample for investigating the minimum and maximum sample absorption.

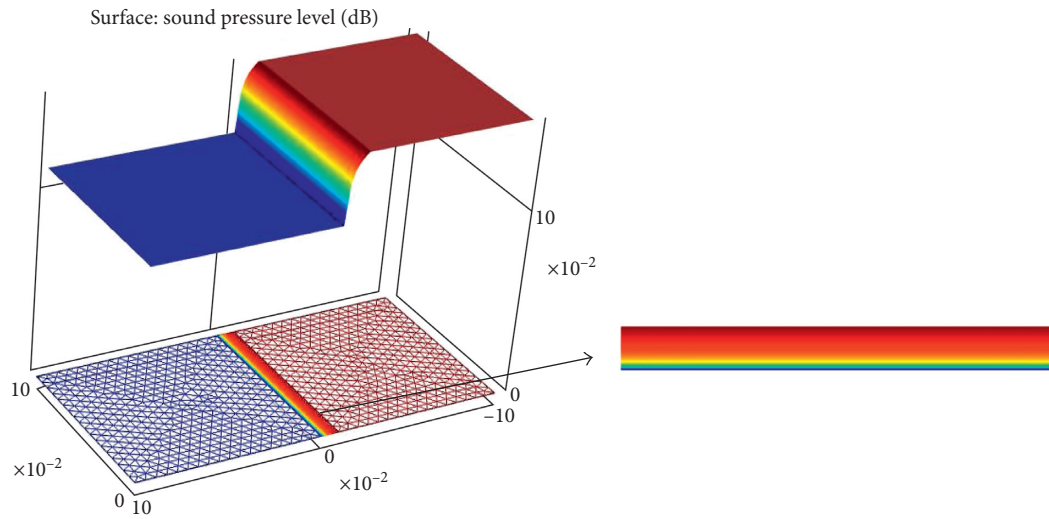


FIGURE 9: FEM model with the cement sample.

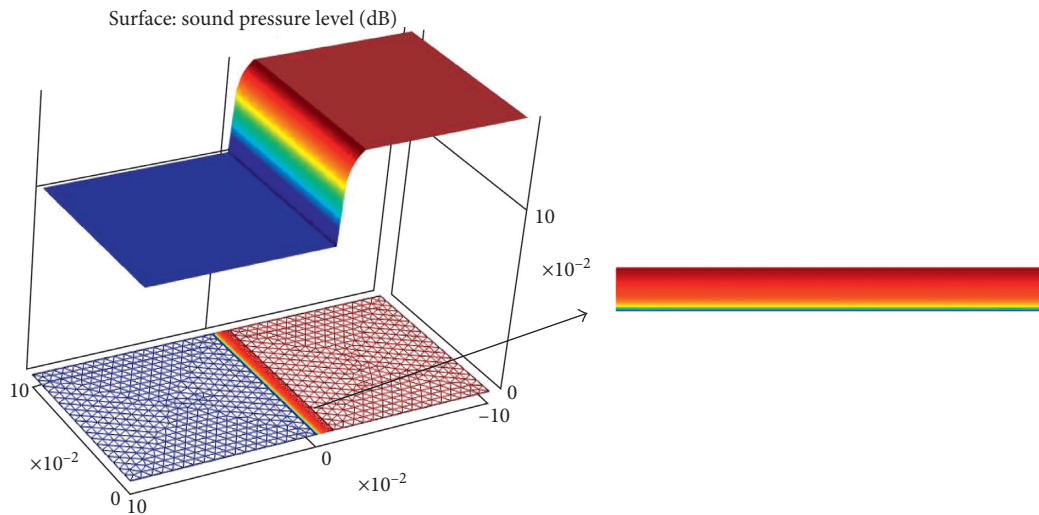


FIGURE 10: FEM model with the gypsum sample.

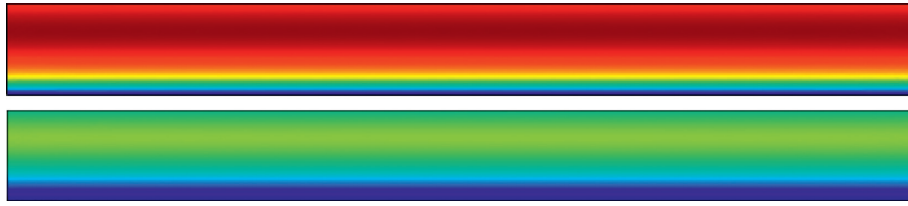


FIGURE 11: Comparison of the FEM model for gypsum with basalt fibre (upper) and gypsum with glass fibres (lower).

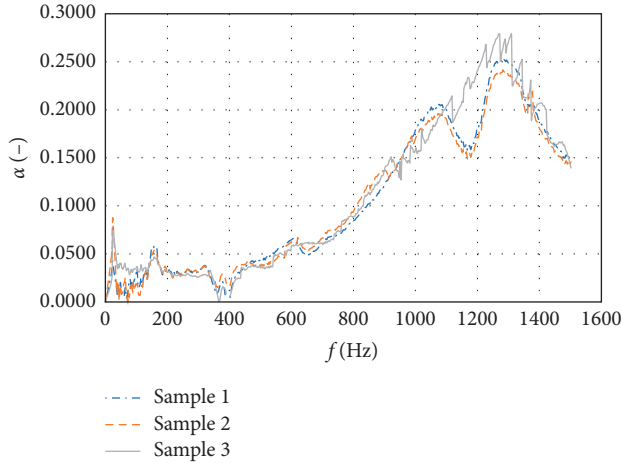


FIGURE 12: Experimental comparison of the cement plaster samples (sample 3 nonideal circularity).

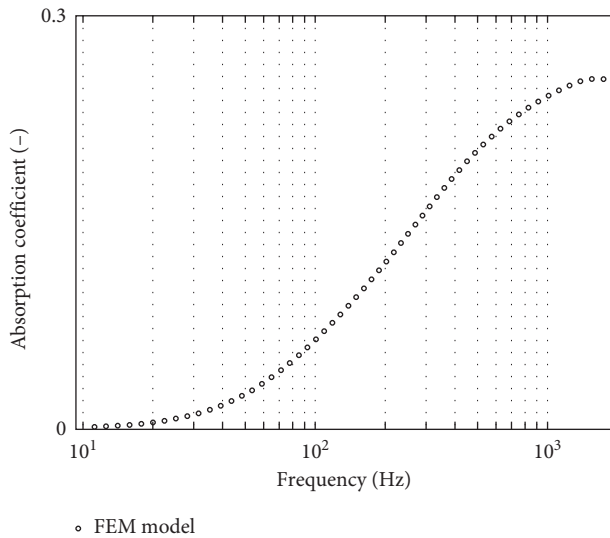


FIGURE 13: Numerical model for the attenuation in pure cement plaster.

of the effective attenuation on the material thickness in different plasters. That is, it is not true to generalise that the wider the plaster layer, the higher the acoustic attenuation will be proportionately (i.e., twice the layer thickness does not exhibit two times better absorption). Nevertheless, when the effective thickness is known, it is possible to combine the suitable fibre dispersion so as to achieve even better results with a significantly thin material layer, which could

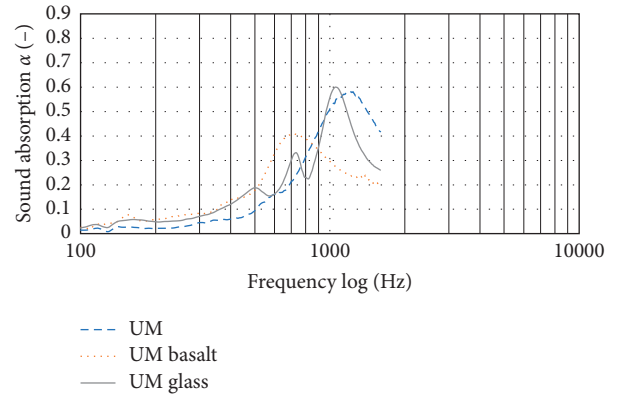


FIGURE 14: Obtained absorption coefficient values for the Thermo UM plaster.

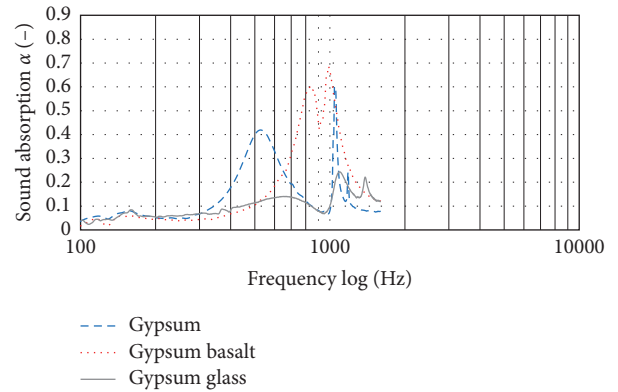


FIGURE 15: Absorption coefficient values obtained for gypsum.

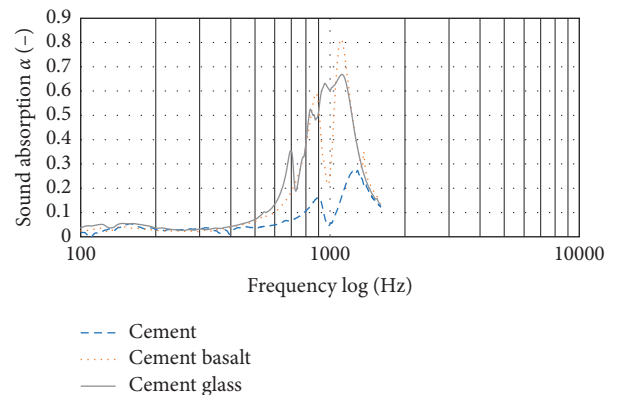


FIGURE 16: Absorption coefficient values obtained for cement.

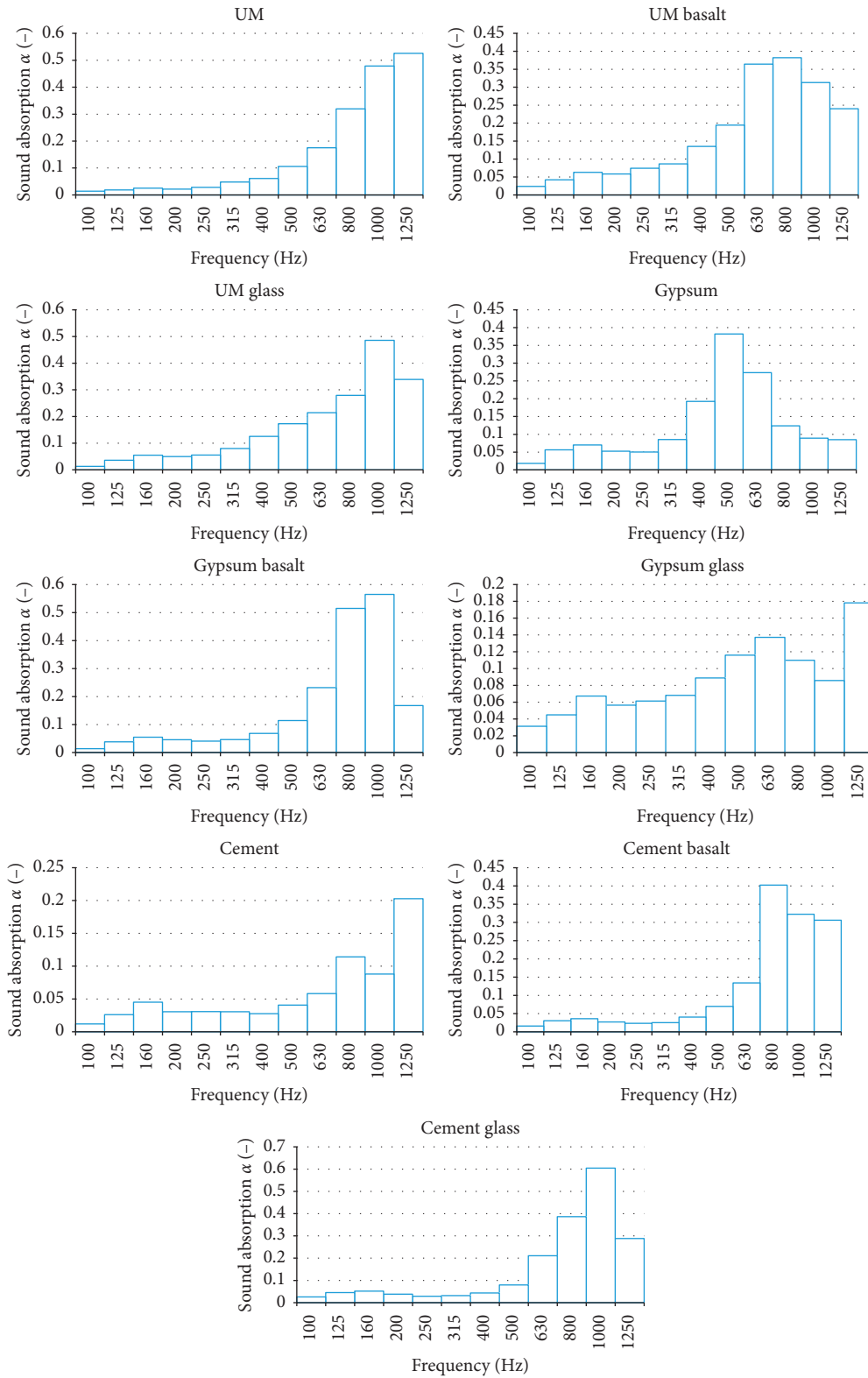


FIGURE 17: Comparison of the individual samples in the third-octave bands.

considerably lead to material and cost savings. As part of our future work, we intend to improve the existing numerical models, especially material models for reinforced plasters, and to extend their applications to electromagnetic shielding.

## Conflicts of Interest

The authors declare that they have no conflicts of interest.

## Acknowledgments

This paper was written at the Technical University of Liberec as part of the results of the project LO1201 which were obtained with cofunding from the Ministry of Education, Youth and Sports as part of targeted support from the “Narodni program udrzitelnosti I” programme and the project Options Reinforcement Plaster Using Fibrous Materials (21195) with the support of the Specific University Research Grant provided by the Ministry of Education.

## References

- [1] P. Baltrenas, D. Butkus, R. Grubliauskas, and J. Kuciaukaite, “Noise studies and reduction possibilities in a residential area located by a highway,” *Ecology*, vol. 55, no. 1, pp. 48–57, 2009.
- [2] C. D. Francis, J. Paritsis, C. P. Ortega, and A. Cruz, “Landscape patterns of avian habitat use and nest success are affected by chronic gas well compressor noise,” *Landscape Ecology*, vol. 26, no. 9, pp. 1269–1280, 2011.
- [3] A. H. Chahrour and K. A. Soudki, “RBS polymer encased concrete wall. Part II: experimental study and theoretical provisions for combined axial compression and flexure,” *Construction Build Materials*, vol. 20, no. 10, pp. 1016–1027, 2006.
- [4] European Commission, *Directive on Environmental Noise*, 2002/49/CE, DOCE L 189, 7/18/02, European Commission, Brussels, Belgium, 2002.
- [5] C. Diaz, A. Diaz, and M. A. Navacerrada, “An experimental study on the effect of rollong shutters on the field measurements of airborne sound insulation of facades,” *Applied Acoustic*, vol. 74, no. 1, pp. 134–140, 2013.
- [6] M. Frontczak and P. Wargocki, “Literature survey on how different factors influence human comfort in indoor environments,” *Building and Environment*, vol. 46, no. 4, pp. 922–937, 2011.
- [7] D. Cuiyun, C. Guang, X. Xinbang, and L. Peisheng, “Sound absorption characteristics of a high-temperature sintering porous ceramic material,” *Applied Acoustic*, vol. 73, no. 865, p. 71, 2011.
- [8] W. J. Cavanaugh, G. C. Tocci, and J. A. Wilkes, *Acoustics Architectural: Principles and Practice*, Wiley, Hoboken, NY, USA, 2009.
- [9] C. Bujoreanu, F. Nedeff, M. Benchea, and M. Agop, “Experimental and theoretical considerations on sound absorption performance of waste materials including the effect of backing plates,” *Applied Acoustics*, vol. 119, pp. 88–93, 2016.
- [10] M. A. Pedreño-Rojas, M. J. Morales-Conde, F. Pérez-Gálvez, and C. Rodríguez-Liñán, “Eco-efficient acoustic and thermal conditioning using false ceiling plates made from plaster and wood waste,” *Journal of Cleaner Production*, vol. 166, pp. 690–705, 2017.
- [11] M. K. Dixit, J. L. Fernández-Solís, S. Lavy, and C. H. Culp, “Identification of parameters for embodied energy measurement,” *Energy and Buildings*, vol. 42, no. 8, pp. 1238–1247, 2010.
- [12] J. Faustino, L. Pereira, S. Soares, D. Cruz, A. Paiva, and H. Varum, “Impact sound insulation technique using corn cob particleboard,” *Construction and Building Materials*, vol. 37, pp. 153–159, 2012.
- [13] T. Janusevicius, J. Mazuolis, and D. Butkus, “Sound reduction in samples of environmentally friendly building materials and their compositions,” *Applied Acoustic*, vol. 113, pp. 132–136, 2016.
- [14] L. Randazzo, G. Montana, A. Hein, A. Castiglia, G. Rodonò, and D. Donato, “Moisture absorption, thermal conductivity and noise mitigation of clay based plasters: the influence of mineralogical and textural characteristics,” *Applied Clay Science*, vol. 132, pp. 498–507, 2016.
- [15] L. Arnaud and E. Gourlay, “Experimental study of parameters influencing mechanical properties of hemp concretes,” *Construction and Building Materials*, vol. 28, no. 1, pp. 50–56, 2012.
- [16] P. Gle, L. Gourdon, and L. Arnaud, “Acoustical properties of material made of vegetable particles with several scales of porosity,” *Applied Acoustics*, vol. 72, no. 5, pp. 249–259, 2011.
- [17] A. Samková, P. Kulhavý, and M. Pechociaková, “Fibre reinforcement effect on plaster composite properties,” in *Proceedings of the NART Conference*, pp. 189–195, Liberec, Czech Republic, August–September 2015.
- [18] P. R. Blankenhorn, M. R. Silsbee, B. D. Blankenhorn, M. DiCola, and K. Kessler, “Temperature and moisture effects on selected properties of wood fiber-cement composites,” *Cement and Concrete Research*, vol. 29, no. 5, pp. 737–741, 1999.
- [19] P. Soroushian, S. Marikunte, and J. P. Won, “Statistical evaluation of mechanical and physical properties of cellulose fiber reinforced cement composites,” *Materials Journal*, vol. 92, no. 2, pp. 172–180, 1995.
- [20] N. Neithalath, J. Weiss, and J. Olek, “Acoustic performance and damping behavior of cellulose-cement composites,” *Cement and Concrete Composites*, vol. 26, pp. 359–370, 2002.
- [21] K. Kalinova, “A sound absorptive element comprising an acoustic resonance nanofibrous membrane,” *Recent Patents on Nanotechnology*, vol. 9, no. 1, pp. 61–69, 2015.
- [22] J. Mohrova and K. Kalinová, “Different structures of PVA nanofibrous membrane for sound absorption application,” *Journal of Nanomaterials*, vol. 2012, Article ID 643043, 4 pages, 2012.
- [23] M. Bentschikou, A. Guidoum, K. Scrivener, K. Silhadi, and S. Hanini, “Effect of recycled cellulose fibers on the properties of lightweight cement composite matrix,” *Construction and Building Materials*, vol. 34, pp. 451–456, 2012.
- [24] A. Izaguirre, J. Lanás, and J. Alvarez, “Effect of polypropylene fibre on the behavior of aerial lime-based mortars,” *Construction and Building Materials*, vol. 25, no. 2, pp. 992–1000, 2011.
- [25] A. Samková, P. Kulhavý, and M. Pechociaková, “Optimization parameters of plaster composites,” in *Proceedings of the 54th International conference on Experimental Stress Analysis*, Srni, Czech Republic, May–June 2016, ISBN: 978-80-261-0624-1.
- [26] D. A. Bies and C. H. Hansen, *Engineering Noise Control-Theory and Practice*, Spon Press, London, UK, 2009.
- [27] J. Slavik, V. Stejskal, and V. Zeman, *Fundamentals of Machine Dynamics*, Czech University of Prague, Prague, Czech Republic, 1997.



- [28] N. Holmes, A. Browne, and C. Montague, "Acoustic properties of concrete panels with crumb rubber as a fine aggregate replacement," *Construction and Building Materials*, vol. 73, pp. 195–204, 2014.
- [29] Z. Fišarova, *Building Acoustics in Theory and Practice*, Brno University of Technology, Brno, Czech Republic, 2014.
- [30] E. Moretti, E. Belloni, and F. Agosti, "Innovative mineral fiber insulation panels for buildings: thermal and acoustic characterization," *Applied Energy*, vol. 169, pp. 421–432, 2016.
- [31] C. N. Wang and J. H. Torng, "Experimental study of the absorption characteristics of some porous fibrous materials," *Applied Acoustics*, vol. 62, no. 4, pp. 447–459, 2001.
- [32] Satsys Technology Ltd., *Material Data Sheets of Plasters*, Satsys Technology Ltd., Czech Republic, 2014.
- [33] D. A. Kontogeorgos and M. A. Founti, "Gypsum board reaction kinetics at elevated temperatures," *Thermochimica Acta*, vol. 529, pp. 6–13, 2012.
- [34] S. L. Manzello, R. G. Gann, S. R. Kukuck, and B. L. David, "Influence of gypsum board type (X or C) on real fire performance of partition assemblies," *Fire and Materials*, vol. 31, pp. 425–442, 2007.
- [35] P. Kulhavy, T. Martinec, O. Novak, M. Petru, and P. Srb, "Testing fireproof materials in a combustion chamber," *EPJ Web of Conferences*, vol. 143, p. 02058, 2017.
- [36] G. B. Myron, *Magmatic and Metamorphic Petrology*, Wiley-Blackwell, Hoboken, NY, USA, 2nd edition, 2002.
- [37] J. Militky and V. Kovacic, "Basalt fibres a new prospectus of old material," *Fiber and textile*, vol. 7, no. 1, 2000.
- [38] K. Singha, "A short review of basalt fiber," *International Journal of Textile Science*, vol. 1, no. 4, pp. 19–28, 2012.
- [39] B. Wei, H. Cao, and S. Song, "Environmental resistance and mechanical performance of basalt and glass fiber," *Material Science and Engineering: A*, vol. 527, no. 18–19, pp. 4708–4715, 2010.
- [40] Material database Matbase, Natural & Synthetic Polymers, <https://www.matbase.com/material-categories/natural-and-synthetic-polymers/>.
- [41] D. Das and B. Neckar, *Theory of Structure and Mechanics of Fibrous Assemblies*, WPI Publishing, New Delhi, India, 2012, ISBN: 978-1-84569-791-4.
- [42] N. Kino and T. Ueno, "Comparison between characteristic lengths and fiber equivalent diameter in glass fiber and melamine foam materials of similar flow resistivity," *Applied Acoustics*, vol. 69, no. 4, p. 325, 2008.
- [43] M. A. Biot, "The theory of propagation of elastic waves in a fluid-saturated porous solid. I. low-frequency range," *Journal of the acoustical Society of America*, vol. 28, no. 2, pp. 168–178, 1956.
- [44] T. J. Cox and P. D. Antonio, *Acoustic Absorbers and Diffusers, Theory, Design and Applications*, Taylor and Francis, Abingdon, UK, 2nd edition, 2009.
- [45] D. McClain, *Numerical Simulation of Pink Noise*, Vol. 1, The Rockefeller University, New York, NY, USA, 2001.
- [46] P. Bak, C. Tang, and K. Wiesenfeld, "Self-organized criticality: an explanation of  $1/f$  noise," *Physical Review Letters*, vol. 59, no. 4, pp. 381–384, 1987.
- [47] D. L. Gilden, T. Thornton, and M. W. Mallon, " $1/f$  noise in human cognition," *Journal of Science*, vol. 267, no. 5205, pp. 1837–1839, 1995.

## Research Article

# Impact Analysis of Brake Pad Backplate Structure and Friction Lining Material on Disc-Brake Noise

Gongyu Pan and Lei Chen 

*School of Automotive and Traffic Engineering, Jiangsu University, Zhenjiang 212013, China*

Correspondence should be addressed to Lei Chen; [js\\_chenlei@126.com](mailto:js_chenlei@126.com)

Received 29 December 2017; Accepted 7 March 2018; Published 29 March 2018

Academic Editor: Rujie He

Copyright © 2018 Gongyu Pan and Lei Chen. This is an open access article distributed under the Creative Commons Attribution License, which permits unrestricted use, distribution, and reproduction in any medium, provided the original work is properly cited.

This study proposes a three-layer brake pad design, on which a six-DOF dynamic model of brake disc-brake pad is established, and the factors affecting the system instability are analyzed. The analysis shows that the change of mass and stiffness of the brake pad will affect the stability of the system. From the linear complex eigenvalue analysis, the unstable vibration modes of the brake system are predicted, and the effectiveness of the complex mode analysis model is verified by the brake system bench test. Brake pads with different structural shapes are designed, and their influence on the stability of the brake system is analyzed. The results show that the design of the three-layer structure and the slotting design of the brake pad can effectively reduce the occurrence of the brake squeal, especially that of the high-frequency squeal noise.

## 1. Introduction

Since the early 1920s, automotive disc-brake squeal noise has been a widespread concern of academics and automobile manufacturers all over the world because brake squeal is an important cause of customer dissatisfaction and warranty problems. In the past three decades, the proportion of disc brake used in sedan has increased year by year. It can be assumed that disc brakes will gradually replace drum brakes in sedan. However, the problem of brake noise of disc brakes still exists, and many brake noise phenomena have not been explained rationally so far [1–3]. Automobile braking process will produce vibration, and unstable vibration will not only lead to noise that both affects the comfort of driving and causes acoustic pollution to the surrounding environment but it will also cause fatigue wear on the automobile brake system [4].

Lars have slotted and surfaced the surface of the brake disc and proved by experiment that improved brake disc can reduce the occurrence of the brake squeal [5]. Oberst and Lai used chaos theory to study the mechanism of

braking noise, which is of great guiding significance [6]. Kung et al. calculated the free modal of the components in the brake and obtained the components and related modalities with the largest contribution rate of unstable mode by the complex eigenvalue analysis [7]. In addition to using the complex eigenvalue analysis to study the brake noise, the transient dynamic analysis is first used by Nagy et al. The four mode frequencies extracted from the results of transient dynamic analysis coincide with the experimental noise [8]. The disadvantages of transient dynamics are that it takes too much computation time and takes up a lot of disk space, and it is also hard for the data to be used directly for design changes. Besides, because of the high frequency of brake squeal, the explicit integral time step is very small, whereas the implicit integral can have a large time step, but it will attenuate the high-frequency mode. Complex eigenvalue analysis and transient dynamic analysis are used by AbuBakar and Ouyang [9] to study the brake squeal, under the same model and boundary condition. The results of the above two analyses are identical with the different contact mechanism and integral method. In the analysis of

the brake system noise, the use of complex eigenvalue analysis, combined with a reasonable combination of transient dynamic analysis, may be a way to analyze the noise generation mechanism.

In the friction-slip experiment of the flat plate, Chen [3] found that the instantaneous squeal may not be caused by the modal coupling, and the transient excitation between the disc and block may be the key mechanism of the squeal. However, this kind of alternating load excitation is a transient process difficult to capture through experiments. The transient dynamic analysis may more clearly show the process and reveal the reasons of this phenomenon. For the dynamic model of the brake disc and brake pad, a four-DOF self-excited frictional oscillator model was proposed by Zhang et al. [10] to explore the difference between the linear analysis and nonlinear analysis on the brake system noise, and corresponding improvement measures are given.

In this context, based on the modal coupling theory, a six-degree-of-freedom motion model of the brake disc and brake pad is established. Combined with finite element complex modal analysis and bench test, it is of great guiding significance to improving the NVH performance by improving the material properties of the brake pad and optimizing the backplate structure of the brake pad to inhibit the brake squeal noise and to exploring the inhibition mechanism of noise, which provides a theoretical basis for reducing the noise of brake squeal.

## 2. Six-DOF Kinematics Model of Brake Disc-Brake Pad

The brake coupling model built by Festjens et al. [11] shows that the structure and damping of backplate of the brake pad have an important influence on the brake noise. Similarly, the damping size of the friction lining material will also have a significant influence on brake noise. Through the research studied by Ruhai et al. [12], it is known that adding a certain proportion of viscoelastic material to the friction lining could reduce the resonance tendency between the brake pad and the brake disc, thereby inhibiting the brake squeal to some extent. Based on the important influence of the friction lining, it is divided into two parts, namely, lining substrate and friction lining mixture. Since the material composition of lining substrate has stronger damping characteristics than the friction lining mixture, it should be treated differently during the modeling and simulating process.

A six-DOF kinematics model of brake disc-brake pad is depicted in Figure 1. Due to the small damping of the system, the effect of damping is neglected in the kinematics analysis. The brake pad is composed of the brake pad backplate  $m_b$ , lining substrate  $m_u$ , and friction lining mixture  $m_1$ .  $m_b$  has a  $z$ -direction degree of freedom  $z_1$ ;  $m_u$  has a  $z$ -direction degree of freedom  $z_2$ ; and  $m_1$  has a  $z$ -direction degree of freedom  $z_3$  and an  $x$ -direction degree of freedom  $x_3$ ; The

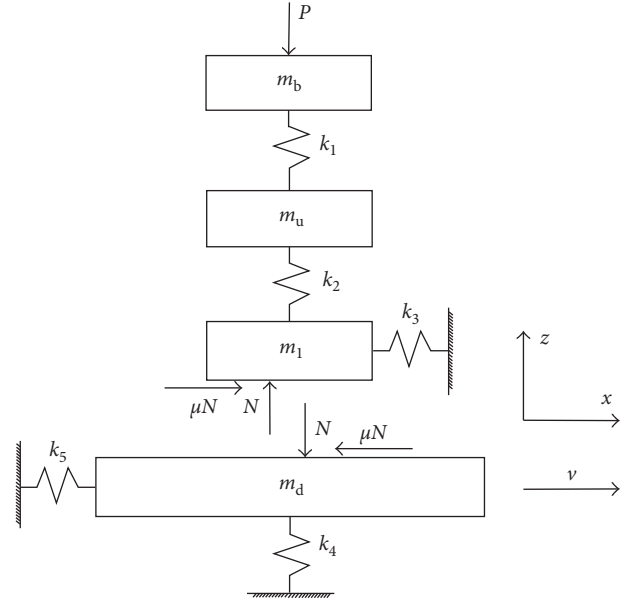


FIGURE 1: Six-DOF kinematics model of brake disc-brake pad.

brake disc  $m_d$  has two degrees of freedom, respectively,  $x$ -direction of  $x_d$  and  $z$ -direction of  $z_d$ .  $\mu$ ,  $P$ , and  $N$  are friction coefficient, force of piston acting on the brake pad, and positive force acting on the brake disc, respectively.

The kinematic equation can be obtained from the kinematic model of Figure 1:

$$[M]\{\ddot{u}\} + [K]\{u\} = \{F\}. \quad (1)$$

In this formula,  $u = (z_1, z_2, z_3, x_3, z_d, x_d)^T$  and  $(\cdot)$  is the differentiation with respect to time. The mass matrix  $[M] = \text{diag}(m_b, m_u, m_1, m_1, m_d, m_d)$ , motivation  $\{F\} = (P, 0, N, \mu N, -N, -\mu N)^T$ , and  $[K]$  is the stiffness matrix:

$$[K] = \begin{bmatrix} k_1 & -k_1 & 0 & 0 & 0 & 0 \\ -k_1 & k_1 + k_2 & -k_2 & 0 & 0 & 0 \\ 0 & -k_2 & k_2 & 0 & 0 & 0 \\ 0 & 0 & 0 & k_3 & 0 & 0 \\ 0 & 0 & 0 & 0 & k_4 & 0 \\ 0 & 0 & 0 & 0 & 0 & k_5 \end{bmatrix}. \quad (2)$$

In the initial stage, the system is in a stable steady state, the brake disc rotates at a constant speed, and the system does not produce vibration, so the steady-state equation can be obtained. Assuming that the brake disc and brake pad are not separated during the process of vibration, the constraint condition is  $z_d = z_3$ , and then we know

$$N = m_1 \ddot{z}_3 - (k_1 + k_2)z_1 + k_2 z_2. \quad (3)$$

Taking (3) into the steady-state equation, we obtain

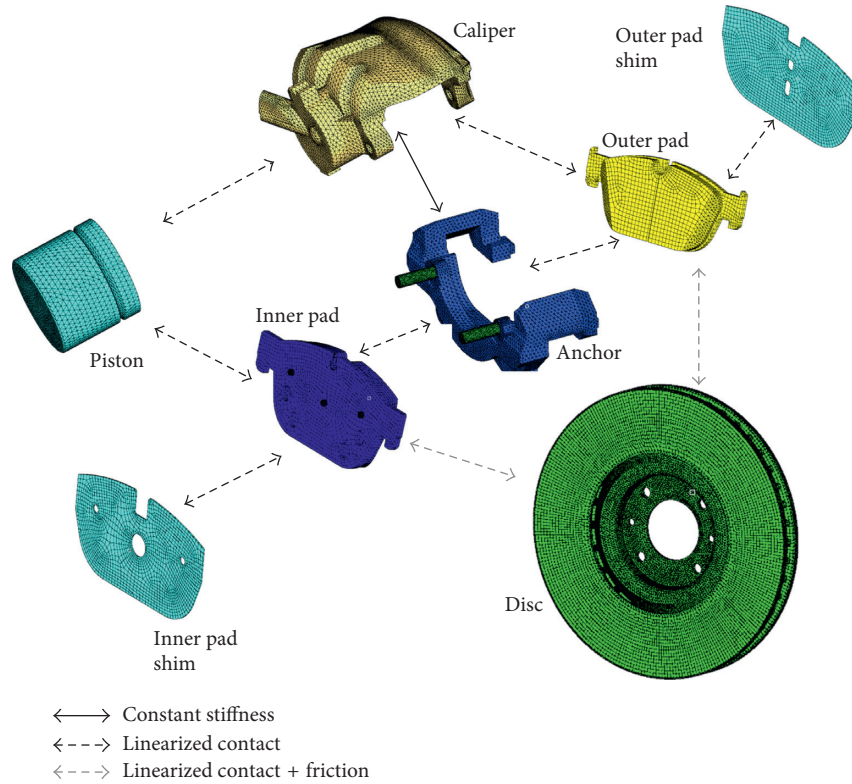


FIGURE 2: Finite element model of brake.

$$\begin{bmatrix} m_b & 0 & 0 & 0 & 0 \\ 0 & m_u & 0 & 0 & 0 \\ 0 & 0 & m_1 + m_d & 0 & 0 \\ 0 & 0 & -\mu m_1 & m_1 & 0 \\ 0 & 0 & \mu m_1 & 0 & m_d \end{bmatrix} \cdot \begin{Bmatrix} \ddot{z}_1 \\ \ddot{z}_2 \\ \ddot{z}_3 \\ \dot{x}_3 \\ \ddot{x}_d \end{Bmatrix} + \begin{bmatrix} k_1 & -k_1 & 0 & 0 & 0 \\ -k_1 & k_1 + k_2 & -k_2 & 0 & 0 \\ 0 & -k_2 & k_2 + k_4 & 0 & 0 \\ \mu(k_1 + k_2) & -\mu k_2 & 0 & k_3 & 0 \\ -\mu(k_1 + k_2) & \mu k_2 & 0 & 0 & k_5 \end{bmatrix} \cdot \begin{Bmatrix} z_1 \\ z_2 \\ z_3 \\ x_3 \\ x_d \end{Bmatrix} = \begin{Bmatrix} 0 \\ 0 \\ 0 \\ 0 \\ 0 \end{Bmatrix}. \quad (4)$$

Equation (4) is the kinematic equation of the brake disc-brake pad system. It can be found that the mass matrix and the stiffness matrix of the kinematic equation of system are both asymmetric due to the existence of friction, so the eigenvalues of the system may be complex numbers. The eigenvalues of the system can be obtained by complex modal analysis, where the imaginary part of eigenvalue represents the modal frequency and the real part represents the tendency of instability. At the same time, it can be found that the change of friction coefficient and the change of mass and stiffness of the brake pad will lead to the change of system mass matrix and the stiffness matrix, so as to change the system eigenvalue and affect the stability of the system. Based on the above, this study will change the system's mass matrix and stiffness

matrix by changing the geometric characteristics of the brake pad backplate, thus affecting the stability tendency of the system, to find out which structural feature of the backplate can reduce the brake system squeal.

### 3. Numerical Model

#### 3.1. Model of Complex Modal Analysis of Brake

**3.1.1. Finite Element Model.** Using CATIA to model the braking system, the HyperMesh is used to establish the mesh models, as shown in Figure 2. Among them, the brake caliper adopts the tetrahedral mesh (C3D4) due to the irregular structure, the remaining parts mainly adopt hexahedral unit (C3D8), supplemented with pentahedron unit (C3D6) and tetrahedral unit (C3D4), and the total number of model units is 327,568. Besides, the contact relationship between the components has been labelled in Figure 2.

**3.1.2. Defining Material Properties.** Define the material properties of each component, including Density, Young's modulus, and Poisson's ratio, as shown in Table 1.

**3.1.3. Setting of Analysis.** The finite element model, which has defined the material properties and assembled, is introduced into the ANSYS for complex eigenvalue analysis. Some nonlinear perturbation modal analysis is used to extract the unstable modes of the brake system.

TABLE 1: Material properties of brake components.

Component	Density ( $\text{kg}\cdot\text{m}^{-3}$ )	Young's modulus (MPa)	Poisson's ratio
Disc	7,190	122,000	0.230
Caliper	7,000	143,000	0.270
Backplate	7,800	197,000	0.300
Lining	2,615	8,600	0.330
Piston	7,220	180,000	0.300
Anchor	7,000	101,400	0.256
Guide pins	7,800	182,000	0.300

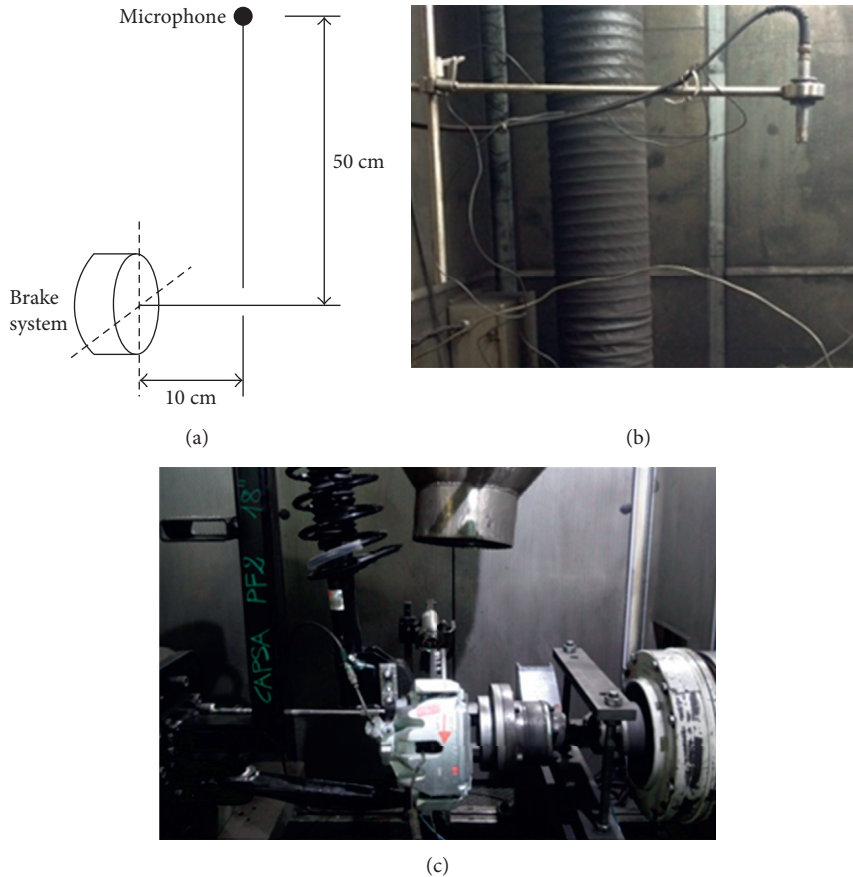


FIGURE 3: (a, b) Location of microphone and picture of real product and (c) disc brake assembled on test bench.

**3.1.4. Settings of Boundary Conditions.** The brake disc cap portion is bolted to the hub, but the brake disc can rotate along the  $z$ -axis, thus restraining the five degrees of freedom of the disc cap portion except for the  $z$ -direction of rotation. The anchor is bolted to the frame to restrain the six degrees of freedom of the cage bolt hole.

**3.1.5. Setting of Load.** In order to quantitatively study the relationship between friction coefficient, braking pressure, and brake noise, a brake system test was carried out under 9 operating conditions: by speed: 60 rpm, 120 rpm, and 180 rpm, and by hydraulic pressure: 1.5 MPa, 2.0 MPa, and 2.5 MPa.

**3.2. Bench Test Verification of Brake Complex Modal Analysis Model.** The test standard of brake noise is the NVH test

standard of the Society of Automotive Engineers, namely, SAE J2521 test standard [13]; the microphone is placed at 10 cm in the horizontal direction of the brake system, and the vertical distance is 50 cm (Figures 3(a) and 3(b)).

In the whole experimental process, 18 stages of braking conditions of the noise test were measured and the total braking process was 1,430 times. Since the initial temperature of this test starts from zero, there is no need to determine the noise in the cold state. The test data were processed to obtain part of the results of bench test shown in Figure 4 (the braking pressure is 2.0 MPa, and the rotational speed is 120 rpm), which is representative. Table 2 shows the noise occurrence rate at different frequency bands. The row data in the table indicate the occurrence rate of noise under each frequency band at the same sound pressure level, and the column data indicate the occurrence rate of noise under

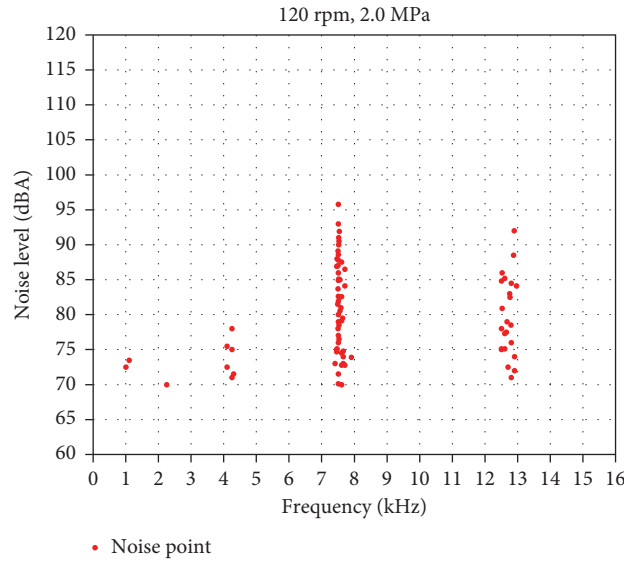


FIGURE 4: Noise frequency distribution and sound pressure level.

TABLE 2: Noise occurrence rate at different frequency bands.

Brake application: 1,430	Number	Rate (%)	$f_1$ (%)	$f_2$ (%)	$f_3$ (%)	$f_4$ (%)	$f_5$ (%)
			Near 7.5 kHz	Near 12.7 kHz	Near 4.1 kHz	Near 1.0 kHz	Near 2.2 kHz
Total noisy brake	325	22.73	10.98	8.18	2.17	1.12	0.28
70–80 dBA	141	9.86	3.71	2.73	2.03	0.28	0.28
80–90 dBA	129	9.02	5.03	3.85	0.14	0.00	0.00
90–100 dBA	46	3.22	1.89	1.33	0.00	0.00	0.00
100–110 dBA	9	0.63	0.35	0.28	0.00	0.00	0.00
110–120 dBA	0	0.00	0.00	0.00	0.00	0.00	0.00
>120 dBA	0	0.00	0.00	0.00	0.00	0.00	0.00

TABLE 3: Comparison between the results of complex eigenvalue analysis and the bench test of brake squeal.

Simulation conditions		The central frequency of squeal (Hz)					
$n = 120$ rpm	Test results	—	—	7,561.6	—	12,737.1	—
$P = 1.5$ MPa	Simulation results	5,954.7	6,404.4	7,598.4	10,360.1	12,804.0	13,969.2
$\mu = 0.8$	Error (%)	—	—	0.49	—	0.53	—
$n = 120$ rpm	Test results	—	7,561.6	—	12,737.1	—	—
$P = 2.0$ MPa	Simulation results	6,301.6	7,571.9	10,892.0	12,752.6	—	—
$\mu = 0.7$	Error (%)	—	0.14	—	0.12	—	—
$n = 120$ rpm	Test results	7,561.6	/	12,737.1	—	—	—
$P = 2.5$ MPa	Simulation results	7,562.7	11,035.2	12,832.5	—	—	—
$\mu = 0.6$	Error (%)	0.01	—	0.75	—	—	—

each sound pressure level at the same frequency. It can be found from Figure 4 and Table 2 that there are five different frequencies of squeals in the braking process, and the frequencies of squeals are mainly distributed around 4.1 kHz, 7.5 kHz, and 12.7 kHz.

The test results at the braking pressure of 1.5 MPa, 2.0 MPa, and 2.5 MPa and friction coefficient of 0.8, 0.7, and 0.6 were, respectively, extracted, and the test results were compared with the unstable modal frequency of brake system obtained by simulating to verify the validity and accuracy of the model, as shown in Table 3. The results show that all the brake squeal frequencies in the test can be predicted by simulation, and the error is controlled within 0.1%.

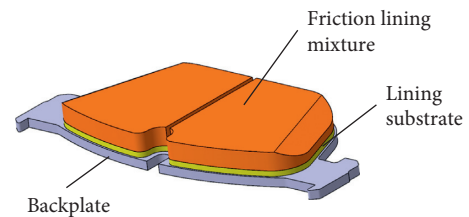


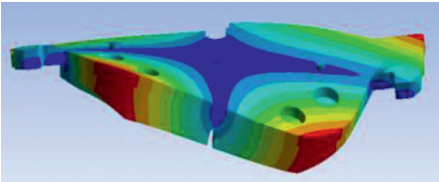
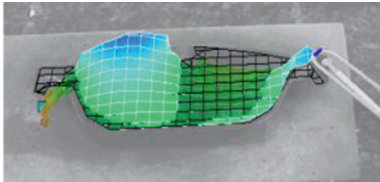
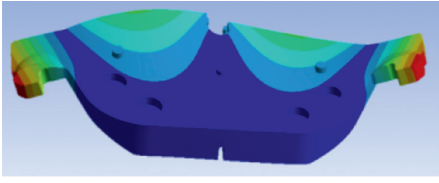
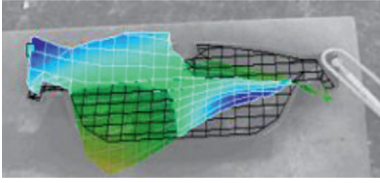
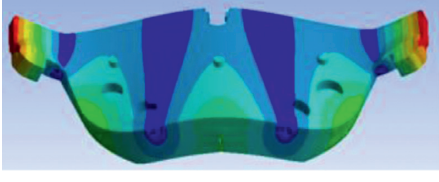
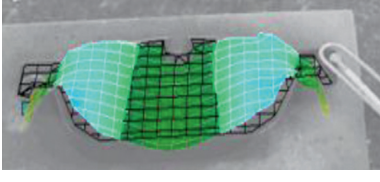
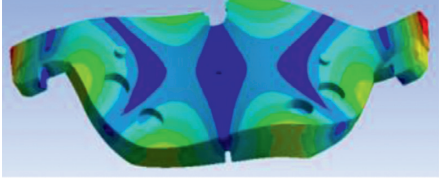
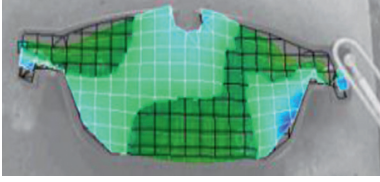

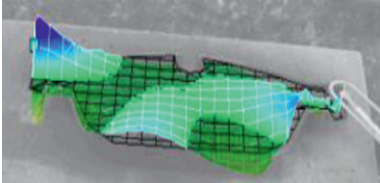
FIGURE 5: Composition of brake pad.

However, the phenomenon of overprediction appeared in the simulation; this is mainly due to the fact that the model of complex eigenvalue analysis does not take into account

TABLE 4: Material properties of each component of brake pad.

Component	Density ( $\text{kg}\cdot\text{m}^{-3}$ )	Young's modulus (MPa)	Poisson's ratio
Backplate	7,800	197,000	0.30
Lining substrate	2,800	5,350	0.35
Friction lining mixture	2,200	10,707	0.32

TABLE 5: Experimental verification on simulation vibration mode of the brake pad.

Order	Simulation vibration mode	Laser vibrometer
1		
2		
3		
4		
5		

factors such as the thermomechanical coupling, the frictional characteristics, and the time-varying characteristics of material properties in the actual braking process, which is mentioned in many literatures, so the model could predict the brake squeal accurately.

#### 4. Verification of Brake Pad

The brake pad is mainly composed of three parts, namely, backplate, lining substrate, and friction lining mixture, as

shown in Figure 5. Because of the simple structure and regular shape of the brake pad, the hexahedral mesh is selected to mesh. The material properties of each component are shown in Table 4.

From the results of real modal analysis of the brake pad, the typical vibration modes of natural frequencies within 10 kHz are extracted, as shown in Table 5, which are mainly manifested as bending and torsional vibration modes. The accuracy of the natural frequency of the brake pad was verified by the FRF resonance tester. As shown in Table 6,

TABLE 6: Experimental verification on simulation modal frequency of the brake pad.

Simulation modal frequency		F.R.F		Error (%)
Order	Frequency (Hz)	Order	Frequency (Hz)	
1	3169	2	3151	0.57
2	4137	3	4130	0.17
3	5689	4	5610	1.41
4	7342	5	7268	1.02
5	9380	6	9395	0.16

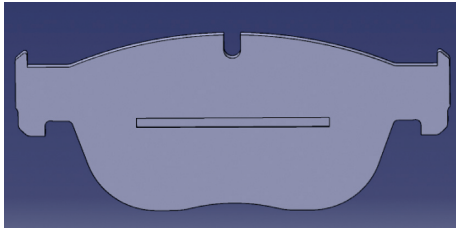


FIGURE 6: Sample 1 (single horizontal slot).

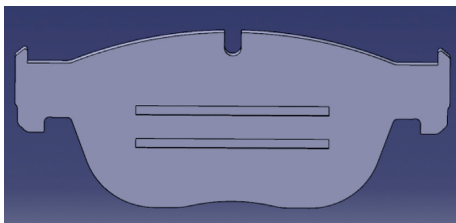


FIGURE 7: Sample 2 (double horizontal slots).

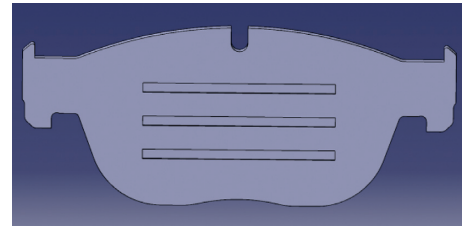


FIGURE 8: Sample 3 (three horizontal slots).

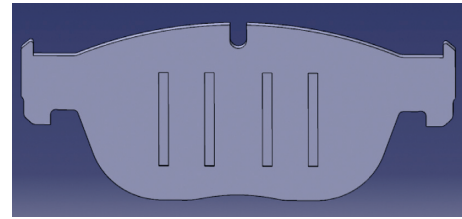


FIGURE 9: Sample 4 (four longitudinal slots).

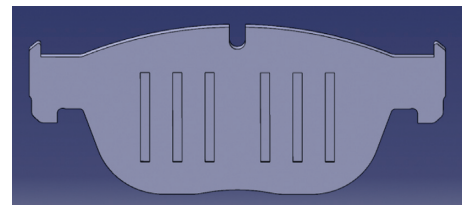


FIGURE 10: Sample 5 (six longitudinal slots).

the natural frequency error of the simulation and experiment was found to be within 2%. At the same time, the laser vibrometer is used to verify the vibration mode. As shown in Table 5, the typical modes measured by the laser vibrometer are exactly the same as those of the simulation vibration mode, so the results of the real modal analysis are accurate and the model of the brake pad is effective.

### 5. Slotting Designs on Brake Pad Backplate

According to the theory of structural dynamic design, changes in the mass of the system or the shape of the structure will lead to the change of system stiffness and damping, which will affect the natural frequency of the system [14]. According to the difficulty of backplate processing and the manufacturing process of the brake pad, five types of slotting methods are designed in this study, as shown in Figures 6–10. The effects of the five types of slotting designs on the natural frequencies and vibration modes of the brake pad are analyzed to determine whether the brake squeal noise will be further affected. The effective total area of the backplate is 4615 mm<sup>2</sup>. The design dimension of horizontal slot is 80 × 4 mm, and single horizontal slot, double horizontal slots, and three horizontal slots are designed on the backplate. The ratio of the slotted area to the total area of the backplate is 6.9%, 13.9%, and 20.8%, respectively. The design dimension of

longitudinal slot is 40 × 4 mm, and four longitudinal slots and six longitudinal slots are designed on the backplate. The ratio of the slotted area to the total area of the backplate is 13.9% and 20.8%, respectively. The depth of slotting designs is both 1 mm. In addition, the large size of the slotting on the backplate will cause the stiffness of the brake pad to drop sharply and affect the manufacturing process of the brake pad, so the ratio of the slotting area of the backplate should not be larger than 25% [15].

The free mode characteristics of the above five slotted backplates are calculated in the frequency range of 10~16 kHz. Then, the six-order critical modal frequencies were extracted and compared with the free modal frequencies of the unslotted backplate, as shown in Table 7. The bench test of the brake system has shown that the frequency of the brake squeal is mainly distributed around 4.1 kHz, 7.5 kHz, and 12.7 kHz. As can be found in Table 7, Sample 3, Sample 4, and Sample 5 are significantly improved for the critical frequency of 4.1 kHz and 7.5 kHz, but only Sample 3 has the best improvement effect on the critical frequency of 12.7 kHz, and Sample 4 and Sample 5 have barely any improvement on the critical frequency of 12.7 kHz. Therefore, Sample 3 was selected for further study.

The model of Sample 3 was made into a test piece (Figure 11), and the bench test was performed. The test results are shown in Figure 12. The test time for these tests shown in Figure 12 is close to that for those tests shown in Figure 4. Table 8 shows the main four test operations and test times of



TABLE 7: Comparison of critical modal frequencies between slotted backplate and unslotted backplate.

Order	Modal frequency (Hz)					
	Unslotted	Sample 1	Sample 2	Sample 3	Sample 4	Sample 5
1	3,276.5	3,257.5	3,240.8	3,214	3,208.6	3,180.3
2	4,101.7	4,064.9	4,046.2	4,010.2	4,031.2	3,997.4
3	6,660.2	6,623.6	6,589.3	6,546.7	6,580.5	6,578
4	7,379.4	7,133.6	7,045.9	6,923.6	7,039.7	6,960.4
5	12,048	12,011	12,000	11,914	11,872	11,825
6	12,891	13,060	12,585	12,121	12,776	12,711



FIGURE 11: Test piece of Sample 3.

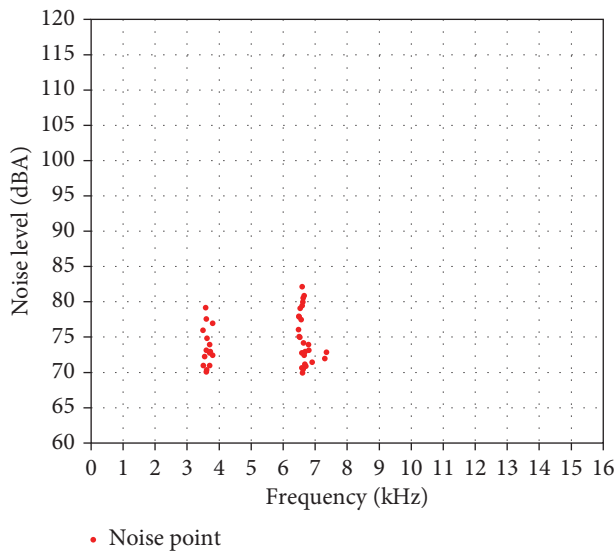


FIGURE 12: Noise frequency distribution and sound pressure level of the test piece.

Sample 3 which could obtain the test results shown in Figures 4 and 12. During the bench test, the braking pressure is 2 MPa and the initial rotational speed is 120 rpm.

From the test results, the brake pad with three horizontal slots on the backplate could effectively reduce the occurrence of brake squeal noise, especially that of the high-frequency squeal noise, and greatly reduce the noise points above 80 dB sound pressure level.

### 6. Results and Discussion

The change rate of the critical frequency between the unslotted brake pad and Sample 3 could be calculated from

TABLE 8: Bench test of Sample 3.

Test operation	Snub brake	Bedding	Deceleration	Cold
Test times	40	55	45	20

TABLE 9: Critical frequency change rate between unslotted backplate and Sample 3.

Order	Modal frequency (Hz)		Change rate (Hz)
	Unslotted	Sample 3	
1	4,101.7	4,010.2	-91.5
2	7,379.4	6,923.6	-455.8
3	12,891	12,121	-770.0

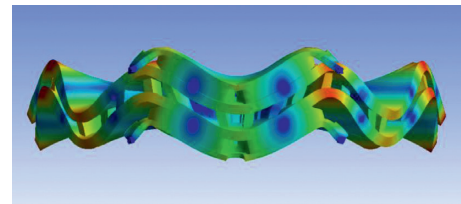


FIGURE 13: Unstable vibration mode at the braking pressure of 2.0 MPa (at 12,752.6 Hz).

Table 7. The frequency changes of the Sample 3 are -91.5 Hz, -455.8 Hz, and -770 Hz, respectively, as shown in Table 9. From Figure 12, it could be found that the original squeal frequency near 7.5 kHz disappears and the new squeal noise is generated near 6.8 kHz. Similarly, the original noise frequency around 4.1 kHz disappears and the new noise is generated near 3.9 kHz. Besides, high-frequency squeal of noise points near 12.7 kHz disappears completely.

The vibration mode of unstable modal frequency at 12,752.6 Hz is extracted from the results of complex modal analysis, as shown in Figure 13. The mode coupling between the brake pad and the brake disc resulting in resonance and the energy generated by the resonance which cannot be dissipated in time are the root causes of concentration near the high frequency 12.7 kHz. The design of three horizontal slots on the brake pad backplate makes the critical frequency change 770 Hz, which leads to the decoupling of the brake pads and the brake disc. Besides, the lining substrate of the brake pad contributes to the dissipation of energy generated by resonance. Similarly, the decoupling between the brake pads and the brake disc is also achieved at frequencies of

4.1 kHz and 7.5 kHz, but the changed brake pad modal frequencies are coupled with the other modal frequencies of the brake disc, which will easily trigger resonance and result in new noise points. At the same time, it is found that the noise distribution of the improved brake system also has a great improvement for the sound pressure level (i.e., the noise points exceeding 80 dB rarely occur). This shows that the improvement of the structure makes the noise frequencies of system near 4.1 kHz and 7.5 kHz move toward the direction of lower frequency and reduce the sound pressure level, thus achieving the effect of restraining the brake squeal noise.

## 7. Conclusions

- (1) In this study, the design of three-layer structure of the brake pad is presented and the six-DOF kinematics model of the brake disc-brake pad is analyzed. Through the analysis of the above model, it is found that the mass and stiffness of the brake pad have an important influence on the stability of the brake system.
- (2) The unstable vibration modes of the brake system are obtained from the linear complex eigenvalue analysis, and the accuracy of predictions of the complex modal analysis model is verified by the bench test of the brake system, but there is overprediction. The test results show that the noise points of the brake system are mainly distributed near the frequency of 4.1 kHz, 7.5 kHz, and 12.7 kHz.
- (3) The proposed slotting design on the backplate of the brake pad by this study could greatly reduce the occurrence of brake squeal noise, especially that of the high frequency at 12.7 kHz, which provides a reliable theoretical guidance for the design of the brake system.
- (4) Due to the limitation of experimental conditions, the single test object and the experimental conditions may not be comprehensive enough, so this study still has some limitations. In addition, further research is needed on how to determine the slot size and slot position accurately according to the simulation analysis and the test structure.

## Conflicts of Interest

The authors declare that there are no conflicts of interest regarding the publication of this paper.

## Acknowledgments

The authors acknowledge the financial support by the National Natural Science Foundation of China (51575238) and Research on key technologies of brake-by-wire system (ZY2015009).

## References

- [1] N. M. Kinkaid, O. M. O'Reilly, and P. Papadopoulos, "Automotive disc brake squeal," *Journal of Sound and Vibration*, vol. 267, no. 1, pp. 105–166, 2003.
- [2] S. Oberst, *Analysis of Brake Squeal Noise*, Ph.D. thesis, School of Engineering and Information Technology, University College, University of New South Wales, Sydney NSW, Australia, 2011.
- [3] F. Chen, "Automotive disk brake squeal: an overview," *International Journal of Vehicle Design*, vol. 51, no. 1, pp. 39–72, 2009.
- [4] G. Genta and L. Morello, "The automotive chassis," *Components Design*, Springer Business Media, vol. 1, New York, NY, USA, 2009.
- [5] L. Hammerstrom and S. Jacobson, "Surface modification of brake discs to reduce squeal problems," *Wear*, vol. 261, no. 1, pp. 53–57, 2006.
- [6] S. Oberst and J. C. S. Lai, "Chaos in brake squeal noise," *Journal of Sound and Vibration*, vol. 330, no. 5, pp. 955–975, 2011.
- [7] S. W. Kung, K. B. Dunlap, and R. S. Ballinger, "Complex eigenvalue analysis for reducing low frequency brake squeal," in *Proceedings of the SAE Technical Paper Series*, p. 109, Pittsburgh, PA, USA, March 2000.
- [8] Y.-K. Hu and L. I. Nagy, "Brake squeal analysis by using nonlinear transient finite element method," in *Proceedings of the SAE Technical Paper Series*, pp. 1–8, Washington, DC, USA, August 1997.
- [9] A. R. AbuBakar and H. J. Ouyang, "Complex eigenvalue analysis and dynamic transient analysis in predicting disc brake squeal," *International Journal of Vehicle Noise and Vibrations*, vol. 2, no. 2, pp. 143–155, 2006.
- [10] Z. Zhang, S. Oberst, and J. S. C. Lai, "On the potential of uncertainty analysis for prediction of brake squeal propensity," *Journal of Sound and Vibration*, vol. 377, pp. 123–132, 2016.
- [11] H. Festjens, C. Gaël, R. Franck et al., "Effectiveness of multilayer viscoelastic insulators to prevent occurrences of brake squeal: a numerical study," *Applied Acoustics*, vol. 73, no. 11, pp. 1121–1128, 2012.
- [12] G. Ruhai, D. Shi, and G. A. Yao, "A research on the effects of viscoelastic ingredients in friction material formulation on the damping characteristics of brake pad," *Automotive Engineering*, vol. 30, no. 7, pp. 608–612, 2008, in Chinese.
- [13] The SAE Dynamometer Test Code Committee, *Disk Brake Dynamometer Squeal Noise Matrix*, SAE J2521, SAE, Washington, DC, USA, 2013.
- [14] Y. Dai, *Structural Dynamic Optimization of Vehicle Brake Pad Design for Squeal Noise Reduction*, The University of Alabama, Tuscaloosa, AL, USA, 2002.
- [15] F. Massi, Y. Berthier, and L. Baillet, "Contact surface topography and system dynamics of brake squeal," *Wear*, vol. 265, no. 11–12, pp. 1784–1792, 2008.

## Research Article

# Strength and Failure Mechanism of Composite-Steel Adhesive Bond Single Lap Joints

Kai Wei , Yiwei Chen, Maojun Li, and Xujing Yang 

State Key Laboratory of Advanced Design and Manufacturing for Vehicle Body, Hunan University, Changsha, Hunan 410082, China

Correspondence should be addressed to Xujing Yang; yangxujing@hnu.edu.cn

Received 19 October 2017; Accepted 16 January 2018; Published 21 March 2018

Academic Editor: Aniello Riccio

Copyright © 2018 Kai Wei et al. This is an open access article distributed under the Creative Commons Attribution License, which permits unrestricted use, distribution, and reproduction in any medium, provided the original work is properly cited.

Carbon fiber-reinforced plastics- (CFRP-) steel single lap joints with regard to tensile loading with two levels of adhesives and four levels of overlap lengths were experimentally analyzed and numerically simulated. Both joint strength and failure mechanism were found to be highly dependent on adhesive type and overlap length. Joints with 7779 structural adhesive were more ductile and produced about 2-3 kN higher failure load than MA830 structural adhesive. Failure load with the two adhesives increased about 147 N and 176 N, respectively, with increasing 1 mm of the overlap length. Cohesion failure was observed in both types of adhesive joints. As the overlap length increased, interface failure appeared solely on the edge of the overlap in 7779 adhesive joints. Finite element analysis (FEA) results revealed that peel and shear stress distributions were nonuniform, which were less severe as overlap length increased. Severe stress concentration was observed on the overlap edge, and shear failure of the adhesive was the main reason for the adhesive failure.

## 1. Introduction

With the aim to save energy and reduce emission, weight saving is of significant importance in the transportation industry. Composite, which exhibits high stiffness-to-weight and strength-to-weight ratios than traditional metal counterparts, has gained widespread usage for lightweight structures. In practical application, it is almost impossible to manufacture a structure as a whole body. Many structures are manufactured as single parts, and then connected through joints. The commonly used methods for joining composite parts are either through mechanical fastening or bonding. Mechanical fasteners including bolts, rivets, and pins have been commonly used for several decades [1–3]. The ease of disassembling components and allowing for reliable inspection has been a great benefit. However, the key problem is that high stress concentrations can develop around the fastener holes, and the joint can be brought to failure at far lower stress levels than expected [4]. Due to its larger bond area to distribute loads and eliminate stress concentration as well as keeping structure integrity, adhesive bonding is more attractive as compared to mechanical fastening joining methods [5].

Extensive researches have been conducted to investigate the bonded joints through analytical, experimental, and numerical methods. Previous researches focused on different affecting factors on the joint strength and damage mechanism [6–10]. The failure load is found to increase with overlap length and adhesive thickness. Material properties and geometry size have been investigated to significantly affect the joint strength and failure modes. On account of the effect of factors mentioned above, researchers latterly focused on improving the strength of the joints. The joint strength increased by modifying the shape of the joint [11, 12] and adding chamfer [13] and fillets [14]. The quality of the bonded joints depends highly on the manufacturing process. Some researchers thus presented surface treatment [15, 16] on the overlap region and curing conditions such as pressure and temperature. For the purpose of optimizing and designing a high-quality joint, stress distributions over the adhesive layer were obtained through numerical methods [17–19]. These simulation works can also predict the joint strength compared to experimental results. Later the finite element method coupled with the cohesive zone model was performed for failure evolution analysis [20, 21]. This can be used to

model the failure initiation and further propagation. Although the mechanical behaviors of the adhesive joints have been investigated as mentioned above, the understanding the strength and failure mechanism of the joints is still local and rough due to the complexity of the mechanical behaviors, especially for joints with composite substrates [22]. Therefore, it is necessary to conduct a detailed research for the CFRP-to-steel adhesive joints.

The present study mainly focused on the mechanical properties and failure behavior of CFRP-to-steel adhesively bonded single lap joints. Different joints were fabricated and tested according to eight different variances, including two kinds of adhesives and four overlap lengths. Mechanical properties were firstly shown and compared with each other. Both the experimental and numerical results about joint strength were then displayed for further detailed analysis. Finite element analysis was then conducted to compare with the experimental results. A detailed stress distribution analysis for various overlap length values was then exhibited, followed by a stress distribution comparison at three typical moments during the tensile process. Failure propagation analysis was carried out for a detailed understanding of the joints' damage evolution. Finally, photographs of the failure joints were exhibited for failure mode analysis.

## 2. Experiments

**2.1. Materials.** Two different structural adhesives were used in this study. Type 1 is 7779 adhesive which belongs to two-component polyurethane structural adhesive produced by Ashland. Type 2 (MA830) is a kind of two-liquid acrylic structural adhesive provided by Plexus. Both structural adhesives were prepared and tested to compare the mechanical properties with each other. In this study, the uniaxial tensile test was conducted based on the ISO standard 527-2, which is the determination of tensile properties of plastics. T-peel test was employed with regard to the ISO standard 11339, which is mainly applied for flexible-to-flexible bonded assemblies. And the thick-adherend testing method based on the ISO standard 11003-2 is employed to determine the shear behavior for both structural adhesives. The mechanical properties are finally summarized in Table 1.

The adherends selected for this study were carbon fiber-reinforced plastic (CFRP) laminates and DC04 steel commonly used for automobiles. The CFRP laminates were prepared using the vacuum-assisted resin infusion molding process. Carbon fiber (CC-P400-12) was employed as the reinforcement, and weft and warp were balanced plain woven. Each ply has a thickness of 0.44 mm, and 4 plies were used with  $0^\circ/90^\circ$  ply orientation. The epoxy (MA-8931A/B) was selected as the matrix. When the carbon fiber was soaked with resin under the impact of atmospheric pressure, the whole specimen was moved to a heating oven for curing at  $120^\circ\text{C}$  for 6 minutes. The whole specimen was then released from the mould after being cured and cut into the required size. The mechanical properties of the CFRP are listed in Table 2. Another selected adherend is DC04 steel, which is a kind of deep drawing steel with low yield strength and high ductility. It is widely used in the complex parts of

TABLE 1: Mechanical properties of the two adhesives.

Mechanical properties	7779	MA830
Young's modulus, $E$ (MPa)	1169	665
Tensile strength, $\sigma$ (MPa)	29.43	25.06
Shear modulus, $G$ (MPa)	389	251
Shear strength, $\tau$ (MPa)	20.40	18.49
Fracture energy release rate in tension, $G_T$ (N/mm)	2.75	0.56
Fracture energy release rate in shear, $G_S$ (N/mm)	2.03	1.23

TABLE 2: Mechanical properties of the CFRP adherend.

Mechanical properties	Value	Mechanical properties	Value
$E1$ (MPa)	26580	$\sigma_1$ (MPa)	883
$E2$ (MPa)	26580	$\sigma_2$ (MPa)	883
$E3$ (MPa)	3880	$\sigma_3$ (MPa)	87
$G12$ (MPa)	8482	V12	0.35
$G13$ (MPa)	3678	V13	0.3
$G23$ (MPa)	3678	V23	0.3

automobile. The mechanical properties of the DC04 steel are listed in Table 3.

**2.2. Single Lap Joints.** The geometry size of the single lap joint for tensile testing according to ISO 4587 is presented in Figure 1. The various overlap length with regard to the experiment requirement between the CFRP laminate and DC04 substrate is denoted as  $L_0$ .  $L$  represents the whole length of the specimen. The compensating plate was prepared with the same thickness corresponding to specific adherend.

According to literature review [14], the abrasive paper of grit size up to 1000 was used to polish the substrates, and acetone was applied to eliminate impurity of the substrate surfaces. Compensating plates were firstly bonded to the corresponding adherends, and lines in both adherends were drawn to dominate the overlap length. Adhesive was then evenly distributed on the overlap region of the DC04 substrates. Four small steel wires were employed to control the adhesive thickness in this process. The two substrates were boned together using a clip, and the whole specimen was finally put into an oven to cure for 2.5 h under the temperature of  $80^\circ\text{C}$ .

A full-factorial experimental design was employed with two levels of adhesive and four levels of overlap length giving total number of 8 tests. The detailed experiment with corresponding factors and levels is listed in Table 4. A quasistatic loading with the velocity of 2 mm/min was applied in tensile testing. For improving experimental accuracy, three replicates were conducted for each trial, and the normalized peak loads and failure displacements were recorded.

## 3. Finite Element Analysis

A numerical model was implemented and developed using the commercial software ABAQUS. The objective of finite element analysis (FEA) is to develop a model that could accurately predict the experimental results and present a detailed

TABLE 3: Mechanical properties of the DC04 adherend.

Adherend material	Young modulus (GPa)	Tensile strength (MPa)	Yield strength (MPa)	Elongation ratio	Poisson's ratio
DC04	203	316	170	78%	0.31

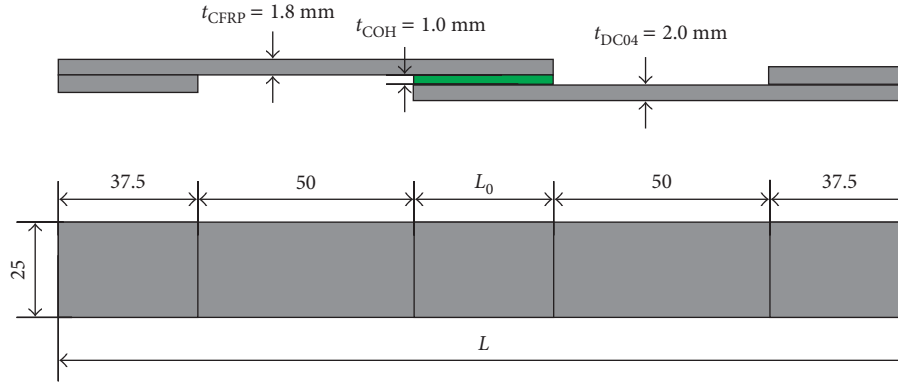


FIGURE 1: Schematic and dimensions of the single lap joints.

TABLE 4: Full-factorial experimental design with corresponding factors and levels.

Specimen	Adhesive type	$L_0$ (mm)	$L$ (mm)
1	7779	12.5	187.5
2	7779	20	195
3	7779	30	205
4	7779	40	215
5	MA830	12.5	187.5
6	MA830	20	195
7	MA830	30	205
8	MA830	40	215

stress distribution and failure evolution analysis of the joints. The single lap joint tests were numerically built in a three-dimensional model with the geometry and boundary conditions exhibited in Figure 2(a). The end with CFRP substrate was fixed thoroughly to clamp, while another end with DC04 substrate could only move in the loading direction. The loading was terminated when the displacement reached the set value with regard to experimental loading cases.

The element type selected to mesh the adhesive was COH2D4, while the CFRP and DC04 adherends were meshed with C3H20. The mesh was refined to have more concentration of elements in both the adherends near the adhesive for further stress analysis. The properties for the adherends were mainly based on the results obtained in experiments (Tables 2 and 3).

To reproduce the behaviors of the adhesive, the bilinear traction separate law was used to simulate the elastic behavior up to a peak and subsequent degradation of material properties up to failure. During tensile testing, the damage occurs under mixed-mode loading (Model I, Model II, and Model III). Figure 2(b) shows the bilinear traction separate law under a single loading mode. The curve associates stress with displacements connecting homologous nodes of the cohesive elements. The initial linear elastic corresponds to the first section until the stress reaching the maximum, after the adhesive stiffness is degraded. The cohesive failure

mainly contains two stages, including damage initiation and crack propagation. In the first stage, a quadratic nominal stress criterion is used to decide the damage initiation, as expressed below:

$$\left\{ \frac{\langle \sigma_I \rangle}{\sigma_I^0} \right\}^2 + \left\{ \frac{\sigma_{II}}{\sigma_{II}^0} \right\}^2 + \left\{ \frac{\sigma_{III}}{\sigma_{III}^0} \right\}^2 = 1, \quad (1)$$

where  $\sigma_i$  and  $\sigma_i^0$  ( $i = I, II, III$ ) are the cohesion and interfacial strength under loading of Model I, Model II, and Model III, respectively. When the sum of the equation on the left is less than 1, there is no initial damage. Otherwise, initial damage will develop in the cohesive layer. B-K fracture criterion is applied to dominate the crack evolution in the second stage, as given below:

$$G_{IC} + (G_{IIC} - G_{IC}) \left( \frac{G_{Shear}}{G_T} \right)^\eta = G_C, \quad (2)$$

where  $G_I$ ,  $G_{II}$ , and  $G_{III}$  represent fracture energy in three directions, respectively ( $G_{Shear} = G_{II} + G_{III}$ ,  $G_T = G_I + G_{Shear}$ ).  $G_{iC}$  ( $i = I, II, III$ ) is the critical strain energy release rate under the respective models, and  $G_C$  is the total of the three.  $\eta$  is a constant that is related to the properties of the materials. When the left of the equation reaches the value of  $G_C$ , the initial crack begins to propagate and finally leads to adhesive failure.

In order to perform further failure evolution analysis, a parameter defined as scalar stiffness degradation (SDEG) is used to represent the degradation degree of the adhesive. This parameter can be any value between 0 and 1. When adhesive is in the initial elastic part of mixed-mode loading, the adhesive elements have no damage to any degree and SDEG is set equal to 0. While, the adhesive elements failure completely, SDEG is set equal to 1, and the element is deleted.

## 4. Results and Discussion

**4.1. Mechanical Properties.** The load-displacement curves for tensile testing are presented in Figure 3, including both

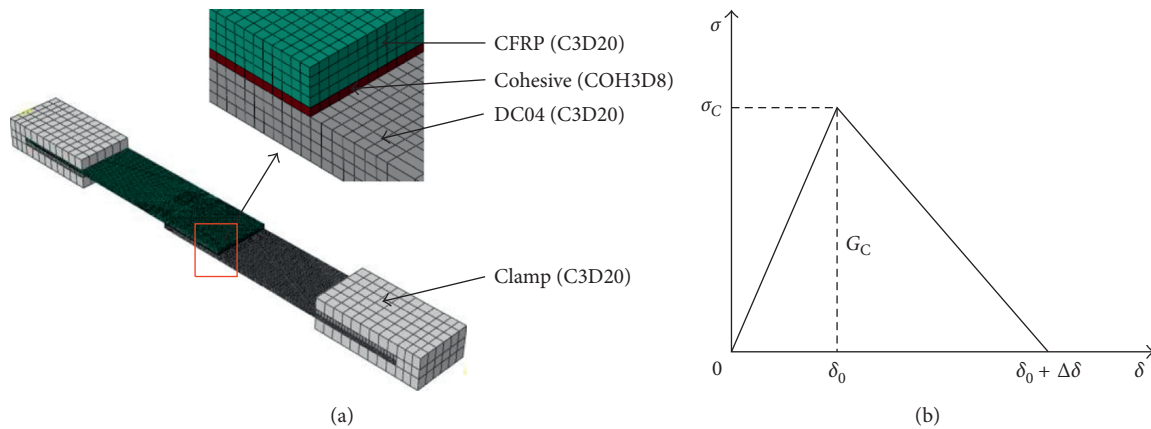


FIGURE 2: (a) The numerical model and (b) bilinear traction separate law for the finite element analysis.

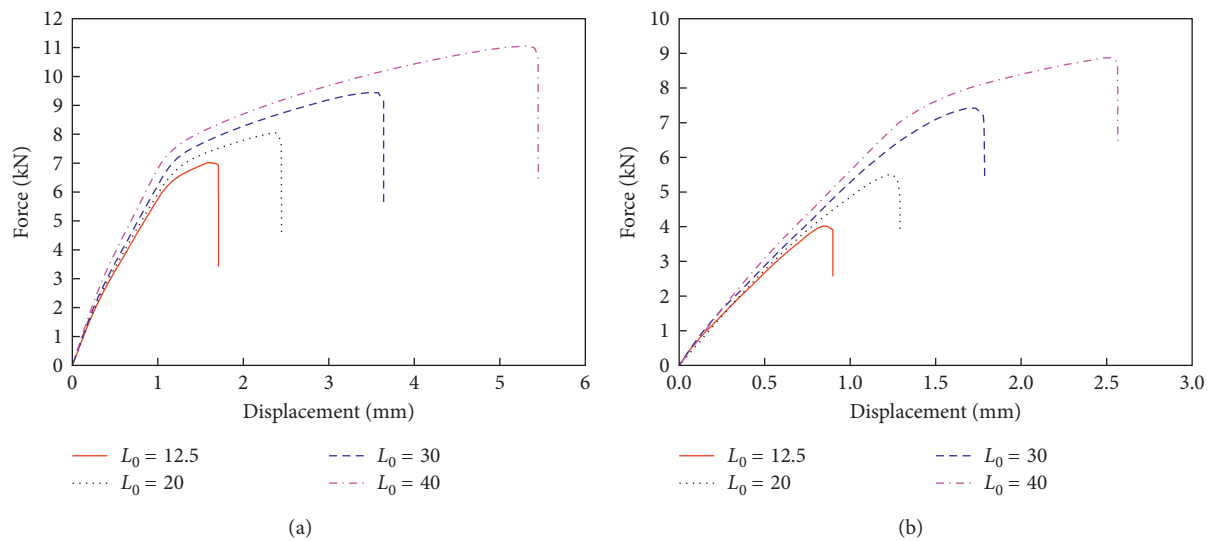


FIGURE 3: Tensile mechanical properties for joints using (a) 7779 structural adhesive and (b) MA830 structural adhesive.

adhesives with various overlap lengths. For joints using 7779 adhesive, the tensile process could be divided into three stages as shown in Figure 3(a). The slopes of the curves are kept constant in the first stage. When the load reached 2.5 kN, it entered the second stage, and the slope of the curves appeared a slight decrease. This mainly resulted from the strong toughness of the 7779 adhesive. As the adhesive was in force and began to soften, the stiffness of the joint decreased. When the load was between 6.5 and 7.5 kN in the third stage, the slope declined obviously, which was mainly due to that DC04 substrates achieved the yield strength, and plastic deformation occurs. As the loading continued, the joint finally failed when the load exceeded the strength. Since the failure load is the maximum force when the joint suffers failure, it is found that the failure load of the joint increased with the overlap length. For the joints using MA830 adhesive, the failure load also increased as overlap length increased, while the trend of the curves was different from those of using 7779 adhesive. When the overlap length was 12.5 and 20 mm, the slope of the curves was constant until complete failure of the joint.

The maximum load was less than 6 kN, and thus there was no plastic deformation for the DC04 adherend. However, for the lap length of 30 and 40 mm, the maximum load was higher than 7 kN, and the slope of the curves appeared an obvious decrease. All the four curves showed no decrease when the load reaching 2.5 kN. This was mainly due to the fact that MA830 adhesive was more brittle, and there was no plastic deformation for MA830 adhesive.

**4.2. Failure Load.** For detailed analysis of the joint, Figure 4 summarizes the failure load and the normalized value. The error bars are also added. The deviation should be caused by deviation of experimental procedure and the dispersion of properties for the materials, especially the adhesive and the CFRP. Numerical results were found to agree well with the experimental results within 5% relative error. It was found that joints bonded with 7779 adhesive damaged at a higher load (2-3 kN) than that of the joints using MA830 adhesive with the same overlap length. This was mainly due to that the 7779 structural adhesive was much more ductile and

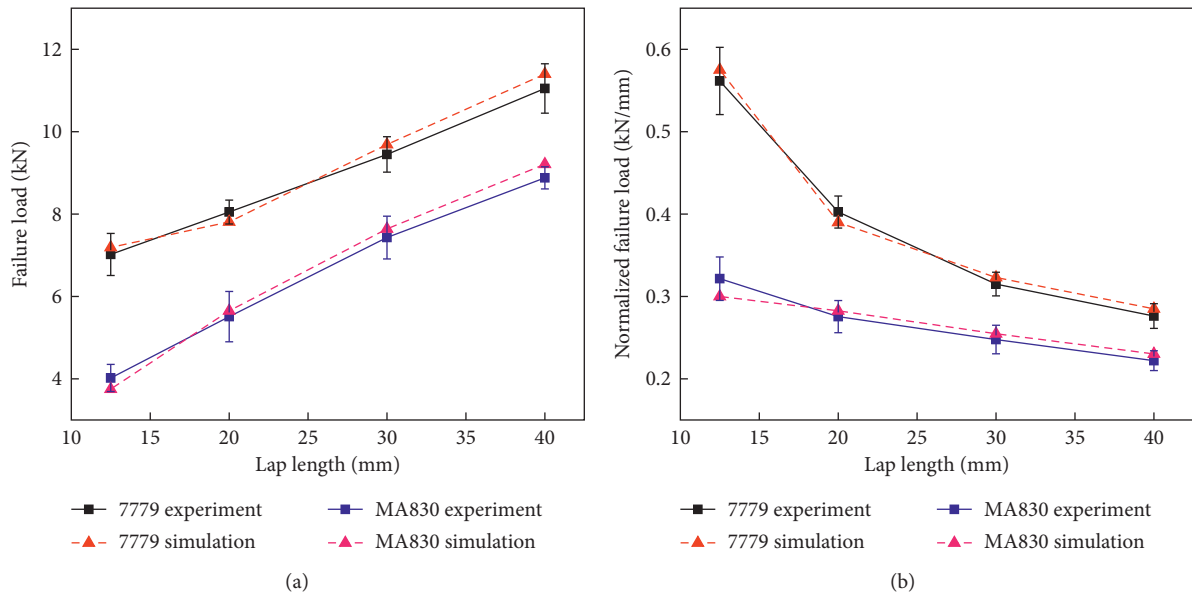


FIGURE 4: Experiment and simulation results: (a) failure load and (b) normalized failure load (failure load divided by overlap length).

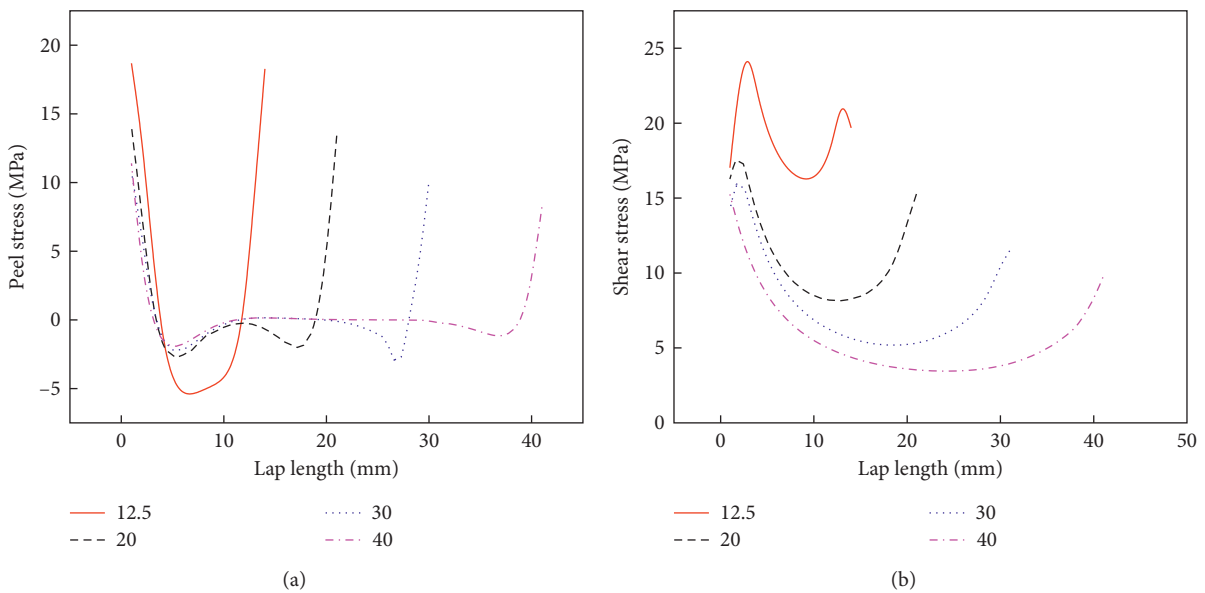


FIGURE 5: (a) Peel stress and (b) shear stress distributions with various overlap lengths.

flexible and could tolerate higher load than MA830 structural adhesive. For the failure load in Figure 4(a), both adhesives increased almost linearly with overlap length. As overlap length increased by 1 mm, the failure load of the 7779 structural adhesive joints increased by an average of about 147 N and that of the MA830 structural adhesive joint increased by an average of about 176 N. Moreover, normalized failure load, which is the failure load divided by the length of the overlap, is defined and plotted in Figure 4(b). The normalized failure load decreased dramatically with the increase of the overlap length which indicated that increasing the overlap length could strengthen the joint with only a limit degree.

**4.3. Stress Distribution.** The peel ( $S_{33}$ ) and shear ( $S_{13}$ ) stress distributions are compared at the adhesive layer in the middle width for various overlap lengths. All the stresses mentioned above were obtained under 6 kN load. Stress distributions in the adhesive layer of three typical moments during the whole tensile testing procedure were exhibited and compared with each other. Joints with MA830 adhesive were not considered in this section for the similar results.

The peel and shear stress distributions in the adhesive layer for different overlap lengths are presented in Figure 5. For the peel stress shown in Figure 5(a), the stress peaks located on the edge of the overlap region. And stress values on the left edge were slightly higher. This is mainly due to the

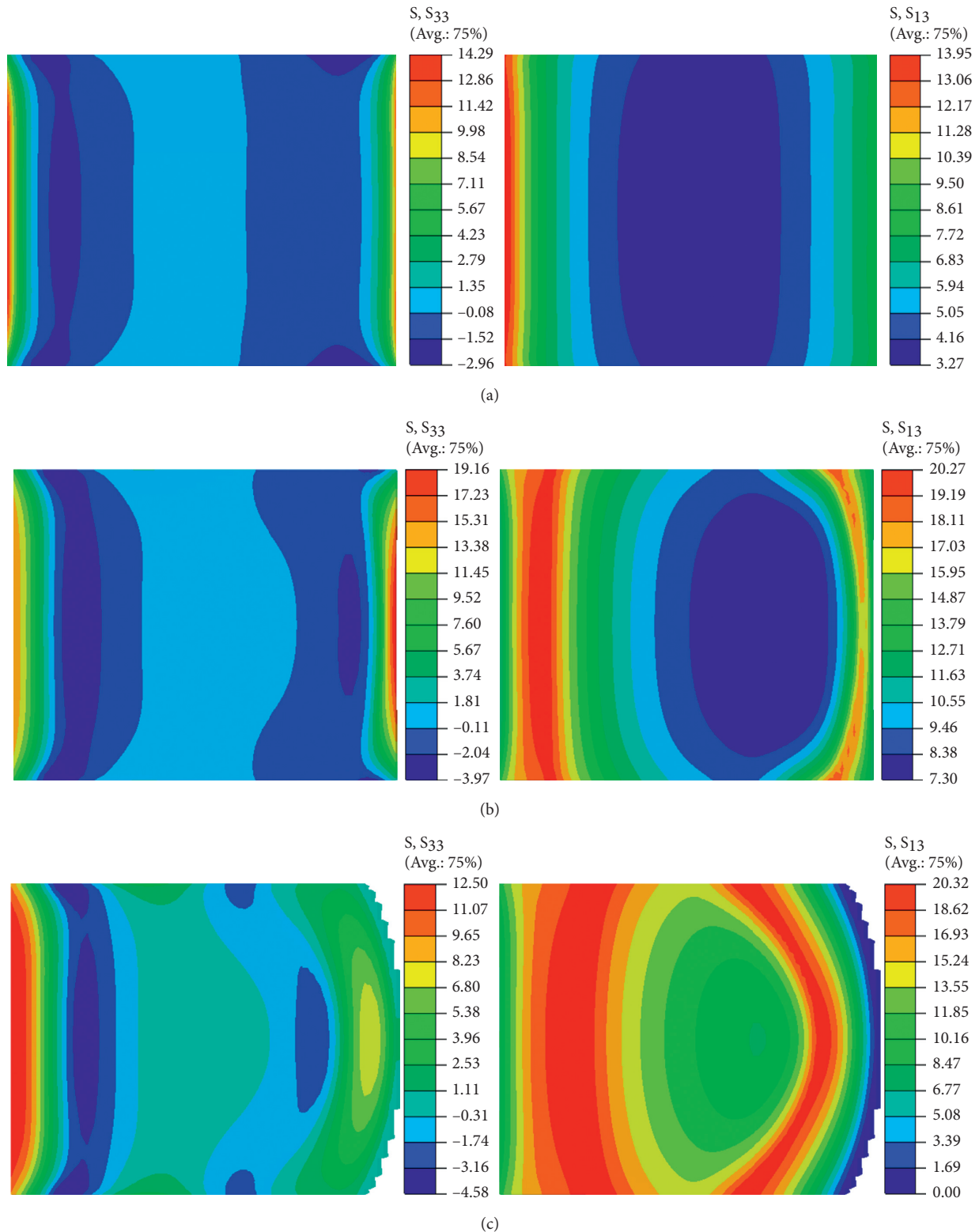


FIGURE 6: Peel and shear stress distributions at three different moments of the joint using 7779 adhesive with 30 mm overlap length. (a)  $t = 6$  s; (b)  $t = 49$  s; (c)  $t = 110$  s.

two types of adherends with different stiffness. Thus, different degrees of adherend flexure appeared at the overlap edges. On the left overlap edge, the higher degree of flexure of the DC04 adherend produced higher peak peel stresses.

As the overlap length increased, peel stress peaks decreased on both edges, and stress distributions were relatively much more uniform. For the shear stress exhibited in Figure 5(b), the maximum stress values on the left were 2–6 MPa higher



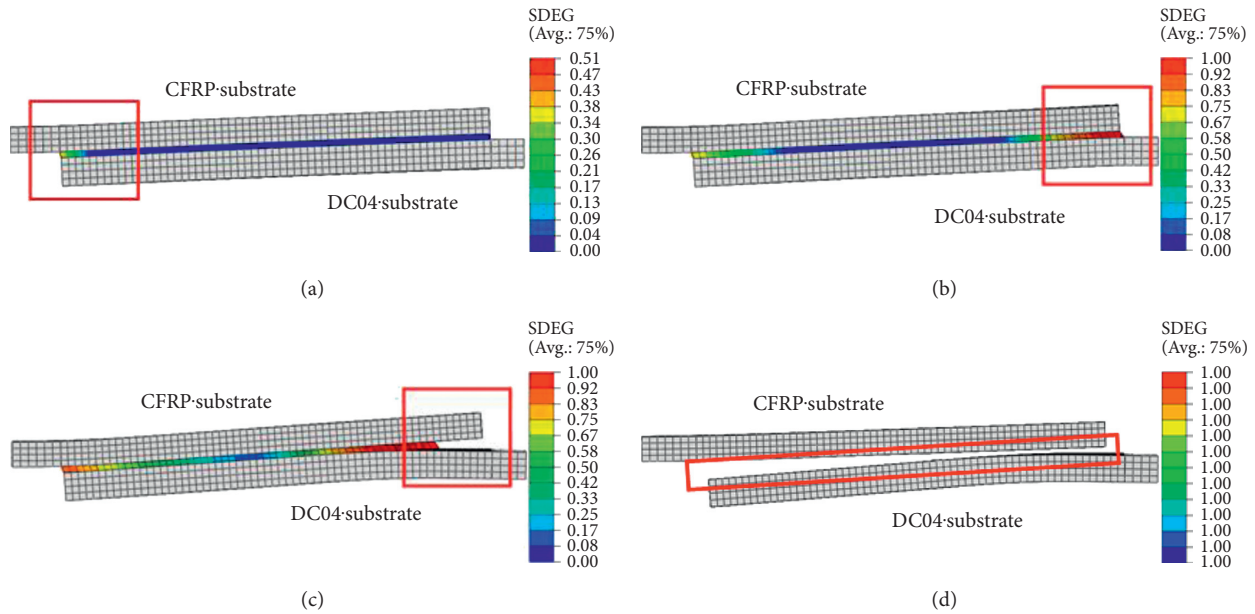


FIGURE 7: Failure process of the joints using 7779 adhesive with 30 mm overlap length: (a) beginning of degeneration; (b) degeneration proceeded; (c) cohesive failure appears and element deletion; (d) completely failure of adhesive layer.

than that on the right, which was mainly due to the fact that the two types of adherends had different tensile modulus. Furthermore, stress peaks of several types of joints located near the edge of the overlap rather than on the edge. As the overlap length increased, the position that peak stress appeared was close to both edges. This was mainly due to that under the 6 kN tensile loading, adhesive on both edges appeared degradation of varying degrees. This degeneration was slightly more severe on the left region. With increasing the overlap length, relatively more uniform peel distributions could be found. All the former analysis indicated that the increase of the lap length could reduce the stress concentration, thus leading to the failure load enhancement. However, both types of stress were distributed near the edges of the overlap region. The stresses in most of the middle regions were relatively small. The distribution characteristics indicated that increasing the overlap length can strengthen the joint with only a limit degree.

In order to investigate the stress distribution alongside the tensile loading process, different moments representing various stages were selected to analyze the stress state. The stress distributions are shown in Figure 6 with regard to three different moments, including  $t = 6$  s,  $t = 49$  s, and  $t = 110$  s, referring to no plastic deformation of the DC04 substrate, large plastic deformation of the DC04 substrate, and approaching to the failure load, respectively. For the moment of  $t = 6$  s, the tensile displacement was about 0.2 mm and in the stage of initial loading. The maximum peel stress of the adhesive was 14.92 MPa, and the maximum shear stress was about 13.95 MPa. While, the two stresses were far from their limits. For the moment of  $t = 49$  s, the displacement approached to be 1.64 mm, which mainly resulted from the deformation of the CFRP since the CFRP produced larger deformation than that of the DC04 adherend. The effect of asymmetric rigidity of the adherends could be seen in stress

distribution for its inhomogeneous distributions of both shear and peel stresses. On the right side of the adhesive layer, the shear stress dropped dramatically; however, the decline trend on the left was much slower. This was mainly due to that DC04 adherend produced a plastic deformation at this moment so that the tensile force was not transmitted to the adhesive on the right. The maximum peel stress reached 19.16 MPa, which was far from the stress limit (29.43 MPa). However, the highest shear stress was about 20.27 MPa and approached shear stress limits (20.4 MPa). When time is  $t = 110$  s, some of the cohesive elements became invalid and were deleted, which meant that complete failure appeared in the adhesive layer. The whole joint assumed to be almost the maximum load at this moment. The peel stress was 12.55 MPa, still far from reaching the limit stress. The maximum shear stress was 20.32 MPa and was very close to the stress limit, which implied that the cause of the joint failure was that the shear stress reached the shear limit of the adhesive.

**4.4. Failure Propagation.** Joint using 7779 structural adhesive with 30 mm overlap length was selected for the failure propagation analysis. As described in Section 3, SDEG is a parameter that represents the degradation degree of the adhesive. Figure 7(a) shows that the adhesive on the left was first degenerated. This was related to the relatively higher peel and shear stresses which was analyzed in Section 4.2. As the tensile loading continued, adhesive on the right shown in the Figure 7(b) also began to degenerate and the degeneration was much more severe than that on the left. Furthermore, SDEG of adhesive on the right firstly reached the value of 1, and the failure elements were deleted as could be seen in Figure 7(c). This phenomenon was mainly due to that two different materials were used as the adherends. Adhesive was fixed to the two substrates with

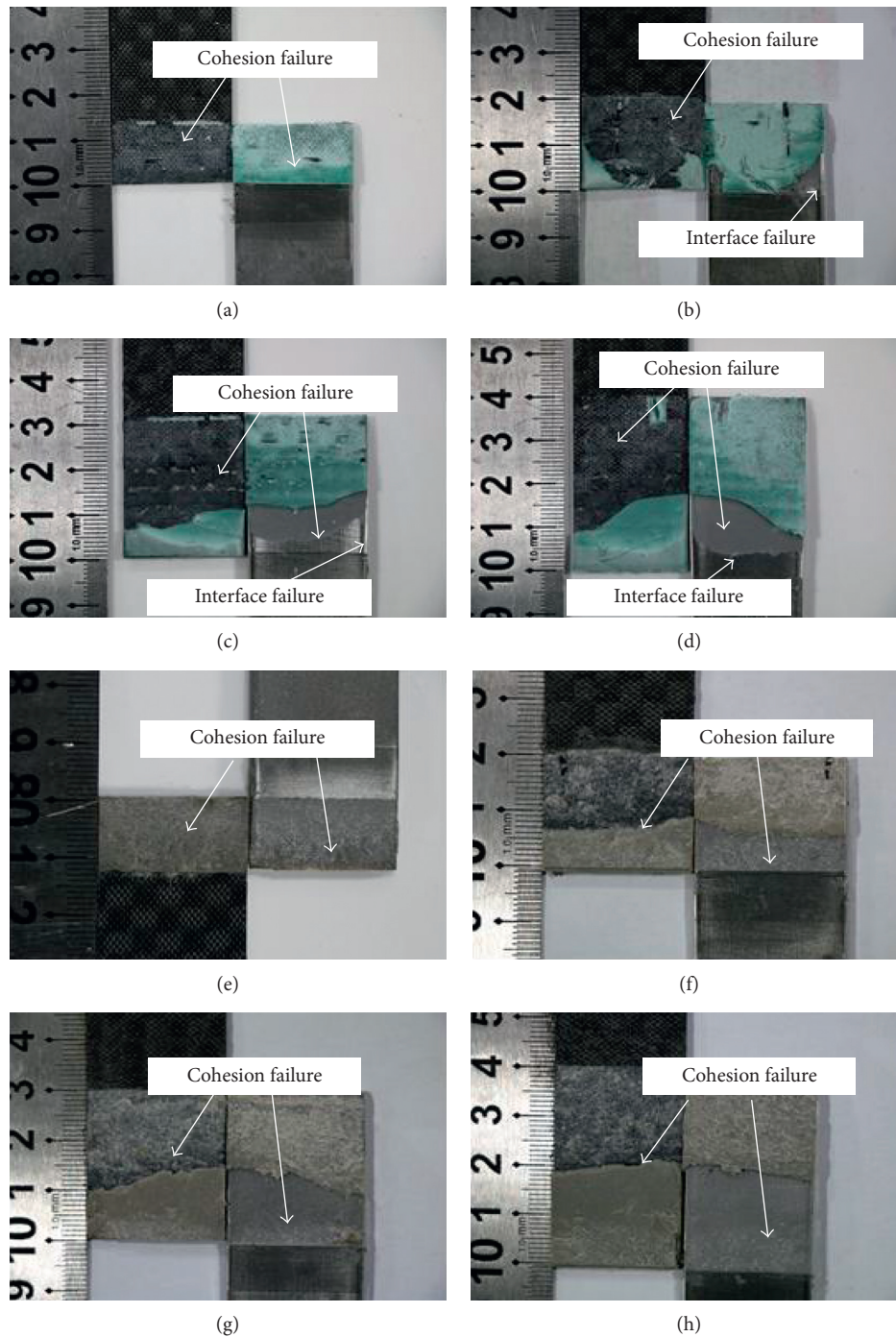


FIGURE 8: Failure models of 7779 adhesive joints with overlap lengths of (a) 12.5 mm, (b) 20 mm, (c) 30 mm, and (d) 40 mm. Failure models of MA830 adhesive joints with overlap lengths of (e) 12.5 mm, (f) 20 mm, (g) 30 mm, and (h) 40 mm.

various stiffness. For a specific loading, CFRP produced a larger deformation than the DC04 adherend. Thus, adhesive on the right edge deformed much more severe, and failure appeared in this region at the early stage. In Figure 7 (d), all the adhesive elements were in failure and deleted, and the DC04 adherends produced permanent plastic deformations in the joint area. The asymmetry degeneration of the adhesive layer could be easily seen from the failure process and this asymmetry distribution mainly resulted from the two different adherends.

**4.5. Failure Modes.** The failure modes of the two adhesives with various overlap lengths are shown in Figure 8. For the 7779 structural adhesive, there were two main failure modes including cohesion failure and interface failure. When the overlap length was 12.5 mm, it merely presented cohesion failure as shown in Figure 8(a). As the overlap length increased, the bending moment caused by load eccentricity became more severe. The peel stress on the edge of the overlap produced higher values and reached the peel stress limit of the adhesive. Thus, interface failure occurred and

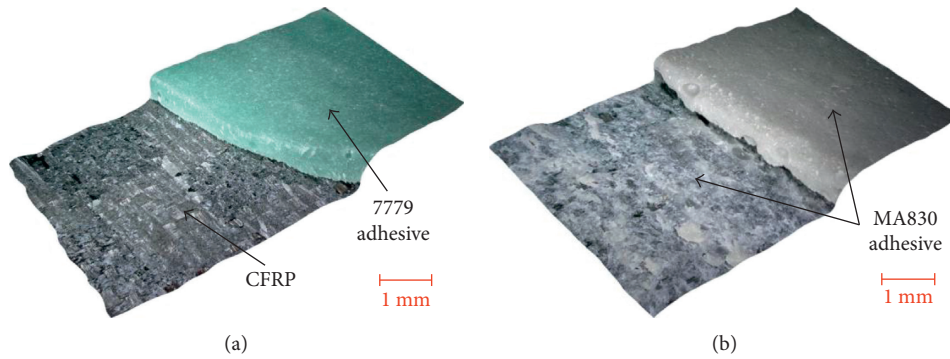


FIGURE 9: The morphology of the failure surfaces confirms the (a) interface failure and (b) cohesion failure (observed through a digital microscope KEYENCE VHX-5000).

became one of the failure modes as seen in Figure 8. Furthermore, the failure of bonding interface only occurred on the bonding surface between adhesive layer and DC04 substrate. This indicated that the 7779 adhesive had a better connection with CFRP adherends than DC04 adherends. As for joints of MA830 structural adhesive as shown in Figure 8, there was only cohesion failure for all different overlap lengths. This is mainly owing to the fact that joints of MA830 adhesive fail at a relative low load. Thus, peel stresses on the edge of the overlap were far from the stress limit of the adhesive, and there was no interface failure.

The detailed observations of the morphology for the failure surfaces were conducted through a digital microscope (KEYENCE VHX-5000). The morphologies of the failure surfaces are presented in Figure 9. As shown in Figure 9(a), for the 7779 adhesive in the joint, the adhesive is completely peeled off from the CFRP, and the CFRP is obviously visible in this specimen. Thus, this observation firmly confirms the interface failure model. On the contrary, as shown in Figure 9(b), residual MA830 adhesive can be clearly found on the CFRP, demonstrating the cohesion failure occurred within the adhesive.

## 5. Conclusions

The present work investigated the influences of the adhesive type and overlap length on the mechanical behavior and failure modes of bonded single lap joints via experimental and numerical studies. Main conclusions can be drawn as follows:

- (1) The joint strength was found to be highly dependent on adhesive type and overlap length. Joints using 7779 structural adhesive provided 2-3 kN failure load higher than that using MA830 structural adhesive. And failure load with two adhesives increased about 147~176 N with increasing 1 mm of the overlap length.
- (2) A finite element analysis model was established, and numerical results were within 5% relative error on predicting the failure load and joint strength compared with the experimental results. There was severe stress concentration on the edge of the joint. And the stress distributions in the overlap area were

nonuniform. The peel stress was responsible for the interface failure, and the cohesion failure is mainly caused by large shear stress. The shear stress reaching the limit stress of the adhesive was the main reason for the failure of the adhesive layer.

- (3) An asymmetry degeneration of the adhesive layer could be easily seen from the failure process analysis, which was mainly due to the asymmetric rigidity of the adherends.
- (4) The type of the adhesive and level of overlap length affected the failure modes significantly. The failure modes of the joints of 7779 structural adhesive presented cohesion failure and interface failure. While, MA830 adhesively bonded joints merely showed interface failure irrespective of the overlap length.

## Conflicts of Interest

The authors declare that they have no conflicts of interest.

## Acknowledgments

The authors are grateful for the support by the National Natural Science Foundation of China under Grant nos. 11602081 and 11302063. This work is also supported by Natural Science Foundation of Hunan Province under Grant no. 2017JJ3031, and the Fundamental Research Funds for the Central Universities under Grant no. 531107040934.

## References

- [1] K. J. Jadee and A. R. Othman, "Fiber reinforced composite structure with bolted joint—a review," *Key Engineering Materials*, vol. 471-472, pp. 939-944, 2011.
- [2] D. V. T. G. Pavan Kumar, S. Sathiya Naarayan, S. Kalyana Sundaram, and S. Chandra, "Further numerical and experimental failure studies on single and multi-row riveted lap joints," *Engineering Failure Analysis*, vol. 20, pp. 9-24, 2012.
- [3] A. T. T. Nguyen, C. K. Amarasinghe, M. Brandt, S. Feih, and A. C. Orifici, "Loading, support and geometry effects for pin-reinforced hybrid metal-composite joints," *Composites Part A: Applied Science and Manufacturing*, vol. 98, pp. 192-206, 2017.

- [4] N. Chowdhury, W. K. Chiu, J. Wang, and P. Chang, "Static and fatigue testing thin riveted, bonded and hybrid carbon fiber double lap joints used in aircraft structures," *Composite Structures*, vol. 121, pp. 315–323, 2015.
- [5] A. Riccio, R. Ricchiuto, F. Di Caprio, A. Sellitto, and A. Raimondo, "Numerical investigation of constitutive material models on bonded joints in scarf repaired composite laminates," *Engineering Fracture Mechanics*, vol. 173, pp. 91–106, 2017.
- [6] G. R. Rajkumar, M. Krishna, H. N. Narasimhamurthy, and Y. C. Keshavamurthy, "Statistical investigation of the effect of process parameters on the shear strength of metal adhesive joints," *Journal of The Institution of Engineers (India): Series C*, vol. 98, pp. 335–342, 2016.
- [7] L. Liao, C. Huang, and T. Sawa, "Effect of adhesive thickness, adhesive type and scarf angle on the mechanical properties of scarf adhesive joints," *International Journal of Solids and Structures*, vol. 50, no. 25–26, pp. 4333–4340, 2013.
- [8] A. J. Gunnion and I. Herszberg, "Parametric study of scarf joints in composite structures," *Composite Structures*, vol. 75, no. 1–4, pp. 364–376, 2006.
- [9] L. F. M. da Silva, T. N. S. S. Rodrigues, M. A. V. Figueiredo, M. F. S. F. de Moura, and J. A. G. Chousal, "Effect of adhesive type and thickness on the lap shear strength," *Journal of Adhesion*, vol. 82, no. 11, pp. 1091–1115, 2006.
- [10] D.-B. Lee, T. Ikeda, N. Miyazaki, and N.-S. Choi, "Effect of bond thickness on the fracture toughness of adhesive joints," *Journal of Engineering Materials and Technology*, vol. 126, no. 1, p. 14, 2004.
- [11] M. You, Z. Li, X.-L. Zheng, S. Yu, G.-Y. Li, and D.-X. Sun, "A numerical and experimental study of preformed angle in the lap zone on adhesively bonded steel single lap joint," *International Journal of Adhesion and Adhesives*, vol. 29, no. 3, pp. 280–285, 2009.
- [12] S. L. S. Nunes, R. D. S. G. Campilho, F. J. G. Da Silva et al., "Comparative failure assessment of single and double lap joints with varying adhesive systems," *Journal of Adhesion*, vol. 92, no. 7–9, pp. 610–634, 2016.
- [13] M. You, Z.-M. Yan, X.-L. Zheng, H.-Z. Yu, and Z. Li, "A numerical and experimental study of adhesively bonded aluminium single lap joints with an inner chamfer on the adherends," *International Journal of Adhesion and Adhesives*, vol. 28, no. 1–2, pp. 71–76, 2008.
- [14] S. Akpinar, M. O. Doru, A. Özel, M. D. Aydin, and H. G. Jahanpasand, "The effect of the spew fillet on an adhesively bonded single-lap joint subjected to bending moment," *Composites Part B: Engineering*, vol. 55, pp. 55–64, 2013.
- [15] A. M. Pereira, J. M. Ferreira, F. V. Antunes, and P. J. Bártolo, "Analysis of manufacturing parameters on the shear strength of aluminium adhesive single-lap joints," *Journal of Materials Processing Technology*, vol. 210, no. 4, pp. 610–617, 2010.
- [16] C. Sperandio, J. Bardon, A. Laachachi, H. Aubriet, and D. Ruch, "Influence of plasma surface treatment on bond strength behaviour of an adhesively bonded aluminium-epoxy system," *International Journal of Adhesion and Adhesives*, vol. 30, no. 8, pp. 720–728, 2010.
- [17] M. Elhannani, K. Madani, E. Legrand, S. Touzain, and X. Feaugas, "Numerical analysis of the effect of the presence, number and shape of bonding defect on the shear stresses distribution in an adhesive layer for the single-lap bonded joint; part 1," *Aerospace Science and Technology*, vol. 62, pp. 122–135, 2017.
- [18] A. Riccio, G. Di Felice, F. Scaramuzzino, and A. Sellitto, "A practical tool for the preliminary design of bonded composite repairs," *Applied Composite Materials*, vol. 21, no. 3, pp. 495–509, 2014.
- [19] K. N. Anyfantis and N. G. Tsouvalis, "Loading and fracture response of CFRP-to-steel adhesively bonded joints with thick adherends—part II: numerical simulation," *Composite Structures*, vol. 96, pp. 858–868, 2013.
- [20] T. E. A. Ribeiro, R. D. S. G. Campilho, L. F. M. da Silva, and L. Goglio, "Damage analysis of composite-aluminium adhesively-bonded single-lap joints," *Composite Structures*, vol. 136, pp. 25–33, 2016.
- [21] A. Riccio, A. Sellitto, S. Saputo, A. Russo, M. Zarrelli, and V. Lopresto, "Modelling the damage evolution in notched omega stiffened composite panels under compression," *Composites Part B: Engineering*, vol. 126, pp. 60–71, 2017.
- [22] W. Xu and Y. Wei, "Strength and interface failure mechanism of adhesive joints," *International Journal of Adhesion and Adhesives*, vol. 34, pp. 80–92, 2012.

## Research Article

# Mechanical Characterization of Lightweight Foamed Concrete

**Marcin Kozłowski**<sup>1</sup> and **Marta Kadela**<sup>2</sup>

<sup>1</sup>*Department of Structural Engineering, Faculty of Civil Engineering, Silesian University of Technology,  
5 Akademicka St., 44-100 Gliwice, Poland*

<sup>2</sup>*Building Research Institute, 1 Filtrowa St., 00-611 Warszawa, Poland*

Correspondence should be addressed to Marta Kadela; [m.kadela@itb.pl](mailto:m.kadela@itb.pl)

Received 3 October 2017; Accepted 20 December 2017; Published 18 March 2018

Academic Editor: Kai Wei

Copyright © 2018 Marcin Kozłowski and Marta Kadela. This is an open access article distributed under the Creative Commons Attribution License, which permits unrestricted use, distribution, and reproduction in any medium, provided the original work is properly cited.

Foamed concrete shows excellent physical characteristics such as low self weight, relatively high strength and superb thermal and acoustic insulation properties. It allows for minimal consumption of aggregate, and by replacement of a part of cement by fly ash, it contributes to the waste utilization principles. For many years, the application of foamed concrete has been limited to backfill of retaining walls, insulation of foundations and roof tiles sound insulation. However, during the last few years, foamed concrete has become a promising material for structural purposes. A series of tests was carried out to examine mechanical properties of foamed concrete mixes without fly ash and with fly ash content. In addition, the influence of 25 cycles of freezing and thawing on the compressive strength was investigated. The apparent density of hardened foamed concrete is strongly correlated with the foam content in the mix. An increase of the density of foamed concrete results in a decrease of flexural strength. For the same densities, the compressive strength obtained for mixes containing fly ash is approximately 20% lower in comparison to the specimens without fly ash. Specimens subjected to 25 freeze-thaw cycles show approximately 15% lower compressive strengths compared to the untreated specimens.

## 1. Introduction

Foamed concrete is known as light-weight or cellular concrete. It is commonly defined as a cementitious material with a minimum of 20% (by volume) mechanically entrained foam in the mortar mix where air-pores are entrapped in the matrix by means of a suitable foaming agent [1]. It shows excellent physical characteristics such as low self weight, relatively high strength, and superb thermal and acoustic insulation properties. It allows for minimal consumption of aggregate, and by replacement of a part of cement by fly ash, it contributes to the waste utilization principles [2]. By a proper selection and dosage of components and the foaming agent, a wide range of densities (300–1600 kg/m<sup>3</sup>) can be achieved for various structural purposes, insulation, or filling applications [2].

Foamed concrete has been known for almost a century and was patented in 1923 [3]. The first comprehensive study of foamed concrete was carried out in the 1950s and 1960s by

Valore [3, 4]. Following this research, more detailed evaluation regarding the composition, properties, and applications of cellular concrete was reported by Rudnai [5], as well as by Short and Kinniburgh [6] in 1963. New mixtures were developed in the late 1970s and early 1980s, which led to the increased commercial use of foamed concrete in building constructions [7, 8].

For many years, the application of foamed concrete has been limited to backfill of retaining walls, insulation of foundations, and sound insulation [8]. However, in the last few years, foamed concrete has become a promising material also for structural purposes [7, 9], for example, stabilization of weak soils [10, 11], a base layer of sandwich solutions for foundation slabs [12], industrial floors [13], and highway as well as subway engineering applications [14, 15].

With the increasing environmental challenges, it is paramount that sustainable materials are researched for a wider range of applications to offer feasible alternatives alongside conventional materials.

TABLE 1: Mix proportions.

Mix symbol	Foaming agent content (l/100 kg C)	Cement (kg)	Fly ash (kg)	Water (kg)	Foaming agent (kg)	$w_{\text{eff}}/c$ (-)
FC1	2.00	25.00	0.00	10.50	0.50	0.44
FC2	4.00	25.00	0.00	10.00	1.00	0.44
FC3	6.00	25.00	0.00	9.50	1.50	0.44
FC4	8.00	25.00	0.00	9.00	2.00	0.44
FC5	10.00	25.00	0.00	8.50	2.50	0.44
FCA1	2.00	25.00	1.25	10.50	0.50	0.44
FCA2	4.00	25.00	1.25	10.00	1.00	0.44
FCA3	6.00	25.00	1.25	9.50	1.50	0.44
FCA4	8.00	25.00	1.25	9.00	2.00	0.44
FCA5	10.00	25.00	1.25	8.50	2.50	0.44

TABLE 2: Cement chemical composition (%).

SiO <sub>2</sub>	Al <sub>2</sub> O <sub>3</sub>	Fe <sub>2</sub> O <sub>3</sub>	CaO	MgO	SO <sub>3</sub>	Na <sub>2</sub> O	K <sub>2</sub> O	Cl
19.5	4.9	2.9	63.3	1.3	2.8	0.1	0.9	0.05

TABLE 3: Physical properties of cement.

Specific surface area (m <sup>2</sup> /kg)	Specific gravity (g/cm <sup>3</sup> )	Compressive strength (MPa)	
		After days	
3840	3.06	2	28
		28.0	58.0

Foamed concrete, being an alternative to ordinary concrete, fulfills the criteria of the principles of sustainability in building constructions [16–18]. The general principles, based on the concept of sustainable development as it applies to the life cycle of buildings and other construction works, are identified in ISO 15392:2008. First, foamed concrete consumes relatively low amount of raw material in relation to the amount of hardened state. Second, during its production, recycled materials such as fly ash can be used. In this way, foamed concrete contributes to the disposal of waste products of thermal power plants. Third, foamed concrete can be recycled and used as replacement of sand in insulation materials. Moreover, the manufacturing of foamed concrete is nontoxic, and the product does not emit toxic gases when it is exposed to fire. At last, it is cost-effective not only during the construction stage but also throughout lifetime operation and maintenance of the structure.

Besides contribution to the disposal of the waste products of thermal power plants, the addition of fly ash improves the workability of the fresh foamed concrete mix and has positive effect on drying shrinkage [2, 19]. On one hand, the only drawback of this mineral additive is lower early strength of mortar in comparison to the mix without fly ash [20]. On the other, it has been proven that the long-term strength is improved [19, 21].

Despite its favourable and promising strength and physical properties, foamed concrete is still utilized in limited scale, particularly for structural applications. This is mainly due to the insufficient knowledge regarding its mechanical properties and small number of research on its fracture behaviour [22–28].

TABLE 4: Fly ash chemical composition (%).

SiO <sub>2</sub>	Al <sub>2</sub> O <sub>3</sub>	Fe <sub>2</sub> O <sub>3</sub>	CaO	MgO	SO <sub>3</sub>	Na <sub>2</sub> O	K <sub>2</sub> O
76.5	1.42	5.80	3.61	1.63	0.263	0.038	0.096

The main objective of this work is to investigate the mechanical characteristics of foamed concrete with varying density (400–1400 kg/m<sup>3</sup>). A series of tests was performed to examine compressive strength, elastic modulus, flexural strength, and material degradation characteristics after freeze-thaw cycles.

## 2. Experimental Program

*2.1. Specimens Preparation and Concrete Mix Composition.* The materials used in this study were Portland cement, fly ash, water, and foaming agent. The compositions of the mix are presented in Table 1. The industrial Portland cement was CEM I 42.5 R [29], according to PN-EN 197-1:2011. Its chemical composition and physical properties, measured as per PN-EN 196-6:2011 and PN-EN 196-6:2011-4, are given in Tables 2 and 3. Tap water was used in all experiments. Compressive strength of cement was determined according to PN-EN 196-1:2016-07 (Table 3).

To improve the workability and reduce shrinkage, fly ash was used in some mixes. The ash used met the requirements of PN-EN 450-1:2012. Its chemical composition is given in Table 4.

A commercial foaming agent was used to produce foam. The liquid agent was pressurized with air at approximately 5 bars in order to make the stable foam with a density of approximately 50 kg/m<sup>3</sup>. Cement pastes with 2 ÷ 10 litres of liquid foaming agent for 100 kg of cement were prepared.

Two different types of concrete mixes (one without fly ash and the other with fly ash) were used. In total, 10 mixes were produced, five specimens for one concrete mix (Table 1). A constant  $w_{\text{eff}}/c = 0.44$  ratio was used for all mixes ( $w_{\text{eff}}$  includes water and liquid foaming agent;  $c$  is the cement content). It was based on the results of Jones and McCarthy [7] and Xianjun et al. [30]. The target densities of hardened foamed concrete to be produced in this study were from 400 to 1400 kg/m<sup>3</sup>.

The entire manufacturing process of foamed concrete must carefully consider the densities of the mix, the foaming production rate, and other factors in order to prepare high-

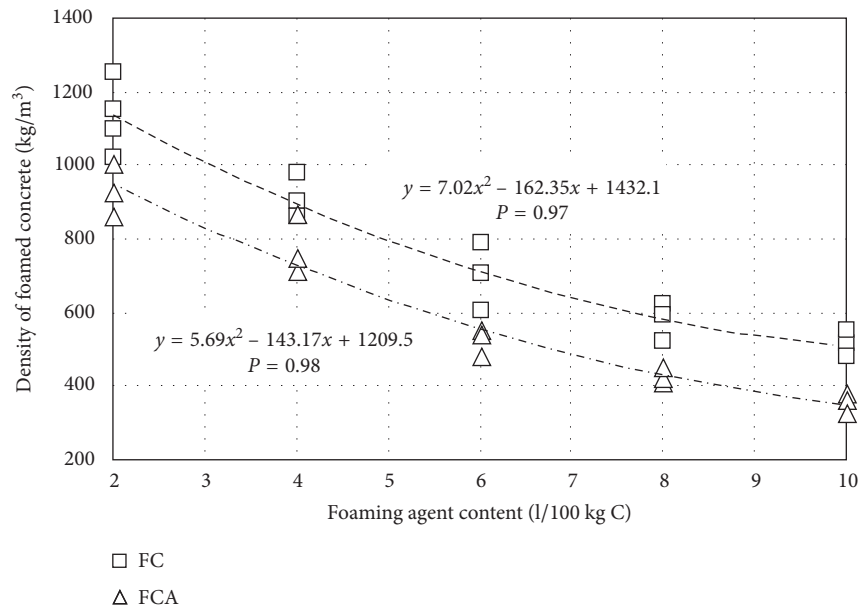


FIGURE 1: Apparent density of foamed concrete specimens FC and FCA as a function of foaming agent content.

quality foamed concrete. The key factors to produce stable foamed concrete were pressurizing of foaming agent at stable pressure and constant rotational speed of mixing the components.

All specimens, after casting in steel moulds, were covered and stored in a curing room at  $20 \pm 1^\circ\text{C}$  and 95% humidity for 24 hours. Subsequently, the samples were removed from the moulds and stored in ambient conditions (at  $20 \pm 1^\circ\text{C}$  and  $60 \pm 10\%$  humidity) for 28 or 42 days before testing.

**2.2. Tests.** Foamed concrete is a relatively new material, and currently there are no standardized test methods to measure its physical and mechanical properties. Therefore, procedures for preparation of specimens and testing methods, usually used for ordinary concrete, were adapted in this research. The compressive strength, modulus of elasticity, and flexural strength were determined according to the recommendations: PN-EN 12390-3:2011 + AC:2012, Instruction of Research Building Institute No. 194/98, PN-EN 12390-13:2014, and PN-EN 12390-5:2011, respectively. The density was measured as per PN-EN 12390-7:2011.

Compressive strength was measured with  $150 \times 150 \times 150$  mm standard cubes as stated in PN-EN 12390-3:2011 + AC:2012. The loading rate was assumed according to PN-EN 772-1:2015 + A1:2015 as for cellular concrete masonry units.

Elasticity modulus was determined according to the Instruction of Research Building Institute No. 194/98 and PN-EN 12390-13:2014-02 with cylindrical specimens with the dimensions of  $150 \times 300$  mm. The loading rate was  $0.1 \pm 0.05$  MPa/s, according to PN-EN 679:2008 as for cellular concrete masonry units. Two electrical resistance strain gauges with 100 mm measurement length were bonded on two opposite sides of the specimens at mid-height. The stress-strain characteristic was recorded for the evaluation of modulus of elasticity.

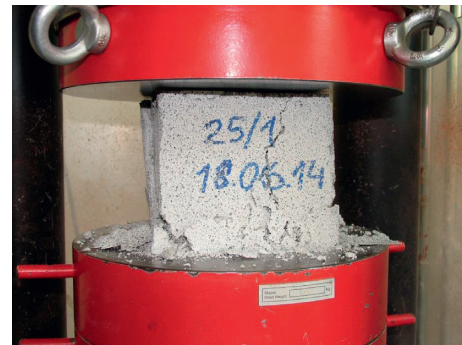


FIGURE 2: Typical failure pattern observed during compression tests with cube specimens.

Flexural strength was tested in three-point bending setup with beams  $100 \times 100 \times 500$  mm, according to PN-EN 12390-5:2011. The nominal distance between the supports was 300 mm. The rollers allowed for free horizontal movement. The specimens were loaded at constant displacement rate of 0.1 mm/min as an optimum value determined experimentally.

Degradation characteristics under freeze-thaw cycles were evaluated with  $150 \times 150 \times 150$  mm standard cubes. The compressive strength was determined with the procedure as described before. The test campaign consisted of 25 cycles of freezing and thawing. Each cycle included cooling of the specimens to the temperature of  $-18^\circ\text{C}$  within 2 h. The samples were then kept frozen for 8 h at  $-18 \pm 2^\circ\text{C}$  and thawed in water at the temperature of  $+19^\circ\text{C} \pm 1^\circ\text{C}$  for 4 h. Reference specimens were kept immerse in water as references.

### 3. Results and Discussion

**3.1. Apparent Density.** The dosage of foaming agent highly influences the density of mix and hardened foamed concrete.

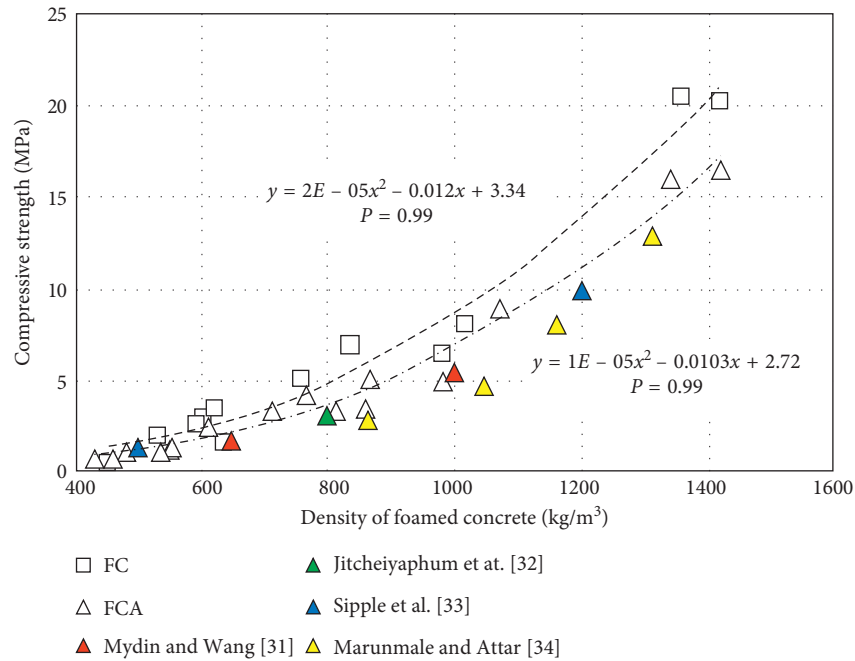


FIGURE 3: Compressive strengths of foamed concrete FC and FCA as a function of density of foamed concrete.

Figure 1 shows the relationship between the dosage of foaming agent and the apparent density of hardened foamed concrete for the specimens without fly ash (FC) and the other with fly ash (FCA). The apparent density of hardened foamed concrete is strongly correlated with the foam content and the composition of cement paste and air voids in fresh mix. The increase of foam content is accompanied by the increase of volume of fresh concrete, which results in a decrease of density of hardened foamed concrete. It can be observed that there are exponential relationships for FC and FCA specimens. Moreover, results obtained in FC show density level of approximately 20% higher than FCA. This can be explained by the fact that the process of hardening is slowed down in the specimens containing fly ash. The physical reaction between fly ash and air-pores results in larger number of air-pores entrapped in the mix. It was also found that the mixes with the foaming agent content above 10 litres per 100 kg of cement resulted in unstable mix. The results were approximated with polynomial functions as shown in Figure 1.

**3.2. Compressive Strength.** Cube foamed concrete specimens tested in compression present the mechanism of failure similar to ordinary concrete. A typical conical postbreakage failure pattern was observed for all specimens (Figure 2).

The compressive strengths of foamed concrete without ash (FC) and foamed concrete with addition of fly ash (FCA) as a function of apparent density are presented in Figure 3. It can be noticed that there are exponential relationships for both FC and FCA; however, there seems to be a difference between the strengths obtained from FC and FCA samples. The specimens without ash seem to show higher strengths than the mixtures containing ash. This is due to the fact that the process of hardening is slowed down due to the presence

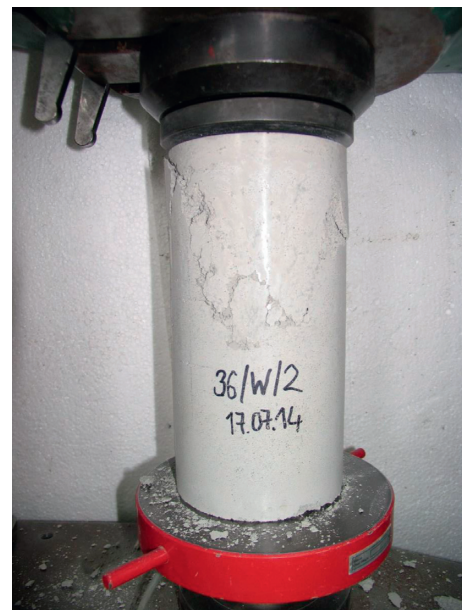


FIGURE 4: Typical failure pattern observed during compression tests with cylindrical specimens.

of fly ash [20]. In addition, this difference increases along with the density. The values of compressive strengths obtained correspond to the results of the works of others [31–34]. The results were approximated with polynomial functions as shown in Figure 3.

**3.3. Modulus of Elasticity.** Cylindrical foamed concrete specimens tested in compression present the mechanism of failure similar to ordinary concrete. A typical conical postbreakage failure pattern was observed for all specimens



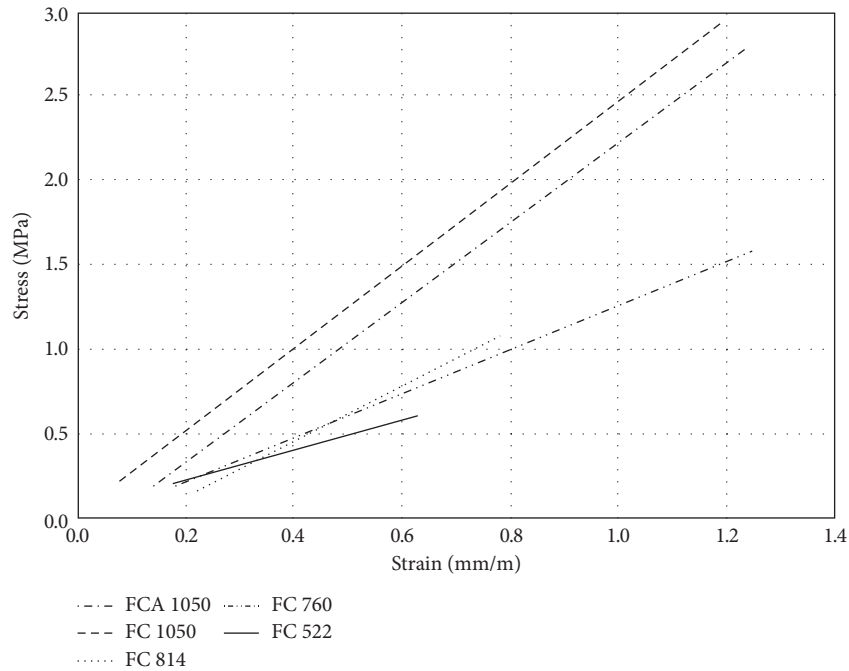


FIGURE 5: Stress-strain relationships of cylindrical specimens FC and FCA.

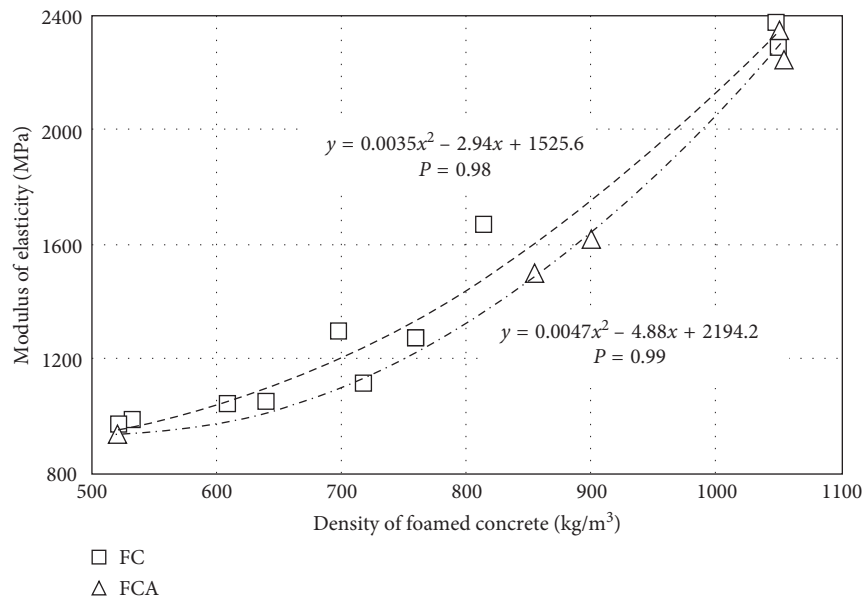


FIGURE 6: Modulus of elasticity of foamed concrete FC and FCA as a function of density of foamed concrete.

(Figure 4). Stress-strain relationships of cylindrical specimens are presented in Figure 5. The plots show the relations in the range of 0.2 MPa until failure, according to PN-EN 12390-13: 2014-02.

Figure 6 shows the relationships between the modulus of elasticity of foamed concrete and its density. It can be observed that there are exponential relationships for FC and FCA. The specimens without fly ash seem to have higher modulus of elasticity than the mixtures containing fly ash

[35]. The values of modulus of elasticity obtained correspond to the results of the works of Aldridge [8].

**3.4. Flexural Strength.** Figure 7 presents the relationship between the density of foamed concrete and the flexural strength. The tests were carried out on specimens without fly ash. Figure 7 includes also the results of experiments carried out by authors and reported in [23–28]. The decrease of

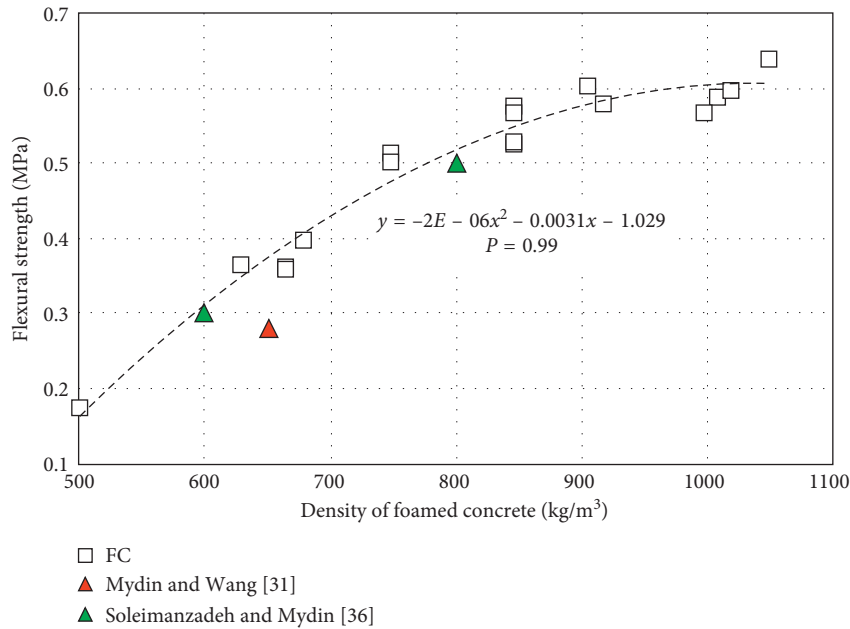


FIGURE 7: Flexural strength as a function of density of foamed concrete.

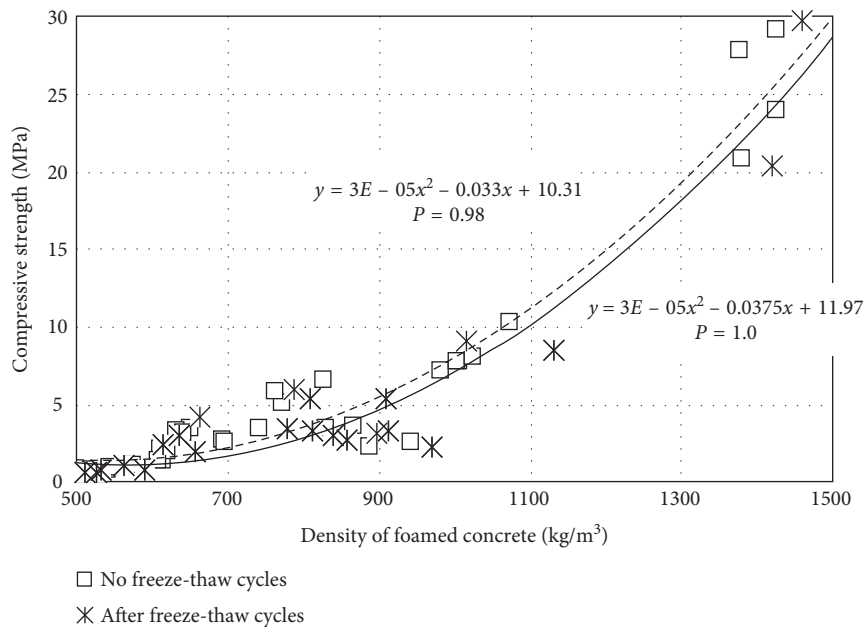


FIGURE 8: Compressive strength of foamed concrete after 25 freeze-thaw cycles as a function of density.

flexural tensile strength with the decrease of the density of the foamed concrete can be noted. The values of flexural strengths correspond to the results of works of Mydin and Wang [31] and Soleimanzadeh and Mydin [36].

3.5. *Degradation Characteristics under Freeze-Thaw Cycles.* Figure 8 shows the results of compressive strength of foamed concrete after 25 freeze-thaw cycles as a function of density. As a reference, results from untreated samples are shown in Figure 8. The freeze-thaw treatment

of the specimens has only minor influence on the compressive strength of foamed concrete. The strengths obtained for the specimens subjected to freeze-thaw cycles showed approximately 15% lower values. The results were approximated with polynomial functions as shown in Figure 8.

#### 4. Conclusions

Foamed concrete can achieve much lower densities (400 to 1400 kg/m³) in comparison to conventional concrete. A

series of tests was carried out to examine the mechanical parameters of foamed concrete: compressive strength, flexural strength, and modulus of elasticity. Furthermore, the influence of 25 cycles of freezing and thawing on the compressive strength was examined.

The main conclusions that can be drawn from this study are the following:

- (i) The dosage of foaming agent influences the density of mix and hardened foamed concrete. The density of foamed concrete is strongly correlated with the foam content in the mix.
- (ii) The compressive strength, modulus of elasticity, and flexural strength decreased with the decrease of the density of the foamed concrete; the polynomial functions were suggested to describe these relationships.
- (iii) The compressive strength and modulus of elasticity of foamed concrete were slightly decreased by the addition of 5% of fly ash.
- (iv) The compressive strength of foamed concrete subjected to freeze-thaw tests shows the values only approximately 15% lower comparing to untreated specimens.

## Conflicts of Interest

The authors declare that they have no conflicts of interest.

## Acknowledgments

This work was supported by the ongoing research project “Stabilization of weak soil by application of layer of foamed concrete used in contact with subsoil” (LIDER/022/537/L-4/NCBR/2013) financed by the National Centre for Research and Development within the LIDER Programme. The authors gratefully acknowledge the skills and commitment of laboratory technician Alfred Kukielka, without whom the present study could not have been successfully completed.

## References

- [1] S. Van Deijk, *Foamed Concrete: In A Dutch View*, British Cement Association, Blackwater, UK, 1992.
- [2] R. Ramamurthy, E. K. Kunhanandan Nambiar, and G. Indu Siva Ranjani, “A classification of studies on properties of foam concrete,” *Cement and Concrete Composites*, vol. 31, no. 6, pp. 388–396, 2009.
- [3] R. C. Valore, “Cellular concrete part 1 composition and methods of production,” *ACI Journal Proceedings*, vol. 50, no. 5, pp. 773–796, 1954.
- [4] R. C. Valore, “Cellular concrete part 2 physical properties,” *ACI Journal Proceedings*, vol. 50, no. 6, pp. 817–836, 1954.
- [5] G. Rudnai, *Lightweight Concretes*, Akademiai Kiado, Budapest, Hungary, 1963.
- [6] A. Short and W. Kinniburgh, *Lightweight Concrete*, Asia Publishing House, Delhi, India, 1963.
- [7] M. R. Jones and A. McCarthy, “Preliminary views on the potential of foamed concrete as a structural material,” *Magazine of Concrete Research*, vol. 57, no. 1, pp. 21–31, 2005.
- [8] D. Aldridge, “Introduction to foamed concrete: what, why, how?,” in *Use of Foamed Concrete in Construction: Proceedings of the International Conference, Dundee, Scotland, UK*, K. Ravindra, D. Moray, and M. Aikaterini, Eds., vol. 5, pp. 1–14, July 2005.
- [9] R. K. Dhir, M. D. Newlands, and A. McCarthy, *Use of Foamed Concrete in Construction*, Thomas Telford, London, UK, 2005.
- [10] M. Drusa, L. Fedorowicz, M. Kadela, and W. Scherfel, “Application of geotechnical models in the description of composite foamed concrete used in contact layer with the subsoil,” in *Proceedings of the 10th Slovak Geotechnical Conference on Geotechnical Problems of Engineering Constructions*, Bratislava, Slovakia, May 2011.
- [11] L. Fedorowicz, M. Kadela, and Ł. Bednarski, “Modeling of the foamed concrete behavior for the layered structures cooperating with subsoil,” in *Technical Notes of Katowice School of Technology*, vol. 6, pp. 73–81, Katowice School of Technology, Katowice, Poland, 2014.
- [12] J. Hulimka, A. Knoppik-Wróbel, R. Krzywoń, and R. Rudišin, “Possibilities of the structural use of foamed concrete on the example of slab foundation,” in *Proceedings of the 9th Central European Congress on Concrete Engineering*, pp. 67–74, Wrocław, Poland, June 2013.
- [13] M. Kadela and M. Kozłowski, “Foamed concrete layer as substructure of industrial concrete floor,” *Procedia Engineering*, vol. 161, pp. 468–476, 2016.
- [14] M. R. Jones and A. McCarthy, “Behaviour and assessment of foamed concrete for construction applications,” in *Use of Foamed Concrete in Construction: Proceedings of the International Conference, Dundee, Scotland, UK*, K. Ravindra, D. Moray, and M. Aikaterini, Eds., vol. 5, pp. 61–88, July 2005.
- [15] W. Tian, L. Li, X. Zhao, M. Zhou, and N. Wang, “Application of foamed concrete in road engineering,” in *Proceedings of International Conference on Transportation Engineering*, ASCE, pp. 2114–2120, Chengdu, China, July 2009.
- [16] K. K. B. Siram and K. Arjun Raj, “Concrete + Green = Foam Concrete,” *International Journal of Civil Engineering and Technology*, vol. 4, pp. 179–184, 2013.
- [17] A. S. Moon and V. Varghese, “Sustainable construction with foam concrete as a green building material,” *International Journal of Modern Trends in Engineering and Research*, vol. 2, pp. 13–16, 2014.
- [18] A. S. Moon, V. Varghese, and S. S. Waghmare, “Foam concrete as a green building material,” *International Journal of Research in Engineering and Technology*, vol. 2, pp. 25–32, 2015.
- [19] P. Chindaprasirt, S. Homwuttivong, and V. Sirivivatnanon, “Influence of fly ash fineness on strength, drying shrinkage and sulfate resistance of blended cement mortar,” *Cement and Concrete Research*, vol. 34, no. 7, pp. 1087–1092, 2004.
- [20] P. Chindaprasirt and S. Rukzon, “Strength, porosity and corrosion resistance of ternary blend Portland cement, rice husk ash and fly ash mortar,” *Construction and Building Materials*, vol. 22, no. 8, pp. 1601–1606, 2008.
- [21] E. P. Kearsley and P. J. Wainwright, “The effect of high fly ash content on the compressive strength of foamed concrete,” *Cement and Concrete Research*, vol. 31, no. 1, pp. 106–112, 2001.
- [22] N. A. Rahman, Z. M. Jaini, and N. N. Zahir, “Fracture energy of foamed concrete by means of the three-point bending tests on notched beam specimens,” *Journal of Engineering and Applied Sciences*, vol. 10, pp. 6562–6570, 2015.
- [23] M. Kozłowski, M. Kadela, and A. Kukielka, “Fracture energy of foamed concrete based on three-point bending test on notched beams in Proceedings of the 7th Scientific-Technical Conference on Material Problems in Civil Engineering MAT-BUD’2015,” *Procedia Engineering*, vol. 108, pp. 349–354, 2015.

- [24] M. Kozłowski, M. Kadela, and M. Gwózdź-Lasoń, “Numerical fracture analysis of foamed concrete beam using XFEM method,” *Applied Mechanics and Materials*, vol. 837, pp. 183–186, 2016.
- [25] M. Kadela, A. Cińcio, and M. Kozłowski, “Degradation analysis of notched foam concrete beam,” *Applied Mechanics and Materials*, vol. 797, pp. 96–100, 2016.
- [26] A. Cińcio, M. Kozłowski, M. Kadela, and D. Dudek, “Numerical degradation analysis of foamed concrete beam,” in *Proceedings of the 13th International Conference on New Trends in Statics and Dynamics of Buildings, Slovak university of Technology*, Bratislava, Slovakia, October 2015.
- [27] M. Kozłowski, M. Kadela, and M. Gwózdź-Lasoń, “XFEM fracture analysis of notched foamed concrete beams,” in *Proceedings of the 13th International Conference on New Trends in Statics and Dynamics of Buildings, Slovak university of Technology*, Bratislava, Slovakia, October 2015.
- [28] M. Kozłowski and M. Kadela, “Experimental and numerical investigation of fracture behavior of foamed concrete based on three-point bending test of beams with initial notch,” in *Proceedings of the International Conference on Mechanical, Civil and Material Engineering*, Barcelona, Spain, August 2015.
- [29] Technical Data Sheet CEM I 42.5 R, <http://www.gorazdze.pl>.
- [30] T. Xianjun, C. Weizhong, H. Yingge, and W. Xu, “Experimental Study of Ultralight (<300 kg/m<sup>3</sup>) Foamed Concrete,” *Advances in Materials Science and Engineering*, vol. 2014, Article ID 514759, 7 pages, 2014.
- [31] M. A. O. Mydin and Y. C. Wang, “Mechanical properties of foamed concrete exposed to high temperatures,” *Construction and Building Materials*, vol. 26, no. 1, pp. 638–654, 2012.
- [32] K. Jitchaiyaphum, T. Sinsiri, and P. Chindaprasirt, “Cellular lightweight concrete containing pozzolan materials,” *Procedia Engineering*, vol. 14, pp. 1157–1164, 2011.
- [33] M. A. Sipple, “High strength self-compacting foam concrete. initial thesis report,” ACME, UNSW@ADFA, [https://www.researchgate.net/publication/265483433\\_Structural\\_Strength\\_Self-Compacting\\_Foam\\_Concrete](https://www.researchgate.net/publication/265483433_Structural_Strength_Self-Compacting_Foam_Concrete), 2009.
- [34] A. K. Marunmale and A. C. Attar, “Designing, developing and testing of cellular lightweight concrete brick (CLC) wall built in rat-trap bond,” *Current Trends in Technology and Sciences*, vol. 3, pp. 331–336, 2014.
- [35] M. Kadela and A. Kukielka, “Influence of foaming agent content in fresh concrete on elasticity modulus of hard foam concrete,” in *Brittle Matrix Composites 11-Proceedings of the 11th International Symposium on Brittle Matrix Composites BMC 2015, Institute of Fundamental Technological Research PAS*, pp. 489–496, Warszawa, Poland, September 2015, ISBN: 978-838968796-8.
- [36] S. Soleimanzadeh and M. A. O. Mydin, “Influence of high temperatures on flexural strength of foamed concrete containing fly ash and polypropylene fiber,” *International Journal of Engineering*, vol. 26, no. 2, pp. 117–126, 2013.